Ludwig-Maximilians-Universität

The internal structure of Cold Dark Matter Haloes

Dissertation der Fakultät für Physik
der Ludwig-Maximilians-Universität München
für den Grad des
Doctor rerum naturalium

vorgelegt von Mark Philipp Vogelsberger
aus Bad Kreuznach

München, 10.9.2009

1. Gutachter: Prof. Dr. Simon D. M. White

2. Gutachter: Prof. Dr. Andreas M. Burkert

Tag der mündlichen Prüfung: 23.4.2010

Contents

Zusammenfassung

Derzeit favorisierte kosmologische Modelle zur Strukturbildung im Universum nehmen an, dass ein großer Anteil der darin enthaltenen Masse "dunkel" ist. Diese Dunkle Materie verrät sich durch ihren gravitativen Einfluss. Beispiele hierfür sind die flachen Rotationskurven von Spiralgalaxien und die hohen Geschwindigkeiten von Galaxien in Galaxienhaufen. Der Gravitationslinseneffekt kann heutzutage dazu verwendet werden, die Verteilung Dunkler Materie zu vermessen. Trotz der Tatsache, dass Hinweise für Dunkle Materie seit nun mehr als 75 Jahre vorhanden sind, ist immer noch nicht verstanden, woraus sie besteht. Die Teilchenphysik bietet einige interessante und gut motivierte Kandidaten, aber das gesuchte Dunkle Materie Teilchen wurde bisher noch nicht entdeckt. Aus diesem Grund ist die Suche nach Dunkler Materie eines der gemeinsamen Hauptanliegen von Kosmologie und Teilchenphysik. Die einzige Möglichkeit, die Dunkle Materie Hypothese zu beweisen, ist der direkte Nachweis von Dunkle Materie Teilchen. Experimente verwenden hierzu verschiedene Techniken zum Nachweis dieser Teilchen. All diese Experimente benötigen jedoch Informationen über die Dichte- und Geschwindigkeitsverteilung der Dunklen Materie. Diese kann nur mittels der Kosmologie und der Theorie der Strukturbildung bestimmt werden. Das Ziel dieser Doktorarbeit ist es, die Phasenraumstruktur der Dunklen Materie nahe des Sonnensystems und im Dunklen Materie Halo der Milchstraße vorauszusagen.

Ein großer Teil dieser Arbeit ist der Analyse der grobkörnigen Phasenraumstruktur der Dunklen Materie nahe der Sonne gewidmet. Diese Analyse basiert auf Simulationen des Aquarius Projektes, der derzeit größten Simulation zum Studium Dunkler Materie Halos von der Art, wie sie die Milchstraße umgeben. Basierend auf diesen Rechnungen sagen wir voraus, dass die lokale Dunkle Materie Verteilung sehr gleichförmig ist: die Dichte nahe der Sonne variiert von dem Mittel über eine bestangepasste ellipsoidale Dichtekontur um weniger als 15% bei 99.9% Konfidenz. Die lokale Geschwindigkeitsverteilung ist ebenfalls sehr gleichmäßig, aber sie weicht systematisch von einer (multivariaten) Gauß-Verteilung ab. Die Ursache hierfür ist nicht das Vorhandensein individueller Dunkler Materie Klumpen oder Strömungen, sondern das Auftreten breiter Merkmale in den Verteilungen des Betrags der Geschwindigkeit und der Energieverteilung. Diese Merkmale sind unveränderlich in Raum und Zeit und spiegeln die Entstehungsgeschichte des Dunkle Materie Halos wider. Weiterhin haben diese Merkmale einen signifikanten Einfluss auf die zu erwartenden Signale in WIMP und Axion Suchexperimenten. Beispielsweise können WIMP-Rückstoß-Raten um bis zu $\sim 10\%$ von den zu erwarteten Raten, basierend auf einer bestangepassten multivariaten Gauß-Verteilung, abweichen. Von der Simulation vorhergesagte Axion-Spektren haben ihr Maximum typischerweise bei niedrigeren Frequenzen, als es aufgrund einer multivariaten Gauß-Verteilung zu erwarten wäre. Auch in diesem Fall zeigen die Spektren Merkmale, die durch die Entstehungsgeschichte des Halos hervorgerufen werden. Dies impliziert, dass falls die Detektion von Dunkler Materie zur Routine geworden ist, diese Art von Experimenten es ermöglichen wird, Einblicke in die Entstehungsgeschichte des Halos zu erlangen. Dann wird das Forschungsfeld der "Dunklen Materie Astronomie" aufkeimen.

Der Hauptteil dieser Arbeit beschäftigt sich mit der feinkörnigen Phasenraumstruktur der Dunklen Materie Verteilung nahe der Sonne. Wir präsentieren eine neue und allgemein gültige Methode, um die feinkörnige Phasenraumstruktur im gesamten galaktischen Halo zu berechnen. Ziel dieser Technik ist es, die Struktur Dunkler Materie auf den

Skalen zu bestimmen, die für direkte und indirekte Detektionsexperimente relevant sind. Unsere Methode basiert auf der Gleichung für die geodätische Abweichung, die für jedes individuelle Simulationsteilchen gelöst wird. Die Technik benötigt keine Annahmen über die Symmetrie oder Stationarität des Halo-Entstehungsprozesses. Wir diskutieren mit der neuen Methode die Phasenraumstruktur allgemeiner statischer Potentiale, die eine kompliziertere Struktur als zuvor analysierte separable Potentiale aufweisen. Wir zeigen, dass für ein ellipsoidales logarithmisches Potential mit einem Kern das Phasenmischen von der Resonanzstruktur und damit von der Zahl unabhängiger fundamentaler Frequenzen abhängt. Unser Methode erlaubt auch die Identifikation chaotischer Phasenraumbereiche, die sich durch einen sehr starken Abfall der Strömungsdichte auszeichnen. Wir berechnen die Strömungsdichten in einem ellipsoidalem NFW Halo Profil mit radial variierender Potentialform und zeigen, dass ein solches Modell ungefähr 10^5 Dunkle Materie Ströme an der Position der Sonne für den dunklen Halo unserer Milchstraße vorhersagt. Der wichtigste und neueste Aspekt der von uns vorgestellten Methode besteht darin, dass sie relativ einfach in kosmologische N-Körper Programme eingebunden werden kann. Wir präsentieren eine solche Implementierung und zeigen, dass Diskretheitseffekte in realistischen Situationen unter Kontrolle gehalten werden können.

Die neu entwickelte Technik erlaubt auch die Analyse von Kaustiken in der Dunklen Materie Verteilung und eine detaillierte Berechnung der durch sie hervorgerufenen Annihilationsstrahlung. Kaustiken sind eine generelle Eigenschaft des nichtlinearen Wachstums kalter Dunkler Materie. Wäre Dunkle Materie absolut kalt, so würde ihre Massendichte in den Kaustiken divergieren, genauso wie die integrierte Annihilationsrate individueller Dunkler Materie Teilchen in der Kaustik. Realistische Dunkle Materie Kandidaten besitzen allerdings eine nicht-verschwindende anfängliche thermische Geschwindigkeit, wodurch dieses divergente Verhalten regularisiert wird. Wir beschreiben ein mathematisches Verfahren zur Analyse dieser Kaustiken. Dieses Schema kann direkt in N-Körper Simulationsprogramme eingebaut werden. Dadurch können dann Kaustiken identifiziert und ihre Annihilationsstrahlung berechnet werden.

Wir verwenden diese Methoden, um die feinkörnige Phasenraumstruktur und Kaustiken von isolierten Halos, die sich aus selbst-ähnlichen und sphärisch symmetrischen Anfangsbedingungen formen, zu analysieren. Wir verwenden ein modifiziertes N-Körper Programm, um die Gleichung für die geodätische Abweichung für jedes einzelne Simulationsteilchen zu lösen. Die radiale Orbitinstabilität hat zur Folge, dass der Halo ein Achsenverhältnis von 10 zu 1 im inneren Bereich entwickelt. Die Halos wachsen ähnlich mit der Zeit und haben ähnliche Dichteprofile wie die sphärische analytische Lösung, aber ihre detaillierte Struktur ist sehr unterschiedlich. Aufgrund der höheren Dimensionalität der Orbits nehmen die Strömungs- und Kaustikdichten viel schneller ab, als in der selbst-ähnlichen Lösung. Hierdurch erhöht sich die Zahl der Strömungen an jedem Punkt des Halos. Bei 1% des Umkehrradius (was ungefähr der Sonnenposition in der Milchstraße entspricht) besitzt der Halo circa 10^6 Strömungen, im Gegensatz zu 10^2 für die selbst-ähnliche Lösung. Die Zahl der Kaustiken im inneren Halo steigt um einige Faktoren an, da ein typischer Orbit nun sechs statt nur zwei Umkehrpunkte hat. Da die Kaustikdichten jedoch signifikant niedriger sind, reduziert sich der Annihilationsbeitrag von Kaustiken zur Gesamtannihilationrate auf 4% im Vergleich zu 6.5% in der selbst-ähnlichen Lösung. Kaustiken tragen sehr viel weniger bei kleinen Radien bei. Diesen

Werten liegt ein 100 GeV c^{-2} Neutralino mit einer heutigen Geschwindigkeitsdispersion von 0.03 cm s^{-1} zugrunde. Eine Reduktion der Dispersion um zehn Größenordnungen führt lediglich zur Verdopplung der Kaustikhelligkeit. Darum sind Kaustiken im Inneren des Halos nicht beobachtbar. Lediglich Kaustiken im Außenbereich können möglicherweise detektiert werden.

Im letzten Teil dieser Arbeit benutzen wir die entwickelten Methoden, um Dunkle Materie Halos, die sich in einem ΛCDM Universum entwickeln, zu analysieren. Wir wenden die Technik auf drei verschiedene Auflösungen des Aq-A Halos aus dem Aquarius Projekt an. Alle Simulationen benutzen die gleiche Softeninglänge, und wir ändern nur die Anzahl der Simulationsteilchen. Wir erreichen damit gute Konvergenz in allen relevanten feinkörnigen Phasenraumeigenschaften: Kaustikdurchgänge, Strömungsdichten, Zahl der Strömungen und Annihilationsstrahlung innerhalb der Strömungen. Nahe des Virialradius finden wir 10^7 Strömungen. Kaustikdichten sind subdominant innerhalb des Virialradius: nahe des Virialradius sind die Kaustikdichten mit der mittleren Halodichte vergleichbar, bei 10% des Virialradius sind die Kaustikdichten allerdings schon um einen Faktor 10^6 kleiner als die mittlere Halodichte. Dies ist eine Folge des effizienten Phasenmischens im Halo. Nahe des Virialradius tragen die Kaustiken ungefähr 10% zur Annihilationsstrahlung bei, aber nur 0.1% bei 10% des Virialradius.

Abstract

Currently favoured cosmological models for structure formation of the Universe assume that a large fraction of the mass of the Universe is "dark". The evidence for dark matter comes from observations of its gravitational influence. Examples such as the flatness of rotation curves of spiral galaxies or the large velocities of galaxies in galaxy clusters are thought to be manifestations of its presence. Gravitational lensing can now also be used to map the dark matter distribution of the Universe. Despite the fact that the evidence for dark matter has existed for more than 75 years, it is still not clear what dark matter is made of. Particle physics provides some interesting and well-motivated candidates, but the elusive dark matter particles have not yet been detected. Therefore, the hunt for dark matter is one of the major joint efforts of cosmology and particle physics. The only way to prove the dark matter hypothesis is the direct detection of dark matter particles in a laboratory. Experiments exploit various techniques to detect dark matter particles. All of these experiments require as input the phase-space distribution of dark matter. This means they require information on the configuration-space and velocity-space distributions. These insights can only come from cosmology and the theory of structure formation in the Universe. The goal of this thesis is to predict the expected dark matter phase-space distribution near the solar system and in the dark matter halo of the Milky Way.

A large part of this thesis is dedicated to a detailed analysis of the coarse-grained dark matter distribution near the Sun based on the Aquarius project, the currently largest set of Milky Way-like dark matter halo simulations. Based on these simulations we predict the local dark matter density distribution to be remarkably smooth: the density at the Sun differs from the mean over a best-fit ellipsoidal equidensity contour by less than 15% at the 99.9% confidence level. The local velocity distribution is also very smooth, but it differs systematically from a (multivariate) Gaussian distribution. This is not due to the presence of individual clumps or streams, but to broad features in the velocity modulus and energy distributions that are stable both in space and time and reflect the detailed assembly history of each halo. These features have a significant impact on the signals predicted for WIMP (weakly interacting massive particle) and axion searches. For example, WIMP recoil rates can deviate by $\sim 10\%$ from those expected from the best-fit multivariate Gaussian models. The axion spectra in the simulations typically peak at lower frequencies than in the case of multivariate Gaussian velocity distributions. Also in this case, the spectra show significant imprints of the formation of the halo. This implies that once direct dark matter detection has become routine, features in the detector signal will allow the study of the dark matter assembly history of the Milky Way. A new field, "dark matter astronomy", will then emerge.

The main part of this thesis focuses on the fine-grained phase-space structure of the dark matter distribution near the Sun. A new and completely general technique for calculating the fine-grained phase-space structure of dark matter throughout the Galactic halo is presented. Its goal is to understand dark matter structure on the scales relevant for direct and indirect detection experiments. The method is based on evaluating the geodesic deviation equation along the trajectories of individual dark matter simulation particles. It requires no assumptions about the symmetry or stationarity of the halo formation process. General static potentials that exhibit more complex behaviour than the separable potentials studied previously are discussed. For ellipsoidal logarithmic potentials with a core, phase mixing is sensitive to the resonance structure, as indicated by the number of

independent orbital frequencies. Regions of chaotic mixing can be identified by the very rapid decrease in the configuration-space density of the associated dark matter streams. A relevant analysis is made on the evolution of the stream density in ellipsoidal NFW haloes with radially varying isopotential shape, showing that if such a model is applied to the Galactic halo, at least 10^5 streams are expected near the Sun. The most novel aspect of the new approach is that general non-static systems can be studied through its implementation in cosmological N-body codes. The new scheme is embedded in a current state-of-the-art N-body code. Tests demonstrating that N-body discreteness effects can be kept under control in realistic configurations are presented.

The new method also allows an analysis of caustics in the dark matter distribution and a detailed calculation of the annihilation radiation associated with them. Caustics are a generic feature of the nonlinear growth of structure in the dark matter distribution. If the dark matter were absolutely cold, its mass density would diverge at caustics, and the integrated annihilation probability would also diverge for individual particles participating in them. For realistic dark matter candidates, this behaviour is regularised by small but non-zero initial thermal velocities. A mathematical treatment of evolution from hot, warm or cold dark matter initial conditions is given. This scheme can be directly implemented in cosmological N-body codes. It allows the identification of caustics and the estimation of their annihilation radiation in fully general simulations of structure formation.

The methods developed for the fine-grained phase-space and caustic analysis are applied to the growth of isolated dark matter haloes from self-similar and spherically symmetric initial conditions. A modified N-body code integrates the geodesic deviation equation in order to track the streams and caustics associated with individual simulation particles. The radial orbit instability causes the haloes to develop major-to-minor axis ratios approaching 10 to 1 in their inner regions. They grow similarly in time and have similar density profiles to the spherical similarity solution, but their detailed structure is very different. The higher dimensionality of the orbits causes their stream and caustic densities to drop much more rapidly than in the similarity solution. This results in a corresponding increase in the number of streams at each point. At 1% of the turnaround radius (corresponding roughly to the Sun's position in the Milky Way) we find of order 10^6 streams in our simulations, as compared to 10^2 in the similarity solution. The number of caustics in the inner halo increases by a factor of several, because a typical orbit has six turning points rather than one, but caustic densities drop by a much larger factor. This reduces the caustic contribution to the annihilation radiation. For the region between 1% and 50% of the turnaround radius, this is 4% of the total in our simulated haloes, as compared to 6.5% in the similarity solution. Caustics contribute much less at smaller radii. These numbers assume a 100 GeV c^{-2} neutralino with present-day velocity dispersion 0.03 cm s^{-1}, but reducing the dispersion by ten orders of magnitude only doubles the caustic luminosity. Therefore, caustics will be unobservable in the inner parts of haloes. Only the outermost caustic might potentially be detectable.

Finally, we present results on the fine-grained phase-space structure of cold dark matter haloes growing in the concordance ΛCDM cosmology. We use the geodesic deviation technique to follow the local phase-space evolution of individual simulation particles, and we apply this method to three different resolutions of the Aq-A halo of the Aquarius project. We use a fixed softening length and only change the number of particles. Good

convergence is achieved for all fine-grained properties of the halo: caustic passages, stream densities, number of streams and intra-stream annihilation radiation. At the virial radius we expect about 10^7 streams. We find caustic densities to be subdominant within the virial radius: at the virial radius the maximum caustic density is comparable to the mean halo density, whereas at 10% of the virial radius the caustic density is already a factor 10^6 smaller than the mean density. We attribute this to the very efficient phase-space mixing. The contribution of caustics to the annihilation radiation at the turnaround radius is about 10%, but well below 0.1% at 10% of the virial radius.

Introduction

Mankind has always asked the question "Where do we come from?". Both religion and philosophy came up with ideas on how to answer this question. But none of these were scientific in the sense they were based on constructions of ideas rather than empirical facts. Astronomy, being the oldest scientific discipline, has contributed to these questions significantly from the very beginning, with human curiosity as the main driver in that field. But it was a long way until cosmology as a branch of astronomical research became a precision science in its modern sense. Early discussions of cosmological ideas had more the flavour of philosophical and metaphysical debates on the origin of our Universe. It was during the last century when this changed for the first time and dramatically. We are nowadays in a position where modern science can attempt to go very close to the creation of the Universe and to understand how it works in detail.

It is the passion for understanding our Universe and our existence that has driven all major breakthroughs in cosmology. The main engines for this progress, especially over the last decades, have been the development of path-breaking observational techniques that could, for the first time, confirm ideas about our Universe and therefore remove the pure philosophical character from cosmology and turn it into one of the most exciting scientific adventures of the current epoch.

It was back in the 60s of the last century when the radiation of the cosmic microwave background (CMB) was accidentally found by Penzias and Wilson. This radiation was predicted by Gamow in the 40s as the afterglow of the Big Bang. It was the first piece of evidence for the hot big bang model, which is today the standard model for the beginning and evolution of our Universe. CMB observations became more precise over the last decades and it is today possible to see what the Universe looked like just about 380.000 years after the Big Bang happened. At the beginning of the 21st century the WMAP satellite has seen the seeds of structure formation in this radiation as tiny temperature variations. Therefore we are today in a position where we are closer to the birth of our Universe than ever before. It is an enormous success of mankind understanding to investigate the full Universe and its history based on observations from a tiny planet called Earth.

It is not only the kind of questions cosmology asks that makes it different from many other scientific disciplines, it is also the speed of development of the field. A good example of dramatic changes in cosmology is the discovery of the cosmological constant. This is a hundred years old story which began when Einstein formulated his theory of general relativity as a necessary extension of Newton's theory of gravity. This theory was a major breakthrough in our interpretation of the space-time, postulating that matter deforms it. When Einstein wrote down his equations, he found that they do not allow a static

Universe. But at this time it was generally believed that the Universe was static, neither expanding nor contracting. Thus his equations seemed to be wrong when applied to the whole Universe. To rescue his theory and get a static solution, he added a now famous term to these equations: the so-called cosmological constant Λ. This made them compatible with a static Universe. Some years later Hubble found that the Universe is not static, but expanding, so there was no need for Λ anymore. Later, Einstein thought that the introduction of the cosmological constant was the biggest mistake he ever made in his life. In following decades most people assumed that Λ was zero and was not required to describe our Universe. The cosmological constant died, so to speak, with Hubble's observation of the expanding Universe. But in the late 90s of the last century two supernovae observation groups realised that our Universe seems to expand faster than in the past: it shows an accelerated expansion. This behaviour could only be explained by a Λ-like term in Einstein's equations. This term contributes about 70% of the total energy density of our Universe today! From one day to the next, cosmologists realised that they had missed 70% of the Universe in all their equations. One should remember that this dramatic change happened just 10 years ago! This shows how fast the field is evolving. Today the phenomena is given the more general name "dark energy".

Although cosmology is evolving so fast it also has long standing problems just like other fields of science. One of the biggest mysteries is the so-called "dark matter" problem. This dates back to observations by Zwicky in 1933. He observed galaxies in the Coma cluster, measuring how fast they move through this cluster. To his surprise, he found that they are moving extremely fast, so fast that they should fly right out of the cluster, because there appeared to be too little mass to gravitationally bind them to the cluster. Since the cluster seems stable and long lived, Zwicky inferred that it must be a lot heavier than expected based on the estimated masses of all the galaxies. Some unseen matter component what glue the cluster together through its gravitational attraction. This was the birth of the "unseen" or "dark" matter problem. This name simply reflects the fact that there appears to be matter present, but it does not emit any electromagnetic radiation. Later in the 70s Rubin found a similar problem when she observed spiral galaxies. She realised that the outer regions of these galaxies are rotating too fast to be held in by the visible stars. The only explanation was to assume some sort of dark matter halo surrounding the galaxy that keeps the stars and gas together. Nowadays we have even more evidence for dark matter coming from detailed observations of the CMB and from gravitational lensing studies. Lensing studies are sensitive to the bending of light by matter as predicted by Einstein's theory of general relativity. This traces all kind of matter, including dark matter. All these different observations consistently indicate that about 25% of the Universe consists of dark matter.

The bottom line of current state-of-the-art cosmology is therefore, that we do not know what $(70 + 25)\% = 95\%$ of the Universe is made of! We only know 5% of the Universe. This tiny amount accounts for all the stars, galaxies, planets, gas, and any life-forms like the reader of this thesis.

This fact shows that although cosmology is evolving fast, it is still facing some of the most fundamental unresolved questions of Nature; it has not given an answer to the question: "What is the Universe made of?" This is a very serious problem, but also an exciting one.

The dark energy and dark matter problems are qualitatively different. The dark energy component accounts for 70% of the Universe today but at earlier times it was subdominant and the Universe was dominated by dark matter or (at very early times) by radiation. To explain the growth of structure and the evolution of the Universe from early times until today, it is more critical to understand the dark matter problem.

Dark matter has another big advantage. Most of the dark matter candidates offer a possibility of direct detection. Modern cosmological theories assume that galaxies like the Milky Way are embedded in a large halo of dark matter particles. If this is true, the Earth is flying through a sea of dark matter particles and everything on Earth is penetrated by a constant flux of dark matter particles. Many theories predict that dark matter particles should interact with ordinary matter via weak interactions. Therefore, it should at least in principle be possible to detect these mysterious particles using a sensitive enough detector. Unfortunately, detection is not straightforward. The main complication is that the cross-section for reactions between the detector material and the elusive dark matter particle is extremely small, even smaller than that for neutrino interactions. Therefore, it is extremely hard to detect these particles. Another problem is that the dark matter particle properties are not strongly constrained. It is therefore, a strange situation: We assume that there is a constant flux of dark matter particles through the solar system, but nevertheless the detection is difficult because of the low reaction cross-sections. Currently more than 20 experiments all over the world search for the elusive dark matter particle.

Another way of dark matter detection exploits the fact that some dark matter candidates are able to self-annihilate: if two of them collide, they can produce γ-radiation and standard model particles. This radiation should be strongest in the densest regions of the dark matter distribution. These are the centres of haloes or subhaloes of dark matter, where, for example, the Milky Way is embedded. Many experiments are also searching for these signals. Recently, PAMELA and other experiments reported anomalies in the cosmic ray spectra that could be due to dark matter annihilation. But until now ordinary astrophysical explanations cannot be excluded.

For dark matter search experiments it is useful to know how the dark matter particles are distributed in the Galactic halo. Especially, for direct searches it is important to know how dark matter is distributed near the solar system, since the detection rates depend on the dark matter phase-space distribution.

How can we predict the distribution of something when we do not know what it is? It is true that we currently do not know what dark matter is made of, but we know how it should behave. It interacts almost exclusively gravitationally with itself and other matter and so evolves like a collisionless self-gravitating fluid. Due to the great progress spend in CMB observations, we now know the initial conditions for nonlinear structure formation in the Universe. Based on these initial conditions we can follow the evolution of the dark matter particles. The equations of motion need to be modified only slightly to account for dark energy that is negligible at the beginning of structure formation but dominant today. Modern cosmology uses large supercomputers to solve these equations and create a virtual Universe in the computer. One can then use these models to get an idea about the dark matter distribution of our Universe.

The goal of this thesis is to use such computer simulations to predict the dark matter

distribution near the Sun and therefore supply dark matter search experiments with the required dark matter phase-space distribution. This is a challenging problem and it has only become possible within the last years to run simulations with enough resolution for this task. In this thesis we will present results based on the biggest computer simulation project following the structure formation of Milky Way-like dark matter haloes. We use a set of simulations to analyse the phase-space structure near the Sun and predict dark matter detector signals for the first time. Although the simulations of this project are the biggest done so far, they are still quite limited if one is interested in the smallest length scales relevant for dark matter searches. We therefore present a completely new technique to analyse the dark matter distribution on scales far below what is possible today with standard dark matter simulations. This new technique allows us to make predictions for the fine-grained phase-space structure of dark matter haloes. In this thesis we present the most detailed predictions for the dark matter distribution to date.

The first three chapters of this thesis present an introduction to the field of cosmology and dark matter. In the first chapter we describe the basics of general relativity. Based on this, we derive the Friedmann equations that describe the evolution of a homogeneous and isotropic Universe. In the second chapter we focus on the question how structure can grow in an expanding Universe. We demonstrate that this can easily be done analytically in the linear regime, where structure formation is driven by small density fluctuations about a uniform density distribution. In the third chapter we will present some observational facts that point towards the existence of dark matter. We close that chapter with explaining the main techniques used to run computer simulations of structure formation. We start our detailed study of the dark matter distribution in the second part of this thesis. In chapter 4 we use a set of very high resolution dark matter simulations to predict the phase-space structure of dark matter near the Sun. There we also present expected direct detection results based on these simulations. In chapter 5 we present a new method that can be used to resolve the fine-grained phase-space structure of cold dark matter haloes. We demonstrate this using static potentials and present a working implementation in a cosmological simulation code. This method allows to go far beyond the coarse-grained phase-space analysis of chapter 4. Chapter 6 is based on chapter 5 and describes how to handle phase-space catastrophes, so-called caustics, to account correctly for their annihilation radiation. We also show there how this can be implemented in simulation codes to track caustics and their radiation correctly. In chapter 7 we apply the methods developed in the previous two chapters to a simplified halo formation model. This model was used by many other authors to analyse the fine-grained structure of cold dark matter haloes. We show that all these studies are incorrect because they do not describe correctly the physics of the formation process. Most notably, they all miss instabilities that completely alter the fine-grained phase-space structure of the developing dark matter halo. This has direct implications for direct and indirect dark matter searches. In chapter 8 we apply the methods of the fifth and sixth chapter to the haloes studied in chapter 4. This allows us finally and for the first time to analyse the fine-grained phase-space structure of haloes forming in the full cosmological framework. In the last part of this thesis we give our conclusions.

What is the path? There is no path. On into the unknown.

Faust, Goethe

Part I

General overview

1

Cosmology - a brief introduction

In this chapter we present the mathematical foundations of modern cosmology. We start by giving a brief overview of our current understanding of gravity as the main actor on cosmological scales. We describe gravity by Einstein's general relativity that relates the geometry of space-time with matter and energy in terms of Einstein's field equations. Based on the cosmological principle we can derive the Friedmann equations that describe the evolution of a homogeneous and isotropic Universe. At the end of this chapter we introduce some cosmological and astrophysical vocabulary that will be used in the rest of this thesis.

The results of this and the next chapter can be found in standard textbooks like Weinberg (1972); Misner et al. (1973); Coles and Lucchin (1995); Peacock (1999).

1.1 Theory of gravity - General Relativity

The dominating force on the large scales of the Universe is gravity. Currently, the best theory for gravity is Einstein's general relativity developed at the beginning of the last century (Einstein, 1916, 1917). We will here describe briefly the key results needed to understand the basic equations of cosmology.

In special relativity the invariant interval $\mathrm{d}s$ between two events at space-time coordinates (t, x, y, z) and $(t + \mathrm{d}t, x + \mathrm{d}x, y + \mathrm{d}y, z + \mathrm{d}z)$ is given by

$$\mathrm{d}s^2 = c^2\mathrm{d}t^2 - (\mathrm{d}x^2 + \mathrm{d}y^2 + \mathrm{d}z^2). \tag{1.1}$$

This is invariant under Lorentz coordinate transformations and describes distances in Minkowski space-time. One of the fundamental ideas of general relativity is that matter can change the metric of space-time from the flat Minkowski space to a curved space-time, where we write (using Einstein's sum convention)

$$\mathrm{d}s^2 = g_{\mu\nu}\mathrm{d}x^\mu\mathrm{d}x^\nu \qquad \mu, \nu = 0, \ldots, 3, \tag{1.2}$$

where $x^0 = ct$ is the time coordinate, x^1, x^2, x^3 are space coordinates and $g_{\mu\nu}$ is the metric. The equations of motion for particles in such a space-time can be derived from the stationarity of their path

$$\delta \int_{\mathrm{path}} \mathrm{d}s = 0. \tag{1.3}$$

From this equation we can deduce the geodesic equation of motion for a test particle

$$\frac{\mathrm{d}^2x^\lambda}{\mathrm{d}s^2} + \Gamma^\lambda_{\mu\nu}\frac{\mathrm{d}x^\mu}{\mathrm{d}s}\frac{\mathrm{d}x^\nu}{\mathrm{d}s} = 0, \tag{1.4}$$

where Γ are the Christoffel symbols

$$\Gamma^\lambda_{\mu\nu} = \frac{1}{2}g^{\lambda\sigma}\left[\frac{\partial g_{\sigma\mu}}{\partial x^\nu} + \frac{\partial g_{\sigma\nu}}{\partial x^\mu} - \frac{\partial g_{\mu\nu}}{\partial x^\sigma}\right]. \tag{1.5}$$

Let us next define the energy-momentum tensor $T_{\mu\nu}$ for a perfect fluid with pressure P and energy density ρ,

$$T_{\mu\nu} = (P + \rho c^2)U_\mu U_\nu - P g_{\mu\nu}, \tag{1.6}$$

where $U_\mu = g_{\mu\nu}\mathrm{d}x^\nu/\mathrm{d}s$ denotes the four-velocity. We can write down a covariant conservation law as

$$T^\nu_{\mu\,;\nu} = 0, \tag{1.7}$$

where ; stands for the covariant derivative of a tensor

$$A^\alpha_{;\beta} = \frac{\partial A^\alpha}{\partial x^\beta} + \Gamma^\alpha_{\beta\gamma}A^\gamma. \tag{1.8}$$

The energy-momentum tensor describes the distribution of matter and so the sources of gravity. The main point of general relativity is the link between matter and metric. Let us therefore first define the Riemann-Christoffel tensor

$$R^{\lambda}_{\mu\nu\rho} = \frac{\partial \Gamma^{\lambda}_{\mu\rho}}{\partial x^{\nu}} - \frac{\partial \Gamma^{\lambda}_{\mu\nu}}{\partial x^{\rho}} + \Gamma^{\lambda}_{\sigma\nu}\Gamma^{\sigma}_{\mu\rho} - \Gamma^{\lambda}_{\sigma\rho}\Gamma^{\sigma}_{\mu\nu}, \tag{1.9}$$

that can be used to measure curvature of space-time. From this tensor we can construct the Ricci tensor $R_{\mu\nu} = R^{\sigma}_{\mu\sigma\nu}$ and the Ricci scalar $R = g^{\sigma\rho}R_{\sigma\rho}$. Finally we can define the Einstein tensor

$$G_{\mu\nu} = R_{\mu\nu} - \frac{1}{2}g_{\mu\nu}R. \tag{1.10}$$

With this tensor we can formulate Einstein's field equations

$$G_{\mu\nu} = \frac{8\pi G}{c^4}T_{\mu\nu}, \tag{1.11}$$

where the prefactor $8\pi G/c^4$ ensures that Poisson's equation results in the limit of a weak gravitational field. As we will show below these field equations do not allow a static Universe. At the time when Einstein developed his theory there were no hints for a non-static Universe, so he introduced a cosmological constant to allow static solutions. The modified Einstein tensor has the following form

$$G_{\mu\nu} = R_{\mu\nu} - \frac{1}{2}g_{\mu\nu}R - \Lambda g_{\mu\nu} = \frac{8\pi G}{c^4}T_{\mu\nu}, \tag{1.12}$$

where Λ is the constant introduced.

1.2 Cosmological Principle and the Metric of the Universe

The cosmological principle states that on sufficiently large scales the Universe is both homogeneous and isotropic. On these scales its properties are therefore identical everywhere in space (homogeneous) and it looks the same in all directions (isotropic). It can be shown that the most general space-time metric describing a Universe in which the Cosmological Principle holds is given by

$$\mathrm{d}s^2 = (c\mathrm{d}t)^2 - a(t)^2\left[\frac{\mathrm{d}r^2}{1-Kr^2} + r^2(\mathrm{d}\theta^2 + \sin^2\theta\mathrm{d}\phi^2)\right], \tag{1.13}$$

where r, θ, ϕ are comoving spherical coordinates, t is the proper time, $a(t)$ is the scale factor describing the time evolution of the homogeneous Universe and K characterises its spatial curvature taking the values 1 (closed), 0 (flat) or -1 (open). This metric is called the Robertson-Walker metric. We note that this result was derived without using Einstein's field equations. The metric is a pure consequence of the Cosmological Principle.

1.3 The Friedmann equations

To derive the time evolution of the Universe as given by the time dependence of the scale factor, we need to relate $a(t)$ to the energy content. For this, we use Einstein's field equations. If we put the Robertson-Walker metric into these field equations and assume a perfect fluid we can derive the following two equations (known as the Friedmann equations) for the scale factor by matching the time-time and space-space components (space-time components merely give $0 = 0$)

$$\frac{\ddot{a}}{a} = -\frac{4\pi G}{3}\left(\rho + 3\frac{P}{c^2}\right), \tag{1.14}$$

$$\left(\frac{\dot{a}}{a}\right)^2 = \frac{8\pi G}{3}\rho - \frac{Kc^2}{a^2}. \tag{1.15}$$

The first Friedmann equation shows that a static Universe is only possible if $\rho = -3P/c^2$, so either the energy density or the pressure must be negative. Adding the cosmological constant to the Einstein tensor yields the following slightly modified Friedmann equations

$$\begin{aligned}\frac{\ddot{a}}{a} &= -\frac{4\pi G}{3}\left(\rho + 3\frac{P}{c^2}\right) + \frac{\Lambda c^2}{3},\\ \left(\frac{\dot{a}}{a}\right)^2 &= \frac{8\pi G}{3}\rho - \frac{Kc^2}{a^2} + \frac{\Lambda c^2}{3}.\end{aligned} \tag{1.16}$$

1.4 Cosmological vocabulary and relations

Hubble function: A very useful quantity is the Hubble function or Hubble parameter defined as

$$H = \frac{\dot{a}}{a}. \tag{1.17}$$

The current value $H(t_0)$, where t_0 stands for the present time, is denoted as H_0 and usually parametrised in the following way

$$H_0 = \left.\frac{\dot{a}}{a}\right|_{t_0} = 100h\frac{\text{km s}^{-1}}{\text{Mpc}}, \tag{1.18}$$

where we introduced h to parametrise H_0.

Redshift: The redshift z has a fundamental importance in cosmology. It is defined as

$$z = \frac{\lambda_{\text{obs}} - \lambda_{\text{em}}}{\lambda_{\text{em}}} = \frac{\lambda_{\text{obs}}}{\lambda_{\text{em}}} - 1 = \frac{\nu_{\text{em}}}{\nu_{\text{obs}}} - 1, \tag{1.19}$$

where λ_{obs} (ν_{obs}) and λ_{em} (ν_{em}) are the wavelengths (frequencies) observed at Earth and emitted by a distant source, respectively. If we neglect peculiar motion of the emitting object and solve the geodesic equation of the light ray we find the relation

$$z + 1 = \frac{a_{\text{obs}}}{a_{\text{em}}} = \frac{a_0}{a_{\text{em}}}, \tag{1.20}$$

where $a_0 = a(t_0)$ denotes the scale factor today. We note that this red-shifting effect is different from the ordinary Doppler-effect. The cosmological redshift arises due to the expansion of space. It is common to use the redshift as a convenient time variable due to its relation to $t_{\rm em}$ mentioned above. The present epoch is then given by $z = 0$ and the past $z > 0$.

Critical density: To characterise densities it is useful to introduce a reference density. Analysing the Friedmann equations in more detail it turns out that a natural choice for this density is the critical density defined as

$$\rho_c(t) = \frac{3H^2(t)}{8\pi G}. \tag{1.21}$$

In the case $\Lambda = 0$ the Universe is always flat ($K = 0$) if its density equals $\rho_c(t)$. If it is larger, the Universe is closed ($K = 1$), if it is smaller it is open ($K = -1$). This justifies the name critical density. It is convenient to express the contributions of the different components of the Universe in terms of the critical density by defining

$$\Omega_l(t) = \frac{\rho_l(t)}{\rho_c(t)}, \tag{1.22}$$

where l denotes the component (e.g. $\Omega_\Lambda = \Lambda c^2/(3H^2)$). If we refer to the present day values at t_0 we will write Ω_{l0} (e.g. $\Omega_{\Lambda 0} = \Lambda c^2/(3H_0^2)$). The density of component l evolves then as a function of redshift

$$\rho_l(z) = \Omega_l(z)\rho_c(z) = \Omega_{l0}\rho_{c0}(1+z)^{3(1+w)}. \tag{1.23}$$

Using the definitions above we can rewrite the two Friedmann equations in the following way

$$\ddot{a} = a\left(\dot{H} + H^2\right), \tag{1.24}$$

$$H^2 = H_0^2 E^2(z), \tag{1.25}$$

where we defined the function

$$E^2(z) = \left[(1-\Omega_{t0})(1+z)^2 + \Omega_{m0}(1+z)^3 + \Omega_{r0}(1+z)^4 + \Omega_{\Lambda 0}\right], \tag{1.26}$$

where $\Omega_{t0}, \Omega_{m0}, \Omega_{r0}$ are the present-day total, matter and radiation density parameters, respectively. By definition the critical density evolves like

$$\rho_c(z) = \rho_{c0}\ E^2(z), \tag{1.27}$$

and therefore

$$\Omega_l(z) = \frac{\rho_{l0}(1+z)^{3(1+w)}}{\rho_{c0}\ E^2(z)} = \frac{(1+z)^{3(1+w)}}{E^2(z)}. \tag{1.28}$$

Time-redshift relation: In the following we will often denote times by their corresponding redshift values. It is therefore desirable to have the explicit relation between time and

redshift to translate between them. Taking the time derivative of the $a - z$ relation, we obtain

$$\frac{\dot{z}}{1+z} = -\frac{\dot{a}}{a} = -H, \tag{1.29}$$

and

$$\mathrm{d}t = -\frac{\mathrm{d}z}{(1+z)H(z)} = -\frac{1}{H_0}\frac{dz}{(1+z)E(z)} = -t_H\frac{\mathrm{d}z}{(1+z)E(z)}, \tag{1.30}$$

where we have defined the Hubble time t_H as

$$t_H = \frac{1}{H_0} \cong 9.7958\ h^{-1}\ \mathrm{Gyr}. \tag{1.31}$$

The time elapsed between $z \to \infty$ (Big Bang) and arbitrary redshift z can then be calculated via integration as

$$t(z) = \int_z^{+\infty} \frac{\mathrm{d}z'}{(1+z')H(z')} = t_H \int_z^{+\infty} \frac{\mathrm{d}z'}{(1+z')E(z')}. \tag{1.32}$$

The current age of the Universe can be derived from this equation by evaluating $t(z = 0)$.

1.5 The Einstein-de Sitter Universe

As an example for a solution of the Friedmann equations, we will here briefly describe the so-called Einstein-de Sitter (EdS) Universe. This is a dust Universe with critical matter density. Although the discovery of dark energy representing a cosmological constant by observations of supernova SNIa in 1998 clearly rules out this model, it is still a very good approximation at early times, where the contribution of the Λ to the energy density of the Universe is negligible.

The solution of the Friedmann equations is straightforward in the EdS model and we simply state the results, assuming $a_0 = a(t_0) = 1$

Age:

$$t_0 = \frac{2}{3H_0} = \frac{2}{3}\ t_H \cong 6.5h^{-1}\ \mathrm{Gyr}. \tag{1.33}$$

Scale Factor:

$$a(t) = \left(\frac{t}{t_0}\right)^{2/3} \tag{1.34}$$

Hubble Function:

$$H(t) = \frac{2}{3t} \tag{1.35}$$

We note that there is also an analytic solution for a flat Universe with cosmological constant Λ, $\Omega_{\Lambda 0} = 1 - \Omega_{m0}$

$$H_0\ t = \frac{2}{3(1-\Omega m0)^{1/2}} \ln\left[\left(\frac{a}{a_{m\Lambda}}\right)^{3/2} + \left(1 + \left(\frac{a}{a_{m\Lambda}}\right)^{3}\right)^{1/2}\right], \qquad a_{m\Lambda} = \left(\frac{\Omega_{m0}}{\Omega_{\lambda 0}}\right)^{1/3}. \tag{1.36}$$

2

Structure Formation

If we look around in our Universe we can clearly see that it is not homogeneous and isotropic. On the scales of clusters of galaxies or galaxies we clearly see dramatic structures. The development of this structure cannot be described with the homogeneous and isotropic models presented in the last chapter. Here we describe how structure evolves. We will focus on the growth of small density perturbations at early times. We will show how these can be described in linear theory. At the end of this chapter we will also introduce the Zel'dovich approximation that is used to set up initial conditions for N-body simulations.

2.1 The growth of perturbations

In the last chapter we described the evolution of a homogeneous and isotropic Universe and we found that the Friedmann equations fully characterise it. On scales up to those of galaxy clusters we see lots of structure in the Universe. This structure is believed to form from weak density and energy inhomogeneities imposed at early times and observed directly in the CMB. These inhomogeneities were probably seeded by quantum fluctuations at very early times and blown up by an exponential growth of the Universe during its inflationary phase. Gravity as the main actor in structure formation then leads to the evolution of these initial seeds that finally give rise to the structures we observe today. Most theories assume that the initial seed field can be well described as a Gaussian random field in the density contrast

$$\delta(\mathbf{x}, t) = \frac{\rho(\mathbf{x}, t) - \rho_b(t)}{\rho_b(t)}, \tag{2.1}$$

where $\rho(\mathbf{x}, t)$ is the density at position $\mathbf{x}$ and time t and $\rho_b(t)$ is the background mean density of the Universe at that time. At early times δ follows a Gaussian distribution with a mean $\langle\delta\rangle = 0$ and a variance $\sigma^2 = \langle\delta^2\rangle$. This random field will then evolve under gravity. Usually the evolution is divided into two regimes: $|\delta| \ll 1$ is called the linear regime, whereas $|\delta| \geq 1$ corresponds to the nonlinear regime of structure formation. Our galaxy, for example, clearly represents a highly nonlinear region of the Universe due to its high density contrast and in structures like these we typically have $\delta \sim 350$ for the Milky Way halo, and $\delta \sim 10^5$ within the orbit of the Sun.

Linear growth

The evolution of the density field can be followed analytically in the linear regime. The idea is that the equations governing the evolution of the system can be expanded in a series and for $|\delta| \ll 1$ all high order terms can be dropped. If we forget for a short moment about the expansion of the Universe, we can write down the equations that govern the evolution of a fluid in a gravitational field Φ. We describe the fluid in terms of its pressure P, density ρ and velocity field $\mathbf{v}$

Continuity equation:

$$\frac{\partial\rho}{\partial t} + \nabla\cdot(\rho\mathbf{v}) = 0, \tag{2.2}$$

Euler equation:

$$\frac{\partial\mathbf{v}}{\partial t} + (\mathbf{v}\cdot\nabla)\,\mathbf{v} = -\frac{\nabla P}{\rho} - \nabla\Phi, \tag{2.3}$$

Poisson's equation:

$$\nabla^2\Phi = 4\pi G\rho. \tag{2.4}$$

Let us next suppose that we have a solution to these equations: $\rho = \rho_b$, $P = P_b$, $\Phi = \Phi_b$ and $\mathbf{v} = 0$. We note that such a solution does actually not exist, but the following calculation nevertheless yields the correct results. We follow here the original derivation of Jeans, where he also assumed the existence of the static solution. Let us slightly perturb

this solution and ask how the perturbations will evolve in time. Since we are interested in linear order effects, we write the perturbed quantities in the following way

$$\begin{array}{rclll} \rho & = & \rho_b + \delta\rho, & |\delta\rho \ / \ \rho_b| & \ll \ 1, \\ P & = & P_b + \delta P, & |\delta P \ / \ P_b| & \ll \ 1, \\ \Phi & = & \Phi_b + \delta\Phi, & |\delta\Phi \ / \ \Phi_b| & \ll \ 1, \\ \mathbf{v} & = & \delta\mathbf{v}. & & \end{array}$$

If we substitute these expressions back into the evolution equations of the fluid and work only up to linear order, we arrive at the following set of linearised equations

Continuity equation:

$$\frac{\partial\delta\rho}{\partial t} + \rho_b \nabla\cdot(\delta\mathbf{v}) = 0, \tag{2.5}$$

Euler equation:

$$\frac{\partial\delta\mathbf{v}}{\partial t} = -\frac{c_s^2}{\rho_b}\nabla\delta\rho - \nabla\delta\Phi, \tag{2.6}$$

Poisson equation:

$$\nabla^2\delta\Phi = 4\pi G\delta\rho, \tag{2.7}$$

where we defined the speed of sound c_s at constant entropy

$$c_s^2 = \left(\frac{\partial P}{\partial\rho}\right)_S = \frac{\delta P}{\delta\rho}. \tag{2.8}$$

Solutions of this set of equations can be found in Fourier space if the dispersion relation

$$\omega^2 - c_s^2 k^2 + 4\pi G\rho_b = 0, \tag{2.9}$$

is fulfilled. Growing and exponentially unstable modes only exist if ω is imaginary, which implies

$$k < 2\frac{\sqrt{\pi G\rho_b}}{c_s} = k_J, \tag{2.10}$$

where we introduced the Jeans wave-number k_J. The typical length scale associated with this wave-number is called the Jeans length

$$\lambda_J \cong \frac{c_s}{\sqrt{G\rho_b}}. \tag{2.11}$$

This means that an object with a typical size λ with $\lambda > \lambda_J$ will be gravitationally unstable and collapse, which implies that the density contrast δ is growing. The typical time that it takes for the collapse is given by the free-fall time

$$t_{\rm coll} \sim \frac{1}{\sqrt{G\rho_b}}. \tag{2.12}$$

So far we worked out the equations for the instabilities in a static Universe. For an expanding Universe, the equations must be slightly modified. This has the consequence

that the exponential growth we just found will be diluted by the expansion, so that in the end only a power-law growth survives. The density contrast in a matter dominated Universe evolves according to

$$\ddot{\delta} + 2\frac{\dot{a}}{a}\dot{\delta} + \left(c_s^2 k^2 - 4\pi G\rho_b\right)\delta = 0, \tag{2.13}$$

where the equation is written in Fourier space.

One can show that the density contrast equation has a growing and decaying solution, which are usually called D_+ and D_-, respectively, and both are power laws in time. The general solution is a linear combination of D_+ and D_-. This implies that after a certain period of time the growing mode will dominate and we have $\delta \propto D_+$.

As an example we briefly state the growth factor for the matter dominated case

$$D_+(a) \propto a, \quad D_+(t) \propto t^{2/3}. \tag{2.14}$$

For simplicity we will set $D_+ = D$ in the following since we are only interested in the growing mode. We note that the derivation here was based on a collisional fluid. Further down we will also discuss the situation for a collisionless fluid. This is very important, because there is strong evidence (see next chapter) that the bulk of matter comes from a collisionless and cold component, namely cold dark matter.

Nonlinear growth

While the linear analysis presented above is straightforward, the analysis of the nonlinear regime $\delta \geq 1$ is a difficult problem. Insights into this stage of evolution come mainly from computer simulations (called N-body simulations) that follow the gravitational interaction of a Monte-Carlo sample of the matter distribution in the Universe. We will come back to this point in the next chapter.

2.2 Collisionless medium

In the next chapter we will see that a large fraction of the Universe seems to consist of a yet unknown dark component, called dark matter. Dark matter is assumed to behave as a collisionless fluid. Furthermore, the number of dark matter particles is very large so that two-body scattering events occur only at a very low rate, and the system can be described in terms of a smooth distribution function $f(\mathbf{x}, \mathbf{v}, t)$ in phase-space.

Since there are no collisions between particles, the phase-space evolution of the dark matter fluid is given by the collisionless Boltzmann equation (also called Vlasov equation). It simply states the conservation of phase-space density along a particle trajectory

$$\frac{\partial f}{\partial t} + \mathbf{v}\frac{\partial f}{\partial \mathbf{x}} - \frac{\partial \Phi}{\partial \mathbf{x}}\frac{\partial f}{\partial \mathbf{v}} = 0. \tag{2.15}$$

The statement that the phase-space density is conserved along the particle trajectory is also known as Liouville's theorem in Hamiltonian dynamics. The gravitational potential Φ is generated in a self-consistent way by the particles themselves and related to the

density distribution by Poisson's equation

$$\nabla^2\Phi\left(\mathbf{x},t\right)=4\pi G\rho\left(\mathbf{x},t\right), \tag{2.16}$$

where the density is given by the velocity integral of the phase-space density

$$\rho\left(\mathbf{x},t\right)=\int \mathrm{d}\mathbf{v}\ f\left(\mathbf{x},\mathbf{v},t\right). \tag{2.17}$$

In the same way we can also define a mean velocity field as

$$\bar{\mathbf{v}}\left(\mathbf{x},t\right)=\frac{1}{\rho}\int \mathrm{d}\mathbf{v}\ \mathbf{v}f\left(\mathbf{x},\mathbf{v},t\right). \tag{2.18}$$

Taking higher velocity moments leads to an equation for the mean streaming velocity that is similar to the Euler equation for the collisional fluids discussed above

$$\frac{\partial\bar{\mathbf{v}}}{\partial t}+\left(\bar{\mathbf{v}}\cdot\nabla\right)\bar{\mathbf{v}}=-\nabla\Phi-\frac{1}{\rho}\left(\mathbf{P}\cdot\overleftarrow{\nabla}\right). \tag{2.19}$$

This equation looks remarkably similar to the Euler equation for fluids. The only difference is that the pressure is not scalar anymore. The last term on the r.h.s. describes an anisotropic kinetic pressure arising from random motions of the particles. This so-called stress tensor $\mathbf{P}$ is defined as

$$P_{ij}=\rho\ \left(\langle v_iv_j\rangle-\langle v_i\rangle\langle v_j\rangle\right), \tag{2.20}$$

where

$$\langle v_i\rangle=\frac{1}{\rho}\int \mathrm{d}\mathbf{v}\ v_if\left(\mathbf{x},\mathbf{v},t\right), \tag{2.21}$$

$$\langle v_iv_j\rangle=\frac{1}{\rho}\int \mathrm{d}\mathbf{v}\ v_iv_jf\left(\mathbf{x},\mathbf{v},t\right). \tag{2.22}$$

We can also introduce a cosmological constant Λ as a pressure of the vacuum. As a simplification we will assume an isotropic velocity pressure in the form of $P=\rho\sigma^2$, where we call σ the velocity dispersion. With these modifications and assumptions we arrive at the following Euler equation for a collisionless fluid ($\dot{\mathbf{x}}=\bar{\mathbf{v}}$)

$$\frac{\partial\dot{\mathbf{x}}}{\partial t}+\left(\dot{\mathbf{x}}\cdot\nabla_x\right)\dot{\mathbf{x}}=-\nabla_x\Phi-\frac{\nabla_xP}{\rho}+\Omega_\Lambda H_0^2\mathbf{x}. \tag{2.23}$$

where ∇_x denotes a derivative w.r.t. x. To discuss evolution in an expanding Universe it is convenient to work in comoving coordinates $\mathbf{x}'$ which we define by the following two relations

$$\mathbf{x}=a\mathbf{x}',\qquad \mathbf{v}=\dot{a}\mathbf{x}'+a\dot{\mathbf{x}}'=H\mathbf{x}+a\mathbf{v}'. \tag{2.24}$$

If we also assume a cold medium with a very small velocity dispersion σ we can neglect the pressure P in the Euler equation. Next we rewrite the Euler equation in comoving coordinates. Therefore, we note that $\ddot{\mathbf{x}}=a\ddot{\mathbf{x}}'+2\dot{a}\dot{\mathbf{x}}'+\ddot{a}\mathbf{x}'$ and $\nabla_x=1/a\nabla_{x'}$. The $\ddot{a}$ term

can be eliminated using the Friedmann equation. Taking these relations into account we can rewrite the Euler equation in the following form that is valid in the linear regime

$$\ddot{\mathbf{x}}' + 2\frac{\dot{a}}{a}\dot{\mathbf{x}}' = -\frac{1}{a}\nabla_x\Phi + \frac{4\pi G}{3}\rho_b\mathbf{x}'. \tag{2.25}$$

In this equation the Ω_Λ term does not explicitly show up. But we note that the $a(t)$ evolution of course depends on Ω_Λ as described by the Friedmann equations. We can further simplify this equation if we introduce the peculiar gravitational potential

$$\phi\left(\mathbf{x}'\right) = -G\int \mathrm{d}\tilde{\mathbf{x}}' \ \frac{\rho'\left(\tilde{\mathbf{x}}'\right) - \rho_b'}{|\mathbf{x}' - \tilde{\mathbf{x}}'|} = a\Phi\left(\mathbf{x}'\right) + \frac{a^2\ddot{a}}{2}\mathbf{x}'^{\,2}, \tag{2.26}$$

where we introduced the comoving density $\rho' = a^3\rho$. If we substitute the peculiar potential we arrive at the following equation in comoving coordinates

$$\ddot{\mathbf{x}}' + 2\frac{\dot{a}}{a}\dot{\mathbf{x}}' = -\frac{1}{a^3}\nabla_{x'}\phi. \tag{2.27}$$

This allows us finally to write down a set of equations that is the counterpart of the three equations we wrote down when analysing the collisional fluid above.

Continuity equation:

$$\dot{\delta} + (1+\delta)\nabla_{x'}\dot{\mathbf{x}}' = 0, \tag{2.28}$$

Euler equation:

$$\ddot{\mathbf{x}}' + 2\frac{\dot{a}}{a}\dot{\mathbf{x}}' = -\frac{1}{a^3}\nabla_{x'}\phi, \tag{2.29}$$

Poisson's equation:

$$\nabla^2_{x'}\phi = 4\pi G\left(\rho' - \rho_b'\right) = 4\pi G\delta\rho_b'. \tag{2.30}$$

If we now assume that the fluctuation field is small and neglect higher order terms in δ, we can combine these three equations and obtain

$$\ddot{\delta} + 2\frac{\dot{a}}{a}\dot{\delta} = 4\pi G\frac{\rho_b'}{a^3}\delta = 4\pi G\rho_b\delta. \tag{2.31}$$

This equation looks exactly like the corresponding equation for the fluid discussed above if we neglect the speed of sound there, equivalent to neglecting the pressure. We already

wrote down the growing mode for a matter dominated Universe. For a general cosmology, the growing solution is given by

$$D(t) = H(t) \int_0^t \frac{\mathrm{d}t'}{a^2\left(t'\right) H^2\left(t'\right)} = H(t) \int_0^{a(t)} \frac{\mathrm{d}a}{\dot{a}^3}. \tag{2.32}$$

The cosmology enters in this equation by the Hubble function H and the scale factor a.

2.3 Zel'dovich approximation

We will now briefly describe another approach for perturbation theory that is equivalent to the treatment above, but is especially useful for setting up initial conditions for cosmological simulations. We have seen that the density contrast evolves according to

$$\delta\left(\mathbf{x}', t\right) = D(t)\delta_0\left(\mathbf{x}'\right), \tag{2.33}$$

if we neglect the subdominant decay mode. Thus the density field grows self-similarly with time in the linear regime. This is also true for the gravitational acceleration and the peculiar velocity. The self-similar density growth implies for the peculiar gravitational potential

$$\phi\left(\mathbf{x}', t\right) = D(t)\phi_0\left(\mathbf{x}'\right) \qquad \text{with} \quad \nabla^2_{x'}\phi_0 = 4\pi G\rho'_b\delta_0 = 4\pi G\rho_b a^3\delta_0. \tag{2.34}$$

We can rewrite the Euler equation in conformal time ($\mathrm{d}\tau = \mathrm{d}t/a$)

$$\ddot{\mathbf{x}}' + 2\frac{\dot{a}}{a}\dot{\mathbf{x}}' = -\frac{1}{a^3}\nabla_{x'}\phi \;\Rightarrow\; a\frac{\mathrm{d}^2\mathbf{x}'}{\mathrm{d}\tau^2} + \frac{\mathrm{d}a}{\mathrm{d}\tau}\frac{\mathrm{d}\mathbf{x}'}{\mathrm{d}\tau} = -\nabla_{x'}\phi \;\Rightarrow\; \frac{\mathrm{d}}{\mathrm{d}\tau}\left(a\frac{\mathrm{d}\mathbf{x}'}{\mathrm{d}\tau}\right) = -\nabla_{x'}\phi, \tag{2.35}$$

and this manipulation allows a straightforward integration of the equation

$$\frac{\mathrm{d}\mathbf{x}'}{\mathrm{d}\tau} = -\left(\frac{1}{a}\int \mathrm{d}\tau\; D\right)\nabla_{x'}\phi_0. \tag{2.36}$$

If we integrate another time we get

$$\mathbf{x}' = \mathbf{q}' - \left(\int \frac{\mathrm{d}\tau}{a}\int \mathrm{d}\tau\; D\right)\nabla_{x'}\phi_0. \tag{2.37}$$

By definition D satisfies the fluctuation growth equation and it can be shown that the double integral on the r.h.s. is proportional to D. We therefore arrive at the following equations

$$\mathbf{x}' = \mathbf{q}' - \frac{D(t)}{4\pi G\rho_b a^3}\nabla_{x'}\phi_0, \qquad \mathbf{v}' = -\frac{\dot{D}(t)}{4\pi G\rho_b a^3}\nabla_{x'}\phi_0, \tag{2.38}$$

where we went back to time t instead of conformal time. This formulation of linear theory is due to Zel'dovich. It is a Lagrangian description where the growth of structure is specified by giving the displacement $\mathbf{x}' - \mathbf{q}'$ and the peculiar velocity $\mathbf{v}'$ of each mass

element as a function of its initial (Lagrangian) position $\mathbf{q}'$. In this so-called Zel'dovich approximation trajectories are straight lines with the distance travelled proportional to D.

3
Dark Matter

In this chapter we motivate and introduce the idea of dark matter as the main actor in structure formation. After discussing evidence for dark matter on various scales, we briefly describe possible dark matter candidates. Although it is not fully clear what dark matter is made of, we will show that computer simulations can nevertheless be used to study its evolution and follow the structure formation in the Universe. We close this chapter by making some critical comments on the dark matter hypothesis and motivate the objectives of this thesis.

3.1 Observational Evidence

The first evidence of the need for a dark matter component came from Zwicky's Coma cluster observation in 1933. Since then the evidence for dark matter has become very strong and we here give a short overview of the observational evidence for dark matter on various scales. A recent review on this subject can be found in Bertone et al. (2005).

Evidence on galactic scales

Evidence for dark matter on galactic scales comes from the observation of rotation curves of spiral galaxies (e.g. Rubin and Ford, 1970). These curves show the circular velocity as a function of radius and are usually measured by optical surface photometry and by HI 21cm line emission in regions where no other optical tracer is available. Based on the Doppler effect circular velocities can then be measured and a rotation curve can be constructed. Nowadays many of these curves have been measured and they show a very interesting behaviour: they are flat out to radii far beyond the edge of the visible disk. This is quite unexpected since Newtonian dynamics says that the circular velocity is expected to be $v(r) = \sqrt{GM(r)/r}$ for a spherical system, where $M(r)$ is the enclosed mass within radius r. Since $M(r)$ is expected to be constant beyond the visible disk, one would expect a typical Kepler falloff $v(r) \propto 1/\sqrt{r}$ for the circular velocity. The fact that the rotation curve is flat beyond the optical disk implies that there must be a halo of matter with $M(r) \propto r$. Therefore, rotation curves require the existence of a extended dark matter halo to explain their flatness far beyond the visible disk.

Evidence on galaxy cluster scales

Historically, clusters of galaxies gave the first evidence for some 'missing mass' component. In 1933, Zwicky inferred from measurements of velocity dispersions of galaxies in the Coma cluster a mass-to-light ratio of about 400 $M_\odot/L_\odot$. This exceeds the ratio in the solar neighbourhood by two orders of magnitude. It was Zwicky's observation that marked the beginning of the 'dark matter problem'.

A detailed measurement of the amount of dark matter in a galaxy cluster requires methods to measure its (total) mass. A common method is the observation of the hot X-ray emitting gas in the cluster. Assuming hydrostatic equilibrium and spherical symmetry yields the following relation between the temperature T of the hot gas and the enclosed mass $M(r)$

$$k_B T \cong (1.3 - 1.8)\mathrm{keV} \left(\frac{M(r)}{10^{14}\ M_\odot}\right) \left(\frac{1\ \mathrm{Mpc}}{r}\right). \tag{3.1}$$

Observations indicate a significantly higher temperature than expected based on this relation. This suggests the existence of a substantial amount of dark matter in clusters of galaxies. These conclusions can also be checked by gravitational lensing mass estimates. These estimates exploit the fact that according to general relativity, light is bent by gravitational fields. This leads to so-called gravitational arcs in images. Based on these arcs it is then possible to estimate the mass of the light bending object.

Evidence on cosmological scales

Observations on galactic and cluster scales clearly indicate the existence of dark matter as discussed above. This can also be done by a detailed analysis of the cosmic microwave

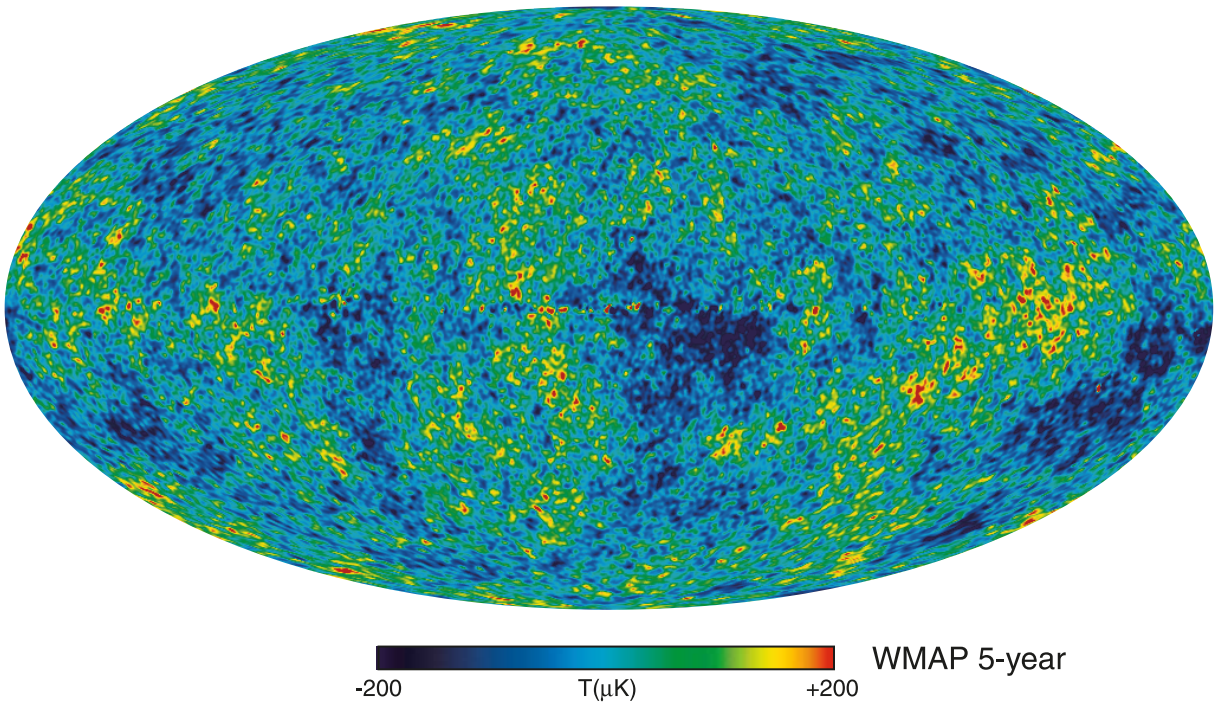

Figure 3.1: CMB temperature map of WMAP 5yr release. (taken from `http://lambda.gsfc.nasa.gov`).

background (CMB) (see Fig. 3.1). Such an analysis allows an accurate testing of cosmological models and puts constraints on cosmological parameters of a given model. In the following table we list the most recent cosmological parameters inferred from the WMAP-5 (Komatsu et al., 2009) measurements of the CMB. We list the parameters inferred from WMAP-5 alone and those derived from combinations of the WMAP-5 data with baryonic acoustic oscillations (BAO) and SNIa measurements.

parameter	symbol	WMAP-5 alone	WMAP-5 + BAO + SNe
total energy density	Ω_t	$1.099 \; ^{+\,0.100}_{-\,0.085}$	1.0052 ± 0.0064
matter density	Ω_{m0}	0.258 ± 0.03	0.279 ± 0.015
baryon density	Ω_{b0}	0.0441 ± 0.0030	0.0462 ± 0.0015
cosmological constant	$\Omega_{\Lambda 0}$	0.742 ± 0.03	0.721 ± 0.015
Hubble constant	h	$0.719 \; ^{+\,0.026}_{-\,0.027}$	0.701 ± 0.013
age of the Universe in Gyr	t_0	13.69 ± 0.13	13.73 ± 0.12

We see that the Universe today is dominated by (cold) dark matter and dark energy in form of a cosmological constant Λ. This model of our Universe is called the concordance ΛCDM model. Nowadays ΛCDM is the standard model of our Universe and we will assume that it describes our Universe throughout the thesis.

3.2 Candidates

Given the fact that many observations point towards the existence of dark matter, the question arises what this non-baryonic component could be made of. It is established today that this material must be non-baryonic, since baryonic candidates are already excluded. These baryonic candidates are usually summarised under the term MACHOs (massive compact halo objects). These include, for example, brown dwarfs, Jupiters, stellar black hole remnants, white dwarfs, and neutron stars. Brown dwarfs have masses below 0.08 $M_\odot$ and therefore never start fusion of hydrogen. They mainly contain H and He. Jupiters have a similar composition, but are lighter with masses of about 0.001 $M_\odot$. But micro-lensing searches ruled out the MACHO hypothesis, they cannot contribute for the whole dark matter content. Therefore, one is faced with the question what dark matter could be made of.

A WIMP?

Although the standard model of particle physics has been very successful in explaining and predicting various experimental results, it is clear today that it does not describe the full story. It has some shortcomings like the hierarchy problem that lead to the assumption that there must be some additional physics beyond the standard model. Therefore, various extensions to the standard model were developed over the last decades. The important point for cosmology is, that most of these extensions naturally predict particles that are suitable dark matter candidates. A very generic class of particles predicted by many theories are so-called weakly interacting massive particles (WIMPs). WIMP masses are typically in the range from 10 GeV c^{-2} to few 1 TeV c^{-2}, and they have interactions with ordinary matter which are characteristic of the weak interactions. WIMPs are thermal relics and in many scenarios Majorana particles and can therefore self-annihilate. They exist in thermal equilibrium and in abundance in the early Universe, when the temperature of the Universe exceeds the mass of the particle. Due to the expansion, the Universe cools at some epoch to a temperature less than the mass of the particle. Then the equilibrium abundance drops exponentially until the rate for the annihilation reaction falls below the expansion rate H. At this time the WIMP freezes out and the relic cosmological abundance is set. It can be shown that the relic abundance of a general WIMP with annihilation cross-section σ_A is approximately given by

$$\Omega_{\mathrm{WIMP}} \sim \frac{3 \times 10^{-27} \ \mathrm{cm^3\ s^{-1}}}{\langle \sigma_A v \rangle}, \tag{3.2}$$

where the brackets denote the thermal average. If the elusive dark matter particle interacts via weak-scale interactions, then its annihilation cross-section can be estimated to be $\langle \sigma_A v \rangle \sim \alpha^2 (100 \ \mathrm{GeV\ c^{-2}})^{-2} \sim 10^{-25} \ \mathrm{cm^3\ s^{-1}}$, where $\alpha \sim 10^{-2}$ is of the order of the fine structure constant. And this cross-section yields a relic density that is remarkably close to the value required for the dark matter content of the Universe. This result is even more surprising if we realise that there is no a priori reason for a weak-scale interaction to have anything to do with a cosmological parameter. This coincidence is the main motivation for the assumption that the dark matter particle should be a WIMP.

An obvious way to find dark matter candidates is therefore to search for WIMPs in the

various extensions of the standard model. The most common feature of most extensions and a feature that some believe to be a requirement of physics beyond the standard model is so-called supersymmetry (e.g. Martin, 1998). One motivation for supersymmetry is already obvious from inspecting the standard model constituents. There is a clear distinction between mediator particles as bosons and the matter particles as fermions. It is therefore natural to ask whether a symmetry exists which relates them, thus providing a sort of unified picture of matter and interactions. There are other more severe reasons that require a supersymmetric extension of the standard model, but we forgo the details here. Supersymmetry is introduced by assigning every boson a fermion and vice versa. The following table lists the superpartners of the standard model particles together with their spin value. The naming convention is obvious from this table and the supersymmetric partners are labelled by a tilde.

Particle	Symbol	Spin	Superparticle	Symbol	Spin
Quark	q	1/2	Squark	$\tilde{q}$	0
Electron	e	1/2	Selectron	$\tilde{e}$	0
Muon	μ	1/2	Smuon	$\tilde{\mu}$	0
Tauon	τ	1/2	Stauon	$\tilde{\tau}$	0
W boson	W	1	Wino	$\tilde{W}$	1/2
Z boson	Z	1	Zino	$\tilde{Z}$	1/2
Photon	γ	1	Photino	$\tilde{\gamma}$	1/2
Gluon	g	1	Gluino	$\tilde{g}$	1/2
Higgs	H	0	Higgsino	$\tilde{H}$	1/2

Clearly, this symmetry must be broken because perfect symmetry implies equal mass superpartners. Since no superpartners have been found so far, they must be heavier than the standard model particles. Supersymmetry also provides some WIMPs. Among them the neutralino is the currently favoured dark matter particle. Neutralinos are the most studied dark matter particles in literature so far. The neutralino is a linear combination of the supersymmetric partners of the photon, Z^0, and neutral Higgs bosons. In the following we will often refer to the neutralino as a handy example for a WIMP.

We note that there are also non-WIMP dark matter candidates. One of them is the axion, originally introduced as a solution to the strong CP problem in quantum chromodynamics. They are expected to be extremely weakly interacting with ordinary particles, so that they never were in thermal equilibrium in the early Universe. This means their relic abundance does not follow from the $\Omega - \sigma_A$ relation above. This implies that axions can be very light and nevertheless form a cold (non-relativistic) component of cosmic matter. In the non-WIMP sector the axion is the currently favoured candidate. When referring to particle properties in the following, we will always use the neutralino and the axion as the most probable and most popular dark matter candidates. Many experiments are currently searching for dark matter. Recent reviews on these searches can be found in Jungman et al. (1996) and Bertone et al. (2005). Dark matter searches can be split in two classes: direct and indirect searches. Direct searches aim to detect the dark matter particle in a laboratory device. Indirect searches exploit the fact that some dark matter candidates can annihilate. Therefore, these experiments search for the

annihilation products, e.g. γ-rays, or anti-particles. We will present some more details on detection schemes in the following chapters.

3.3 N-body simulations

As we saw in the last chapter the linear regime of structure formation can be described analytically. This is not true for the nonlinear regime. As in other disciplines of physics, the emergence of supercomputers allows us to solve complicated systems of physical equations numerically in a very short time. Nowadays this is also exploited in theoretical cosmology, where the evolution of the nonlinear regime can be followed by computer simulations, e.g. van Albada (1968); Hénon (1971); Ahmad and Cohen (1973); White (1976); Lucy (1977); Fall (1978); Larson (1978); White (1978); Aarseth et al. (1979); Giuricin et al. (1984); Efstathiou et al. (1985).

In this thesis we are interested in the distribution of the dark matter particles in haloes. Therefore, we need to understand how the dark matter distribution has evolved with time. This is clearly a highly nonlinear problem. Cold dark matter behaves as a collisionless fluid and its phase-space density evolution is dictated by the collisionless Boltzmann equation presented in the previous chapter. Hence, a solution $f(\mathbf{x}, \mathbf{v}, t)$ of this equation will tell us for every time t the dark matter phase-space distribution. Unfortunately, solving this partial differential equation is computational very demanding. In case we want to sample the phase-space with 10^3 grid cells along each of the six directions, we would require a mesh of 10^{18} cells in total. That is far from practically possible and even with 10^3 cells in each direction the resulting phase-space sampling would still be quite coarse.

A simpler and superior approach is provided by so-called N-body simulations. These simulations sample the dark matter phase-space distribution $f(\mathbf{x}, \mathbf{v})$ with a set of N particles, which represent δ-functions in phase-space. These particles evolve then under self-gravity. If N is sufficiently large, the collective potential of the particles will be a good approximation to the true potential of the underlying distribution function and the particles will move along characteristic curves of the true solution of the collisionless Boltzmann equation. In the end the particles provide a fair sampling of the phase-space of the true distribution function $f(\mathbf{x}, \mathbf{v})$. One can think of the N-body method as a Monte-Carlo technique to solve the collisionless Boltzmann equation. It is therefore similar to Monte-Carlo simulations in other fields of research like solid state physics.

The initial conditions for cosmological simulations are generated according to the predictions of inflationary cosmology summarised by the power spectrum $P(k)$. Inflation predicts $P(k) \propto k$ at very early times. This scale-invariant primordial power spectrum is modified by the linear growth of fluctuations during the early phase of the Universe. The growth rates of individual modes differ depending on whether they are in or outside the horizon. The growth of modes outside the horizon needs a full general relativistic calculation, and the effect on the power spectrum is, that it bends at some scale. The initial conditions for the simulation are then generated based on this power spectrum using the Zel'dovich approximation to displace the simulation particles from a regular grid or glass-like configuration.

The most challenging and main task for N-body simulations is the calculation of the

gravitational forces, since all other interactions can be neglected for pure dark matter simulations. Two important characteristics of these simulations is their mass and length resolution. The mass resolution is specified by the mass of the simulation particles considered. Length resolution is limited by the softening scale that we introduce below. Different techniques were developed over the last decades to solve this N-body problem. The main complication is the long range character of gravitation that leads to a N^2 scaling in case of a direct summation for N simulation particles. In the following we briefly describe some of the methods used to solve the N-body problem.

Particle-Particle (PP) computations

The simplest, oldest but also most inefficient way of solving the problem is a direct summation of the force contributions of all particles. Since the particle distribution is not supposed to mimic the evolution of a discrete set of particles but rather that of a collisional fluid, it is necessary to soften the gravitational force between two particles i and j. A common procedure is to use a Plummer force softening

$$\mathbf{F}_{ij} = \frac{Gm^2}{(\epsilon^2 + |\mathbf{x}_i - \mathbf{x}_j|^2)^{3/2}} \quad (\mathbf{x}_j - \mathbf{x}_i)\,, \tag{3.3}$$

where $\mathbf{x}_i$ and $\mathbf{x}_j$ are the positions of two particles with mass m, $\mathbf{F}_{ij}$ is the force between them and ϵ is the softening length. The introduction of a gravitational softening length ϵ is equivalent to replacing point masses by extended bodies with a size of order ϵ. Another possible softening scheme uses a spline kernel. This has the advantage that its support is finite and the force becomes exactly Newtonian for distances larger than the characteristic softening length. Clearly, this is not the case for the Plummer softening shown above. Unfortunately, the particle-particle method requires of the order of N^2 evaluations per time step. This implies that PP methods are limited to about $10^4 - 10^5$ particles. This is not sufficient for larger cosmological simulations, but can be used for other applications like star cluster simulations.

Particle-Mesh (PM) computations

The PP method sums up the force contributions of every simulation particle to a given target particle. The PM method (e.g. Bertschinger and Gelb, 1991) exploits the fact, that once the potential field of the computational volume is known, the forces at each point can be calculated by finite differencing methods. To compute the potential field the PM method exploits the fact that the Poisson equation can be solved very efficiently with the help of the Fast Fourier Transform (FFT). For the force calculations the particles (mass points) are assigned to a regular grid. Poisson's equation is then solved on this grid with a FFT. The mass assignment can be done in various ways, e.g. nearest grid point (NGP), cloud-in-cell (CIC) and triangular-shaped-clouds (TSC). Once the potential field is known, the force field is calculated on the grid. Then the forces are interpolated to the particle positions. Although, the PM method is significantly faster than PP computations, the force resolution is limited by the mesh-size. A way out of this problem is the combination of PP and PM methods which lead to so-called P^3M methods (e.g. Couchman, 1991). In this schemes, the short-range contribution of the forces is calculated by a direct summation and the long-range part is carried out via PM methods.

Tree codes

Another very common scheme for improving the performance of N-body simulations is the usage of tree codes. The basic idea is to treat distant groups of particles as single massive pseudo-particles. The interaction of a target particle is then calculated with this pseudo-particles. Only nearby particles will be summed directly. This improves the problem scaling from $\mathcal{O}(N^2)$ of the PP method to a significantly better $\mathcal{O}(N \log N)$ scaling. In this thesis we will use the simulation code GADGET (Springel et al., 2001; Springel, 2005). This code combines a tree-code with a particle mesh code. The short-range forces are calculated via the tree, whereas long-range forces are computed using the mesh. This scheme is then called TreePM and we will describe it in some more detail later.

3.4 A critical comment and thesis objectives

Clearly, the observational evidence for dark matter is overwhelming today. The dark matter hypothesis is generally accepted and may be proven by the detection of the elusive dark matter particle in the next decades. Nevertheless, we should stay critical and not only believe in dark matter because it is currently fashionable to do so. The observational "evidence" in principle only states that we do not understand something. This is very similar to other epochs in science when anomalies appeared without an appropriate explanation. For example the anomalous motion of Uranus, lead to the prediction that there must be some missing mass in terms of an undiscovered planet. Some years later Neptune was observed and the missing mass problem was solved. Another famous anomaly is the perihelion precision of Mercury. This time it turned out that the underlying theory, namely Newton's law of gravity, was not fully correct and needed to be extended to general relativity. The question nowadays is: Is the dark matter anomaly of the first or second type? We have discussed the implications of the first type of interpretation in this chapter, but we should also mention that there are theories that modify gravity to explain for example the flat rotation curves (e.g. Milgrom, 1983; Bekenstein, 2004). These theories therefore interpret the dark matter problem as a type 2 anomaly.

In the following chapters of this thesis we will assume that the type one interpretation is correct. The reason for this is mainly, that the dark matter hypothesis is not only able to explain one observation, but it can explain a whole bunch of observations on very different scales and at very different times. This is significantly different from the Neptune or Mercury anomalies. Therefore, we assume the existence of dark matter in the following and try to answer the question:

- What is the distribution of dark matter near the Sun?
- How is it distributed on very small scales?
- How does this influence detector signals?

The work presented in the following chapters is the first and most detailed study of the dark matter distribution on small scales carried out so far. This has become possible due to the enormous growth in computing power over the last years and to the algorithmic

developments described in the second part of this thesis. This allows the first detailed predictions for many aspects of dark matter detector signals, and should help in the hunt for the elusive dark matter particle.

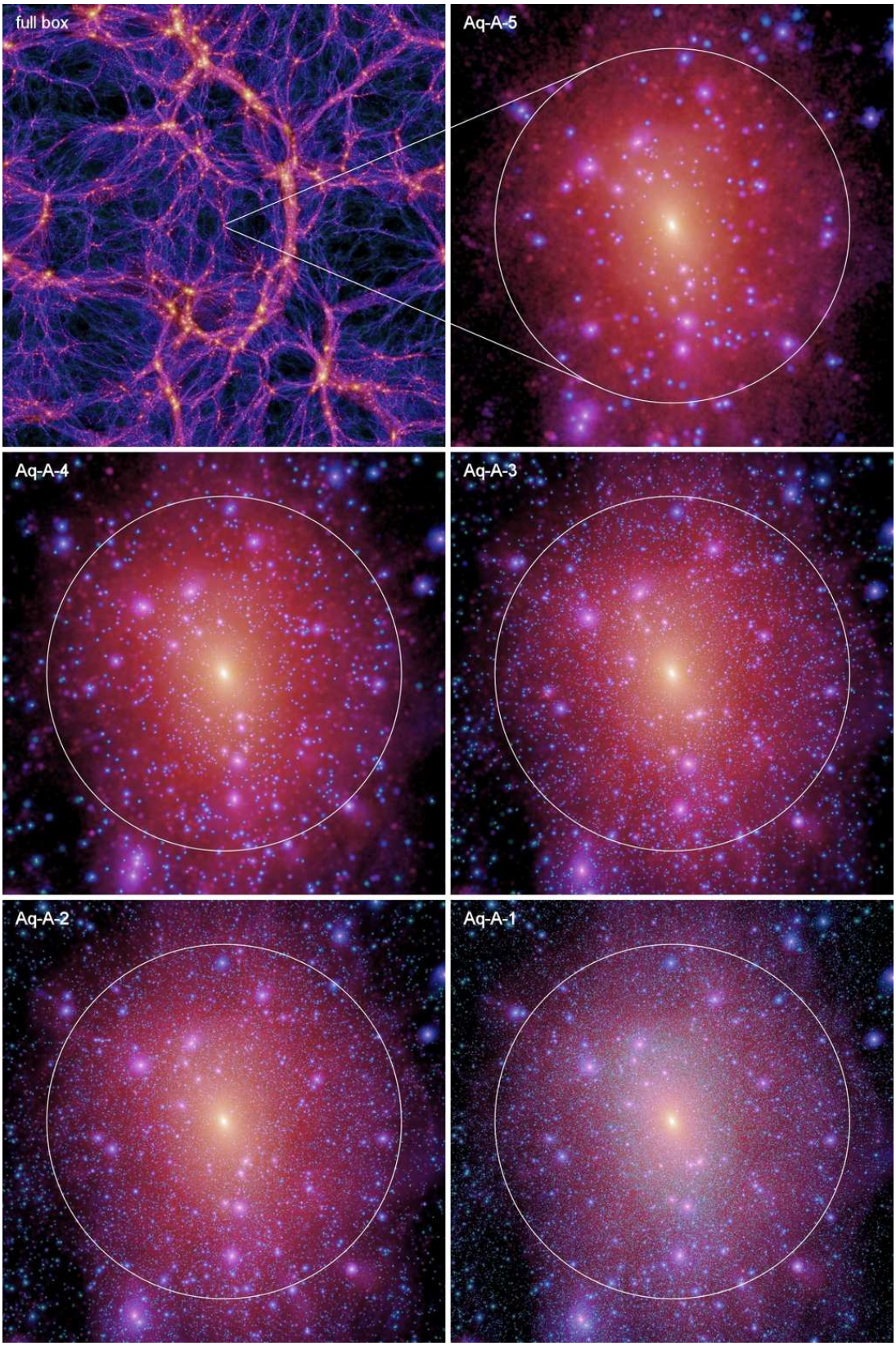

Figure 3.2: Density field of one of the haloes simulated within the Aquarius project (see chapter 4). The different panels show the different resolutions (5 to 1) and the full box (upper left) from which the halo was taken. The full box has a sidelength of 100 Mpch^{-1}. The circles in the other panels mark the virial radius (taken from Springel et al., 2008a)

Part II

Coarse-grained dark matter distribution

4

Phase-space structure in the local dark matter distribution and its signature in direct detection experiments

In this chapter we study predictions for dark matter phase-space structure near the Sun based on high-resolution simulations of six galaxy haloes taken from the Aquarius Project. The local DM density distribution is predicted to be remarkably smooth; the density at the Sun differs from the mean over a best-fit ellipsoidal equidensity contour by less than 15% at the 99.9% confidence level. The local velocity distribution is also very smooth, but it differs systematically from a (multivariate) Gaussian distribution. This is not due to the presence of individual clumps or streams, but to broad features in the velocity modulus and energy distributions that are stable both in space and time and reflect the detailed assembly history of each halo. These features have a significant impact on the signals predicted for WIMP and axion searches. For example, WIMP recoil rates can deviate by $\sim 10\%$ from those expected from the best-fit multivariate Gaussian models. The axion spectra in our simulations typically peak at lower frequencies than in the case of multivariate Gaussian velocity distributions. Also in this case, the spectra show significant imprints of the formation of the halo. This implies that once direct DM detection has become routine, features in the detector signal will allow us to study the dark matter assembly history of the Milky Way. A new field, "dark matter astronomy", will then emerge. [1]

[1] published in Vogelsberger et al, MNRAS, 395, 2, 797-811 (2009)

4.1 Introduction

In the 75 years since Zwicky (1933) first pointed out the need for substantial amounts of unseen material in the Coma cluster, the case for a gravitationally dominant component of non-baryonic dark matter has become overwhelmingly strong, as we demonstrated in the last chapter. It seemed a long shot when Peebles (1982) first suggested that the dark matter might be an entirely new, weakly interacting, neutral particle with very low thermal velocities in the early Universe, but such Cold Dark Matter (CDM) is now generally regarded as the most plausible and consistent identification for the dark matter. In the previous chapter we mentioned, that particle physics has suggested many possible CDM particles beyond the standard model. Two promising candidates are WIMPs (weakly interacting massive particles, see Lee and Weinberg, 1977; Gunn et al., 1978; Ellis et al., 1984) and axions (Peccei and Quinn, 1977b,a; Weinberg, 1978; Wilczek, 1978). Among the WIMPs, the lightest supersymmetric particle, the neutralino, is currently favoured as the most likely CDM particle, and the case will be enormously strengthened if the LHC (Large Hadron Collider) confirms supersymmetry. However, ultimate confirmation of the CDM paradigm can only come through the direct or indirect detection of the CDM particles themselves. Neutralinos, for example, are their own antiparticles and can annihilate to produce γ-rays and other particles. One goal of the recently launched Fermi Gamma-ray space telescope is to detect this radiation (Gehrels and Michelson, 1999; Springel et al., 2008b).

Direct detection experiments, on the other hand, search for the interaction of CDM particles with laboratory apparatus. For WIMPs, detection is based on nuclear recoil events in massive, cryogenically cooled bolometers in deep underground laboratories (Jungman et al., 1996); for axions, resonant microwave cavities in strong magnetic fields exploit the axion-photon conversion process (Sikivie, 1985). Despite intensive searches, the only experiment which has so far reported a signal is DAMA (Bernabei et al., 2007) which has clear evidence for an annual modulation of their event rate of the kind expected from the Earth's motion around the Sun. The interpretation of this result is controversial, since it appears to require dark matter properties which are in conflict with upper limits established by other experiments (see Savage et al., 2004; Gondolo and Gelmini, 2005; Gelmini, 2006, for a discussion and possible solutions). Regardless of this, recent improvements in detector technology may enable a detection of WIMPS or axions within a few years.

Event rates in all direct detection experiments are determined by the local DM phase-space distribution at the Earth's position. The relevant scales are those of the apparatus and so are extremely small from an astronomical point of view. As a result, interpreting null results as excluding specific regions of candidate parameter space must rely on (strong) assumptions about the fine-scale structure of phase-space in the inner Galaxy. In most analyses the dark matter has been assumed to be smoothly and spherically distributed about the Galactic Centre with an isotropic Maxwellian velocity distribution (e.g. Freese et al., 1988) or a multivariate Gaussian distribution (e.g. Ullio and Kamionkowski, 2001; Green, 2001; Helmi et al., 2002). The theoretical justification for these assumptions is weak, and when numerical simulations of halo formation reached sufficiently high resolution, it became clear that the phase-space of CDM haloes contains considerable

substructure, both gravitationally bound subhaloes and unbound streams. As numerical resolution has improved it has become possible to see structure closer and closer to the centre, and this has led some investigators to suggest that the CDM distribution near the Sun could, in fact, be almost fractal, with large density variations over short length-scales (e.g. Kamionkowski and Koushiappas, 2008). This would have substantial consequences for the ability of direct detection experiments to constrain particle properties.

Until very recently, simulation studies were unable to resolve any substructure in regions as close to the Galactic Centre as the Sun (see Moore et al., 2001; Helmi et al., 2002, 2003, for example). This prevented realistic evaluation of the likelihood that massive streams, clumps or holes in the dark matter distribution could affect event rates in Earth-bound detectors and so weaken the particle physics conclusions that can be drawn from null detections (see Savage et al., 2006; Kamionkowski and Koushiappas, 2008, for recent discussions). As we shall show in this chapter, a new age has dawned. As part of its Aquarius Project (Springel et al., 2008a) the Virgo Consortium has carried out a suite of ultra-high resolution simulations of a series of Milky Way-sized CDM haloes. Simulations of individual Milky Way haloes of similar scale have been carried out and analysed by Diemand et al. (2008), Zemp et al. (2009) and Stadel et al. (2009). Here we use the Aquarius simulations to provide the first reliable characterisations of the local dark matter phase-space distribution and of the detector signals which should be anticipated in WIMP and axion searches.

4.2 The Numerical Simulations

The cosmological parameters for the Aquarius simulation set are $\Omega_{m0} = 0.25, \Omega_{\Lambda 0} = 0.75, \sigma_8 = 0.9, n_s = 1$ and $H_0 = 100\ h$ km s^{-1} Mpc^{-1} with $h = 0.73$, where all quantities have their standard definitions. These parameters are consistent with current cosmological constraints within their uncertainties, in particular, with the parameters inferred from the WMAP 1-year and 5-year data analyses (Spergel et al., 2003; Komatsu et al., 2008). Milky Way-like haloes were selected for resimulation from a parent cosmological simulation which used 900^3 particles to follow the dark matter distribution in a $100h^{-1}$Mpc periodic box. Selection was based primarily on halo mass ($\sim 10^{12} M_\odot$) but also required that there should be no close and massive neighbour at $z = 0$. The Aquarius Project resimulated six such haloes at a series of higher resolutions. The naming convention uses the tags Aq-A through Aq-F to refer to these six haloes. An additional suffix 1 to 5 denotes the resolution level. Aq-A-1 is the highest resolution calculation, with a particle mass of $1.712 \times 10^3\ M_\odot$ and a virial mass of $1.839 \times 10^{12}\ M_\odot$ it has more than a billion particles within the virial radius R_{200} which we define as the radius containing a mean density 200 times the critical value. The Plummer equivalent softening length of this run is 20.5 pc. Level-2 simulations are available for all six haloes with about 200 million particles within R_{200}. Further details of the haloes and their characteristics can be found in Springel et al. (2008a).

In the following analysis we will often compare the six level-2 resolution haloes, Aq-A-2 to Aq-F-2. To facilitate this comparison, we scale the haloes in mass and radius by the constant required to give each a maximum circular velocity of $V_{\rm max} = 208.49$ km/s,

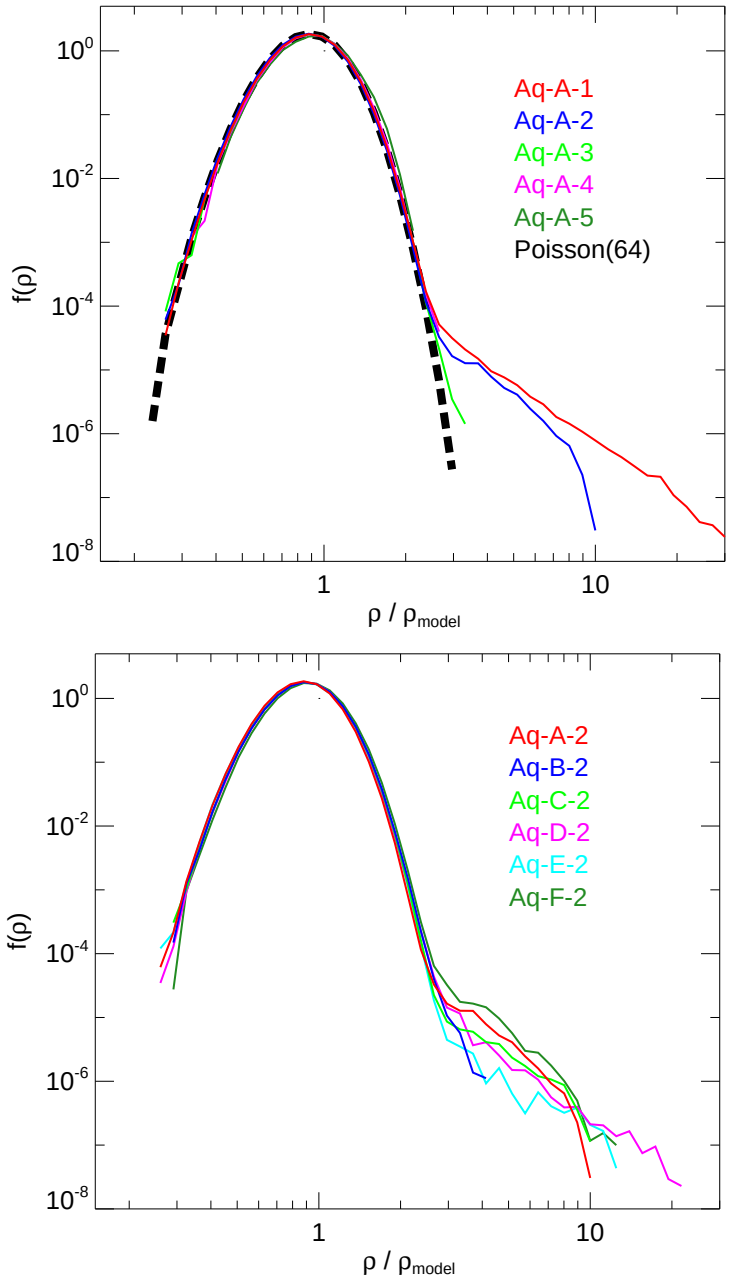

Figure 4.1: Top panel: Density probability distribution function (DPDF) for all resimulations of halo Aq-A measured within a thick ellipsoidal shell between equidensity surfaces with major axes of 6 and 12 kpc. The local dark matter density at the position of each particle, estimated using an SPH smoothing technique, is divided by the density of the best-fit, ellipsoidally stratified, power-law model. The DPDF gives the distribution of the local density in units of that predicted by the smooth model at random points within the ellipsoidal shell. At these radii only resolution levels 1 and 2 are sufficient to follow substructure. As a result, the characteristic power-law tail due to subhaloes is not visible at lower resolution. The fluctuation distribution of the smooth component is dominated by noise in our 64-particle SPH density estimates. The density distribution measured for a uniform (Poisson) particle distribution is indicated by the black dashed line. Bottom panel: As above, but for all level-2 haloes after rescaling to $V_{\rm max} = 208.49$ km/s. In all cases the core of the DPDF is dominated by measurement noise and the fraction of points in the power law tail due to subhaloes is very small. The chance that the Sun lies within a subhalo is $\sim 10^{-4}$. With high probability the local density is close to the mean value averaged over the Sun's ellipsoidal shell.

the value for Aq-A-2.

4.3 Spatial distributions

The density of DM particles at the Earth determines the flux of DM particles passing through laboratory detectors. It is important, therefore, to determine not only the mean value of the DM density 8 kpc from the Galactic Centre, but also the fluctuations around this mean which may result from small-scale structure.

Throughout this section we will refer to a coordinate system that is aligned with the principal axes of the inner halo, and which labels particles by an ellipsoidal radius $r_{\rm ell}$ defined as the semi-major axis length of the ellipsoidal equidensity surface on which the particle sits. We determine the orientation and shape of these ellipsoids as follows. For each halo we begin by diagonalising the moment of inertia tensor of the dark matter within the spherical shell 6 kpc $< r <$ 12 kpc (after scaling to a common $V_{\rm max}$). This gives us a first estimate of the orientation and shape of the best fitting ellipsoid. We then reselect particles with 6 kpc $< r_{\rm ell} <$ 12 kpc, recalculate the moment of inertia tensor and repeat until convergence. The resulting ellipsoids have minor-to-major axis ratios which vary from 0.39 for Aq-B-2 to 0.59 for Aq-D-2. The radius restriction reflects our desire to probe the dark matter distribution near the Sun. We note that we make use of $r_{\rm ell}$ only in this section. In the other parts of this chapter we will always use the standard spherical radius r.

We estimate the local DM distribution at each point in our simulations using an SPH smoothing kernel adapted to the 64 nearest neighbours. We then fit a power law to the resulting distribution of $\ln\rho$ against $\ln r_{\rm ell}$ over the ellipsoidal radius range 6 kpc $< r_{\rm ell} <$ 12 kpc. This defines a smooth model density field $\rho_{\rm model}(r_{\rm ell})$. We then construct a density probability distribution function (DPDF) as the histogram of $\rho/\rho_{\rm model}$ for all particles in 6 kpc $< r_{\rm ell} <$ 12 kpc, where each is weighted by ρ^{-1} so that the resulting distribution refers to random points within our ellipsoidal shell rather than to random mass elements. We normalise the resulting DPDFs to have unit integral. They then provide a probability distribution for the local dark matter density at a random point in units of that predicted by the best fitting smooth ellipsoidal model.

We have chosen an ellipsoidal radial range rather than a spherical one because we wish to characterise the variations in density caused by small-scale structure. We must therefore remove the strong angular dependence produced by the prolate structure of our haloes; the large minor-to-major axis ratios mentioned above lead to variations in density of up to an order of magnitude at fixed distance from halo centre. Since the stellar component of the Milky Way has a major effect on the shape of its dark halo at the Solar circle, most likely causing it to be substantially rounder than our baryon-free haloes (e.g. Kazantzidis et al., 2004), only the small-scale structure of our simulations is directly relevant to dark matter detection experiments. The large-scale dark matter density distribution is more reliably inferred from dynamical modelling of Milky Way observations than from simulations of the kind we present here.

In Fig. 4.1 we show the DPDFs measured in this way for all resimulations of Aq-A (top panel) and for all level-2 haloes after scaling to a common $V_{\rm max}$ (bottom panel).

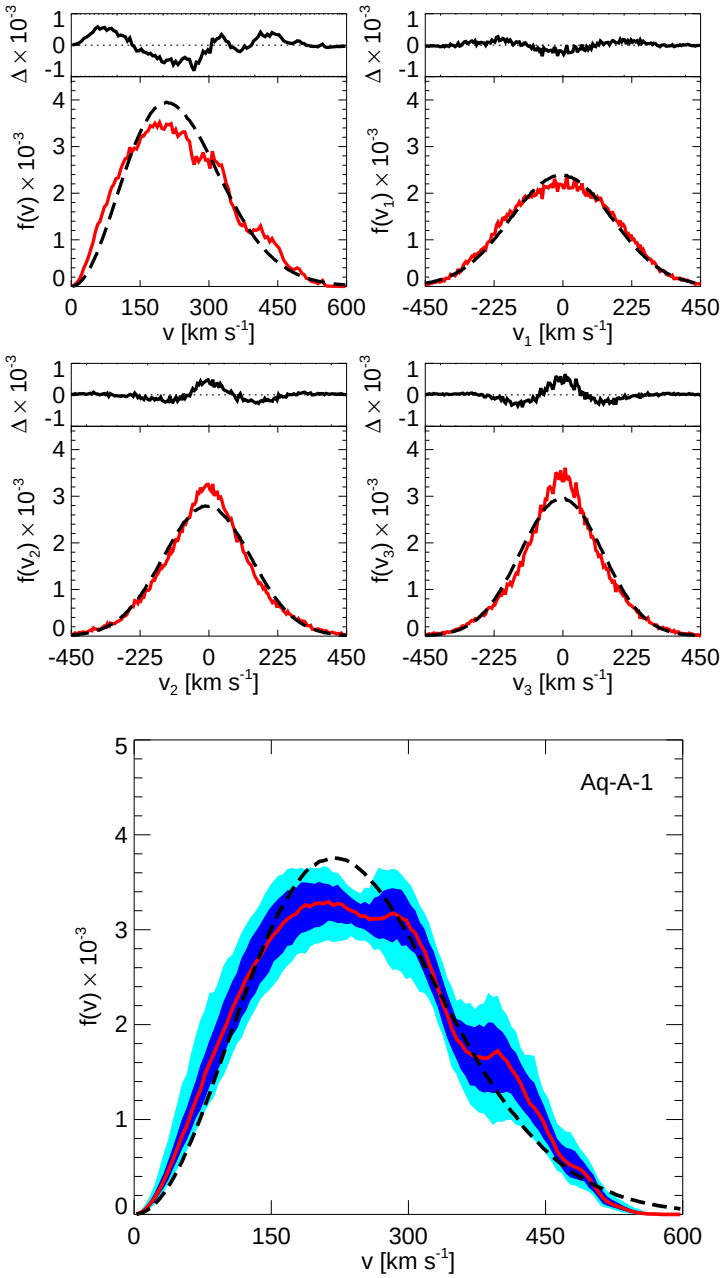

Figure 4.2: Top four panels: Velocity distributions in a 2 kpc box at the Solar Circle for halo Aq-A-1. v_1, v_2 and v_3 are the velocity components parallel to the major, intermediate and minor axes of the velocity ellipsoid; v is the modulus of the velocity vector. Red lines show the histograms measured directly from the simulation, while black dashed lines show a multivariate Gaussian model fit to the individual component distributions. Residuals from this model are shown in the upper part of each panel. The major axis velocity distribution is clearly platykurtic, whereas the other two distributions are leptokurtic. All three are very smooth, showing no evidence for spikes due to individual streams. In contrast, the distribution of the velocity modulus, shown in the upper left panel, shows broad bumps and dips with amplitudes of up to ten percent of the distribution maximum. Lower panel: Velocity modulus distributions for all 2 kpc boxes centred between 7 and 9 kpc from the centre of Aq-A-1. At each velocity a thick red line gives the median of all the measured distributions, while a dashed black line gives the median of all the fitted multivariate Gaussians. The dark and light blue contours enclose 68% and 95% of all the measured distributions at each velocity. The bumps seen in the distribution for a single box are clearly present with similar amplitude in all boxes, and so also in the median curve. The bin size is 5 km/s in all plots.

Two distinct components are evident in both plots. One is smoothly and log-normally distributed around $\rho = \rho_{\rm model}$, the other is a power-law tail to high densities which contains less than 10^{-4} of all points. The power-law tail is not present in the lower resolution haloes (Aq-A-3, Aq-A-4, Aq-A-5) because they are unable to resolve subhaloes in these inner regions. However, Aq-A-2 and Aq-A-1 give quite similar results, suggesting that resolution level 2 is sufficient to get a reasonable estimate of the overall level of the tail. A comparison of the six level 2 simulations then demonstrates that this tail has similar shape in different haloes, but a normalisation which can vary by a factor of several. In none of our haloes does the fraction of the distribution in this tail rise above 5×10^{-5}. Furthermore, the arguments of Springel et al (2008) suggest that the total mass fraction in the inner halo (and thus also the total volume fraction) in subhaloes below the Aq-A-1 resolution limit is at most about equal to that above this limit. Hence, the chance that the Sun resides in a bound subhalo of any mass is of order 10^{-4}.

The striking similarity of the smooth log-normal component in all the distributions of Fig. 4.1 has nothing to do with actual density variations in the smooth dark matter distribution. It is, in fact, simply a reflection of the noise in our local density estimates. We demonstrate this by setting up a uniform Poisson point distribution within a periodic box and then using an SPH smoothing kernel adapted to the 64 nearest neighbours to associate a local density with each particle in exactly the same way as for our halo simulations. We can then construct a DPDF for these estimates (relative to their mean) in exactly the same way as before. The result is shown in the top panel of Fig. 4.1 as a dashed black line. It is an almost perfect fit to the smooth component in the simulations, and it would fit the other haloes equally well if plotted in the lower panel.

The fit is not perfect, however, and it is possible to disentangle the true scatter in density about the smooth model from the estimation noise. The latter is expected to be asymptotically log-normal for large neighbour numbers, and Fig. 4.1 shows that it is very close to log-normal for our chosen parameters. If we assume that the scatter in intrinsic density about the smooth model is also approximately log-normal, we can estimate its scatter as the square root of the difference between the variance of the simulation scatter and that of the noise: symbolically, $\sigma_{\rm intr} = \sqrt{\sigma^2_{\rm obs} - \sigma^2_{\rm noise}}$. Indeed, it turns out that the variance in $\ln(\rho/\rho_{\rm model})$ which we measure for our simulated haloes (excluding the power-law tail) is consistently higher than that which we find for our uniform Poisson distribution. Furthermore, tests show that the differences are stable if we change the number of neighbours used in the SPH estimator to 32 or 128, even though this changes the noise variance by factors of two. This procedure gives the following estimates for rms intrinsic scatter around the smooth model density field in our six level-2 haloes, Aq-A-2 to Aq-F-2: 2.2%, 4.4%, 3.7%, 2.1%, 4.9% and 4.0% respectively. The very large particle number in the radial range we analyse results in a standard error on these numbers which is well below 0.01 for all haloes. Thus, we can say with better than 99.9% confidence that the DM density at the Sun's position differs by less than 15% from the average over the ellipsoidal shell on which the Sun sits. This small scatter implies that the density field in the inner halo is remarkably well described by a smooth, ellipsoidal, power-law model. This qualitative behaviour was predicted analytically by Kamionkowski and Koushiappas (2008), although the fluctuation level we find for the smooth component is much smaller than they suggested.

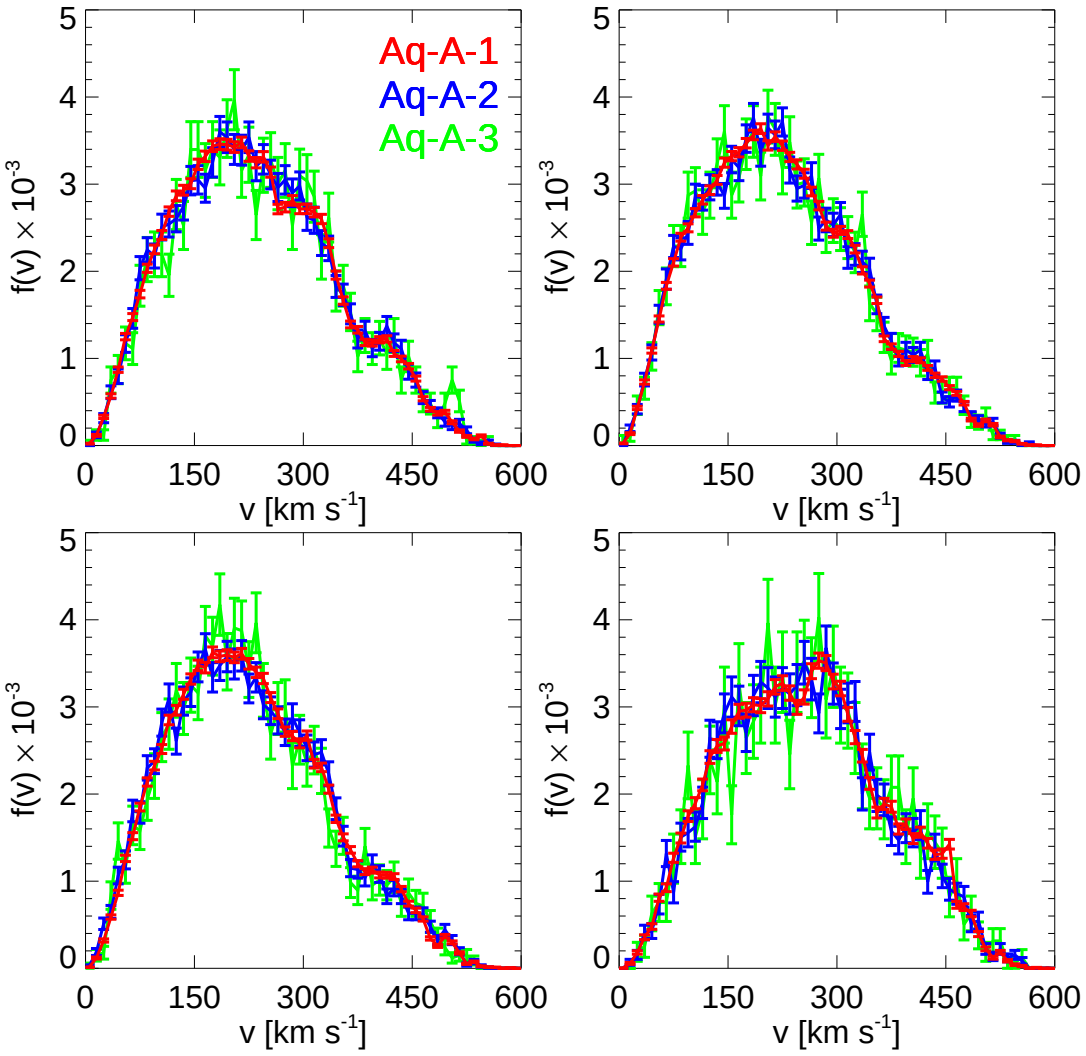

Figure 4.3: Distributions of the velocity modulus in four well separated 2 kpc boxes about 8 kpc from the centre of Aq-A. Results are shown for each region from each of the three highest resolution simulations. Error bars are based on Poisson statistics. The different resolutions agree within their error bars, and show the same bumps in all four boxes. For the purpose of this plot, we have chosen a larger bin for our histograms, 10 km/s as compared to 5 km/s in our other velocity plots. For this bin size the statistical noise in Aq-A-1 is barely visible.

We conclude that the local density distribution of dark matter should be very smooth. Bound clumps are very unlikely to have any effect on direct detection experiments. The main reason for this is the short dynamical time at the solar radius (about 1% of the Hubble time). This results in very efficient mixing of unbound material and the stripping of all initially bound objects to a small fraction of the maximum mass they may have had in the past (see the next chapter for a discussion of these processes). Note that the actual density of DM in the Solar neighbourhood and the shape of the equidensity surfaces of the Milky Way's dark matter distribution will depend on how the gravitational effects of the baryonic components have modified structure during the system's formation. Unfortunately, the shape of the inner DM halo of the Milky Way is poorly constrained observationally (Helmi, 2004b; Law et al., 2005). The dissipative contraction of the visible components probably increased the density of the dark matter component and made it more axisymmetric (e.g. Gnedin et al., 2004; Kazantzidis et al., 2004) but these processes are unlikely to affect the level of small-scale structure. The very smooth behaviour we find in our pure dark matter haloes should apply also to the more complex real Milky Way.

4.4 Velocity distributions

The velocity distribution of DM particles near the Sun is also an important factor influencing the signal expected in direct detection experiments. As mentioned in the Introduction, most previous work has assumed this distribution to be smooth, and either Maxwellian or multivariate Gaussian. Very different distributions are possible in principle. For example, if the local density distribution is a superposition of a relatively small number of DM streams, the local velocity distribution would be effectively discrete with all particles in a given stream sharing the same velocity (Sikivie et al., 1995; Stiff et al., 2001; Stiff and Widrow, 2003). Clearly, it is important to understand whether such a distribution is indeed expected, and whether a significant fraction of the local mass density could be part of any individual stream.

We address this issue by dividing the inner regions of each of our haloes into cubic boxes 2 kpc on a side, and focusing on those boxes centred between 7 kpc$< r <$ 9 kpc from halo centre. In Aq-A-1, each 2 kpc box contains 10^4 to 10^5 particles, while in the level-2 haloes they contain an order of magnitude fewer. For every box we calculate a velocity dispersion tensor and study the distribution of the velocity components along its principal axes. In almost all boxes these axes are closely aligned with those the ellipsoidal equidensity contours discussed in the last section. We also study the distribution of the modulus of the velocity vector within each box. The upper four panels of Fig. 4.2 show these distributions of a typical 2 kpc box at the solar circle in Aq-A-1 (solid red lines). Here and in the following plots we normalise distributions to have unit integral. The black dashed lines in each panel show a multivariate Gaussian distribution with the same mean and dispersion along each of the principal axes. The difference between the two distributions in each panel is plotted separately just above it, This particular box is quite typical, in that we almost always find the velocity distribution to be significantly anisotropic, with a major axis velocity distribution which is platykurtic, and distributions of the other two

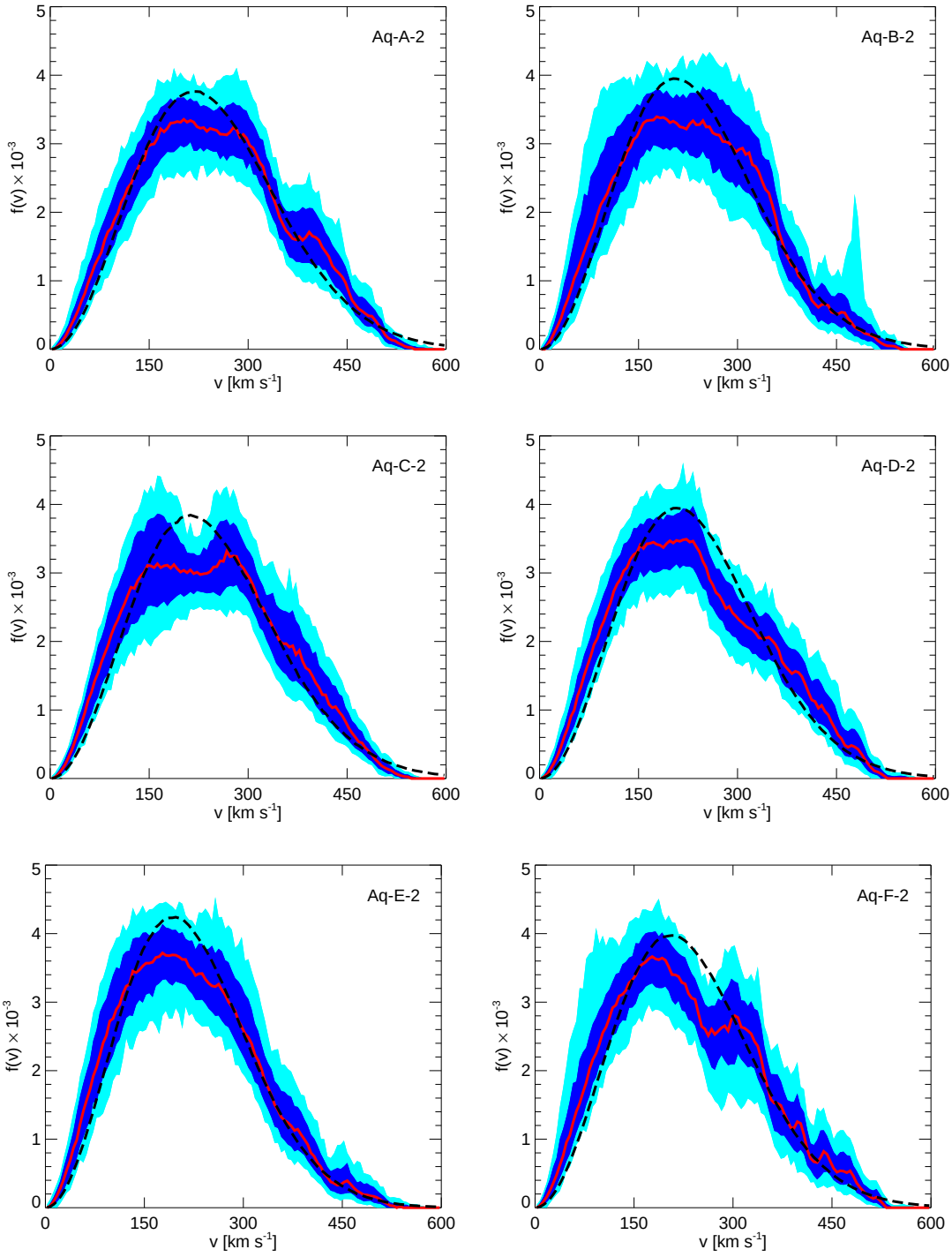

Figure 4.4: Velocity modulus distributions in exactly the same format as the bottom panel of Fig. 4.2 but for all six of our haloes at level-2 resolution. All distributions are smooth. Only in Aq-B-2 do we see a strong spike which is due to a single box which has 60% of its mass (though a small fraction of its volume) in a single subhalo. No other box in any of the distributions has a subhalo contributing more than 1.5% of the mass. All distributions show characteristic broad bumps which are present in all boxes in a given halo, and so in its median distribution. These bumps are in different places in different haloes.

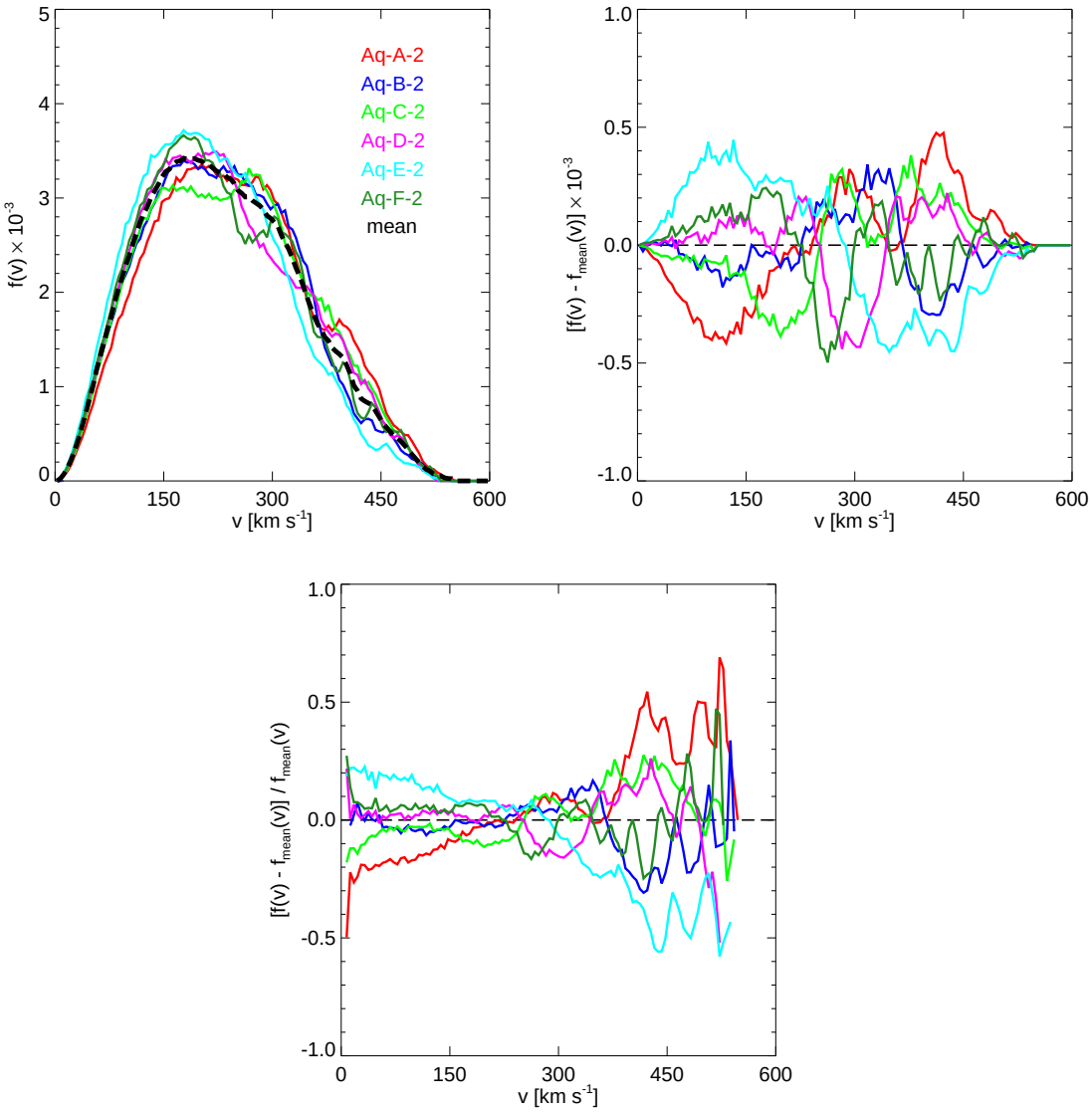

Figure 4.5: Top left panel: Median velocity modulus distributions for all six level-2 haloes repeated from Fig. 4.4. The black dashed line is the mean of these distributions. Top right panel: Deviations of the velocity modulus distribution of each of the six haloes from the sample mean. The amplitude of the various bumps is similar in different haloes and over the whole velocity range. It reaches more than 10% of the amplitude of the mean distribution. Bottom panel: Relative deviations of the individual velocity modulus distributions from their sample mean. Typical relative deviations are about 30%, but they can exceed 50% at higher velocities.

components which are leptokurtic. Thus the velocity distribution differs significantly from Maxwellian, or even from a multivariate Gaussian. The individual velocity components have very smooth distributions with no sign of spikes due to individual streams. This also is a feature which is common to almost all our 2 kpc boxes. It is thus surprising that the distribution of the velocity modulus shows clear features in the form of bumps and dips with amplitudes of several tens of percent.

To see how these features vary with position, we overlaid the distributions of the velocity modulus for all 2 kpc boxes centred between 7 and 9 kpc from the centre of Aq-A-1 (bottom panel of Fig. 4.2). We superpose both the directly measured distributions and the predictions from the best-fit multivariate Gaussians. At each velocity, the solid red line show the median value of all the directly measured distributions, while the dashed black line is the median of all the multivariate Gaussian fits. The dark and light regions enclose 68% and 95% of all the individual measured distributions at each velocity.

It is interesting to note that the bumps in the velocity distribution occur at approximately the same velocity in all boxes. This suggests that they do not reflect local structures, but rather some global property of the inner halo. In Fig. 4.3 we show velocity modulus distribution for four different boxes in Aq-A at the three highest resolutions (levels 1, 2 and 3). The error bars are based on Poisson statistics in each velocity bin. Clearly the same bumps are present in all boxes and at all resolutions. Thus, they are a consequence of real dynamical structure that converges with increasing numerical resolution.

In Fig. 4.4 we make similar plots of the velocity modulus distribution for all level-2 haloes. These distributions are quite smooth. The sharp peak in Aq-B-2 is due to a single 2 kpc box where 60% of the mass is contained in a single subhalo. No other box in this or any other halo has more than 1.5% of its mass in a single subhalo. The great majority of boxes contain no resolved subhalo at all. Although the details of the median distributions vary between haloes, they share some common features. The low velocity region is more strongly populated in all cases than predicted by the multivariate Gaussian model. In all cases, the peak of the distribution is depressed relative to the multivariate Gaussian. At moderately high velocities there is typically an excess. Finally, and perhaps most importantly, all the distributions show bumps and dips of the kind discussed above. These features appear in different places in different haloes, but they appear at similar places for all boxes in a given halo. The left panel of Fig. 4.5 superposes the median velocity modulus distributions of all level-2 haloes and plots their mean as a black dashed line. The middle panel shows the deviations of the individual haloes from this mean. The amplitudes of the deviations are similar in different haloes and at low and high velocities. In percentage terms the deviations are largest at high velocity reaching values of 50% or more, as can be seen from the right panel of Fig. 4.5.

The bumps in the velocity distribution are too broad to be explained by single streams. Furthermore, single streams are not massive enough to account for these features. This is shown more clearly in Fig. 4.6 where we illustrate some streams in velocity space for a 2 kpc box in halo Aq-A-1. Different colours here indicate particles that belonged to different FoF groups at redshift 4.2. For clarity we only show streams from groups that contribute at least 10 particles to this volume (0.025% of the total number of particles present at this location). There are 27 such objects. If we consider all FoF groups that

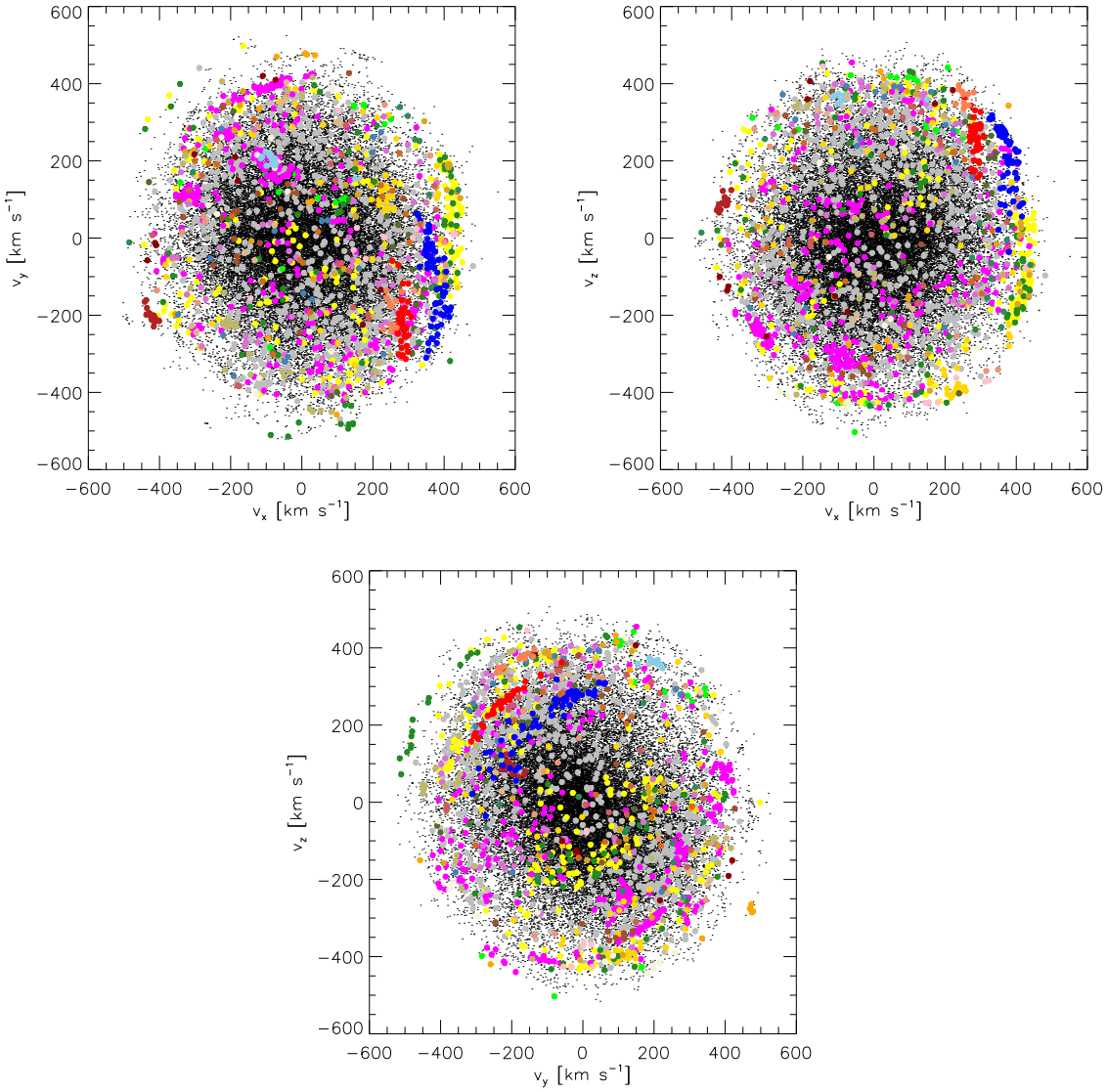

Figure 4.6: Streams in velocity space for a 2 kpc box $\sim$ 8 kpc from the centre of Aq-A-1. Different colours stand for particles associated to different FoF groups at redshift 4.2. Only groups contributing more than ten particles are shown. The box contains 27 such objects and has in total 41143 particles (shown as small black points) of which 1796 come from these groups. Clearly, particles originating from the same group cluster in velocity space and build streams; often many streams per group.

contribute more than 2 particles to the volume shown in Fig. 4.6, we find that a given FoF group contributes streams that are typically only populated by 2 particles (0.005% of the total mass in the box). This implies that most of the groups contribute several streams of very low density. The most prominent streams have ~ 40 particles, i.e. $\sim 0.1\%$ of the mass in this volume. This clearly shows that streams are expected to be neither dense nor massive in the Solar vicinity.

The most prominent streams typically occupy the tail of the velocity distribution in these local boxes. The excess of particles moving with similar velocities and high kinetic energies can be measured using a velocity correlation function, as shown by Helmi et al. (2002).

4.5 Energy distributions

We have seen that the distributions of individual velocity components in localised regions of space are very smooth, whereas the velocity modulus distribution shows clear bumps. Taken together with the fact that these bumps occur at similar velocities in regions on opposite sides of the halo centre, this indicates that we must be seeing features in the energy distribution of dark matter particles.

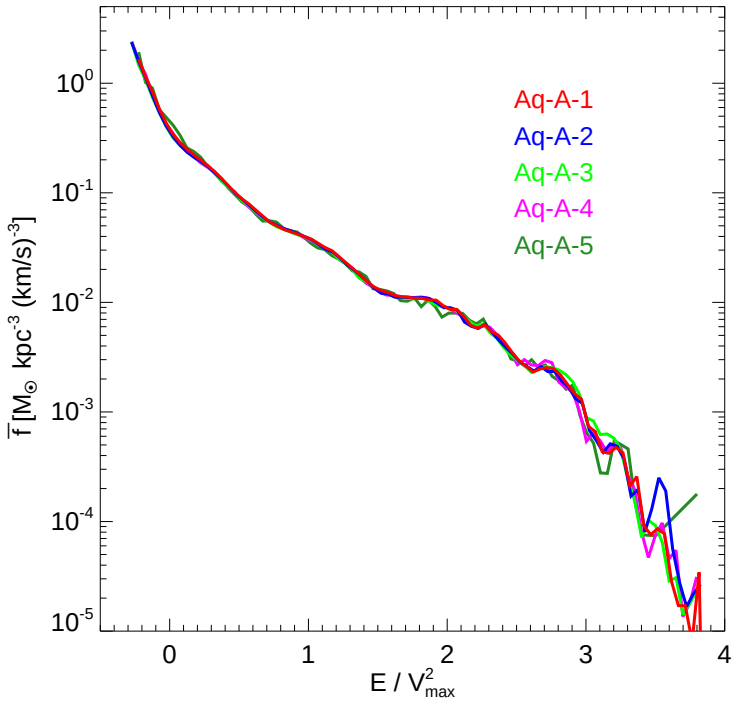

Figure 4.7: Mean phase-space density distribution as a function of energy for Aq-A for particles in a spherical shell between 6 and 12 kpc and for all five resolution levels. Especially at high-binding energies the convergence is very good. Features in the distribution function are visible at all resolutions for energies below 2.7 $V^2_{\rm max}$, despite the fact that the mass resolution differs by more than a factor of 1800 between Aq-A-1 and Aq-A-5. The less bound parts show more variation from resolution to resolution but still agree well between Aq-A-1 and Aq-A-2.

To investigate this further, we estimate the mean phase-space density $\bar{f}$ as a function of energy in each of our haloes using the properties of the particles at radii r between 6 and 12 kpc. Clearly our haloes are not perfectly in equilibrium and they are far from spherical. Thus their phase-space densities will only approximately be describable as functions of the integrals of motion, and they will depend significantly on integrals other than the energy. Nevertheless we can estimate a mean phase-space density as a function of energy by taking the total mass of particles with 6 kpc $< r <$ 12 kpc and energies in some small interval and dividing it by the total phase-space volume corresponding to this radius and energy range, e.g.

$$\bar{f}(E) = \frac{\mathrm{d}M}{\mathrm{d}E}\,\frac{1}{g(E)}, \tag{4.1}$$

where $\bar{f}(E)$ is the energy-dependent mean phase-space density and

$$g(E) \;=\; 4\pi \int\limits_{\mathcal{V}, E>\Phi(\mathbf{x})} \mathrm{d}^3\mathbf{x}\;\sqrt{2\,(E-\Phi(\mathbf{x}))}, \tag{4.2}$$

where $g(E)\,\mathrm{d}E$ is the phase-space volume with orbital energy in the range $(E, E+\mathrm{d}E)$ and halocentric radius in the range 6 kpc$< r <$ 12 kpc. In Appendix A we present more details on the calculation of the mean phase-space density.

The differential energy distribution is easily calculated by binning the energies of all particles between 6 and 12 kpc. The phase-space volume can be calculated by solving for the gravitational potential at the position of all simulation particles and then using these as a Monte-Carlo sampling of configuration-space in the relevant integrals. Taking the ratio then yields the desired estimate of $\bar{f}(E)$. We note that both the mass M and the differential phase-space volume per unit energy $g(E)$ depend strongly on the geometric region over which they are evaluated, in the present case, a thick spherical shell between 6 and 12 kpc. We find, however, that the mean phase-space density defined by Eq. (4.1) depends only very weakly on the region chosen, for example on the radii of our spherical shell. Indeed, as can be inferred from Fig. 4.2, it is very similar to that obtained for any 2 kpc cube at R=8 kpc. Thus, in practise, the weighting implied by the average over the other integrals of motion which is implicit in Eq. (4.1) does not depend much on the geometry of the region chosen.

In Fig. 4.7 we show $\bar{f}(E)$ measured in this way for all our simulations of Aq-A. We express the energy in units of V_{max}^2 and we take the zero-point of the gravitational potential to be its average value on a sphere of radius 8 kpc. As a result the measured energy distribution extends to slightly negative values. Note how well the distribution converges at the more strongly bound energies. At higher energies the convergence between the level-1 and 2 resolutions is still very good. This demonstrates that we can robustly measure the mean phase-space density distribution. Furthermore, we see clear wiggles that reproduce quite precisely between the different resolutions.

Fig. 4.8 shows similarly estimated mean phase-space density distributions for Aq-A-2 at five different times separated by about 300 Myr. This is longer than typical orbital periods in the region we are studying. Despite this, the wiggles at energies below 2.4 V_{max}^2 are present over the complete redshift range shown. This demonstrates that these features are well-mixed, and that the phase-space distribution function has reached

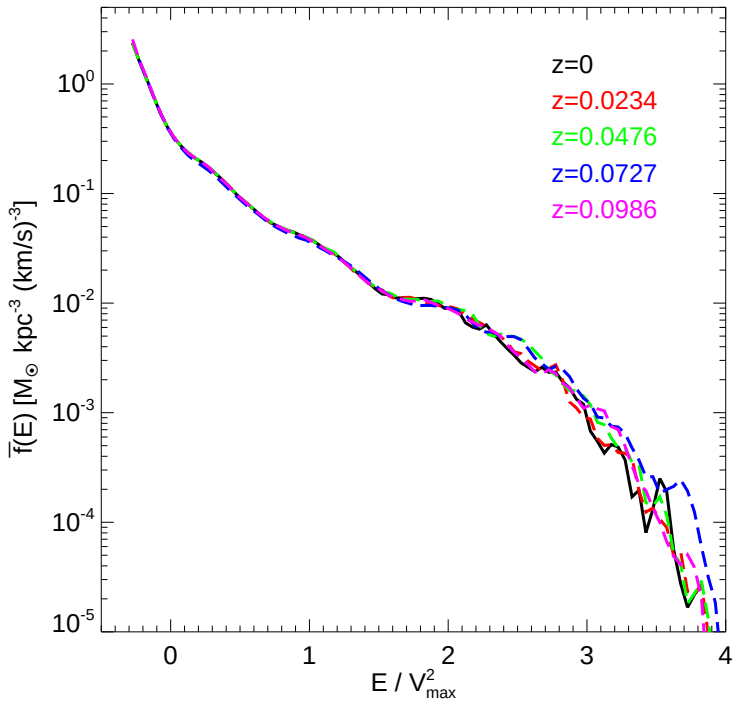

Figure 4.8: Evolution of the mean phase-space density distribution of Aq-A-2 over four time intervals of about 300 Myr. Below 2.4 $V^2_{\rm max}$ the phase-space distribution function is time-independent, implying that the system has reached coarse-grained equilibrium. The small bumps at these energies are therefore well-mixed features in action space. The variability of the features in the weakly bound part of the distribution shows that they are due to individual streams and therefore change on the timescale of an orbital period. Note that the phase-space density at these energies is almost three orders of magnitude below that of the most bound particles.

a coarse-grained equilibrium. In contrast, the variability of the wiggles in the part of the distribution corresponding to weakly bound particles (where the orbital periods are much larger) shows that these must be due to individual streams or to superpositions of small numbers of streams, which have not yet phase-mixed away.

To estimate what these phase-space distribution functions should look like for a "smooth" system, we average the functions found in our six individual level-2 haloes. In Fig. 4.9 we superpose these six functions and their mean $\langle \bar{f} \rangle$ (the black dashed line). The similarity of the different distribution functions at high binding energies suggests a near-universal shape for $\bar{f}(E)$. At lower binding energies, individual haloes deviate quite strongly from $\langle \bar{f} \rangle$. This can be seen more clearly in Fig. 4.10 where we plot $\log(\bar{f}/\langle \bar{f} \rangle)$, the decimal logarithm of the ratio of the phase-space density of an individual halo to the mean. The lower axis is orbital energy in units of $V^2_{\rm max}$, while the upper axis is the corresponding dark matter particle velocity at the Solar Circle. In this plot one can clearly see the wiggles, which are located at different energies for different haloes. For $V_{8\ \rm kpc} < 350$ km/s the distribution functions for all haloes satisfy $0.7 < \bar{f}/\langle \bar{f} \rangle < 1.4$. For low binding energies (velocities of 600 km/s or more at the Solar Circle) this ratio can exceed a factor of ten.

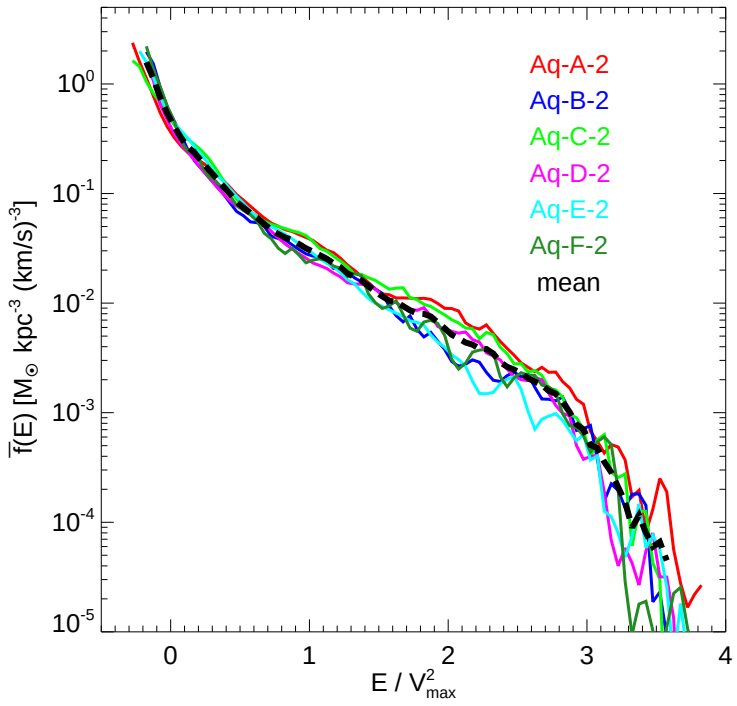

Figure 4.9: Scaled phase-space distribution functions for all level-2 haloes. In addition to scaling according to $V_{\rm max}$ we have also corrected for a zero-point offset in the potential energy between different haloes. The black dashed line shows the average distribution function based for our halo sample. At high binding energies the scatter between average and individual halo distribution functions is quite small, showing that this part of the distribution function is near-universal. At low-binding energies large amplitude features are visible in all haloes. These features differ from halo to halo and are related to recent events in their formation histories.

These features in the phase-space density distribution must be related to events in the formation of each halo. To demonstrate this explicitly, we have computed $\bar{f}(E)$ separately for particles which were accreted onto two of our haloes (i.e. first entered the main progenitor FoF group) at different epochs. The upper left panel of Fig. 4.11 shows that Aq-A-2 had a very "quiet" merger history. Material accreted at different times is arranged in a very orderly way in energy space. All the most strongly bound particles were accreted before redshift 5, and material accreted at successively later times forms a series of "shells" in energy space. The most weakly bound wiggles are due entirely to the most recently accreted material, and progressively more bound bumps can be identified with material accreted at earlier and earlier times. In contrast, the top right panel shows that Aq-F-2 had a very "active" merger history, with a major merger between $z = 0.75$ and $z = 0.68$. The correspondence between binding energy and epoch of accretion is much less regular than for Aq-A-2, and much of the most bound material actually comes from the object which fell in between $z = 0.75$ and $z = 0.68$. It is also striking that many of the wiggles in this object are present in material that accreted at quite different times, suggesting that they may be non-steady coherent oscillations rather than stable structures in energy space. Nevertheless, in both haloes one can identify features in the phase-space

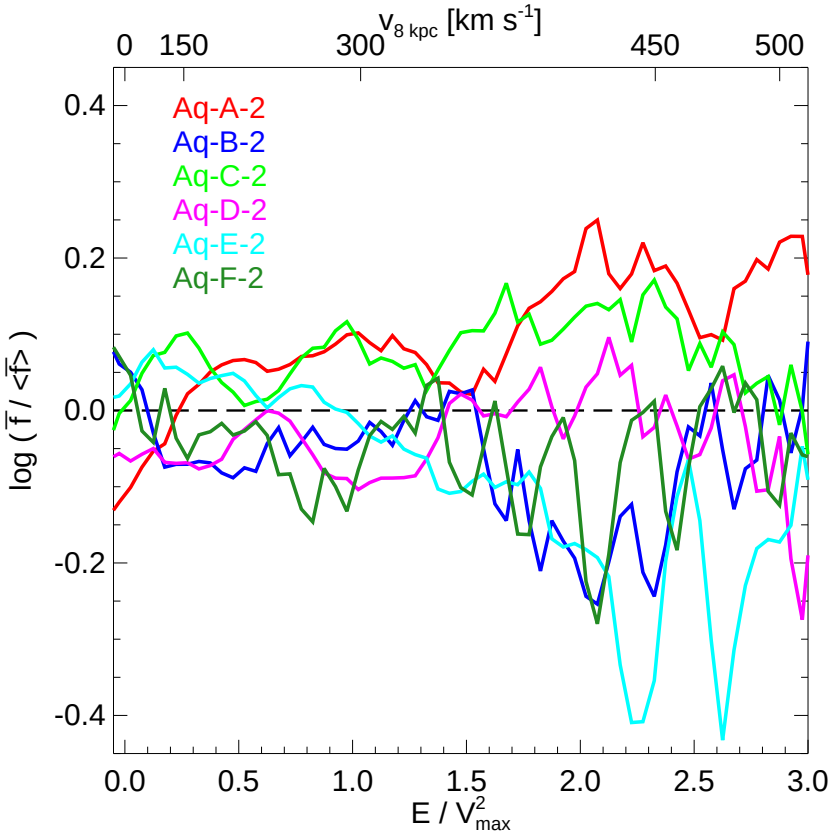

Figure 4.10: Deviations of the individual phase-space density distributions from the mean over our sample of level-2 haloes. We focus here on the more bound part. The lower x-axis shows the orbital energy while the upper one shows the corresponding velocity 8 kpc distance from halo centre. The amplitude of features increases for $V_{8\ \mathrm{kpc}} > 350$ km/s. At even lower binding energies, $E > 3\ V_{\mathrm{max}}$ deviations can reach an order of magnitude, see Fig. 4.9.

density distribution with particles accreted at certain epochs, and in both haloes the most weakly bound particles were added only very recently. Note that the phase-space density of this material is very low, so it contributes negligibly to the overall local dark matter density. In the bottom panels of Fig. 4.11 we show the $\bar{f}(E)$ distributions of particles which were associated with a single, massive FoF-group which was identified at $z = 6.85$ in the case of Aq-A-2 and at $z = 0.75$ in the case of Aq-F-2. The wiggles in the strongly bound part of Aq-A-2 are clearly due to this early merger event, while the later merger in Aq-F-2 is responsible for most of the material accreted in $0.56 < z < 0.81$ and for most of the strong features in the phase-space density distribution.

We conclude that these features in the energy distribution should open the window to "dark matter astronomy" once experiments reach the sensitivity needed for routine detection of DM particles. We will then be able to explore the formation history of the Milky Way using the DM energy distribution.

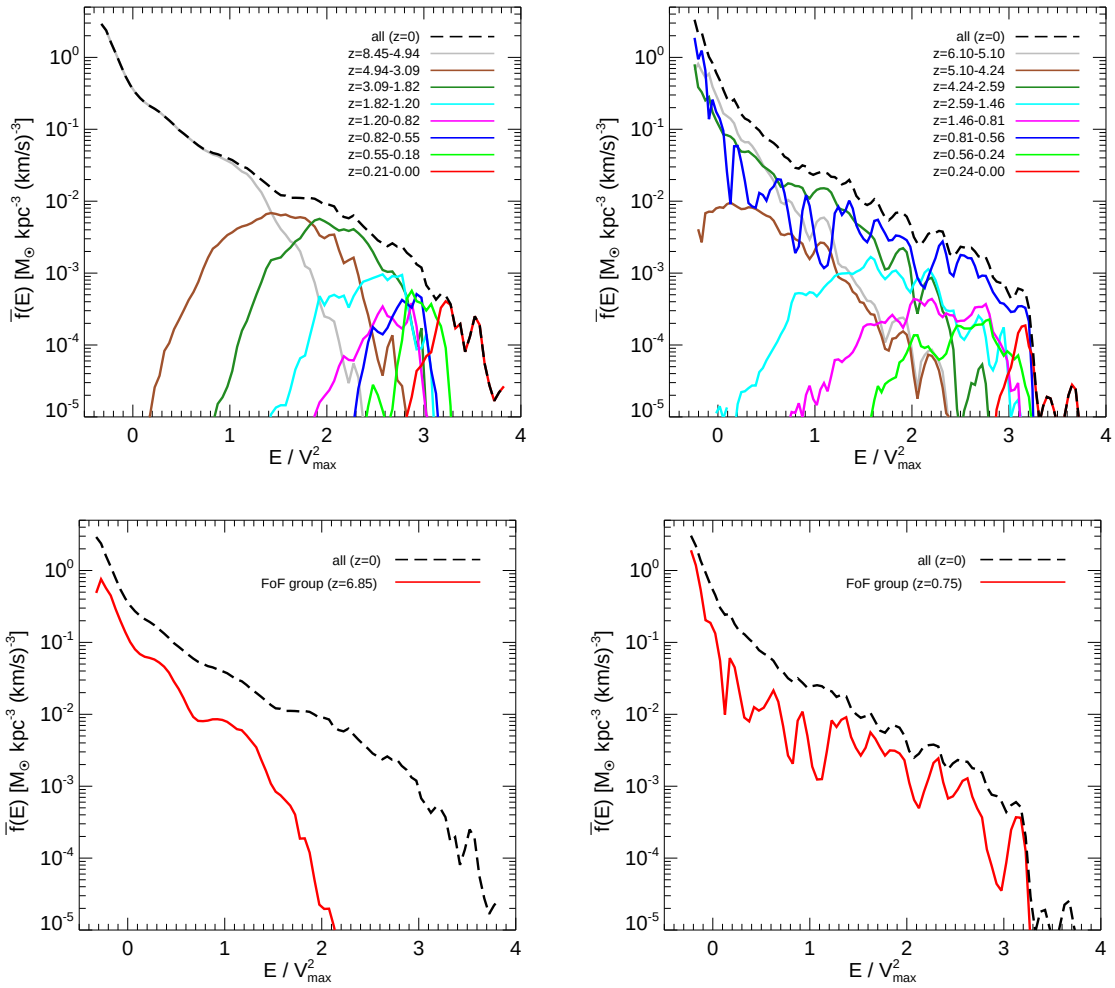

Figure 4.11: Top row: Contributions to the present-day phase-space density distribution from particles accreted at different epochs (indicated by different colours). The top left panel shows the build-up of the distribution function for halo Aq-A-2. This halo has a quiescent formation history with no recent mergers. The top right panel is a similar plot for Aq-F-2, which underwent a major merger between $z = 0.75$ and $z = 0.68$. Bottom row: These plots isolate the contribution of a single, massive FoF group to the $z = 0$ phase-space density distributions. For Aq-A-2 this group was identified at $z = 6.85$, for Aq-F-2 at $z = 0.75$. In both cases it is clear that material from the group is responsible for some of the features seen in the present-day phase-space density distribution.

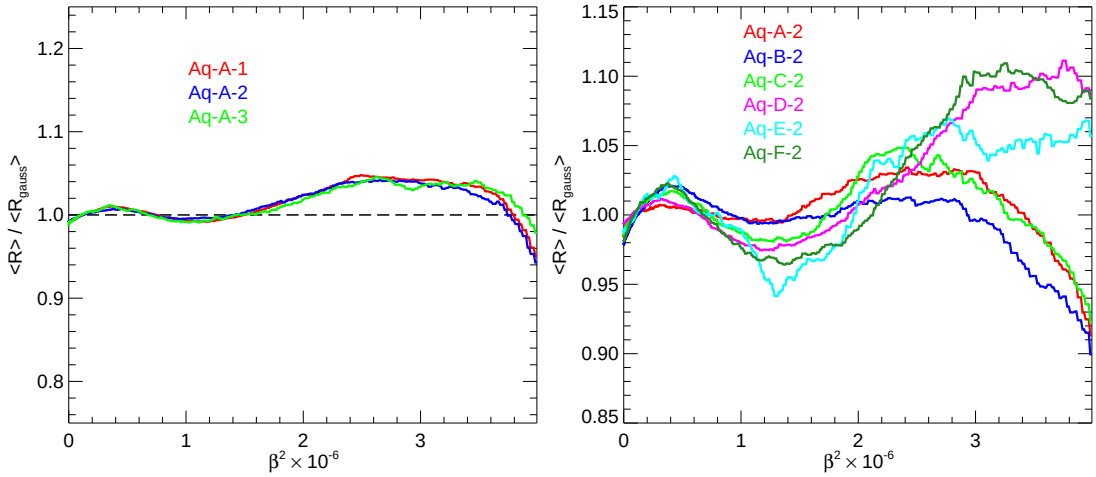

Figure 4.12: Recoil spectra ratio for the three highest resolution simulations of Aq-A (left) and the level-2 (right) simulations of the other haloes. For these plots we averaged the recoil rate over a year for every box and then calculated the median recoil rate ratio $\langle R\rangle/\langle R_{\rm gauss}\rangle$ of the rates for the simulation and for the best-fit multivariate Gaussian distribution. The x-axis is directly proportional to the energy. In all level-2 haloes the expected recoil spectrum based on a multivariate Gaussian can be wrong by about 10% depending on the energy. Furthermore the behaviour of the deviations seems quite similar. This is due to the fact that the velocity distributions differ in a characteristic way from a multivariate Gaussian. The deviations in the recoil spectra are typically highest at high energies.

4.6 Detector signals

We will now use the spatial and velocity distributions explored above to calculate expected detector signals. The main question here is how the non-Gaussian features of the velocity distribution influence these signals. Our results show that features due to subhaloes or massive streams are expected to be unimportant. On the other hand, deviations of the velocity distributions from a perfect Gaussians in terms of general shape, bumps and dips can have an impact on detector signals.

There are currently more than 20 direct detection experiments searching for Galactic DM, most of them focusing on WIMPs. For these, the detection scheme is based on nuclear recoil with the detector material. The differential WIMP elastic scattering rate can be written as (Jungman et al., 1996)

$$\frac{\mathrm{d}R}{\mathrm{d}E} = \mathcal{R}\ \rho_0\ T(E,t), \tag{4.3}$$

where $\mathcal{R}$ encapsulates the particle physics parameters (mass and cross-section of the WIMP; form factor and mass of target nucleus), ρ_0 is the local dark matter density that we assume to be constant based on the results of section 3, and

$$T(E,t) = \int_{v_{\rm min}}^{\infty} \mathrm{d}v\ \frac{f_v(t)}{v}, \tag{4.4}$$

where f_v is the WIMP speed distribution in the rest frame of the detector integrated over the angular distribution. $v_{\rm min}$ here is the detector-dependent minimum WIMP speed that can cause a recoil of energy E

$$v_{\rm min} = \left(\frac{E\ (m_\chi + m_A)^2}{2 m_\chi^2 m_A} \right)^{1/2}, \tag{4.5}$$

where m_χ is the WIMP mass and m_A the atomic mass of the target nucleus. To get detector independent results we set $\mathcal{R} = 1$ in the following[2].

The recoil rate shows a annual modulation over the year (Drukier et al., 1986). To take this into account we add the Earth's motion to the local box velocities to transform Galactic rest frame velocities into the detector frame. We model the motion of the Earth according to Lewin and Smith (1996) and Binney and Merrifield (1998). Let $\vec{v}_E = \vec{u}_r + \vec{u}_S + \vec{u}_E$ be the velocity of the Earth relative to the Galactic rest frame decomposed into Galactic rotation $\vec{u}_r$, the Sun's peculiar motion $\vec{u}_S$ and the Earth's velocity relative to the Sun $\vec{u}_E$. In Galactic coordinates these velocities can be written as

$$\begin{aligned} \vec{u}_r &= (0, 222.2, 0)\ \text{km/s}, \\ \vec{u}_S &= (10.0, 5.2, 7.2)\ \text{km/s}, \\ e_{E,i} &= u_E(\lambda)\ \cos(\beta_i)\ \sin(\lambda - \lambda_i), \\ u_E(\lambda) &= \langle u_E \rangle\ [1 - e \sin(\lambda - \lambda_i)], \end{aligned} \tag{4.6}$$

where $i = R, \phi, z$, λ is the ecliptic longitude ($\lambda_0 = (13 \pm 1)^\circ$),$\langle u_E \rangle = 29.79$ km/s is the mean velocity of the Earth around the Sun, and the ellipticity of the Earth orbit $e = 0.016722$. The $\vec{u}_r$ value is based on a combination of a large number of independent determinations of the circular velocity by Kerr and Lynden-Bell (1986). We note that this value has a standard deviation of 20 km/s. For the constant β and λ angles we take

$$\begin{aligned} (\beta_R, \beta_\phi, \beta_z) &= (-5.5303^\circ, 59.575^\circ, 29.812^\circ), \\ (\lambda_R, \lambda_\phi, \lambda_z) &= (266.141^\circ, -13.3485^\circ, 179.3212^\circ). \end{aligned} \tag{4.7}$$

The ecliptic longitude can be written as

$$\begin{aligned} \lambda(t) &= L(t) + 1.915^\circ \sin g(t) + 0.020^\circ \sin 2g(t), \\ L(t) &= 280.460^\circ + 0.9856474^\circ t, \\ g(t) &= 357.528^\circ + 0.9856003^\circ t, \end{aligned} \tag{4.8}$$

where t is the fractional day number relative to noon (UT) on 31 December 1999 (J2000.0). We refer to a day number relative to 31 December 2008 in our plots. In what follows we will assume that the R-direction is always aligned with the major axis of the principal axis frame of the velocity ellipsoid in each box and the ϕ- and z-directions, with the intermediate and short axes. This is needed to add the Earth's motion to the box velocities,

[2]This also implies that we assume the form factor to be constant. Any other form factor will change the shape of the recoil spectrum. Since we are not interested in the exact shape of the spectrum, but in deviations expected due to different velocity distributions, we neglect form factor effects in the following.

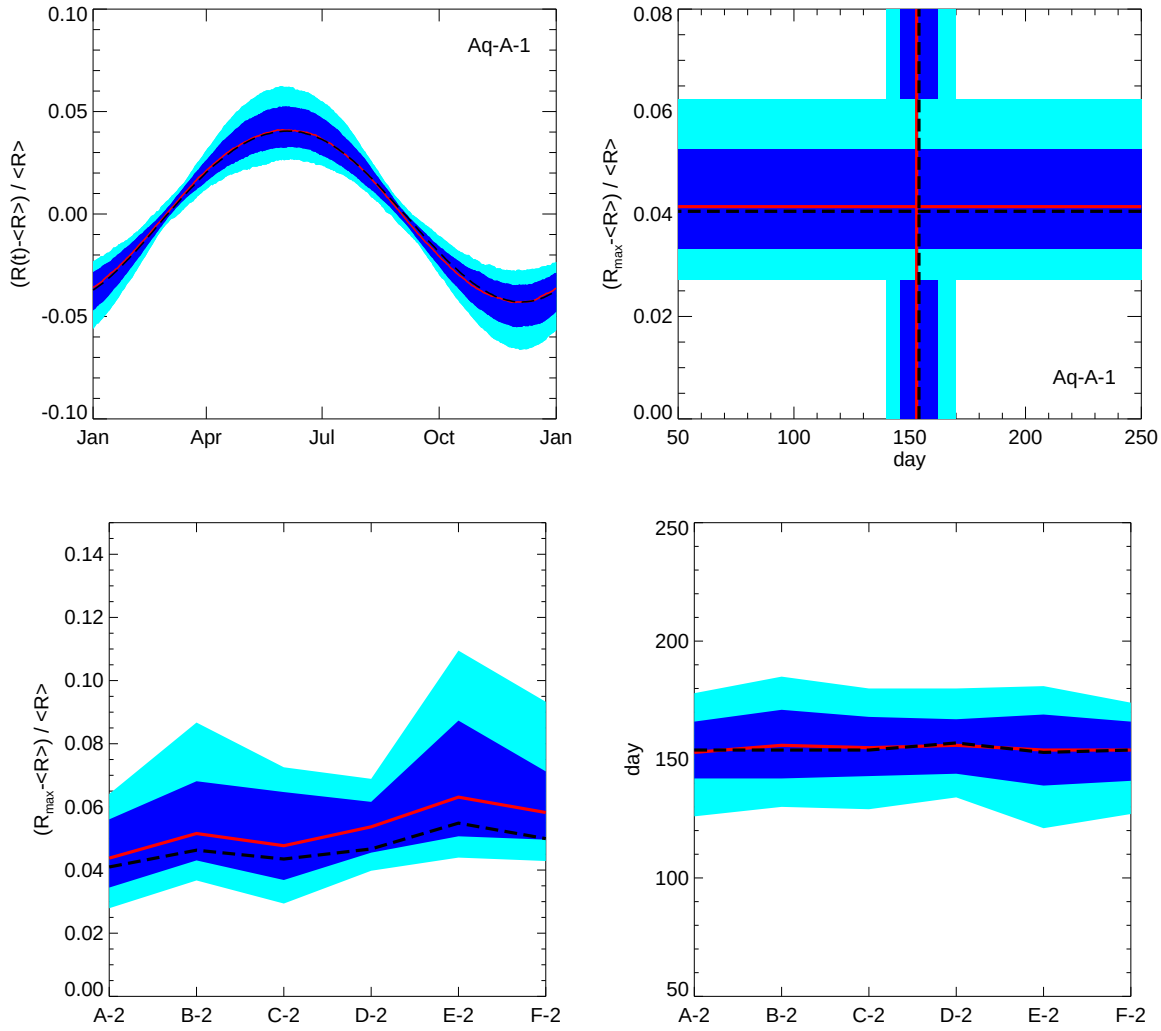

Figure 4.13: Top panels: Annual modulation for all 2 kpc boxes with halocentric distance between 7 and 9 kpc in halo Aq-A-1 assuming $v_{\min} = 300$ km/s. The left plot shows how the dimensionless recoil rate $(R(t) - \langle R\rangle)/\langle R\rangle$ changes over the year. The right plot shows the corresponding modulation parameter space defined by the peak day (x-axis) and maximum amplitude $(R_{\max} - \langle R\rangle)/\langle R\rangle$ (y-axis). Bottom panels: Modulation parameters for the local 2 kpc boxes of all level-2 resolution haloes. There is no clear trend visible in the day of maximum behaviour over the halo sample. On the other hand, the median amplitude in all boxes is higher than expected based on the Gaussian sample for $v_{\min} = 300$ km/s. The line and contour scheme is the same as in Fig. 4.2.

and to transform the velocity vectors in each box to the detector frame.

Clearly the deviations of the velocity distribution from a perfect multivariate Gaussian found in the previous sections will also alter the recoil spectrum, because the velocity integral $T(E,t)$ effectively measures the $1/v$-weighted area under the velocity curve. As in the previous sections we compare the results obtained directly from the simulations to the expectation for a best-fit multivariate Gaussian distribution. In Fig. 4.12 we plot recoil spectra ratios for the three highest resolution simulations of Aq-A (left) and the level-2 (right) simulations of the other haloes. For these plots we averaged the recoil rate over a year for individual boxes. The rates are calculated using the simulation velocity distribution ($\langle R\rangle$) and the best-fit Gaussian model for each box ($\langle R_{\rm gauss}\rangle$). The plots show the median of the ratios $\langle R\rangle/\langle R_{\rm gauss}\rangle$ over all boxes. Since we assume that the density ρ_0 is constant in a given box, it drops out when calculating the ratios. The x-axis measures the energy in dimensionless $\beta = v/c$ values. For a given detector this can easily be converted to keV, assuming the masses m_χ and m_A are given in GeV/c^2

$$E = \frac{2\ m_\chi^2\ m_A}{(m_\chi + m_A)^2}\ c^2\ \ \beta^2\ \ \times\ \ 10^6\ \ \text{keV}. \tag{4.9}$$

Fig. 4.12 clearly shows that in all level-2 haloes the expected recoil spectrum based on a multivariate Gaussian model can differ by up to 10% from the directly predicted simulation result. Furthermore, the behaviour of the deviations seems to be similar in all cases, especially at low energies, where we already found that the phase-space density is nearly universal. The similarity in the deviations between the different haloes is due to the fact that the velocity distributions all differ in a characteristic way from the Gaussian distributions as shown in section 4. The deviations in the recoil spectra are typically highest at high energies.

The 10% deviations in the recoil spectra are larger than the typical deviations expected due to the annual modulation. Therefore these deviations from the Gaussian model can also influence the annual modulation signal. In Fig. 4.13 (top row) we plot the dimensionless recoil rate $(R(t) - \langle R\rangle)/\langle R\rangle$ of all local 2 kpc boxes at ~ 8 kpc from the centre of Aq-A-1 (left),where $\langle R\rangle$ is the annual mean recoil. We have assumed $v_{\rm min} = 300$ km/s for all plots in this figure. The maximum can clearly be seen around the month of June. The plot on the right in Fig. 4.13 shows the modulation parameter space that we define by the day of maximum amplitude (x-axis) and the maximum modulation amplitude of the recoil rate over the year defined as $(R_{\rm max} - \langle R\rangle)/\langle R\rangle$ (y-axis). The bottom row of Fig. 4.13 shows the maximum amplitude (left) and day of maximum (right) for all level-2 haloes (solid red) and the corresponding best-fit multivariate Gaussian model (dashed black).

Comparing the Gaussian median values to the box median values one can see that the day of maximum amplitude does not deviate significantly from that predicted for a multivariate Gaussian; in particular there is no clear trend visible over the halo sample. On the other hand, the median amplitude in all haloes is slightly higher than expected based on the Gaussian sample for $v_{\rm min} = 300$ km/s.

The amplitude differences for various $v_{\rm min}$ values are shown in Fig. 4.14. Here we calculated the maximum amplitude and day of maximum for different $v_{\rm min}$ values for

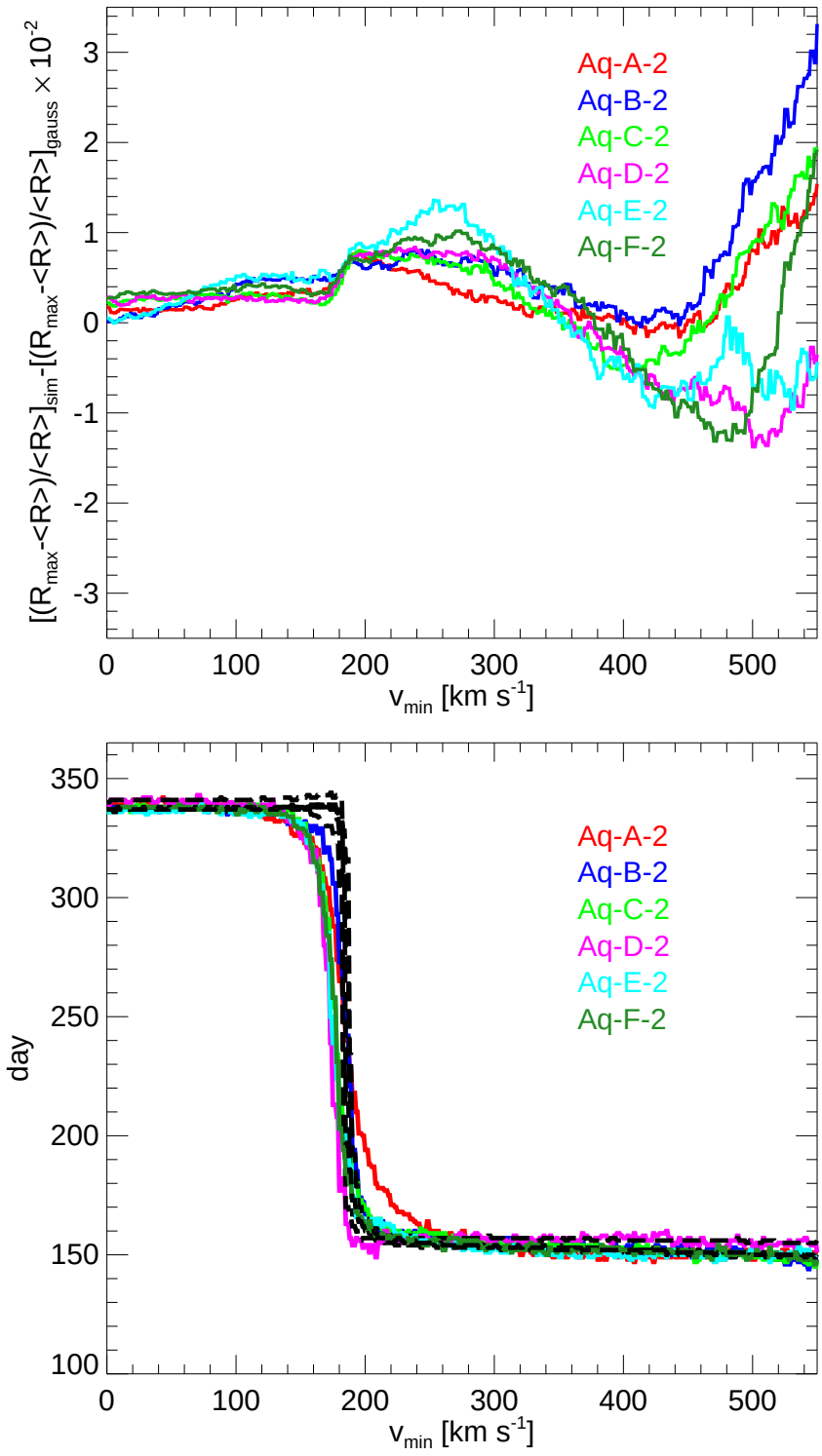

Figure 4.14: Top panel: Median recoil rate amplitude for all 2 kpc boxes with halocentric distance between 7 and 9 kpc for all level-2 haloes. The plot shows the difference between the relative maximum modulation amplitude observed in the simulation and that expected for the best-fit multivariate Gaussian distribution. Bottom panel: Median day of maximum amplitude for the same haloes (solid red) compared to their Gaussian predictions (dashed black). The day of maximum amplitude is the same for all boxes and is well reproduced in the Gaussian model. The phase-reversal can clearly be seen.

all level-2 haloes. The amplitude plot (top) shows the difference between the maximum relative modulation amplitude observed in the simulation and that expected for the best-fit multivariate Gaussian model. The maximum amplitude $v_{\rm min}$-dependence is similar for the six haloes. Since only the velocity distribution enters into the recoil calculation, this similarity is due to the fact that deviations of the halo velocity distribution from the Gaussian model are also quite similar for all six haloes. The bottom plot of Fig. 4.14 shows the day of maximum amplitude is well predicted by the multivariate Gaussian for all haloes. The sharp transition in the day of maximum is due to the well-known phase-reversal effect (Primack et al., 1988). We checked that the subhalo dominated box in Aq-B-2, where by chance about 60% of the box mass is in a single subhalo, leads to a very different modulation signal. The day of maximum in that case shifts about 100 days from the Gaussian distribution. We note that although the subhalo mass fraction in this particular box is high, the subhalo volume fraction is tiny, so even within this box, almost all observers would see the smooth regular signal.

Although most of the direct experiments currently search for WIMPs the axion provides another promising candidate for CDM. It arises from the Peccei-Quinn solution to the strong CP-problem. One axion detection scheme is based on using the axion-electromagnetic coupling to induce resonant conversions of axions to photons in the microwave frequency range. Galactic axions have non-relativistic velocities ($\beta = v/c \sim 10^{-3}$) and the axion-to-photon conversion process conserves energy, so that the frequency of converted photons can be written as

$$\nu_a = \nu_a^0 + \Delta\nu_a = 241.8 \left(\frac{m_a}{1\mu{\rm eV}/c^2}\right)\left(1+\frac{1}{2}\beta^2\right) {\rm MHz}, \tag{4.10}$$

where m_a is the axion mass that lies between 10^{-6} eV$/c^2$ and 10^{-3} eV$/c^2$. 5μeV axions would therefore convert into $\nu_a^0 \cong 1200$ MHz photons with an upward spread of $\Delta\nu_a \sim\cong$ 2 kHz due to their kinetic energy. An advantage of axion detection compared to WIMP searches is the fact that it is directly sensitive to the energy rather than to the integral over the velocity distribution. The power P, developed in the axion search cavity due to resonant axion-photon conversion can be written as (Sikivie, 1983)

$$P = \mathcal{P}\ \rho_a(\nu_{\rm cavity}), \tag{4.11}$$

where $\mathcal{P}$ encapsulates the experimental properties (cavity volume, magnetic field, quality factor) and particle physics properties (model dependent coupling parameter, axion mass). The only astrophysical input is the local density $\rho_a(\nu_{\rm cavity})$ of axions with energies corresponding to the cavity frequency. For simplicity we set $\mathcal{P} = 1$. We can produce axion spectra from our simulations by taking a local volume element (a box) and computing the distribution of kinetic energies K of the particles found in this location. The number of particles with a given K is then directly proportional to ρ_a at this frequency, and so to the power in the frequency bin.

To make the results independent of axion mass and other experimental properties we present histograms of β^2 normalised to one. For a given axion mass m_a (in μeV$/c^2$) the x-axis must be transformed according to $x \rightarrow 241.8\ m_a\ (1{+}1/2x)$ to get the corresponding

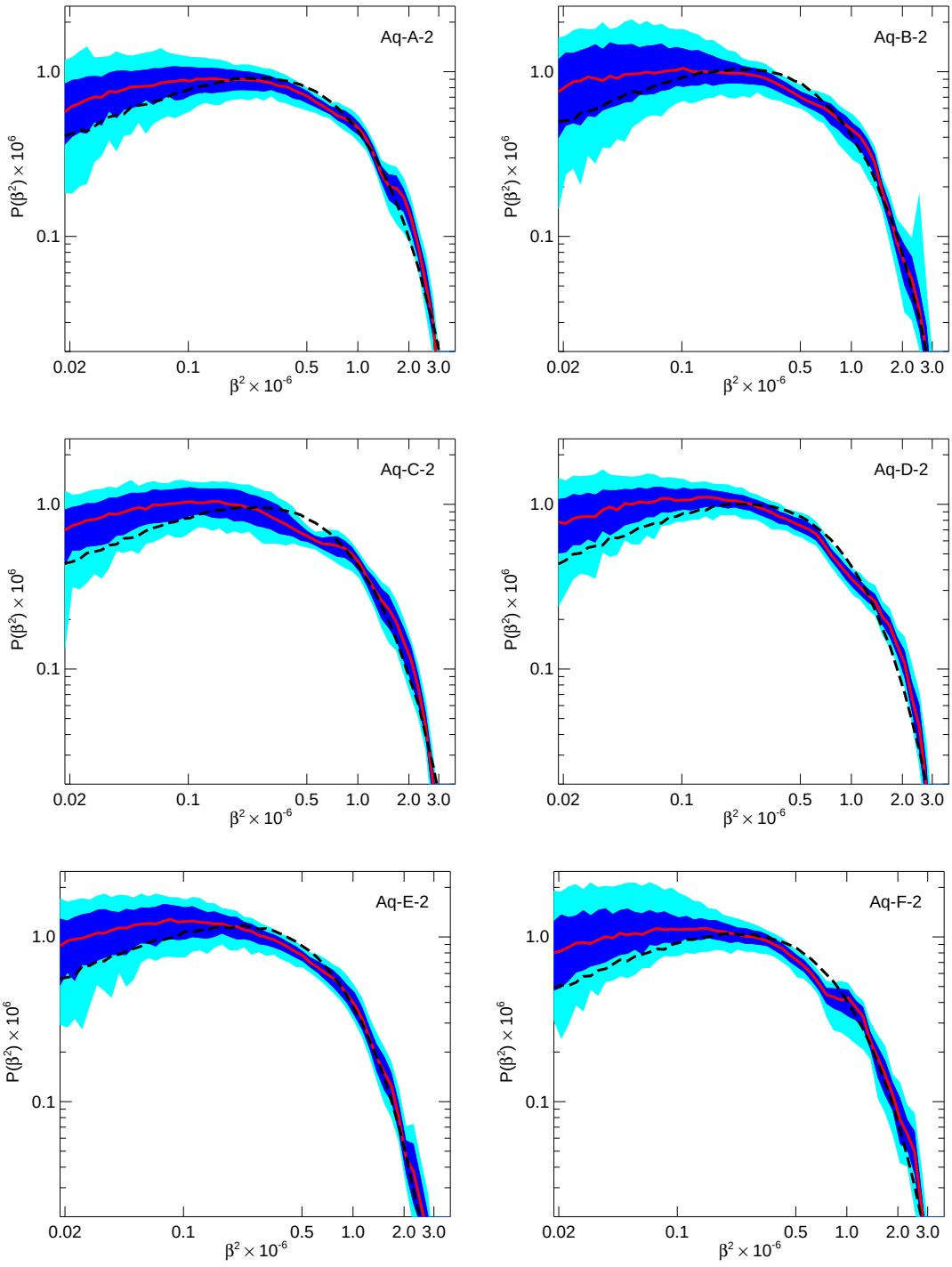

Figure 4.15: Axion spectra of level-2 haloes for all 2 kpc boxes with halocentric distance between 7 and 9 kpc. Rescaling the x-axis according to $x \to 241.8\ m_a\ (1 + 1/2x)$ for an axion mass m_a in μeV yields the x-axis in MHz. The y-axis is proportional to the power P developed in the detector cavity. Therefore the panels show the predicted frequency spectra expected for an axion search experiment like ADMX. These spectra can be reasonably described by a multivariate Gaussian but significant differences remain. The maximum in the power is at lower frequencies in the simulation than in the Gaussian model. The bumps already found in the velocity and energy distribution are clearly visible in these spectra. In all haloes the power at low frequencies is higher than expected from the Gaussian model. The line and contour scheme are the same as in Fig. 4.2.

frequencies in MHz.

A long-running axion search experiment is ADMX at LLNL (Hagmann et al., 1996). It has channels at medium (MR) and high resolution (HR). The latter has a frequency resolution of about 0.02 Hz. For $\nu_a^0 = 500$ MHz and an axion velocity of $v = 200$ km/s this translates into a velocity width of only 0.018 km/s[3]. Our numerical resolution prevents us from predicting the behaviour on such small scales. For wider bin searches and especially for the medium resolution (MR) channel (125 Hz corresponding to a typical velocity spread of about 100 km/s) we can, however make reliable predictions by binning particles with respect to β^2.

In Fig. 4.15 we show axion spectra for all level-2 haloes[4]. In a broad sense, the spectra obtained from our simulations look similar to those of multivariate Gaussian models. However there are a number of differences. For example, the peak power is shifted to lower frequencies. The Gaussian distribution is also a poor description of the spectrum at low frequencies. In all haloes the power at low and high frequencies is higher then expected from a multivariate Gaussian model. This effect is quite small for high frequencies but very significant for low frequencies. The higher power at low frequencies can be understood from the velocity distributions in Fig. 4.4. In Aq-B-2 the subhalo dominated box that was seen in Fig. 4.4 is clearly visible as a peak in the power spectrum at high frequency. The bumps in the velocity distribution also result in quite significant features in the axion spectra that might be visible in the MR channel given enough signal-to-noise.

4.7 Conclusion and Discussion

We have characterised the local phase-space distribution of dark matter using the recently published ultra-high resolution simulations of the Aquarius Project. Our study provides new insights relevant to searches for the elusive CDM particles. This results from the unprecedented resolution and convergence (in a dynamical sense) of our simulations, as well as from the fact that they provide a sample of six Milky Way-like dark matter haloes.

We have measured the probability distribution function of the DM mass density between 6 and 12 kpc from the centre of the halo, finding it to be made up of two components: a truly smooth distribution which scatters around the mean on ellipsoidal shells by less than 5% in all the haloes of our sample, and a high-density tail associated with subhaloes. The smooth DM component dominates the local DM distribution. With 99.9% confidence we can say that the Sun lies in a region where the density departs from the mean on ellipsoidal shells by less then 15%. Experimentalists can safely adopt smooth models to estimate the DM density near the Sun.

We find that the local velocity distribution is also expected to be very smooth, with no sign of massive streams or subhalo contributions. The standard assumption of a Maxwellian velocity distribution is not correct for our haloes, because the velocity distribution is clearly anisotropic. The velocity ellipsoid at each point aligns very well with

[3]For non-relativistic motion we can write $\mathrm{dv} = (\mathrm{c}^2/\mathrm{v})\ (\mathrm{d}\nu/\nu_\mathrm{a}^0)$.

[4]We neglect the effects of the Earth's motion when constructing the spectra since here our focus is on the general spectral shape. This motion typically leads to a shift of about 100 Hz due to annual modulation and a daily shift of about 1 Hz due to the Earth's rotation (Duffy et al., 2005).

the shape of the halo. A better fit to the simulations is given by a multivariate Gaussian. Even this description does not reproduce the exact shape of the distributions perfectly. In particular the modulus of the velocity vector shows marked deviations from such model predictions. Velocity distributions in our six different haloes share common features with respect to the multivariate Gaussian model: the low-velocity region is more populated in the simulation; the peak of the simulation distribution is depressed compared to the Gaussian; at high velocities there is typically an excess in the simulation distribution compared to the best-fit multivariate Gaussian. Furthermore the velocity distribution shows features which are stable in time, are reproduced from place to place within a given halo, but differ between different haloes. These are related to the formation history of each individual halo.

The imprints in the modulus of the velocity vector reflect features in the energy distribution. We explicitly show that the phase-space distribution function as a function of energy contains characteristic wiggles. The amplitude of these wiggles with respect to the average distribution function of our sample of six haloes rises from high to low-binding energies. After appropriate scaling, the most bound part of the distribution function looks very similar in all haloes, suggesting a (nearly) universal shape. The weakly bound part of the distribution, on the other hand, can deviate in any given halo by an order of magnitude from the mean.

We have used our simulations to predict detector signals for WIMP and axion searches. We find that WIMP recoil spectra can deviate about 10% from the recoil rate expected from the best-fit multivariate Gaussian model. The energy dependence of these deviations looks similar in all six haloes; especially at higher binding energies. We find that the annual modulation signal peaks around the same day as expected from a multivariate Gaussian model with no clear trend over our halo sample for varying recoil velocity thresholds. The maximum recoil modulation amplitude, on the other hand, shows a clear threshold-dependent difference between the signal expected for a multivariate Gaussian model and that estimated from the simulation. We have also explored the expected signal for direct detection of axions. We find the axion spectra to be smooth without any sign of massive streams. The spectra show characteristic deviations from those predicted by a multivariate Gaussian model; the power at low and high frequencies is higher than expected. The most pronounced effect is that the spectra peak at lower frequencies than predicted. Since the frequencies in the axion detector are directly proportional to the kinetic energy of the axion particles, the bumps in the DM velocity and energy distributions are also clearly visible in the axion spectra. All the effects on the various detector signals are driven by differences in the velocity distribution. Individual subhaloes or streams do not influence the detector signals however, since they are sub-dominant by a large factor in all six haloes.

Our study shows that, once direct dark matter detection has become routine, the characterisation of the DM energy distribution will provide unique insights into the assembly history of the Milky Way halo. In the next decade, a new field may emerge, that of “dark matter astronomy”.

Part III

Fine-grained dark matter distribution

5

The fine-grained phase-space structure of cold dark matter haloes

In the previous chapter we analysed the coarse-grained phase-space structure of an ultra-high resolution simulation. In this chapter we present a new and completely general technique for calculating the fine-grained phase-space structure of dark matter throughout the Galactic halo. Our goal is to understand this structure on the scales relevant for direct and indirect detection experiments. Our method is based on evaluating the geodesic deviation equation along the trajectories of individual DM particles. In this chapter we study general static potentials which exhibit more complex behaviour than the separable potentials studied previously. For ellipsoidal logarithmic potentials with a core, phase mixing is sensitive to the resonance structure, as indicated by the number of independent orbital frequencies. Regions of chaotic mixing can be identified by the very rapid decrease in the configuration-space density of the associated dark matter streams. We also study the evolution of stream density in ellipsoidal NFW haloes with radially varying isopotential shape, showing that if such a model is applied to the Galactic halo, at least 10^5 streams are expected near the Sun. The most novel aspect of our approach is that general non-static systems can be studied through implementation in a cosmological N-body code. Such an implementation allows a robust and accurate evaluation of the enhancements in annihilation radiation due to fine-scale structure such as caustics. We embed the scheme in the current state-of-the-art code GADGET-3 and present tests which demonstrate that N-body discreteness effects can be kept under control in realistic configurations. [1]

[1] published in Vogelsberger et al, MNRAS., 385, 1, 236-254 (2008)

5.1 Introduction

In the last chapter we presented a very high-resolution simulation that we used to infer information on the local dark matter (DM) phase-space structure. We also pointed out that the detection of DM is the crucial test of the standard paradigm saying the DM dominates and drives structure formation in the Universe.

Furthermore, we said that today many experiments are searching for the elusive DM particle, (Akerib and et al, 2004; Sanglard and et al, 2005; Schnee, 2006; Aprile et al., 2007; Spooner, 2007). The main challenge lies in the large background they encounter. Having an idea what the detector signal might look like can help substantially in fine-tuning the experiments in order to increase the chance of a detection. In addition, many experiments are attempting to detect WIMPs indirectly by searching for γ-ray emission from their annihilation (de Boer, 2005; de Boer et al., 2005; Bergström and Hooper, 2006; Hooper and Serpico, 2007). Predictions for this radiation are currently uncertain because very substantial enhancements are possible, at least in principle, from fine-scale structure such as caustics in the dark matter distribution (Hogan, 2001; Mohayaee et al., 2007).

As we also said in the last chapter, the differential rate for WIMPs-nucleus scattering is sensitive to the local velocity distribution (Jungman et al., 1996)

$$\frac{\mathrm{d}R}{\mathrm{d}E} = AF^2(E)\int_{v_{\min}}^{\infty}\left[\frac{f_v(v)}{v}\right]\mathrm{d}v, \tag{5.1}$$

where E is the energy deposited in the detector, $F(E)$ is the elastic nuclear form factor and $f_v(v)$ is the local velocity distribution of the WIMPs relative to the detector. The coefficient A is defined as

$$A = \frac{\rho_0\sigma_{N\chi}}{2m_\chi m_r^2}, \tag{5.2}$$

where ρ_0 is the WIMP density near the Earth and $\sigma_{N\chi}$ the WIMP-nucleus cross-section. The reduced mass m_r is given by

$$m_r = \frac{m_\chi m_{\mathrm{N}}}{m_\chi + m_{\mathrm{N}}}, \tag{5.3}$$

where m_χ is the WIMP mass and m_{N} the nucleus mass. The minimal incoming velocity of incident WIMPs that can deposit the energy E is given by

$$v_{\min} = \sqrt{\frac{m_{\mathrm{N}}E}{2m_r^2}}. \tag{5.4}$$

In the last chapter we used the result of our N-body simulation to evaluate Eq. (5.1), and it is evident that the count rate in a direction-insensitive experiment depends on the velocity distribution of the incident particles and will be modulated by the orbital motion of the Earth around the Sun (Drukier et al., 1986) as we showed. We also mentioned that in most studies, an isotropic Maxwellian distribution relative to the galactic halo has been assumed, (e.g. Freese et al., 1988), although there are other models in the literature, discussing, for example, multivariate Gaussians (Evans et al., 2000). We showed that both distributions do not describe the velocity distribution in our simulation correctly.

Therefore, it seems that the last chapter already answered all possible questions on the expected DM distribution in the solar system. We specified the spatial and velocity distribution and could also calculate detector signals. But we have not yet discussed one very important point. Although, the results of the last chapter were based on an impressively large and detailed simulation, its length-scale resolution is of the order of 10 pc. From a cosmological point of view this is a very impressive resolution, but from the perspective of a direct detection experiment, it is very huge. DM detectors operate on scales of meters and are therefore many orders of magnitude off from the scales current high-resolution simulation can resolve. This does not imply that our results of the last chapter are useless, but it implies that there might be smaller features in the DM phase-space distribution that we could not resolve, but might play a role for DM search experiments. This might affect direct and indirect searches. It is the goal of this chapter to explain what kind of features we might expect and how important they are for search experiments. Standard N-body simulations sample the phase-space quite coarse and they therefore can only resolve the coarse-grained phase-space of CDM haloes. In this chapter we are concerned about the fine-grained structure. Some attempts at understanding the effect of fine-scale structure in the velocity distribution of DM particles have also been made (Sikivie, 1998; Stiff et al., 2001; Hogan, 2001). In this chapter and in the following, we will show why this early calculations are wrong and what can be done to understand the fine-grained phase-space structure in a better way.

The first question is, what kind of fine-grained features could influence the DM search experiments and alter the results of the last chapter? A significant signal could come from what are known as streams of DM (Sikivie et al., 1995; Helmi et al., 2002; Natarajan and Sikivie, 2005). Both axions and WIMPs are cold. In the absence of clustering their present day velocity dispersion would be negligible ($\delta v \sim 10^{-10}c$ for WIMPs and $\delta v \sim 10^{-17}c$ for axions). They are effectively restricted to a 3D hypersurface, a sheet in 6D phase-space. The growth of structure results in continual stretching and folding in phase-space of this initially almost uniform sheet. This process is called mixing. The more strongly the system mixes, the more streams of DM particles are present at a given location in configuration-space. Mixing stretches each sheet and so its density decreases. The existence of distinct streams is a direct consequence of the collisionless character and the coldness of CDM. The situation is sketched in Fig. 5.1. At the points where the number of streams changes by two, the local configuration-space density of dark matter becomes extremely high. These are caustics of the kind studied by catastrophe theory (Gilmore, 1982; Tremaine, 1999). Note that Liouville's Theorem prevents the CDM phase-space sheet from ever tearing, although it can be arbitrarily strongly stretched.

If the dark matter density in the solar neighbourhood is dominated by a small number of streams, its velocity distribution will effectively consist of a few discrete values, one for each stream. If, on the other hand, the number of streams is very large, the velocity distribution will be smooth and individual streams will be undetectable. In the second case the results of the last chapter will not be alter at all. But if there were massive streams near the Sun, this could alter the phase-space distribution and therefore the detector signals significantly compared to the results of the last chapter. This issue has so far been addressed only under simplified conditions and divorced from its proper cosmological context (Helmi et al., 2002; Natarajan and Sikivie, 2005). This is largely because the only

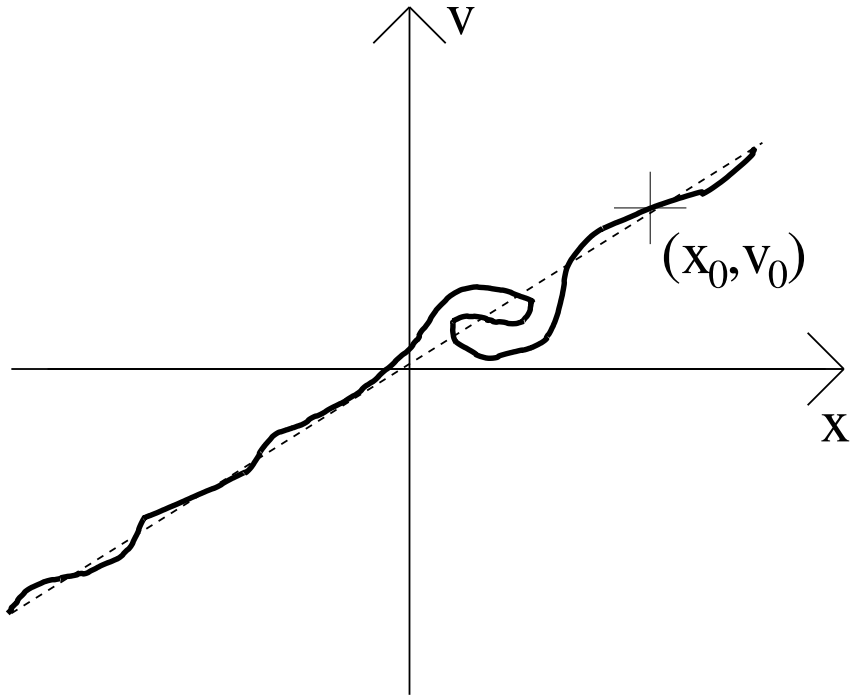

Figure 5.1: Sketch of an idealised CDM phase-space sheet in the x, v plane. The thickness of the line represents the local velocity dispersion within each stream. The small wiggles correspond to initial density perturbations and the multi-valued region reflects the multiple streams created by winding in nonlinear regions. Depending on x position an observer sees one or three streams. At points where the number of streams changes by two, a caustic with a very high DM density is present. Such caustics may be significant for the total annihilation flux. The number of streams at each point is a measure of the local amount of mixing. The dashed line represents the Hubble Flow. The cross marks the phase-space coordinates of a particular CDM particle embedded in the flow.

tool capable of studying cosmological structure formation in full generality, namely N-body simulations, cannot resolve the relevant scales. For example, Natarajan and Sikivie (2005) estimate that of the order of 10^{12} particles would be required in a simulation of the Milky Way's halo to begin to resolve the streams in the solar neighbourhood. It is thus impossible to figure out the number of streams near the Sun and the properties of "typical" streams with current N-body capabilities. We note that some simulations under quite restricted conditions and with very special care taken could resolve some fine-grained phase-space features (Stiff et al., 2001; Alard and Colombi, 2005).

A related issue that has been much discussed is whether caustics can affect direct or indirect detection experiments. Some authors claim that caustics play an important role as stable phenomena connected to any collapsing CDM halo and taking the form of relatively massive rings, shells or other geometries (Sikivie, 1999; Natarajan and Sikivie, 2006). Other authors have argued that caustics should be more abundant, weaker and dynamically negligible (Helmi et al., 2002). Even if caustics negligibly affect the gravitational potential, they may have very substantial effects on the annihilation rate of dark matter (Hogan, 2001; Bergström et al., 2001; Pieri and Branchini, 2005; Mohayaee and Shandarin,

2006; Mohayaee et al., 2007; Natarajan, 2007). All these papers were able to evaluate the enhancements due to caustics only under restrictive and unrealistic assumptions about symmetry, formation history, etc. Although there are some claims that there are observational hints for their correctness (Kinney and Sikivie, 2000; Sikivie, 2003; Onemli and Sikivie, 2007). While they demonstrate that large enhancement factors may be possible, they do not provide reliable estimates for the actual enhancement expected. The method we present below is capable of providing such estimates for haloes growing as predicted by the ΛCDM model.

In this chapter we will present a novel approach that directly analyses structure in the fine-grained phase-space distribution. We circumvent the "number of particle" problem by solving the geodesic deviation equation (GDE) for every DM particle. This allows us to calculate the local properties of the DM stream each simulation particle is embedded in, in particular, its configuration-space density and its local velocity distribution. The mass-weighted number of streams near any point is then the total local density divided by the mean density of the individual local streams. Caustic passages can be detected robustly from the properties of each particle's local stream, and the particle's instantaneous annihilation probability within this stream can be evaluated simply and integrated accurately through caustics.

In the following chapters of this thesis we will use the methods and results of this chapter. Here we introduce our method and apply it to study the evolution of streams in static potentials that are too complex to be analysed using previous techniques. We also implement our scheme in a state-of-the-art N-body simulation code, and use simple test problems to demonstrate that N-body discreteness effects can be kept under control in realistic applications. Later chapters will address issues associated with mixing, caustics and annihilation radiation in the full cosmological context.

The outline of this chapter is the following: In section 2 we present a detailed derivation of the GDE and show how it can be used to quantify mixing, to locate caustics, and to calculate stream densities and annihilation rates. Section 3 describes our code, DaMaFlow, which is designed to solve the GDE for single orbits in a wide variety of potentials. In section 4 we analyse static, separable potentials and compare results from our method to previous work. The fifth section applies our scheme to non-integrable, but still static potentials, revealing their complex phase-space structure. In section 6 we turn to more realistic non-spherical CDM halo potentials and discuss the influence of halo shape on stream density behaviour. Section 7 discusses the implementation of our method in an N-body code and presents results of simple tests of when discreteness effects compromise studies of stream densities and caustics. The final section summarises our results and gives some conclusions.

5.2 The geodesic deviation equation

Our scheme for calculating the evolution of the fine-grained phase-space distribution in the neighbourhood of a DM particle is based on the evolution of the distance between two infinitesimally separated particle trajectories. This evolution is described by the Geodesic Deviation Equation (GDE). We use the following notation to clearly distinguish between

three- and six-dimensional quantities: an underline denotes a $\mathbb{R}^3$ vector and two of them denote a $\mathbb{R}^{3\times3}$ matrix. An overline denotes a $\mathbb{R}^6$ vector and two of them denote a $\mathbb{R}^{6\times6}$ matrix. Thus a general phase-space vector is composed of two three-dimensional vectors: $\overline{x} = (\underline{x}, \underline{v})$.

To derive the GDE we first write down the equations of motion for a DM particle. These are simply

$$\ddot{\underline{x}}(t; \underline{q}, \underline{p}) = -\underline{\nabla}_x \Phi(\underline{x}(t; \underline{q}, \underline{p})) \tag{5.5}$$

with initial conditions $\underline{x}(t_0; \underline{q}, \underline{p}) = \underline{q} \quad \underline{v}(t_0; \underline{q}, \underline{p}) = \underline{p}$.

As $\dot{\underline{x}} = \underline{v}$ the equation of motion in phase-space can be written

$$\dot{\overline{x}}(t; \overline{q}) = \begin{pmatrix} \underline{v} \\ -\underline{\nabla}_x \Phi(\underline{x}(t; \overline{q})) \end{pmatrix} = \overline{\Psi}(\overline{x}(t; \overline{q})) \tag{5.6}$$

with initial conditions $\overline{x}(t_0; \overline{q}) = \overline{q} = (\underline{q}, \underline{p})$.

We want to calculate the local stream density around the DM particle whose trajectory in phase-space is given by $\overline{x}(t; \overline{q})$. To do so, we first ask how the displacement vector to a neighbouring DM particle in phase-space evolves with time

$$\overline{\delta}(t) = \overline{x}(t; \overline{q} + \overline{\delta}) - \overline{x}(t; \overline{q}). \tag{5.7}$$

Note that $\overline{\delta}(t)$ is the displacement between the reference DM particle, which was at $\overline{q}$ at time t_0, and another particle which was at $\overline{q}+\overline{\delta}_0$ at t_0. We are interested in properties in the immediate neighbourhood of the reference particle, so $\overline{\delta}_0$ is an infinitesimal displacement. This allows us to work to linear order

$$\overline{\delta}(t) \cong \left(\overline{\delta}_0 \cdot \overline{\nabla}_q\right) \overline{x}(t; \overline{q}). \tag{5.8}$$

Introducing the phase-space distortion tensor $\overline{\overline{D}}$ (note that this is a 6×6 tensor)

$$\overline{\overline{D}}(t; \overline{q}) \equiv \frac{\partial \overline{x}}{\partial \overline{q}}(t; \overline{q}) \tag{5.9}$$

we can rewrite Eq. (5.8) as a simple linear transformation from the starting phase-space displacement $\overline{\delta}_0$ to the displacement $\overline{\delta}(t)$ at time t

$$\overline{\delta}(t) \cong \overline{\overline{D}}(t; \overline{q})\overline{\delta}_0. \tag{5.10}$$

Because $\overline{\delta}_0$ is an arbitrary displacement vector, the distortion tensor describes how the complete local phase-space neighbourhood around the reference DM particle gets distorted while it is orbiting in the given potential. The time evolution of $\overline{\delta}(t)$ follows from the time

evolution of the two trajectories. Again we can work this out in linear order[2]

$$\begin{aligned}
\dot{\overline{\overline{D}}}(t;\overline{q})\overline{\delta} &\cong \dot{\overline{\delta}}(t) \\
&= \overline{\Psi}(\overline{x}(t;\overline{q})+\overline{\delta}(t)) - \overline{\Psi}(\overline{x}(t;\overline{q})) \\
&\cong \left(\overline{\delta}(t)\cdot\overline{\nabla}_x\right)\overline{\Psi}(\overline{x}(t;\overline{q})) \\
&\cong \left(\left(\overline{\overline{D}}(t;\overline{q})\overline{\delta}_0\right)\cdot\overline{\nabla}_x\right)\overline{\Psi}(\overline{x}(t;\overline{q})).
\end{aligned} \tag{5.11}$$

To derive the equation of motion for the distortion tensor itself we evaluate Eq. (5.11) for six unit vector phase-space displacements $\overline{\delta}_0^{(j)}$ with $\delta_{0,\alpha}^{(j)} = \delta_{\alpha j}$ where $\alpha, j = 1, 2, \ldots, 6$, and δ_{ab} is the Kronecker delta. Taking into account Einstein's sum convention this yields for each component of Eq. (5.11)

$$\begin{aligned}
\dot{D}_{ij}(t;\overline{q}) &= \dot{D}_{i\alpha}(t;\overline{q})\delta_{0,\alpha}^{(j)} \\
&\cong \left(D_{\beta\gamma}(t;\overline{q})\delta_{0,\gamma}^{(j)}\frac{\partial}{\partial x_\beta}\right)\Psi_i(\overline{x}(t;\overline{q})) \\
&= \left(D_{\beta\gamma}(t;\overline{q})\delta_{\gamma j}\frac{\partial}{\partial x_\beta}\right)\Psi_i(\overline{x}(t;\overline{q})) \\
&= \left(D_{\beta j}(t;\overline{q})\frac{\partial}{\partial x_\beta}\right)\Psi_i(\overline{x}(t;\overline{q})) \\
&= T_{i\beta}(t;\overline{q})D_{\beta j}(t;\overline{q}),
\end{aligned} \tag{5.12}$$

where we have introduced the phase-space tidal tensor

$$\overline{\overline{T}}(t;\overline{q}) = \begin{pmatrix} \underline{\underline{0}} & \underline{\underline{1}} \\ \underline{\underline{T}}(t;\underline{q}) & \underline{\underline{0}} \end{pmatrix}, \tag{5.13}$$

and $\underline{\underline{T}}$ is the configuration-space tidal tensor given by the second derivatives of the gravitational potential $T_{ij} = -\partial^2\Phi/\partial x_i \partial x_j$. As we are are only interested in linear order we replace $\cong$ by $=$ in Eq. (5.12) and get an equation of motion for the 6D distortion tensor

$$\dot{\overline{\overline{D}}}(t;\overline{q}) = \overline{\overline{T}}(t;\overline{q})\overline{\overline{D}}(t;\overline{q}). \tag{5.14}$$

Note that this first-order tensor differential equation represents a system of 36 coupled ordinary first-order differential equations. To solve them we need to specify initial conditions. These follow from the constraint

$$\overline{\delta}_0 = \overline{\overline{D}}(t_0;\overline{q})\overline{\delta}_0 \quad \Rightarrow \quad \overline{\overline{D}}(t_0;\overline{q}) = \overline{\overline{1}}. \tag{5.15}$$

DM behaves like a collisionless fluid and its fine-grained phase-space density $f(\overline{x},t)$ is described by the well-known Vlasov equation, what is equivalent to the collisionless Boltz-

[2] As $\overline{\delta}_0$ can be chosen arbitrarily small, this is always possible.

mann equation

$$\frac{\partial f}{\partial t} + \underline{v} \cdot \underline{\nabla}_x f - \underline{\nabla}_x \Phi \cdot \underline{\nabla}_v f = 0. \tag{5.16}$$

Using the Lagrangian derivative this reads $\mathrm{D}f/\mathrm{D}t = 0$, meaning that the local fine-grained phase-space density has to be conserved along the orbit of every particle in the system. Imagine N particles that fill a small phase-space volume $\mathrm{d}V_0 = \mathrm{d}\underline{q}\mathrm{d}\underline{p}$ around the DM reference particle at time t_0. At a later time t these particles fill a volume $\mathrm{d}V = \mathrm{d}\underline{x}\mathrm{d}\underline{v}$ around the reference particle at $\overline{x}(t;\overline{q})$. Conservation of phase-space density implies that the two volumes are the same $\mathrm{d}V_0 = \mathrm{d}V$. The evolution of the initial displacement vectors $\overline{\delta}_0^{(n)}$ from the reference particle to one of the N other particles in the volume is described by the distortion tensor associated with the reference particle

$$\overline{\delta}^{(n)}(t) = \overline{\overline{D}}(t;\overline{q})\overline{\delta}_0^{(n)} \qquad n = 1, 2, \ldots, N. \tag{5.17}$$

The change in volume due to this linear transformation is given by the determinant $\det(\overline{\overline{D}}(t;\overline{q}))$. As this volume has to be conserved, the determinant of the phase-space distortion tensor has to be conserved. Note that not only must the volume be conserved, but also the orientation of the volume element. This means that the sign of the determinant is also fixed. From the initial conditions Eq. (5.15) one gets $\det(\overline{\overline{D}}(t;\overline{q}))=1$ at all times. This fact can be used to check numerical solutions of the equations.

The structure of Eq. (5.14) allows the equations of motion for the distortion to be broken down to a set of equations that is more convenient to work with. Let us first rewrite Eq. (5.14) using blocks of 3×3 tensors:[3]

$$\begin{aligned} \frac{\mathrm{d}}{\mathrm{d}t}\begin{pmatrix} \underline{\underline{D}}_{xq} & \underline{\underline{D}}_{xp} \\ \underline{\underline{D}}_{vq} & \underline{\underline{D}}_{vp} \end{pmatrix} &= \begin{pmatrix} \underline{\underline{0}} & \underline{\underline{1}} \\ \underline{\underline{T}} & \underline{\underline{0}} \end{pmatrix}\begin{pmatrix} \underline{\underline{D}}_{xq} & \underline{\underline{D}}_{xp} \\ \underline{\underline{D}}_{vq} & \underline{\underline{D}}_{vp} \end{pmatrix} \\ &= \begin{pmatrix} \underline{\underline{D}}_{vq} & \underline{\underline{D}}_{vp} \\ \underline{\underline{T}}\ \underline{\underline{D}}_{xq} & \underline{\underline{T}}\ \underline{\underline{D}}_{xp} \end{pmatrix}. \end{aligned} \tag{5.18}$$

Writing down the equation for each matrix block yields four equations

$$\dot{\underline{\underline{D}}}_{xq} = \underline{\underline{D}}_{vq} \quad ; \quad \dot{\underline{\underline{D}}}_{xp} = \underline{\underline{D}}_{vp}, \tag{5.19}$$

and

$$\dot{\underline{\underline{D}}}_{vq} = \underline{\underline{T}}\ \ \underline{\underline{D}}_{xq} \quad ; \quad \dot{\underline{\underline{D}}}_{vp} = \underline{\underline{T}}\ \ \underline{\underline{D}}_{xp}. \tag{5.20}$$

These can be combined to give

$$\ddot{\underline{\underline{D}}}_{xq} = \underline{\underline{T}}\ \ \underline{\underline{D}}_{xq} \quad ; \quad \ddot{\underline{\underline{D}}}_{xp} = \underline{\underline{T}}\ \ \underline{\underline{D}}_{xp}. \tag{5.21}$$

Thus we get two identical differential equations of second-order for two 3×3 tensors whose dynamics is driven by the ordinary tidal tensor. From the initial condition for the 6D distortion one can see that the only difference between $\underline{\underline{D}}_{xq}$ and $\underline{\underline{D}}_{xp}$ lies in the appropriate initial conditions: $\underline{\underline{D}}_{xq}(t_0;\overline{q}) = \underline{\underline{1}}$, $\dot{\underline{\underline{D}}}_{xq}(t_0;\overline{q}) = \underline{\underline{0}}$ and $\underline{\underline{D}}_{xp}(t_0;\overline{q}) = \underline{\underline{0}}$, $\dot{\underline{\underline{D}}}_{xp}(t_0;\overline{q}) = \underline{\underline{1}}$ in the

[3] We suppress the argument $t;\overline{q}$ to avoid confusion.

two cases. From the solutions of these two initial condition problems the 6D distortion solution can then be constructed

$$\overline{\overline{D}} = \begin{pmatrix} \underline{\underline{D}}_{xq} & \underline{\underline{D}}_{xp} \\ \mathrm{d}/\mathrm{d}t\underline{\underline{D}}_{xq} & \mathrm{d}/\mathrm{d}t\underline{\underline{D}}_{xp} \end{pmatrix}. \tag{5.22}$$

Up to this point we have worked out all equations in phase-space. As we are interested in the stream density in configuration-space, we need to project down to this space. As already mentioned, CDM lies on a thin sheet in phase-space. This sheet has a certain orientation at the starting point of the reference DM particle. Take $(\underline{q},\underline{p}) : \underline{p} = \underline{V}(\underline{q};t_0)$ to be the local parametrisation of the sheet surrounding this particle at time t_0[4]. Now we ask how an infinitesimal displacement $\underline{\delta}_{0,q}$ in configuration-space is distorted by evolution. First we note that any displacement in $\underline{q}$ implies a displacement in velocity-space due to the restriction of particles to the sheet

$$\underline{\delta}_{0,p} = \underline{\underline{V}}_q(\underline{q})\underline{\delta}_{0,q} \quad ; \quad \underline{\underline{V}}_q(\underline{q}) = \frac{\partial \underline{V}}{\partial \underline{q}}(\underline{q};t_0). \tag{5.23}$$

The phase-space distortion $\overline{\overline{D}}$ describes how the corresponding phase-space displacement $(\underline{\delta}_{0,q},\underline{\delta}_{0,p})$ evolves. We are here interested in the configuration-space part of the phase-space displacement at time t

$$\underline{\delta}_x(t) = \underline{\underline{D}}_{xq}(t;\overline{q})\underline{\delta}_{0,q} + \underline{\underline{D}}_{xp}(t;\overline{q})\underline{\underline{V}}_q(\underline{q})\underline{\delta}_{0,q}. \tag{5.24}$$

The evolution of the displacement in configuration-space can also be described by a linear transformation

$$\underline{\delta}_x(t) = \underline{\underline{D}}(t;\overline{q})\underline{\delta}_{0,q}, \tag{5.25}$$

where we have introduced the configuration-space distortion tensor (note that this is a 3×3 tensor)

$$\underline{\underline{D}}(t;\overline{q}) = \underline{\underline{D}}_{xq}(t;\overline{q}) + \underline{\underline{D}}_{xp}(t;\overline{q})\underline{\underline{V}}_q(\underline{q}). \tag{5.26}$$

This tensor can also be derived with the help of two projection operators

$$\underline{\underline{D}}(t;\overline{q}) = \begin{pmatrix} \underline{\underline{1}} & \underline{\underline{0}} \end{pmatrix} \overline{\overline{D}}(t;\overline{q}) \begin{pmatrix} \underline{\underline{1}} \\ \underline{\underline{V}}_q(\underline{q}) \end{pmatrix}. \tag{5.27}$$

As in the case of phase-space distortion, the change in volume due to the linear transformation in Eq. (5.25) is given by the determinant, so that the stream density in configuration-space is proportional to the inverse of this determinant

$$\rho_{\mathrm{stream}}(t) \propto \frac{1}{\left|\det\left(\underline{\underline{D}}(t;\overline{q})\right)\right|}. \tag{5.28}$$

[4]Such a parametrisation is always possible locally, but due to mixing there is, in general, no simple global parametrisation of the stream. This is only possible for very early times, where the sheet is dominated by the Hubble Flow, the $\underline{q}-\underline{p}$ relation is one-to-one, and the stream density is almost uniform.

At time t_0 the configuration-space distortion tensor equals unity. Thus, if we norm the stream density to its initial value, we get the following relation for the normed stream density

$$\rho_{\rm stream}^{\rm normed}(t) = \frac{1}{\left|\det\left(\underline{\underline{D}}(t;\overline{q})\right)\right|}. \tag{5.29}$$

In the rest of this chapter we will almost always discuss this normed stream density.

In Fig. 5.2 we sketch the distortion of the infinitesimal cloud around the reference DM particle. Note the difference between the stream density evolution in configuration-space and in phase-space. The volume of the small cloud grows in Fig. 5.2 and is not constant anymore! This is a result of the projection from phase-space to configuration-space. Nearby trajectories spatially diverge in time.

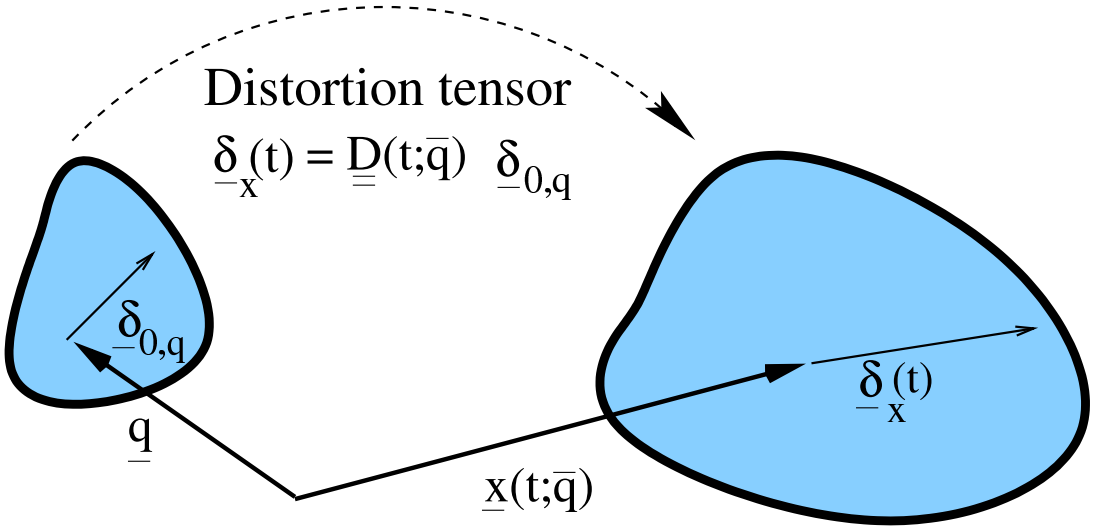

Figure 5.2: The configuration-space distortion tensor $\underline{\underline{D}}$ describes how an initial small configuration-space displacement $\underline{\delta}_{0,q}$ evolves in time. This reflects the stretching of an infinitesimally small cloud of virtual particles around the reference particle that is placed at $\underline{q}$ at time t_0. The stretching of the cloud is driven by the tidal field that the DM particle encounters as it orbits.

This formalism can be used to identify caustics in a very efficient way. If the DM particle passes through a caustic along its orbit $\det(\underline{\underline{D}})$ passes through zero, and the stream density goes to infinity (for perfectly cold DM). A small cloud surrounding the reference particle turns inside out as it passes through the caustic. This corresponds to a change in sign of the determinant, and thus can easily identified numerically. This property allows the location of caustics to be mapped accurately even in complex configurations. Note that the possibility of sign changes explains why we took the modulus of the determinant in Eq. (5.28).

The complex fine-grained phase-space structure and especially the caustics expected in CDM haloes are likely to substantially enhance annihilation radiation. These effects have so far been analysed only under quite simplified conditions (Hogan, 2001; Bergström et al., 2001; Pieri and Branchini, 2005; Mohayaee and Shandarin, 2006; Mohayaee et al., 2007; Natarajan, 2007). As a result, it is unclear how strong such enhancement effects will

be in the proper cosmological context. Previous studies of annihilation radiation from N-body haloes had realistic formation histories but were unable to resolve caustics. They estimated emissivities from the local mean CDM density, thus effectively excluding contributions from single streams (Stoehr et al., 2003; Diemand et al., 2007). Hogan (2001) noted that this results in an underestimation of the annihilation rate, and suggested that annihilation might, in fact, be dominated by contributions from the neglected caustics (which he baptised as "micropancakes").

Our formalism enables a robust and accurate calculation of the contribution to the annihilation radiation from individual streams. The annihilation rate for each particle due to encounters with other particles in its own stream can be evaluated directly from the local stream velocity distribution and density. Integrating these rates along the trajectories of all particles produces a Monte Carlo estimate of the intrastream annihilation rate for the system as a whole. This automatically includes the contributions from all caustics and is exactly the fine-scale contribution which is missing from standard N-body-based estimates of annihilation luminosities.

We now discuss briefly how this is done. Given the very small primordial velocity dispersion σ of CDM, and approximating the initial configuration-space density as a constant ρ_0 we can write the phase-space density around a reference particle at the initial time t_0 as follows [5]

$$f(\overline{x}, t_0) = \rho_0 N_0 \exp(-\frac{1}{2}(\overline{x} - \overline{x}(t_0; \overline{q}))^\dagger \overline{\overline{W}}_0 (\overline{x} - \overline{x}(t_0; \overline{q}))), \tag{5.30}$$

where

$$\overline{\overline{W}}_0 = \sigma^{-2} \mathrm{diag}(\underline{\underline{0}}, \underline{\underline{1}}), \tag{5.31}$$

and $N_0 = (2\pi)^{-3/2}\sigma^{-3}$. Note that this represents a Gaussian distribution in velocity-space and a constant density in configuration-space.

Using $\overline{\delta}(t) = \overline{\overline{D}}(t; \overline{q})\overline{\delta}_0$ we obtain the phase-space density around the particle at the later time t

$$f(\overline{x}, t) = \rho_0 N_0 \exp(-\frac{1}{2}(\overline{x} - \overline{x}(t; \overline{q}))^\dagger \overline{\overline{W}}(t; \overline{q})(\overline{x} - \overline{x}(t; \overline{q}))), \tag{5.32}$$

where

$$\overline{\overline{W}}(t; \overline{q}) = \left(\overline{\overline{D}}(t; \overline{q})^{-1}\right)^\dagger \overline{\overline{W}}_0 \left(\overline{\overline{D}}(t; \overline{q})^{-1}\right). \tag{5.33}$$

The configuration-space density around the reference particle at $\underline{x}(t; \overline{q})$ is simply the integral of the phase-space density over all velocities evaluated at $\underline{x}(t; \overline{q})$

$$\rho(t) = \rho_0 \frac{\sigma_1(t)\sigma_2(t)\sigma_3(t)}{\sigma^3}, \tag{5.34}$$

where the velocity dispersions $\sigma_i(t)$ are given by $1/\sqrt{\lambda_i(t)}$ and $\lambda_i(t)$ are the eigenvalues of the velocity submatrix of $\overline{\overline{W}}(t; \overline{q})$. The velocity distribution in the principal axis frame

[5] $\dagger$ denotes the transpose of a matrix

of the velocity ellipsoid centred on the particle's position and velocity is given by

$$g(\underline{v}) = N(t)\exp(-\frac{1}{2}\underline{v}^{\dagger}\mathrm{diag}(\sigma_1(t),\,\sigma_2(t),\,\sigma_3(t))^{-2}\underline{v}), \tag{5.35}$$

where $N(t) = 1/((2\pi)^{3/2}\sigma_1(t)\sigma_2(t)\sigma_3(t))$. Note that this velocity distribution is normalised, i.e. its integral over velocity space is unity.

These quantities allow us to calculate the instantaneous annihilation rate at each point on the particle's trajectory

$$\frac{\mathrm{d}P}{\mathrm{d}t} = \frac{\rho(t)}{m_p}\int \mathrm{d}^3v\,\sigma_A(v)vg(\underline{v}) = \frac{\rho(t)\langle\sigma_A v\rangle}{m_p}, \tag{5.36}$$

where m_p is the particle mass and $\sigma_A(v)$ the annihilation cross-section. We note that in many WIMP models the annihilation cross-section is inversely proportional to encounter velocity, and in this case $\langle\sigma_A v\rangle$ is independent of the actual local velocity distribution (Jungman et al., 1996). An image of the system in annihilation radiation can be constructed by integrating all particles forward over a short time interval and summing their annihilation contributions into a pixel array. We note that equation (5.36) exhibits near-singular behaviour as particles pass through caustics and as a result special care is needed to obtain the correct contribution to the annihilation luminosity in this situation. This will be discussed more fully in the next chapter, where we present an analytic calculation of the intra-stream annihilation rate.

5.3 The DaMaFlow code

We have developed the code DaMaFlow to test our GDE scheme by analysing the behaviour of streams in a broad range of static potentials. DaMaFlow integrates the equations of motion and in parallel the GDE for a single orbit within user-specified potentials. This requires solving $3 + 18$ second-order differential equations in parallel. The integration algorithm can be chosen to be a symplectic second-order leapfrog (Drift-Kick-Drift or Kick-Drift-Kick formulation) or alternatively the energy-conserving and adaptive Dop853 algorithm (Hairer et al., 1993) of order 8 that allows dense output and is very fast. Studies focusing on complex phase-space structures, especially in the field of chaos analysis, often use the Dop853 algorithm (or even higher order schemes) because of its high precision. On the other hand N-body codes often implement the leapfrog method because it is the best compromise between performance and accuracy. We find that with a moderate fixed time-step, both formulations of leapfrog are able to give comparable results to Dop853. This is an important point because it is not possible to run N-body simulations with slow but accurate high-order ODE solvers like Dop853.

DaMaFlow is also set up to do a Numerical Analysis of Fundamental Frequencies (NAFF) (Laskar, 1988, 1990; Papaphilippou and Laskar, 1996; Laskar, 2003) and of the resonances associated with the chosen orbit. The fundamental frequencies are revealed by an integer programming routine. This is needed so that we can study the relation between the existence of well-defined fundamental frequencies or resonances and stream density

behaviour. The NAFF method determines a quasi-periodic approximation to the orbital motion. For ordinary Fast-Fourier-Transforms (FFT) the accuracy of the determination of the frequencies is of the order of $1/T$, where T is the sampling interval. The NAFF method has an accuracy of $1/T^4$. Thus it makes spectral analysis a lot faster compared to classical Fourier techniques, for example, those used in Binney and Spergel (1982).

To scan large parts of phase-space, DaMaFlow can be run in parallel on batch systems in order to integrate a large number of different orbits simultaneously. A fast automated stream density fitting routine was built in to facilitate efficient analysis of the underlying phase-space without user interaction. Before this fitting can be done, the stream density has to be smoothed to remove the large density spikes produced by caustics. DaMaFlow does this by extracting and fitting the lower envelope of the stream density time series. This envelope is constructed while the orbit integration is running by an iterative on-the-fly minimum finder.

From a numerical point of view, solving the GDE is quite difficult in chaotic regions of phase-space. In these regions the infinitesimal phase-space volume around the reference particle gets distorted very strongly. This produces large numerical values in the phase-space distortion tensor. And this can lead to overflows and round-off errors in numerical computations. In chaos analysis it is an established method to do some kind of re-norming to suppress these problems. We can do something similar to follow the evolution of phase-space density evolution. We use the transitivity of the phase-space distortion tensor

$$\overline{\overline{D}}_{t_1\to t_3} = \overline{\overline{D}}_{t_2\to t_3} \quad \overline{\overline{D}}_{t_1\to t_2}, \tag{5.37}$$

where $\overline{\overline{D}}_{t_i\to t_j}$ with $i<j$ is the solution of the GDE with $\overline{\overline{D}}_{t_i\to t_j}(t_i) = \overline{\overline{1}}$ evaluated at time t_j. So the phase-space volume can be written as

$$\det\left(\overline{\overline{D}}_{t_1\to t_3}\right) = \det\left(\overline{\overline{D}}_{t_2\to t_3}\right) \quad \det\left(\overline{\overline{D}}_{t_1\to t_2}\right). \tag{5.38}$$

Thus dividing the time integration interval and re-initialising the distortion after each interval avoids large numerical values. This is very similar to the re-norming techniques used for calculating the largest Lyapunov exponents of chaotic systems, where the re-norming frequency is usually chosen to be of the order of the dynamical timescale (Lichtenberg and Lieberman, 1983; El-Zant, 2002). Although this approach works nicely for such applications, it does not help us when calculating the stream density evolution, because we need the entire phase-space distortion information from initial to final time. It is not possible to separate the configuration-space part of the phase-space distortion and to do a similar re-norming. Thus one cannot avoid large numbers during the calculation. DaMaFlow therefore calculates all quantities in double-precision (64 bits=8 bytes). Even in chaotic regions this is enough to follow the system for a substantial amount of time. We note that the phase-space density calculation involves the determinant of a 6×6 matrix, whereas the stream density only involves the determinant of a 3×3 matrix. As a result stream density calculations are less strongly affected by large numbers and overflows. We note that special software libraries can provide even higher precision (e.g. the GMP library [6]).

[6] `http://www.gmplib.org`

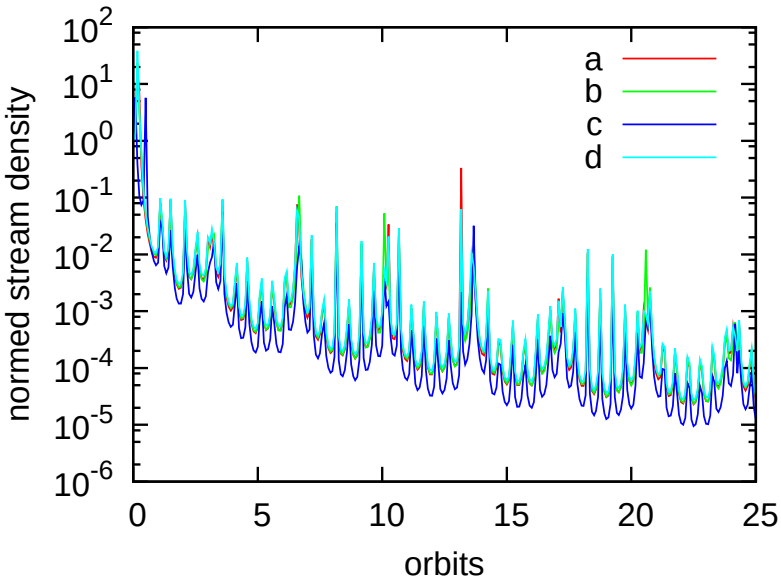

Figure 5.3: Stream density evolution for different initial sheet orientations $\underline{\underline{V}}_q(\underline{q})$ in a static Hernquist potential. The general shape of the four curves is very similar. The long-term behaviour does not in general depend on the initial sheet orientation.

Since we wish to implement the GDE formalism also into an N-body code, execution speed and memory consumption are important considerations. For each particle we need to store the full 6D phase-space distortion tensor and the particle's tidal tensor. This results in $36 + 6$ extra numbers per particle. Thus a 500^3 particle simulation in double-precision needs already about 39 Gbytes of random access memory (RAM) just for the GDE calculation, assuming we store all information for every particle.

5.4 Integrable potentials

Before presenting some results for the evolution of stream densities in integrable potentials we want briefly to discuss the choice of the initial sheet orientation that goes into $\underline{\underline{V}}_q(\overline{q})$ in equation (5.23). This depends, of course, on the starting time t_0 and the problem that is to be studied. For example, in a cosmological context $\underline{\underline{V}}_q(\underline{q})$ is given by the linear initial conditions, so by the coupled initial density and velocity fields. We note that, to zeroth order, the sheet orientation is simply given by the Hubble Flow: $\underline{v}(\underline{q}, t_0) = H(t_0)\underline{q}$.

What is the impact of the initial orientation on later evolution? In Fig. 5.3 we show the evolution of the normed stream density, as calculated from Eq. (5.29), for a single orbit with four different choices of initial stream orientation. For this test we have used a spherical Hernquist potential

$$\Phi(r) = -\frac{GM}{r+a} \tag{5.39}$$

with $M = 1.86 \times 10^{12} \mathrm{M}_\odot$ and $a = 34.5$ kpc. The reference particle begins its orbit with $\underline{q} = (35, 17.6, 4)$ kpc and $\underline{p} = (-316.9, -16.3, -4)$ km s^{-1}. The initial sheet orientations

were chosen to be (in units of km s^{-1} kpc^{-1}): $a : \underline{\underline{0}},\ b : \underline{\underline{1}}$,

$$c : \begin{pmatrix} 1 & 10 & 0 \\ 10 & 1 & 0 \\ 0 & 0 & 1 \end{pmatrix} \quad \text{and} \quad d : \begin{pmatrix} 1 & 1 & -2 \\ -1 & 1 & -1 \\ 2 & -1 & 1 \end{pmatrix}. \tag{5.40}$$

It is striking that all four curves have very similar shape and very similar caustic spacings, although the caustic locations vary. The long-term behaviour does not depend on initial sheet orientation, at least in this case. Orientation c produces lower densities than the others because the scale of $\underline{\underline{V}}_q(\underline{q})$ is larger, but the shape of the lower envelope is very similar.

Natarajan and Sikivie (2006) show that the caustic shape in configuration-space is, in general, affected by the relative size of the $\underline{\underline{V}}_q(\underline{q})$ matrix elements. A detailed analysis of caustic shape thus requires choosing $\underline{\underline{V}}_q(\underline{q})$. For example, in their model of a CDM halo Natarajan and Sikivie (2006) initialised trajectories at the turnaround sphere with a $\underline{\underline{V}}_q(\underline{q})$ loosely motivated by tidal torque theory. This restricted the form and scale of the matrix, but still left a lot of freedom. Here our main motivation is not to analyse caustic shapes, but rather the long-term behaviour of the fine-grained phase-space distribution, in particular of stream densities. The initial sheet orientation is thus not an important issue for us. In the following we will consider quite general orbits, but will arbitrarily set $\underline{\underline{V}}_q(\underline{q}) = \underline{\underline{0}}$ unless otherwise stated [7]. Note that the choice of $\underline{\underline{V}}_q(\underline{q})$ does not influence the dynamical evolution of the distortion tensor as it is not part of the initial conditions for the GDE. Only the final projection to configuration-space is affected by initial sheet orientation.

From a dynamical point of view, static, integrable potentials are very simple. The motion within them can be described in terms of action/angle variables and their Hamiltonian can be expressed solely as a function of the actions $H = H(\mathbf{J})$. All motion in these potentials is regular, so there are no chaotic regions in their phase-space. In action-angle space the orbits lie on tori and are characterised by a fixed number of fundamental frequencies. DM particles in integrable potentials will experience only phase mixing.

Because of these simple properties Helmi and White (1999), hereafter HW, were able to develop an analytic linearised treatment based on action-angle variables to derive results for the stream density behaviour. In their paper they did not specifically focus on CDM, but rather analysed how Gaussian clouds in action-angle space evolve with time.

As an example of an integrable potential, we apply our method to several Eddington potentials $\Phi(r,\theta) = \Phi_1(r) + \eta(\beta\cos\theta)/r^2$ (Lynden-Bell, 1962). These are separable in spherical coordinates. The third integral for this type of potential is $I_3 = \frac{1}{2}L^2 + \eta(\beta\cos\theta)$. We chose the following example of an Eddington potential,

$$\Phi(r,\theta) = v_{\rm h}^2 \log\left(r^2 + d^2\right) + \frac{\beta^2\cos^2\theta}{r^2} \tag{5.41}$$

[7] Orbits starting on axes of symmetry in phase-space can show non-generic stream density behaviour for $\underline{\underline{V}}_q(\underline{q}) = \underline{\underline{0}}$ as we will discuss in the section on non-integrable potentials (section 5).

with $v_h = 1$ km s^{-1}, $d = 1$ kpc, $\beta = 2.5$ kpc km s^{-1} [8], and studied an orbit which starts at $\underline{q} = (5, 3, 2)$ kpc with a velocity of $\underline{p} = (0.62, 0.62, 0.104)$ km s^{-1}.

In Fig. 5.4 we show the evolution of the stream density for this orbit, i.e. the projection from phase-space to configuration-space for an initial condition with $\underline{\underline{V}}_q(\underline{q}) = \underline{\underline{0}}$. Here and elsewhere (unless otherwise stated) we define the "orbital period" as the radial oscillation period for the purpose of making such plots. The late-time behaviour of the stream density can be fitted by an analytic formula derived by HW

$$\rho(\underline{x}, t) = A \frac{1}{r^2 \sin\theta |p_r p_\theta|} \frac{1}{(t/t_{\rm orbital})^3} \tag{5.42}$$

with only one fitting parameter A. Comparing this to the result for the long-term behaviour in HW (Eq. (37)) it is clear that A just reflects the initial phase-space distribution and the orbital parameters (the derivatives of the fundamental frequencies with respect to the actions). The results in HW are calculated for a Gaussian cloud in phase-space, not a cold sheet as in our case. Since the initial distribution only affects A, the long-term behaviour of the two configurations is the same, as shown in Fig. 5.4.

One can clearly see that our method produces caustics at the correct positions and is also able to recover the secular evolution of the stream density, the $1/(t/t_{\rm orbital})^3$ density decrease. We note also the initial quasi-exponential stream density decrease that is often referred to as Miller's instability (Miller, 1964). Recently Helmi and Gomez (2007), hereafter HG, showed this is a generic feature of Hamiltonian dynamics and not, as long believed, an artifact specific to N-body integrations (Hemsendorf and Merritt, 2002; Kandrup and Sideris, 2003). HG discuss the effect in detail for spherical potentials. All our tests with spherical, axisymmetric and triaxial potentials show a similar quasi-exponential initial decay. Since DaMaFlow integrates the equations of motion for a single particle in a perfectly smooth potential, it is evident that this behaviour has nothing to do with N-body effects.

A NAFF frequency analysis of particle orbits in the Eddington potential reveals, as expected, three linearly independent frequencies. It is this number that dictates the speed with which stream densities decrease in static, separable potentials. One can see this very clearly from Fig. 5.5. Here we show the density decrease in a simple Kepler-like toy-model

$$\Phi(r) = -\frac{1}{r^\alpha}. \tag{5.43}$$

For $\alpha = 1$ the orbit was started from $\underline{q} = (-0.33, 0.97, 0)$ and $\underline{p} = (-1.0, -0.07, 0)$ with an energy $E = -0.5$. This orbit has only one fundamental frequency. Changing α to 0.75 increases the number of frequencies to two; the loops of the orbit no longer close. The starting point for this second case has been set to $\underline{q} = (-0.27, 1.28, 0)$ and $\underline{p} = (-0.76, 0.24, 0)$, corresponding also to $E = -0.5$. The increased number of frequencies results in a more rapid decrease in stream density: $1/(t/t_{\rm orbital})$ for one fundamental frequency, and $1/(t/t_{\rm orbital})^2$ for two. In this sense the long-term behaviour of streams in static, integrable systems is very simple and is determined only by the number of fundamental frequencies.

[8] These values do not have any specific meaning. We have chosen them just in a convenient way.

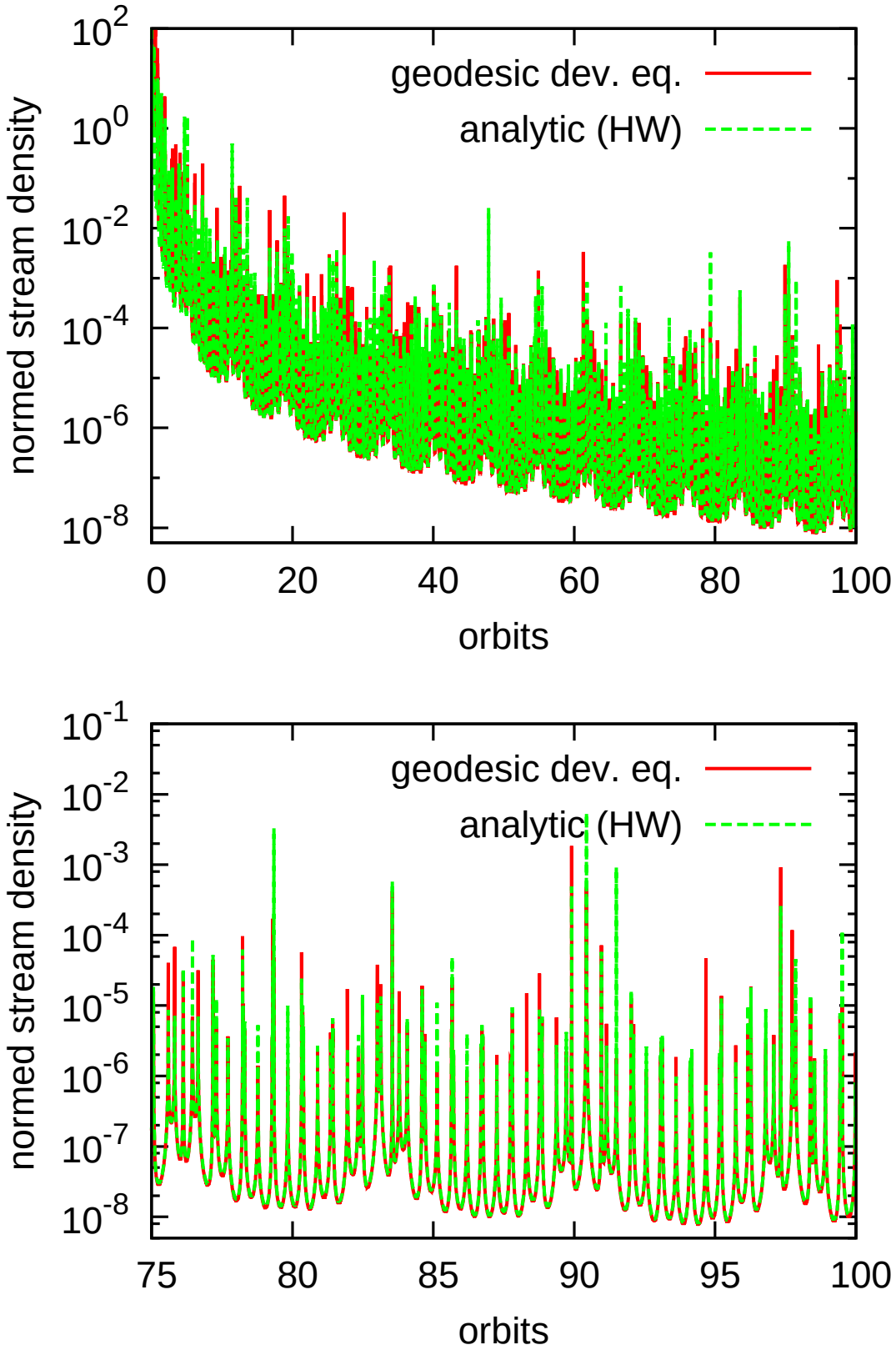

Figure 5.4: The stream density evolution calculated using the GDE integrator DaMaFlow is compared to the analytic result obtained by a linearised treatment in action/angle variables (Helmi and White, 1999). The results agree essentially perfectly. Notice how well the numerical calculation matches the caustics. The upper panel clearly shows that the numerical result also has the correct $1/(t/t_{\rm orbital})^3$ behaviour at late times. The initial quasi-exponential decay is also visible.

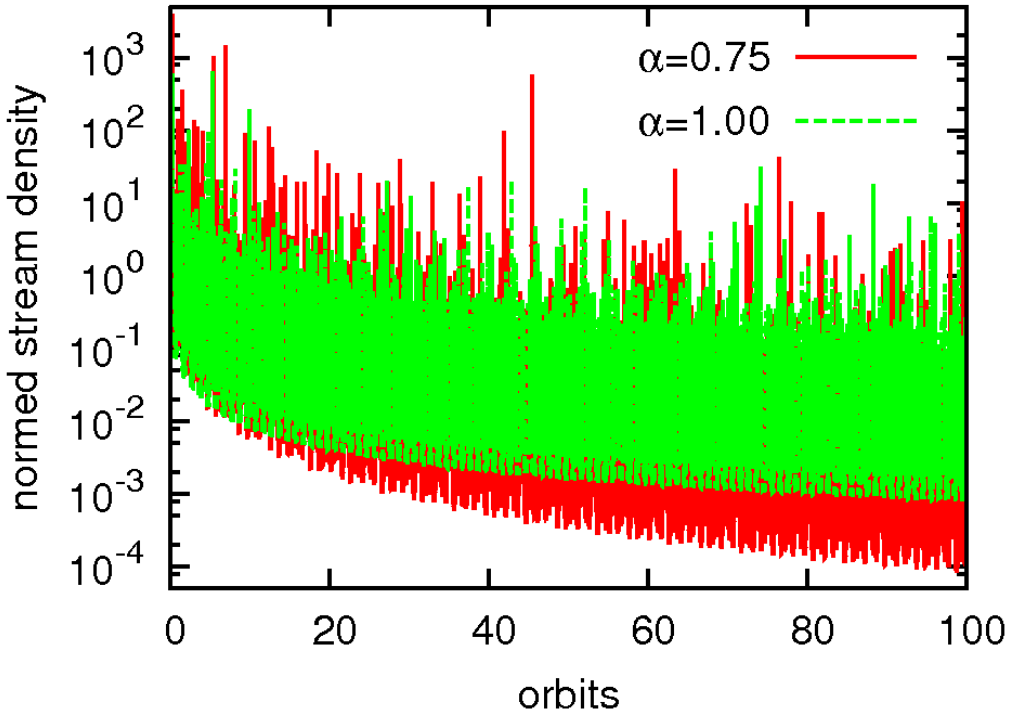

Figure 5.5: Stream density evolution for the normal Kepler potential ($\alpha = 1$) and for a modified potential ($\alpha = 0.75$). Orbits in the Kepler potential have a single fundamental frequency. Changing the potential exponent from $\alpha = 1$ to $\alpha = 0.75$ increases the number of fundamental frequencies to two. As a result, the long-term stream density behaviour changes from $1/(t/t_{\rm orbital})$ to $1/(t/t_{\rm orbital})^2$. For integrable potentials the long-term stream density decrease on each orbit is dictated by the number of fundamental frequencies.

5.5 Non-integrable potentials

Analytic methods like the HW formalism are only able to deal with integrable potentials. This is a serious limitation since realistic potentials are rarely integrable. To demonstrate that the GDE method can also deal with more complex phase-space structure we now discuss the well-known ellipsoidal logarithmic potential with a core,

$$\Phi(x,y,z) = \frac{1}{2}v_0^2 \ln(r_c^2 + x^2 + (y/q)^2 + (z/p)^2), \tag{5.44}$$

analysing its stream density behaviour and its phase-space structure. There are two reasons why we have chosen this potential: first there has been substantial previous work on its phase-space structure (Binney and Spergel, 1982; Papaphilippou and Laskar, 1998), so we can compare directly with these earlier results. Second this potential is often considered as a good model for galactic haloes because it reproduces a flat rotation curve and its shape can easily be tuned by two parameters that correspond to the axial ratios of the ellipsoidal isopotential surfaces. It has been used, for example, for dynamical studies of the debris streams of the Sagittarius dwarf galaxy (Helmi, 2004a). The ellipsoidal logarithmic potential without a core ($r_c = 0$) has also been used to study the influence of

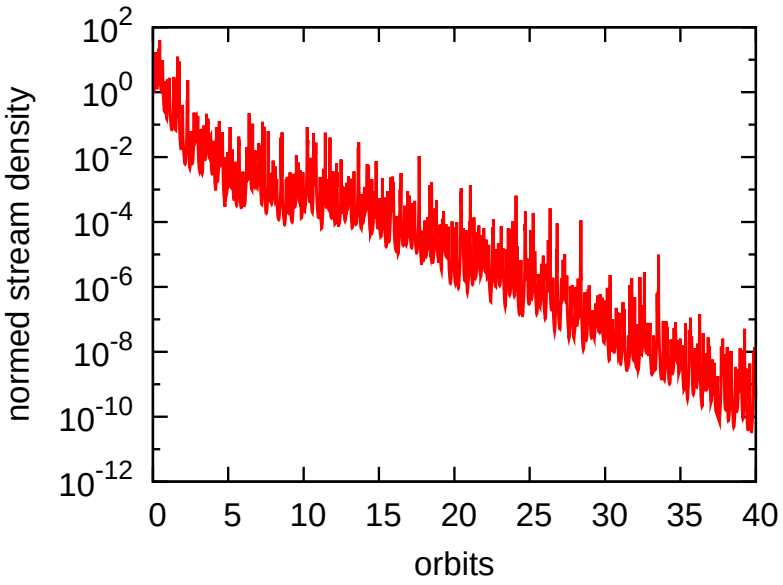

Figure 5.6: Stream density evolution along a chaotic orbit in the ellipsoidal logarithmic potential with $q = 1.5, p = 0.5$. The density decreases very rapidly, reflecting the chaotic mixing along this orbit. Note that the decrease is no longer a power-law, as in the case of regular motion.

halo shape on the annual modulation signal in dark matter detectors (Evans et al., 2000).

It is known that, depending on the degree of triaxiality, the phase-space of the logarithmic potential can be occupied to a large extent by chaotic orbits. This was demonstrated, for example, by Papaphilippou and Laskar (1998). In Fig. 5.6 we show how the stream density evolves along one of these chaotic orbits. This orbit was integrated in a potential with $q = 1.5, p = 0.5, v_0 = 1, r_c = 1, E = 3$ and started at $\underline{q} = (10, 1, 5), \underline{p} = (0.16, 80, -0.16)$. Here we apply the same system of units as Papaphilippou and Laskar (1998) and write all quantities as dimensionless numbers. It is evident from this plot that the system mixes very rapidly along this orbit. This is chaotic mixing, and contrasts with the phase mixing that we found before for regular motion in separable potentials. We note that chaotic orbits are difficult to handle from a numerical point of view because of the rapid spread in phase-space that characterises them. To check whether we can rely on our stream density values, we also calculated the 6-D phase-space density along this orbit. Over the full integration range shown in Fig. 5.6 (40 orbits) it remained constant to an accuracy of 10^{-7}.

Using DaMaFlow we have scanned the phase-space of box orbits within the logarithmic potential, identifying chaotic and regular regions by calculating the stream density evolution for about 5×10^4 different orbits. Each orbit was integrated for a fixed time interval of 2000 using 2×10^5 time-steps. This corresponds to about 10^3 orbital periods. We chose this very long integration time in order to distinguish between chaotic and regular regions[9].

[9]For chaotic orbits elements of the distortion matrices can become very large. Here we are only interested in separating chaotic and regular orbits reliably. Thus we do not care about round-off errors

Our results can be compared directly to previous work where the same potential was analysed using frequency shifts (Papaphilippou and Laskar, 1998). This method is based on the fact that chaotic motion, contrary to regular motion, has no stable fundamental frequencies, so that frequency estimates shift with time. By looking for such shifts one can distinguish between chaotic and regular motion. Fig. 5.7 shows maps of orbit type for two different sets of axial ratios q, p. This figure can be compared directly to Fig. 6(c) and Fig. 4(b) in Papaphilippou and Laskar (1998). For the first of these calculations we adopted the following values: $q = 1.8, p = 0.9, v_0 = \sqrt{2}, r_c = 0.1$ and $E = -0.404858$. For the second case we changed the potential shape by instead taking $q = 1.1, p = 0.9$.

The maps of Fig. 5.7 are constructed as follows. We start each orbit at the centre of the potential to be sure to get a box-orbit with zero angular momentum. Each individual orbit can be labelled by its initial v_x and v_y velocity components. The value of v_z is then determined by the chosen value of the energy, $E = -0.404858$. This is, of course, a very special point within the potential, and it turned out that our standard choice of initial stream orientation, $\underline{\underline{V}}_q(\underline{q}) = \underline{\underline{0}}$, produces highly non-generic stream density behaviour in this case; the stream density remains constant! In order to get properly representative behaviour we therefore took $\underline{\underline{V}}_q(\underline{q}) = \underline{\underline{1}}$ when producing Fig. 5.7. With this set-up, we scanned the whole $v_x - v_y$ plane and saved the stream density of each orbit after a fixed amount of time. The greyscale in the plots corresponds to the stream density decrease after that fixed time. Black points denote a very rapid stream density decrease, thus regions of chaotic mixing. Grey regions show a slower density decrease, reflecting phase mixing and regular motion. Much of the box-orbit phase-space is chaotic for $q = 1.8, p = 0.9$. Reducing the asphericity to $q = 1.1, p = 0.9$ results in a much larger fraction of the boxes being regular.

A comparison of Fig. 5.7 to Fig. 6(c) and Fig. 4(b) in Papaphilippou and Laskar (1998) shows excellent and detailed agreement. Regions of high frequency shift correspond, as expected, to those of rapid stream density decrease and chaotic mixing. Thus the GDE and the frequency shift technique work equally well for delineating regions of chaotic and normal phase mixing. We note that the Lyapunov exponent technique for identifying chaotic behaviour is closely related to the GDE (Lichtenberg and Lieberman, 1983; El-Zant, 2002), since these exponents are obtained from the eigenvalues of the 6D distortion tensor. Identifying and characterising chaotic behaviour is not the main goal of our work here, so we will not pursue this connection further in this chapter.

So far we have classified orbits as either regular or chaotic, but the regular part of phase-space has substructure in the form of resonances (Carpintero and Aguilar, 1998; Wachlin and Ferraz-Mello, 1998; Merritt and Valluri, 1999). These are regions where the frequencies of motion are commensurate $m_1\omega_1 + m_2\omega_2 + m_3\omega_3$ where the m_i are integers and the ω_i are the three frequencies of the regular motion. As shown above, resonances influence the stream density behaviour over long timescales (Helmi and White, 1999; Siegal-Gaskins and Valluri, 2007). This is because they restrict the motion to a lower dimensional region in phase-space, implying that the orbit does not fill its KAM (Kolmogorov-Arnold-Moser) torus densely. In simple terms, the system cannot spread as fast as it would do in the non-resonant case because it occupies a space of lower dimension.

in the calculation of these matrices.

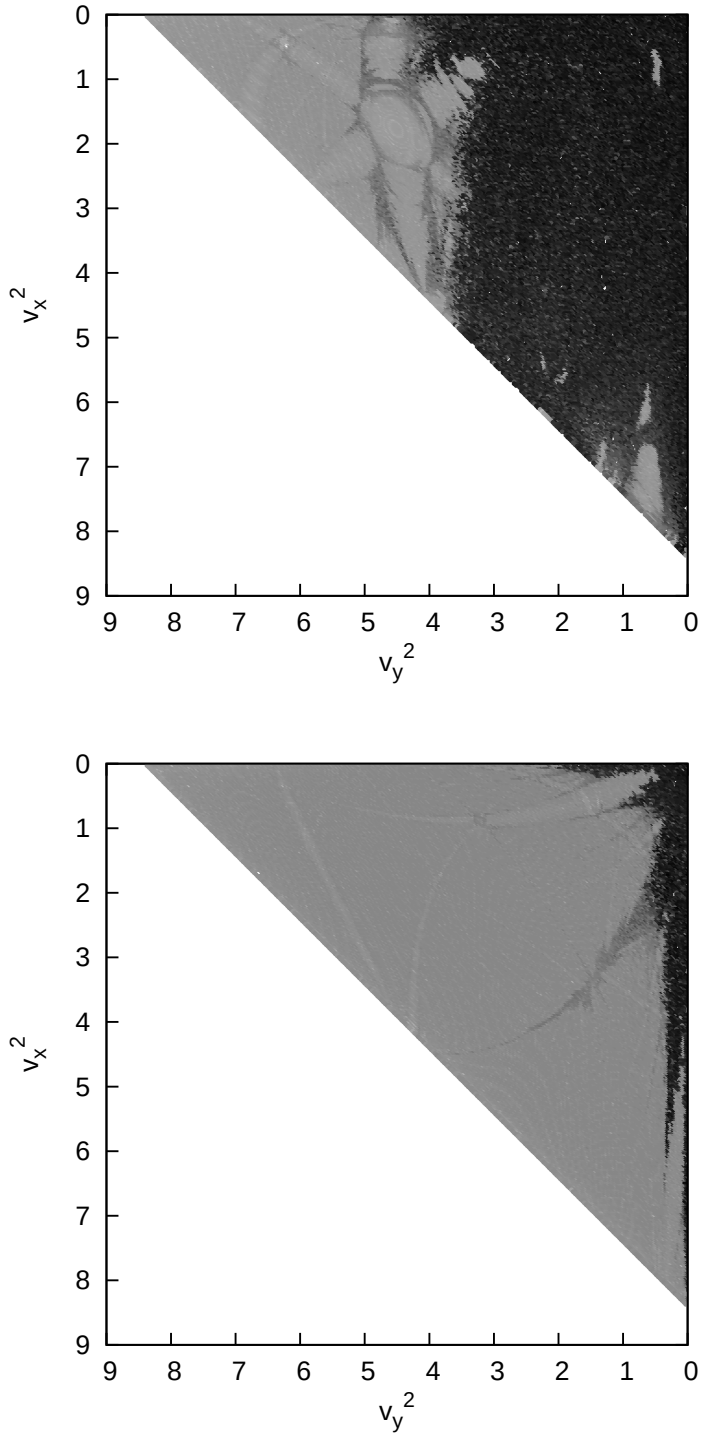

Figure 5.7: Chaos maps for box orbits in the logarithmic ellipsoidal potential for two different sets of axial ratios. The upper plot is for a highly aspherical potential with $q = 1.8, p = 0.9$, whereas the lower plot is for a rounder potential with $q = 1.1, p = 0.9$. The greyscale indicates the stream density decrease after a fixed time interval (2000 time units or about 100 orbital periods). Black regions mark the very low final stream densities found for chaotic orbits, while grey regions mark the higher stream densities found for regular orbits. Densities decay quasi-exponentially in the former case, but only as a power law of time in the latter. These plots can be directly compared to Fig. 6(c) and Fig. 4(b) in Papaphilippou and Laskar (1998), where a frequency shift analysis of the same system reveals exactly the same structures.

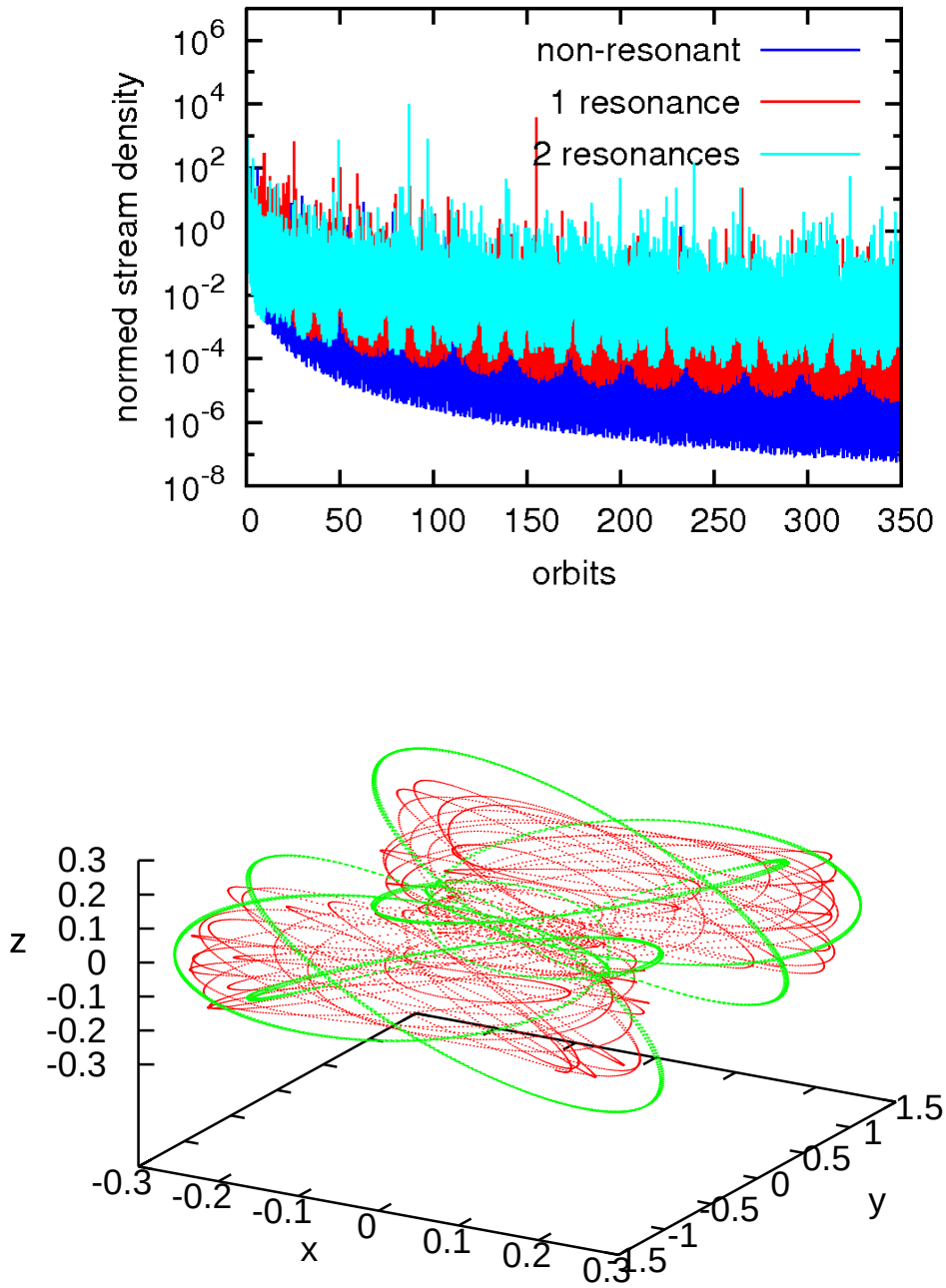

Figure 5.8: Stream density evolution on resonant orbits. Stream density drops at a rate which depends on the number of independent orbital frequencies. Non-resonant orbits have three independent frequencies, and their stream density decreases like $(t/t_{\rm orbital})^{-3}$ at late times. Resonances reduce the number of independent frequencies and slow the decrease of stream densities. With one resonance there are two independent frequencies; the stream density then falls as the inverse square of time. With two resonances, only one independent frequency remains and density falls as the inverse first power of time. The number of resonances also strongly affects the orbit shape in configuration-space. As is visible for the examples in the lower plot, non-resonant orbits (red) fill a 3D volume, whereas orbits with two resonances (green) are restricted to a line.

Fig. 5.8 shows the stream density evolution along three different box orbits for $q = 1.8, p = 0.9, v_0 = \sqrt{2}, r_c = 0.1, E = -0.404858$. The initial conditions for these orbits were chosen so that they have different numbers of orbital resonances (non-resonant, one resonance, two resonances) $\underline{q} = (-0.08, -0.70, -0.090)$, $\underline{p} = (-0.60, -1.50, -0.07)$, $\underline{q} = (-0.01, -0.67, -0.08)$, $\underline{p} = (-0.53, -1.60, -0.06)$ and $\underline{q} = (0.08, -0.63, -0.14)$, $\underline{p} = (-0.51, -1.51, -0.52)$. It is clear that the number of resonances has a major effect on the final stream density decrease over timescales similar to those shown in this plot. The difference in stream density between the non-resonant case and the case with two resonances is about 3 orders of magnitude after 350 orbits! Resonances also have a strong influence on the shape of the orbit in configuration-space, as shown in the lower panel of Fig. 5.8. Two resonances restrict the orbit to a line. From the shape of the orbits it is evident why the stream density changes so much with the resonances. The particles cannot spread over a large region if they are confined to a space of small dimension.

The regular region of phase-space for the logarithmic potential is occupied by resonant and non-resonant regions. We used DaMaFlow to scan the regular region (as for the chaos maps above) and fitted the stream density decrease by a power law in time. A non-resonant motion then gives an exponent of 3, whereas regions with two resonances should give 1. We binned these power law exponents (bin size 0.1) and coloured them. The result of this procedure is shown in Fig. 5.9. For this map we integrated a total 450×450 orbits for about 10^4 orbital periods. Each integration required 25×10^6 KDK leapfrog time-steps. The chaotic regions are shown in grey, while the regular regions are shown in three different colours depending on their stream density behaviour. We note that the chaos detection here was carried out by imposing a threshold 10^{-15} on the stream density decrease. Every orbit that crosses this threshold during its evolution is considered as chaotic and marked as grey in the map. This is the reason why the chaotic pattern here is not identical to that in Fig. 5.7.

Most of the regular phase-space in this figure is occupied by non-resonant orbits shown in green. Superposed on these is a fine network of resonance lines shown in red. In blue regions the stream density decreases linearly with time because there are two resonances. Note how well our method locates the resonance lines in the initial condition space spanned by v_y and v_x. Papaphilippou and Laskar (1998) analysed resonances with frequency maps by plotting the rotation numbers defined as $a_1 = \nu_L/\nu_S$ and $a_2 = \nu_M/\nu_S$, where ν_i are the fundamental frequencies along the long (L), short (S) and middle (M) axes. It is straightforward to identify the resonance lines in Fig. 5.9 with those in the frequency map of Papaphilippou and Laskar (1998) by applying a NAFF frequency analysis to the orbit corresponding to any specific initial condition, for example, one on a given resonance line. It turns out that we can identify all resonance lines in Fig. 5.9 with similar lines in the frequency map. At the intersection of these lines we have periodic orbits (satisfying two resonance conditions) with the same rotation numbers as those found in Papaphilippou and Laskar (1998). For example, the line going from the upper left corner to the lower right corresponds to the $(3, 1, -2)$ resonance, meaning that $3a_1 + 1a_2 - 2 = 0$.

We conclude that our method can resolve the structure of phase-space equally as well as the standard frequency mapping technique.

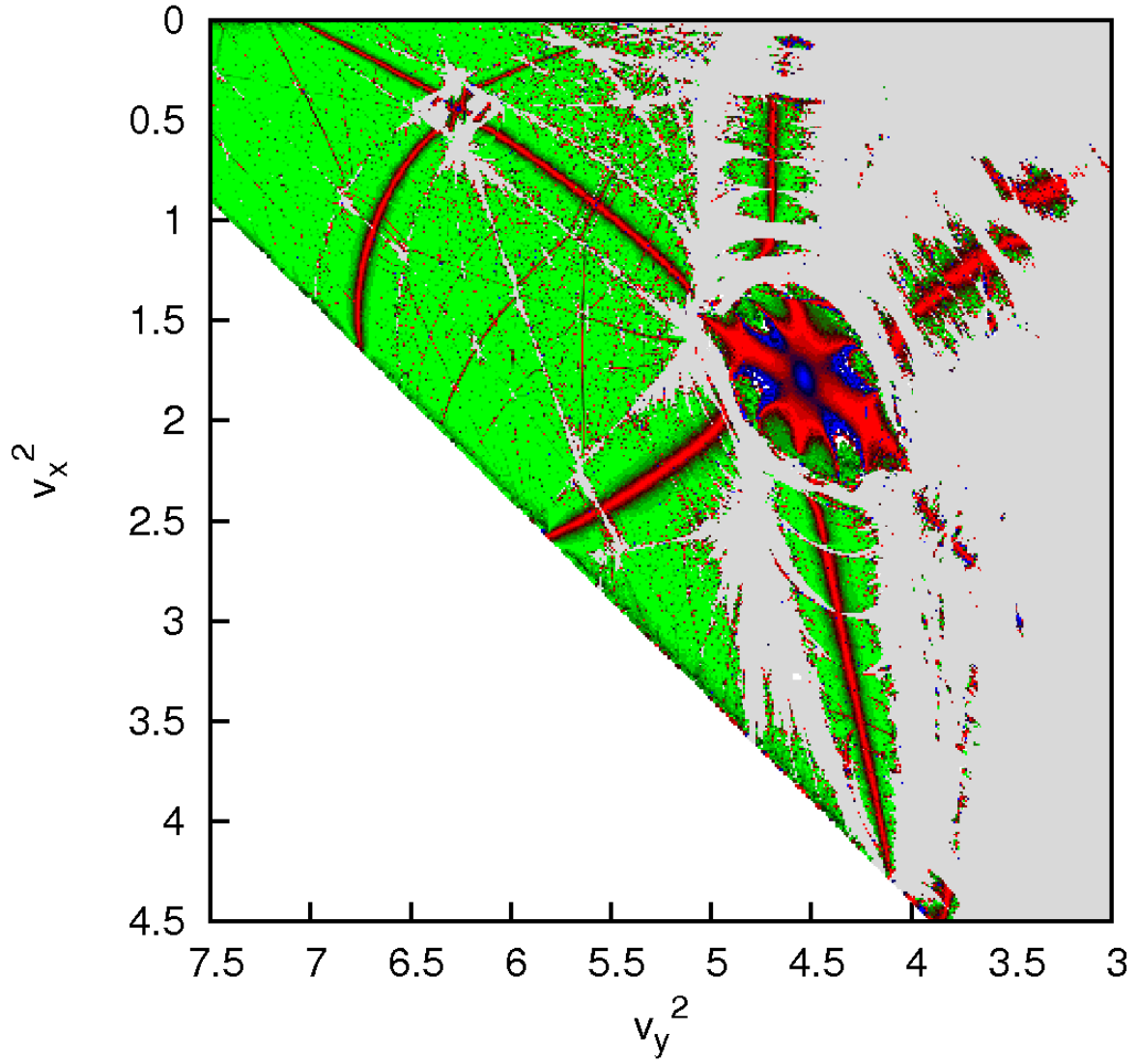

Figure 5.9: Resonance structure of a logarithmic potential as revealed by the GDE. Green indicates regions with no resonance (i.e. three independent orbital frequencies). Stream densities for these orbits decrease as $(t/t_{\rm orbital})^{-3}$ at late times. Red indicates orbits with one resonance, for which stream densities decreases as $(t/t_{\rm orbital})^{-2}$. Orbits with two resonances are coloured blue. This map was constructed by integrating 450×450 orbits, each for about 10^4 orbital periods, using DaMaFlow in parallel. Each orbit required 25×10^6 time-steps using a KDK leapfrog algorithm.

5.6 Triaxial Dark Matter haloes

In CDM cosmologies dark matter haloes are not spherical. Furthermore, simulations suggest that their shape should vary with radius, both equidensity and equipotential surfaces being rounder (on average) at larger radii. Several studies have tried to constrain the shape of the Milky Way's halo by analysing the properties of observed tidal streams like that of the Sagittarius dwarf galaxy (Ibata et al., 2001; Helmi, 2004a,b; Johnston et al., 2005; Fellhauer et al., 2006), but there is still an ongoing controversy what the shape actually looks like. Recently, Hayashi et al. (2007) analysed the radial variation in potential shape of simulated haloes that might correspond to that of the Milky Way. Although there is substantial object-to-object scatter, on average they found a relatively rapid transition from aspherical to almost spherical which occurs near the scale radius r_s of the best fitting NFW profile. They provide a simple fitting formula for this mean behaviour,

$$\log\left(\frac{b}{a} \text{ or } \frac{c}{a}\right) = \alpha\left[\tanh\left(\gamma \log\frac{r}{r_\alpha}\right) - 1\right], \tag{5.45}$$

for the principal axial ratios b/a and c/a. (Note that they actually provide two different sets of fitting parameters for Eq. (5.45) depending on the principal axial ratios.) They also propose a modified NFW potential that takes into account the variation in shape, but this potential is not very convenient because it is not straightforward to derive the corresponding equations of motion. The examples given above show that potential shape can have a substantial effect on stream density evolution, so it is interesting to see how strong such effects can be in a realistic model.

To analyse this we have built a simple extension of the NFW model that qualitatively reproduces the shape variation found by Hayashi et al. (2007) but which has simple equations of motion that can easily be implemented in DaMaFlow. (For another similar model, see Adams et al. (2007).)

We model the variable shape of the NFW halo by replacing the euclidean radius in the formula for the potential of a spherical NFW halo by a more general "radius" $\tilde{r}$ given by

$$\tilde{r} = \frac{(r_a + r)\, r_E}{(r_a + r_E)}. \tag{5.46}$$

Here r_a is a transition scale where the potential shape changes from ellipsoidal to near spherical and r_E is an ellipsoidal "radius" given by

$$r_E = \sqrt{\left(\frac{x}{a}\right)^2 + \left(\frac{y}{b}\right)^2 + \left(\frac{z}{c}\right)^2}, \tag{5.47}$$

where we require $a^2 + b^2 + c^2 = 3$. Thus for $r \ll r_a$ $\tilde{r} \cong r_E$ and for $r \gg r_a$ $\tilde{r} \cong r$. We then take the potential to be $\Phi(x, y, z) = \Phi_{\rm NFW}(\tilde{r}(x, y, z))$ which reproduces the general behaviour found by Hayashi et al. (2007) with a smooth transition around r_a.

For a specific example, we have chosen the transition scale to be the scale radius of the NFW profile and have taken values for a, b and c that give central principal axial ratios that are comparable to those found by Hayashi et al: $b/a = 0.78$ and $c/a = 0.72$. Our

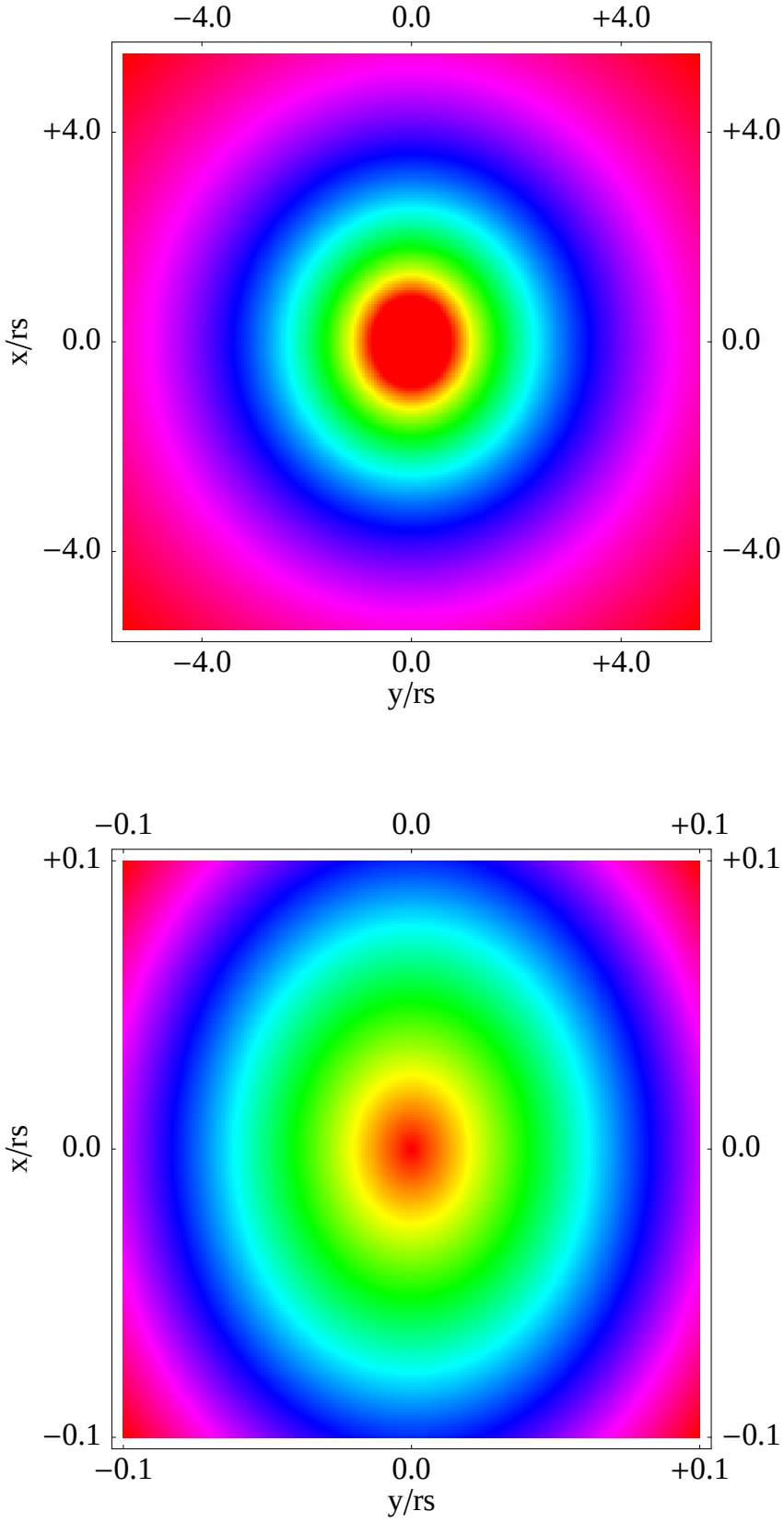

Figure 5.10: Isopotentials for the outer and inner parts of one of our triaxial NFW haloes. It is obvious that the halo becomes rounder as one moves outwards. In this case the transition scale r_a was chosen to be equal to the scale radius r_s of the NFW profile.

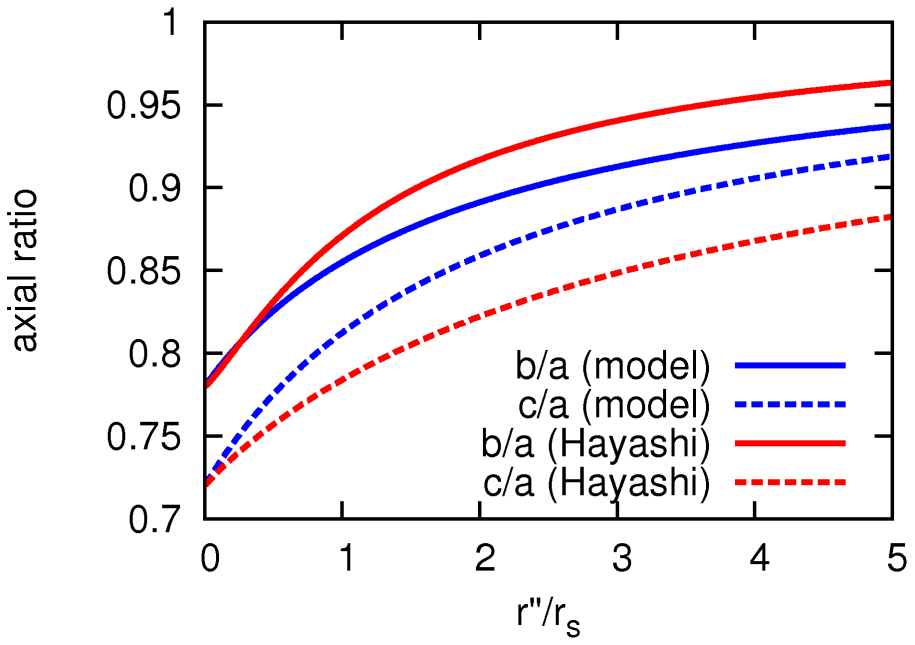

Figure 5.11: Comparison of the radial variation of isopotential axial ratios for N-body haloes (Hayashi et al., 2007) to that for our simple triaxial NFW model. The N-body values are the average of those found in Hayashi et al. (2007). The transition scale r_a of our model has been set equal to the scale radius r_s of the underlying NFW profile.

choice is $a = 1.18, b = 0.92, c = 0.85$. For the NFW profile we used a concentration of $r_{200}/r_s = 7.0$. We checked Poisson's equation for this potential to ensure that it implies a positive density everywhere. The check was performed by DaMaFlow evaluating the negative of the trace of the tidal field on a fine 3D grid. This is just the Laplacian of the potential and so proportional to the corresponding density. Since the density field is continuous, positive density values on the grid should guarantee a positive density everywhere.

Fig. 5.10 shows isopotentials in the outer and inner parts of the halo. All distances are expressed in terms of the scale radius r_s of the NFW profile. The transition from spherical to aspherical can clearly be seen as the centre is approached. Fig. 5.11 compares the radial variation in axial ratios in our model and in the simulations of Hayashi et al. (2007). The simulation axial ratios are calculated with Eq. (5.45) using the average values for α, γ, r_α found in Hayashi et al. (2007). The lines for our model are calculated as follows. For a given value of $\tilde{r}$ we computed the intersections of the corresponding isocontour with the x, y and z axes. So we get three values a'', b'', c''. To look for their variation over distance we define the mean distance $r'' = \sqrt{(a'')^2 + (b'')^2 + (c'')^2}$. This is essentially the same procedure which Hayashi et al. (2007) applied when fitting the isopotentials of their simulated haloes. Thus we can compare directly with their results as in Fig. 5.11. The qualitative behaviour of our model is very similar to that of the simulations. It is not necessary to demand an exact fit since the scatter between different haloes studied by Hayashi et al. (2007) is quite large.

We implemented this potential into DaMaFlow and looked at four different orbits with

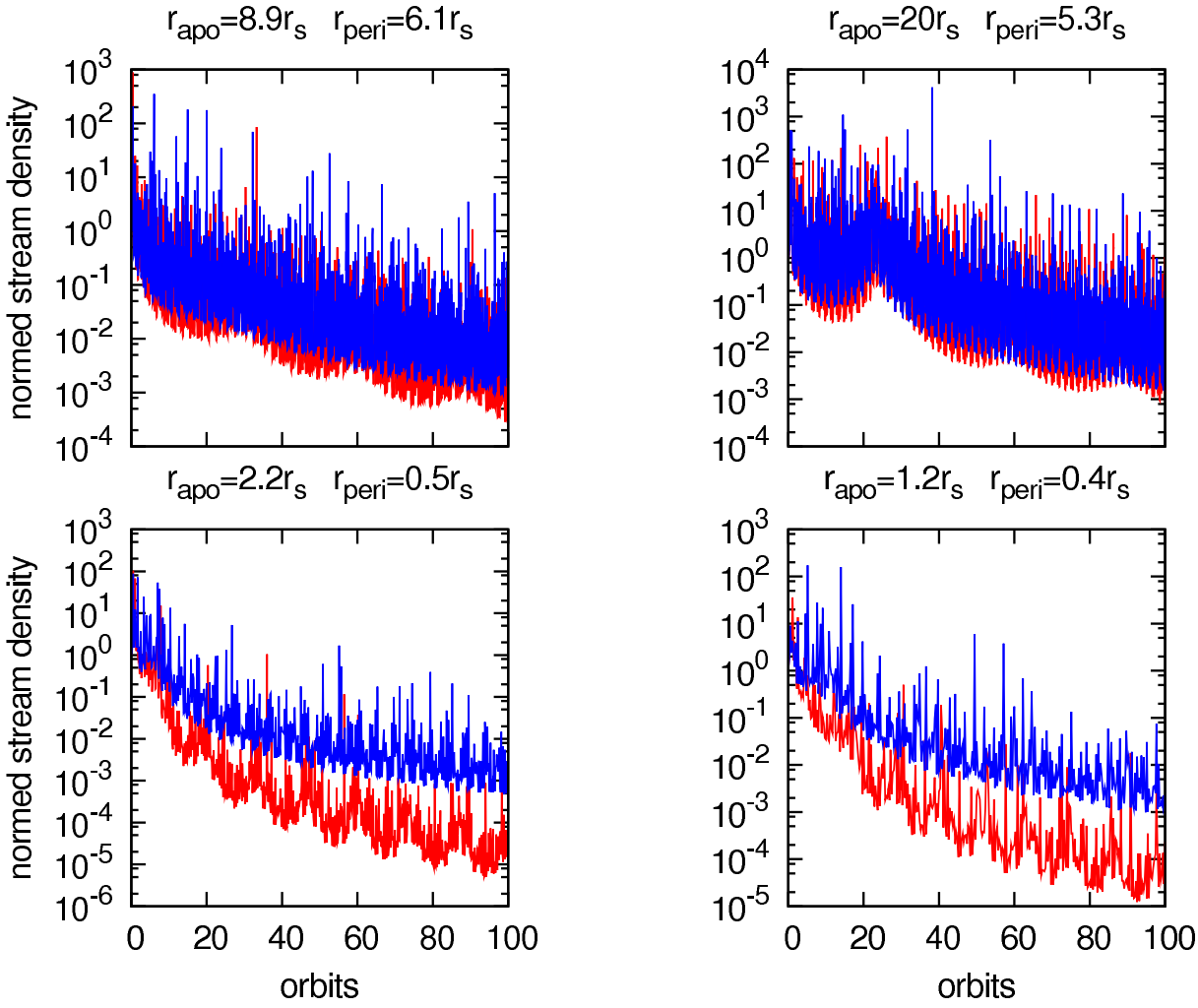

Figure 5.12: Stream densities in a spherically symmetric NFW potential are compared to those expected in a more realistic DM halo with a shape that varies with radius. Orbits with pericentre inside the transition scale $r_a = r_s$ show a substantial difference between the two cases. After about 100 orbits streams are roughly 100 times less dense in a triaxial halo than in a spherical one. Thus spherical models for the Milky Way's halo are likely to underestimate the number of streams in the solar neighbourhood by two orders of magnitude.

the following apo-/pericentre distances in units of r_s: $8.9/6.1, 20/5.9, 2.2/0.5, 1.2/0.4$. We compared the stream densities predicted for our triaxial model to those predicted in the corresponding spherical NFW profile. We fixed the starting point and the velocity direction to be the same in the two cases. The amplitude of the velocity was then set to give the same energy in the two cases. With this procedure the orbits covered comparable regions in configuration-space and had nearly the same apo- and pericentre distances. Note that it is impossible to get identical orbital shapes in the two potentials. Especially in the inner parts of the halo, where the two potentials differ substantially, the orbits have different shapes. In a spherical potential orbits are confined to a plane by conservation of angular momentum, but this is not the case in a triaxial potential.

In Fig. 5.12 we show the stream density evolution for these four orbits. Two belong to the outer halo with peri- and apocentre beyond the scale radius. As expected their stream density behaviour is very similar in the two potentials. As soon as orbits penetrate the inner halo, however, the behaviour is quite different in the two cases. After 100 orbits, streams are about 100 times less dense in a triaxial halo than in a spherical one. Note that this is just what one would predict, given the $(t/t_{\rm orbital})^{-2}$ and $(t/t_{\rm orbital})^{-3}$ density evolution expected for regular motion in spherical and triaxial potentials, respectively.

In the case of a cored ellipsoidal potential we showed above that, depending on the level of triaxiality, substantial fractions of phase-space can be occupied by chaotic orbits. Thus we may expect such orbits to be present in our triaxial NFW profile also. Previous work on galactic dynamics has demonstrated the presence of chaotic orbits in the potentials corresponding to a variety of cuspy, triaxial density profiles (Merritt and Fridman, 1996; Merritt and Valluri, 1996; Valluri and Merritt, 1998; Kandrup and Siopis, 2003; Capuzzo-Dolcetta et al., 2007). To search for chaotic orbits in our model, we have integrated 2×10^4 different representative orbits and studied the predicted behaviour for the density of their associated streams. For simplicity we have chosen the initial conditions for these orbits at random from the known analytic distribution function of a Hernquist sphere matched to the mean radial density profile of our triaxial NFW model. A self-consistent Hernquist sphere has density profile and potential

$$\rho(r) = \frac{M}{2\pi}\frac{a}{r}\frac{1}{(r+a)^3}; \qquad \Phi(r) = -\frac{G\,M}{r+a}. \tag{5.48}$$

We match to our NFW model by an appropriate choice of the scale length a (Springel et al., 2005a). A standard inversion technique can then be used to select a random set of initial orbital positions from this (spherically symmetric) distribution. Appropriate initial velocities can be generated by applying the von Neumann rejection technique (Press et al., 1992; Ascasibar and Binney, 2005) to the analytically known distribution function of the self-consistent Hernquist model (Hernquist, 1990). This procedure does not, of course, sample orbits with a weighting which would self-consistently reproduce our triaxial NFW model. Nevertheless, the similarity of the NFW and Hernquist models should ensure that our selected orbits cover the regions of phase-space which would be populated in a truly self-consistent model in a reasonably representative way. This is sufficient to evaluate the overall importance of chaotic orbits in the model.

We integrated each orbit as long as required to guarantee $\max(x_{\rm cross}, y_{\rm cross}, z_{\rm cross}) = 10^3$,

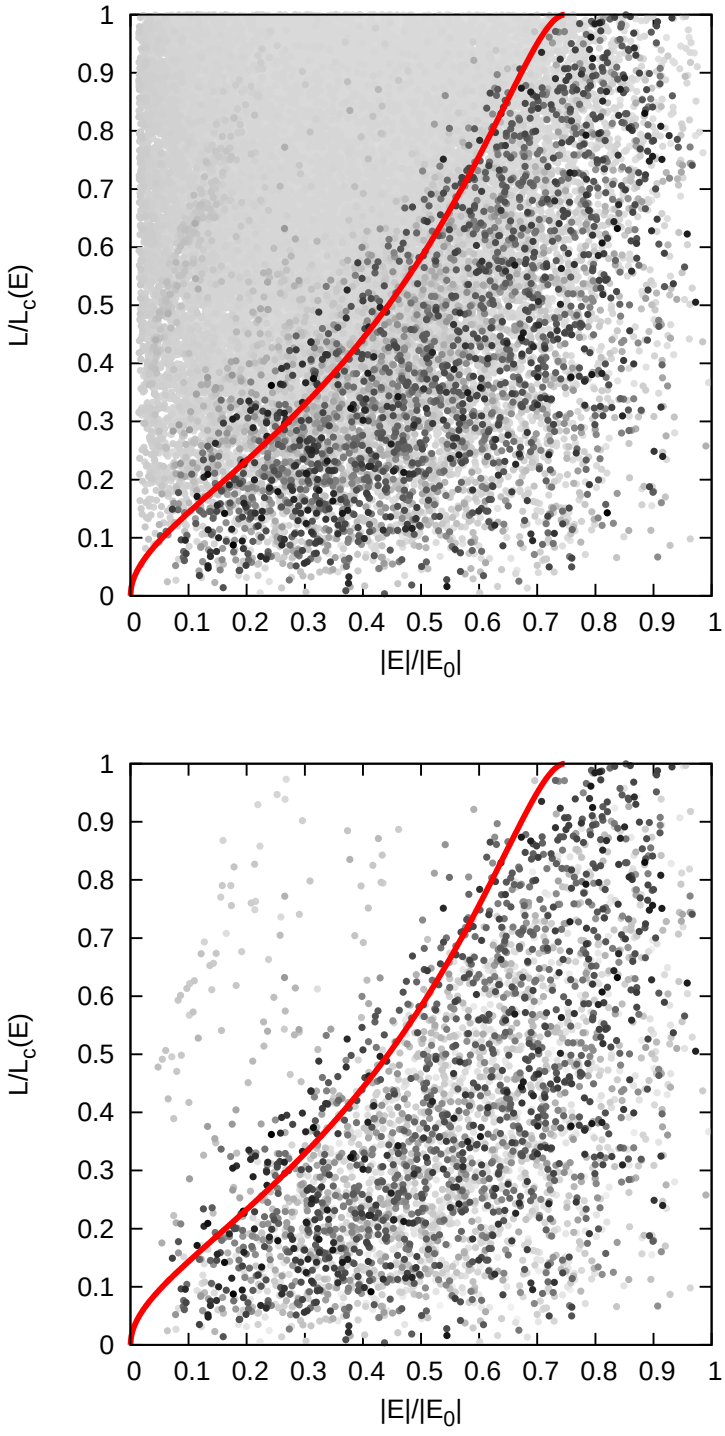

Figure 5.13: Qualitative view of the phase-space structure of our triaxial NFW potential. These plots give results for 2×10^4 orbits. The greyscale represents the stream density decrease after $\max(x_{\rm cross}, y_{\rm cross}, z_{\rm cross}) = 10^3$. Black points correspond to orbits with a very strong density decrease, thus to non-regular orbits. Such orbits are found primarily in the inner regions of the potential. Orbits with lower binding energy are mostly regular, showing a much smaller stream density decrease. The black points were plotted last to avoid over-plotting by the grey ones. E_0 corresponds to a particle at rest at the centre of the potential. The solid red line represents the constant pericentre line ($r_{\rm peri} = 1/3 r_s$). In the lower panel only the box orbits are plotted. Most of the non-regular orbits are boxes deep inside the potential.

where $i_{\rm cross}$ is the number of crossings along the i-coordinate, $i = x, y, z$. The integration was done by the Dop853 algorithm with a very high precision to get an relative energy error below 10^{-10} over the whole integration time. We have chosen such high energy conservation to be sure that the integration works correctly even though the potential is cuspy.

We plot the final stream density using a greyscale just as in Fig. 5.7. The axes of the resulting plots in Fig. 5.13 are the orbital energy in the triaxial NFW potential and the circularity based on the spherical Hernquist profile that was used to generate the initial conditions. Black points correspond to very large decreases in stream density, hence to non-regular motion. The upper panel shows all orbits whereas the lower panel takes only box orbits into account. We distinguished box and tube orbits by looking at the angular momenta around the symmetry axes. For a box orbit the sign of all three momenta changes along the orbit. On the other hand a tube orbit has one axis along which the angular momentum has a fixed sign.

First of all it is quite striking from these plots that there are orbits that are not regular and show up as black points. A line of fixed pericentre ($1/3r_s$) in Fig. 5.7 clearly shows that these are orbits that reach the innermost part of the halo, where they feel the strong triaxiality and the cusp. This is not surprising because previous studies showed that cuspy, triaxial potentials exhibit chaos (Valluri and Merritt, 1998; Kandrup and Siopis, 2003). These studies found that box orbits are primarily affected but also some tube orbits. This behaviour can clearly be seen in Fig. 5.13

It is not clear how to distinguish between regular and chaotic motion based on the stream density decrease after a given number of orbital periods. There is no "gap" in the stream density distribution which might separate regular and chaotic motion. Methods like the frequency shift derived from a NAFF analysis run into the same problem (Valluri and Merritt, 1998). Lyapunov methods are better suited to this problem, but may also have problems making a clear distinction (Kandrup and Sideris, 2002). As our objective here is not a precise chaos analysis of our triaxial NFW potential, we take a fiducial value of 10^{-25} for the stream density which separates regular and chaotic motion. This value is based on the stream density distribution function and corresponds to a stream density below the "regular motion bump". Orbits with a stream density below 10^{-25} will be considered as chaotic. With this criterion about 35% of the orbits with binding energy between 0.91 $|E_0|$ and 1.00 $|E_0|$ are chaotic. This fraction is not particular high compared to previous studies. Valluri and Merritt (1998), for example, find fractions up to 80% depending on the parameters they use for their triaxial density profile. Recent studies of self-consistent models of cuspy triaxial galaxies with dark matter haloes (Capuzzo-Dolcetta et al., 2007) also find chaotic orbits to play an important role. Although we have carried out only a qualitative analysis it is clear that chaos plays a role in the centre of our model also. Box orbits are mostly affected by chaotic mixing because they reach the innermost part of the halo. We note that the four orbits shown in Fig. 5.12 are regular. None of them has a pericentre distance below the "critical" distance $1/3r_s$.

These results show that stream densities near the Sun are predicted to be much lower for a realistic triaxial potential than for the corresponding spherical potential. The orbital period near the Sun is about 2.5×10^8 yrs and the distance of the Sun from the Galactic Centre is roughly 0.2 to $0.3r_s$. Figure 5.12 suggests that mixing will have reduced stream

densities from their values at infall by roughly 4 orders of magnitude for typical streams in the solar neighbourhood. Since the mean DM density near the Sun is substantially greater than typical stream densities at infall, we expect at least 10^5 CDM streams to contribute to the density in the solar neighbourhood. We note that this is still likely to be a substantial underestimate, as it is based on a static, smooth halo model and so neglects additional mixing effects which may be important, in particular mixing in precursor objects, mixing due to scattering by halo substructure, and chaotic mixing. Such effects can only be treated properly by applying the GDE to structure formation in its proper cosmological context. This requires the use of N-body simulations. We note that particles orbiting the innermost part of the halo are also affected by the disk potential leading to a non-spherical contribution to the potential.

5.7 Fine-grained phase-space analysis in N-body codes

The main motivation of our work is the desire to address issues of mixing and fine-scale structure in full generality by building the GDE into current state-of-the-art N-body codes. We have done this for the current version of the GADGET code (Springel, 2005). This is a massively parallel N-body code which has already been used to carry out very large cosmological simulations (Springel et al., 2005b). It calculates the gravitational forces with an efficient TreePM method (Bode et al., 2000; Xu, 1995; Bagla, 2002) and uses a domain decomposition scheme based on space-filling (fractal) Peano-Hilbert curves to achieve good work-load balance in parallel operation.

To implement the GDE within GADGET we needed to extend various parts of the code. The dynamics of the distortion tensor are driven by the ordinary gravitational tidal field. The corresponding tidal tensors for each DM particle have to be calculated using the same Tree- or TreePM-Method as the forces in order to provide the correct driving term in the GDE. While the forces are given by the first derivative of the potential, the tidal tensor is made up of second derivatives. The particles in an N-body simulation can be thought of as a Monte-Carlo sampling of the real DM phase-space distribution, but the coarseness of this sampling introduces unwanted discreteness or "two-body" effects which are likely to be more serious for higher derivatives of the potential. Such effects are usually mitigated by softening the gravitational potential of each particle. GADGET uses a spline softening kernel function with compact support

$$W_2(u) = \begin{cases} \frac{16}{3}u^2 - \frac{48}{5}u^4 + \frac{32}{5}u^5 - \frac{14}{5}, & 0 \le u < \frac{1}{2}, \\ \frac{1}{15u} + \frac{32}{3}u^2 - 16u^3 + \frac{48}{5}u^4 & \\ \qquad - \frac{32}{15}u^5 - \frac{16}{5}, & \frac{1}{2} \le u < 1, \\ -\frac{1}{u}, & u \ge 1. \end{cases}$$

The softened potential of a point mass is then given by $\Phi^s(\underline{x}) = (Gm/h)W_2(|\underline{x}|/h)$ with a softening length $h = 2.8\epsilon$, where ϵ is the Plummer equivalent softening length. The potential (and so force and tidal field) become Newtonian if $|\underline{x}| \ge h$. From this softened

potential we can calculate the softened tidal field of a point mass

$$T^s_{ij}(\underline{x}) = -\frac{\partial^2 \Phi^s(\underline{x})}{\partial x_i \partial x_j} = \delta_{ij} m g_1(\frac{|\underline{x}|}{h}) + x_i x_j m g_2(\frac{|\underline{x}|}{h}), \tag{5.49}$$

where

$$g_1(u) = \frac{1}{h^3} \begin{cases} -\frac{32}{3} + \frac{192}{5}u^2 - 32u^3, & u \le \frac{1}{2}, \\ \frac{1}{15u^3} - \frac{64}{3} + 48u & \\ \quad - \frac{192}{5}u^2 + \frac{32}{3}u^3, & \frac{1}{2} < u < 1, \\ -\frac{1}{u^3}, & u > 1, \end{cases} \tag{5.50}$$

and

$$g_2(u) = \frac{1}{h^5} \begin{cases} \frac{384}{5} - 96u, & u \le \frac{1}{2}, \\ -\frac{384}{5} - \frac{1}{5u^5} + \frac{48}{u} + 32u, & \frac{1}{2} < u < 1, \\ \frac{3}{u^5}, & u > 1. \end{cases} \tag{5.51}$$

Thus the softened tidal field acting on particle k at position $\underline{x}_k$ (its tidal tensor) is given by

$$\begin{aligned} T_{ij}(\underline{x}_k) &= \sum_{l \neq k} \left[\delta_{ij} m_l g_1 \left(\frac{|\underline{x}_l - \underline{x}_k|}{h} \right) \right. \\ &+ \left. (x_{l,i} - x_{k,i}) (x_{l,j} - x_{k,j}) m_l g_2 \left(\frac{|\underline{x}_l - \underline{x}_k|}{h} \right) \right] \\ &= \sum_{l} \left[\delta_{ij} m_l g_1 \left(\frac{|\underline{x}_l - \underline{x}_k|}{h} \right) \right. \\ &+ \left. (x_{l,i} - x_{k,i}) (x_{l,j} - x_{k,j}) m_l g_2 \left(\frac{|\underline{x}_l - \underline{x}_k|}{h} \right) \right] \\ &- \delta_{ij} m_k g_1(0) . \end{aligned} \tag{5.52}$$

The last step highlights a difference between the tidal field calculation and the normal force calculation. The tidal field is obtained using the same tree-walk as the forces. The latter are calculated by evaluating the full sum $\sum_l$ without excluding particle k. This is simply to avoid additional bookkeeping; the particle-particle force vanishes when $l = k$ so including the self-term does not affect the result. This is not the case for the tidal field, for which one must add an extra term to the diagonal tidal tensor elements to remove the self-tidal field. This is similar to the self-energy correction that is needed when using the tree to evaluate the total potential energy of the system.

For larger simulations it is not efficient to use the tree alone. In such cases the TreePM method can be much faster. In this scheme the potential is split into short-range and long-range parts $\Phi = \Phi^{\rm short} + \Phi^{\rm long}$. Specifically, in Fourier space GADGET takes

$$\Phi^{\rm long}_k = \Phi_k \exp(-k^2 r_s^2), \tag{5.53}$$

where r_s defines the spatial scale of the force split and should not be confused with the

scale radius of the NFW profile. The long-range potential is calculated by mesh-based Fourier techniques. In Fourier space the tidal field can be calculated by just pulling down $-(ik_j)^2$ with $j = x, y, z$. The short-range potential in real space is given by

$$\Phi_{\rm short}(\underline{x}) = \sum_l \Phi^s(r_l) {\rm erfc}\left(\frac{r_l}{2r_s}\right), \tag{5.54}$$

and the corresponding short-range part of the tidal field by

$$\begin{aligned} T_{ij}(\underline{x}) = \sum_l \Bigg(& T^s_{ij}(\underline{x}_l) \left({\rm erfc}\left(\frac{r_l}{2r_s}\right) + \frac{r_l}{\sqrt{\pi} r_s} \exp\left(-\frac{r_l^2}{4r_s^2}\right)\right) \\ - \quad & F^s_i(\underline{x}_l) \frac{x_{l,j} r_l}{2\sqrt{\pi} r_s^3} \exp\left(-\frac{r_l^2}{4r_s^2}\right)\Bigg), \end{aligned} \tag{5.55}$$

where $\underline{F}^s$ is the softened point mass force, $x_{l,i}$ is defined as the smallest distance of any of the periodic images of particle l to the coordinate x_i of $\underline{x}$, and $r_l = \sqrt{x_{l,x}^2 + x_{l,y}^2 + x_{l,z}^2}$.

The time integration also needs modification in order to integrate the GDE in parallel with the equations of motion. For this it is desirable to write both the equations of motion and the GDE in a time-symmetric way. This fits best into GADGET's quasi-symplectic integration scheme which is a second-order leapfrog. For the GDE we need to integrate two differential equations of second-order to solve for $\underline{\underline{D}}_i$ with $i = xq, xp$. Let $\underline{\underline{W}}_i$ denote the first time derivative of $\underline{\underline{D}}_i$. We can then define the system state vector $\tilde{S}$ as,

$$\tilde{S} = \left(\underline{x}, \underline{v}, \underline{\underline{D}}_{xq}, \underline{\underline{D}}_{xp}, \underline{\underline{W}}_{xq}, \underline{\underline{W}}_{xp}\right)^\dagger. \tag{5.56}$$

The equations of motion and the GDE can now be written as one equation for $\tilde{S}$

$$\dot{\tilde{S}}(t; \overline{q}) = f(\tilde{S}(t; \overline{q})). \tag{5.57}$$

The right hand side does not depend on the time derivative of $\tilde{S}$. This allows the use of a time-symmetric leapfrog scheme with the following Drift- and Kick-operators

$$D_t(\Delta t) = \begin{cases} \underline{v} & \rightarrow & \underline{v} & \\ \underline{x} & \rightarrow & \underline{x} + \underline{v}\Delta t & \\ \underline{\underline{W}}_i & \rightarrow & \underline{\underline{W}}_i & i = xq, xp \\ \underline{\underline{D}}_i & \rightarrow & \underline{\underline{D}}_i + \underline{\underline{W}}_i \Delta t & i = xq, xp \end{cases} \tag{5.58}$$

$$K_t(\Delta t) = \begin{cases} \underline{x} & \rightarrow & \underline{x} & \\ \underline{v} & \rightarrow & \underline{v} + \underline{F}\Delta t & \\ \underline{\underline{D}}_i & \rightarrow & \underline{\underline{D}}_i & i = xq, xp \\ \underline{\underline{W}}_i & \rightarrow & \underline{\underline{W}}_i + \underline{\underline{T}}\Delta t & i = xq, xp \end{cases}, \tag{5.59}$$

where $\underline{\underline{T}}$ is the ordinary tidal tensor and $\underline{F}$ the gravitational force. Although the time integration now needs to solve 18 additional non-trivial coupled second-order differential equations, it turns out that the loss in performance is not dramatic, even if we do the

calculation for all DM particles in the simulation box. From a computational point of view, the strongest impact comes from the extra memory that is needed to keep track of the distortion tensor. Every particle needs the tidal tensor (6 numbers due to symmetry) and the distortion tensor (36 numbers). Nevertheless, with current computer capabilities this is not a major limitation.

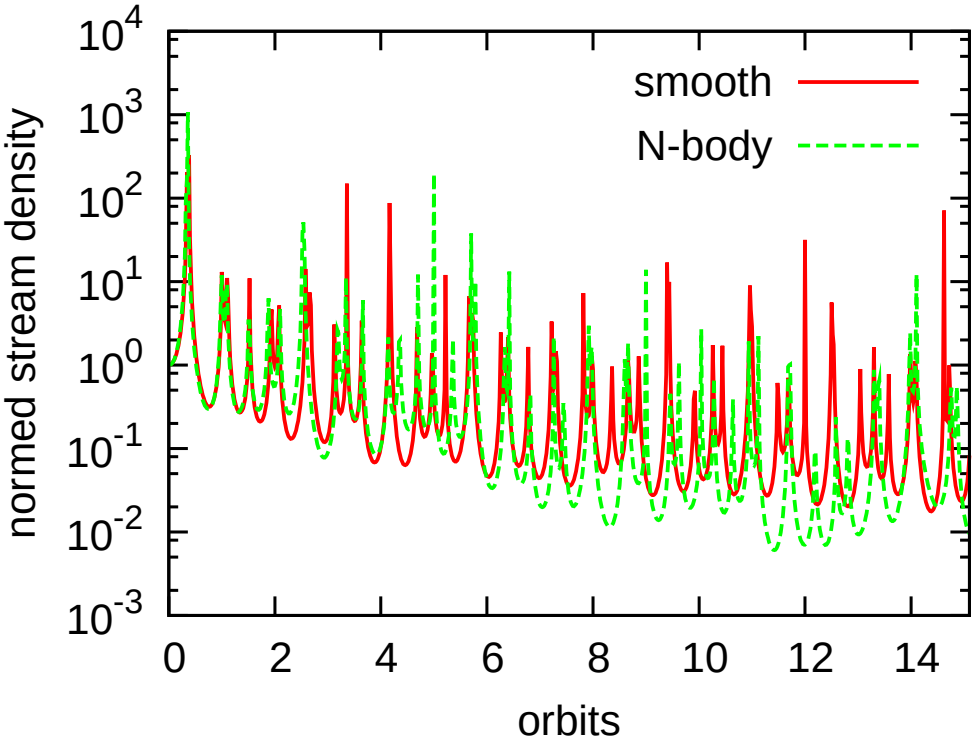

Figure 5.14: The stream density evolution found by integrating the GDE along an orbit in a live N-body realisation of a Hernquist sphere is compared to that predicted for the same initial condition in the corresponding analytic potential. The N-body halo was realised with $N = 10^5$ particles using a softening length, $\epsilon = 1.5$ kpc. The N-body evolution is very similar in shape and caustic frequency to that in the smooth potential. The 6-D phase-space density remained constant to an accuracy of 10^{-8} over the full N-body integration.

In general the state of an N-body simulation is not stored frequently enough to catch the caustics that occur along each particle's orbit. To avoid missing these we implemented a caustic finder that examines every drift operation of the time integration. As described above, sign changes in the determinant of the configuration-space distortion tensor $\underline{\underline{D}}$ indicate that a particle has passed though a caustic. Whenever this happens the event is logged. We are then limited only by the time-step of the simulation and this is normally small enough to catch all large-scale caustics.

For flexibility in testing, we have also implemented the GDE formalism in a version of GADGET which allows certain static potentials, in particular, NFW, Hernquist and cored ellipsoidal logarithmic potentials, to be included in addition to the self-gravity of the particles.

As a first test of our implementation in GADGET, we have compared the behaviour

predicted for N-body realisations of a static Hernquist sphere to that found for an integration in the corresponding smooth potential. To get a system which resembles the Milky Way's halo we take $M = 1.86 \times 10^{12}\mathrm{M}_{\odot}$ and $a = 34.5$ kpc in equation (5.48). The N-body realisation was constructed as described in section 6.

In Fig. 5.14 we compare the evolution of stream density for a specific orbit in an $N = 10^5$ live Hernquist halo to that found when integrating the same orbit in the corresponding smooth potential. The Hernquist sphere had the parameters given above and the particular orbit chosen here had peri- and apocentre of 25 kpc and 33 kpc, respectively, giving a period of about 0.5 Gyr. It was integrated for about 15 orbits or 7.5 Gyr. The N-body softening was taken to be $\epsilon = 1.5$ kpc. The 6-D phase-space density remained constant to better than 1 part in 10^8 in both integrations, but the stream density evolution still differs significantly between them, in particular in the timing of the caustics and in the detailed behaviour of the lower envelope. This is a consequence of the well known divergence between nearby orbits in N-body systems which is caused by the cumulative effect of many small perturbations due to discreteness (Kandrup and Sideris, 2003). The GDE is very sensitive to such noise. The features in the two curves are, nevertheless very similar, in particular the number and spacing of caustics and the overall shape.

Fig. 5.15 shows the normed stream densities after 5 Gyr of integration for all particles in a live Hernquist halo with $N = 10^5$ and the parameters assumed above. For this integration we adopted $\epsilon = 2.0$ kpc. We divide the particles into 9 radial bins containing approximately equal numbers of particles and then histogram the stream densities, both for the N-body simulation and for integrations from the same initial conditions in a smooth Hernquist potential. Typical stream densities in Fig. 5.15 decrease towards the centre of the sphere. This is because shorter dynamical times result in enhanced mixing in the inner regions. (Recall that stream densities decrease as $(t/t_{\mathrm{orbital}})^{-2}$ in a spherical potential, and so are smallest where the orbital periods are shortest.) The two outermost radial shells are dominated by particles with long orbital periods which, as a result, have stream densities of order unity. The high stream density tails of the histograms are due to particles which are close to caustic passage.

The two sets of histograms in Fig. 5.15 are very similar. Although stream densities evolve differently along orbits from a given initial condition in the N-body and smooth potential cases (see Fig. 5.14) the statistical results for ensembles of initial conditions are similar. N-body discreteness effects do not cause substantial systematic shifts in the stream density distributions predicted for this test problem. A small systematic effect is visible at low stream densities. The N-body integration produces more very low-density streams than the integration in the corresponding smooth potential. This is indeed due to discreteness effects, as evidenced by the fact that we find the excess to depend on the N-body softening; smaller softenings result in a larger tail of extremely low-density streams. On the other hand, too large a softening leads to incorrect representation of the mean force near the centre of the system. Thus a trade-off is needed to define the optimal softening. This has been much discussed with reference to conventional N-body simulations (Merritt, 1996; Athanassoula et al., 2000; Dehnen, 2001; Rodionov and Sotnikova, 2005; Zhan, 2006) but we note that the situation is worse for our current application, since the evolution of our extended state vector (equation 5.57) depends on the tidal tensor. The additional spatial derivative relative to the force makes our GDE integrations

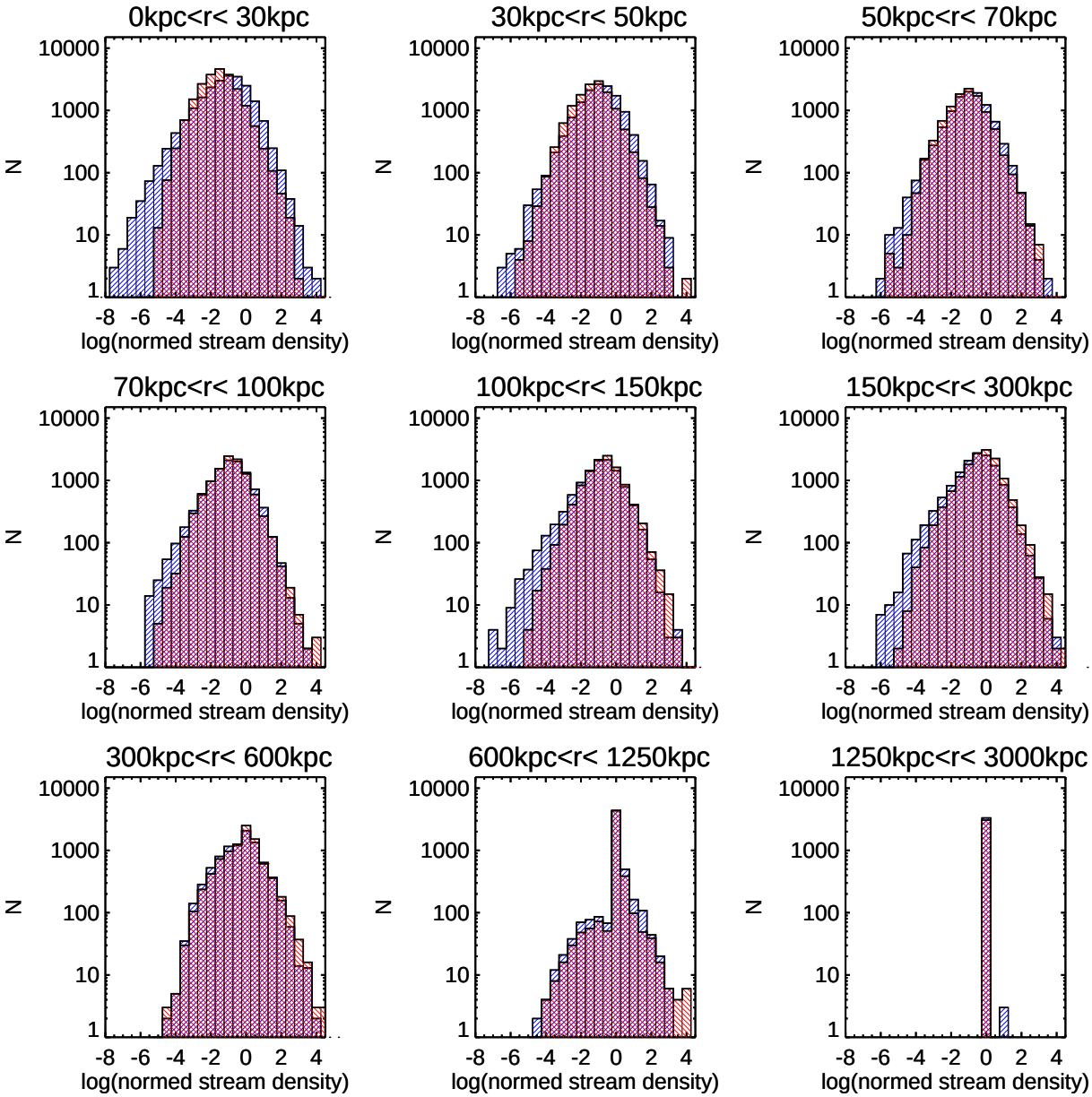

Figure 5.15: Stream densities for an $N = 10^5$ spherical Hernquist N-body model of the Galactic halo after 5.0 Gyr of integration (blue hatching from bottom left to top right) are compared to those found by integrating from the same initial conditions in the corresponding smooth potential (red hatching from bottom right to top left). In each case the sphere was divided into nine spherical shells and the normed stream densities of all particles in each shell at the final time were histogrammed with bin width 0.5 in log(density). As expected, the lowest stream densities are reached near the centre of the sphere where the dynamical time scale is shortest. In the two outermost spherical shells most of the particles have not yet undergone many caustics. The stream density distribution there has a strong bias towards values > 1. The agreement between the N-body live halo and the smooth potential is good.

substantially more sensitive to discreteness than a standard N-body integration. This suggests that the optimal choice of softening will be larger for GDE integrations than for conventional N-body integrations.

Fig. 5.15 shows that the high-density tails of the stream density distribution agree well between the N-body and smooth potential integrations. This suggests that the number and the strength of the caustics must be similar in the two cases. We can check this explicitly by again dividing the sphere into radial shells and then calculating the median number of caustic passages by the final time for the particles which end up in each shell. In Fig. 5.16 we compare the results of this exercise for the N-body and smooth potential integrations using 50 shells. The level of agreement is striking. Only within about 3 kpc of the centre is there a significant difference between the two curves. This is comparable to the softening used for the N-body system, so it is not surprising that particles in this inner core pass through fewer caustics in the N-body case.

The number of caustic passages depends very little on N-body parameters. In Fig. 5.17 we plot median caustic count against radius for two different mass resolutions and for a fixed softening length of 0.5 kpc, four times smaller than in Fig. 5.16. After 5 Gyr, the highest resolution simulation produces a median caustic count at 1 kpc which agrees with that for the smooth potential integration in Fig. 5.16, confirming that the disagreement in that figure was due to the softening of the N-body simulation. It is remarkable that particle number has no strong impact on the median caustic count. The two simulations in Fig. 5.17 differ by a factor of 32 in particle mass, yet outside 4 kpc they agree very well both with each other and with the more softened integration of Fig. 5.16. The reason for this stability is that the caustic count is an integer which is augmented only when the determinant of the distortion tensor changes sign. As a result, it is much less sensitive to the exact values of the distortion tensor elements than is the stream density (which depends on the value of the determinant).

We can estimate the median number of caustic passages for particles at radius r very simply as $\kappa t/T(r)$ where t is the age of the system, $T(r)$ the period of a circular orbit at radius r, and κ a proportionality constant. Then $T(r) = 2\pi r/V_c(r)$, where $V_c(r) = \sqrt{GM(r)/r}$ is the circular velocity at radius r. For a Hernquist sphere, the mass $M(r)$ within radius r is $M(r) = Mr^2/(r+a)^2$. Putting all this together we get

$$c(r,t;\kappa) = \kappa\frac{t}{T(r)} = \frac{\kappa}{2\pi}\frac{t\sqrt{GM/r}}{(r+a)}, \tag{5.60}$$

where $c(r,t;\kappa)$ is the predicted median caustic count at radius r. This estimate works very well, with a best fit $\kappa = 4.2$. The deviation at large radii where the caustic number is low can be accommodated simply by adding a small constant offset, as indicated by the dashed line in the figure. HW (Eq. (37)) already showed that caustics occur in a spherical potential when $p_\theta = 0$ or $p_r = 0$, thus at the turning points in the θ and r coordinates. If p_θ and p_r go through zero at different times we would expect four caustics per orbital period. This is surprisingly close to the value of κ that we estimate directly from the simulation, given that the particles seen at radius r actually have a wide range of orbital periods, rather than all having the circular orbit period $T(r)$.

Rather than focussing on the median count of caustic passages as a function of radius,

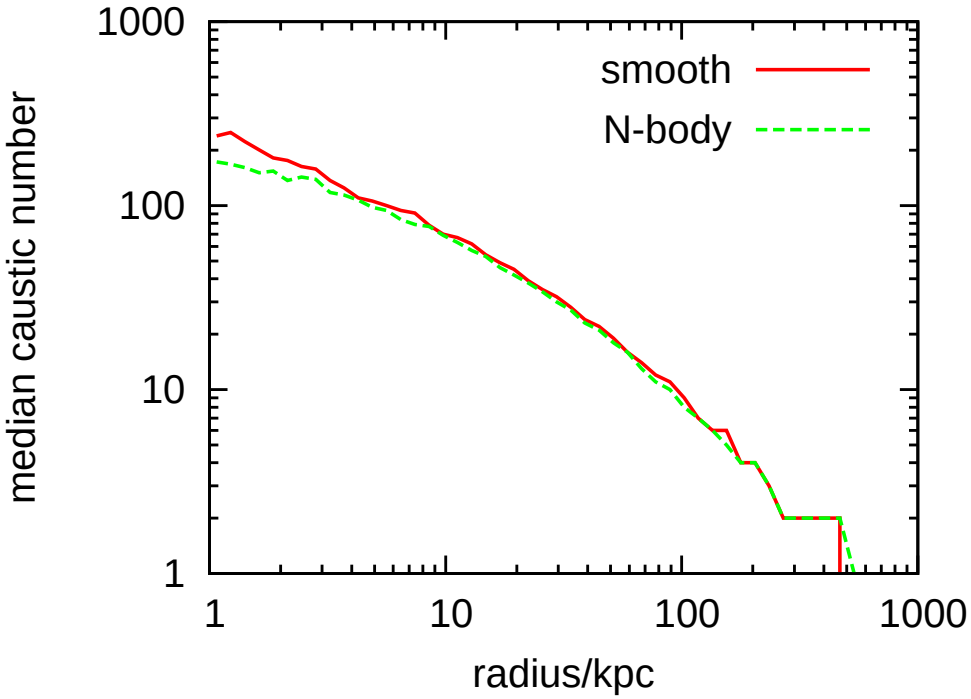

Figure 5.16: Number of caustic passages after 5 Gyr as a function of final distance from the centre for 10^5 orbits in a Hernquist sphere. The green dashed curve gives the median number of caustic passages at each radius for particles in an N-body realisation of the system integrated with softening parameter, $\epsilon = 2$kpc. The red solid curve shows the result when these same initial conditions are integrated within the corresponding analytic Hernquist potential. The results coincide except within about 1.5 softening lengths of the centre. This demonstrates that caustic counting is very robust against discreteness effects.

one can examine the distribution of the number of caustic passages, i.e. the number of particles that have passed through a given number of caustics after some given time. Figure 5.18 shows such distributions after 2.5, 5 and 10 Gyr for our highest resolution ($N = 2048000$) simulation. With increasing time the characteristic number of caustic passages increases and the number of particles with a small number of caustic passages decreases.

We can make a simple analytic model for these distributions based on Eq. (5.60). There are $4\pi\rho(r)r^2/m\,\mathrm{d}r$ particles in the interval $(r, r+\mathrm{d}r)$, where m is the mass of a simulation particle and $\rho(r)$ the (analytic) density profile of the Hernquist sphere. If we make the approximation that all particles at radius r have a caustic count equal to the median count predicted by Eq. (5.60), the number of particles with caustic counts in the interval $(c(r,t;\kappa), c(r,t;\kappa)+\mathrm{d}c(r,t;\kappa))$ will be the same as the number of particles in $(r, r+\mathrm{d}r)$, so

$$\begin{aligned} f(c)\mathrm{d}c &\cong 4\pi\rho(r)\frac{1}{m}r^2\mathrm{d}r \\ &= 4\pi\frac{M}{2\pi}a\frac{r(c,t;\kappa)}{(r(c,t;\kappa)+a)^3}\frac{1}{m}\left|\frac{\mathrm{d}r(c,t;\kappa)}{\mathrm{d}c}\right|\mathrm{d}c, \end{aligned} \tag{5.61}$$

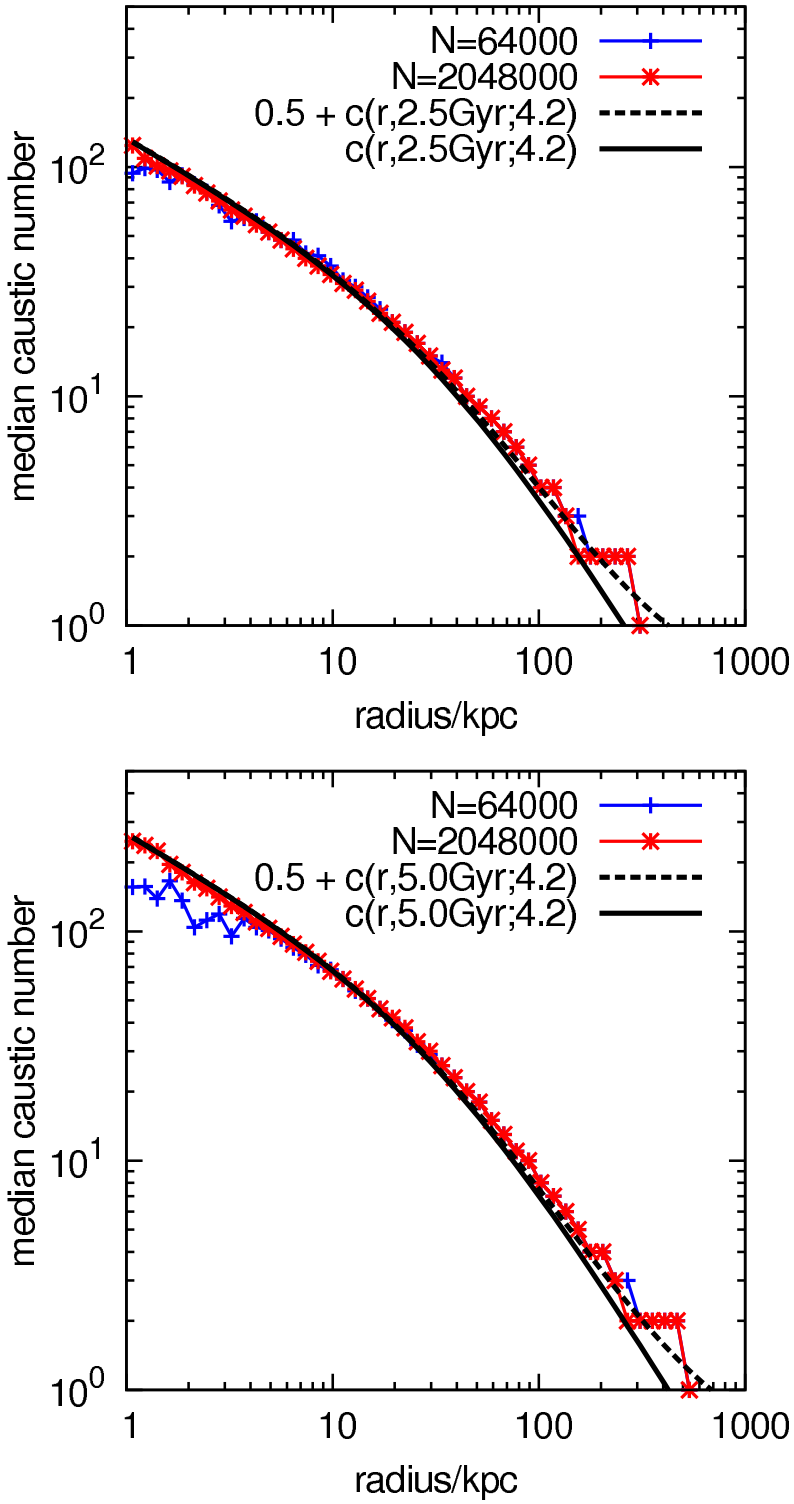

Figure 5.17: Median caustic passage count against radius, as in Fig. 5.16, but for different particle numbers and for a smaller softening ($\epsilon = 0.5$ kpc). The panels show results after 2.5 (top) and 5.0 (bottom) Gyr of evolution. Clearly the caustic count goes up between the two times, so the curves are higher in the lower panel. The radial dependence is very well represented by Eq. (5.60). Increasing the number of particles by a factor of 32 has very little effect on these curves, which also agree with those of Fig. 5.16. This shows that the caustic count along an orbit is very insensitive to the N-body parameters (particle number and softening) used to integrate the system.

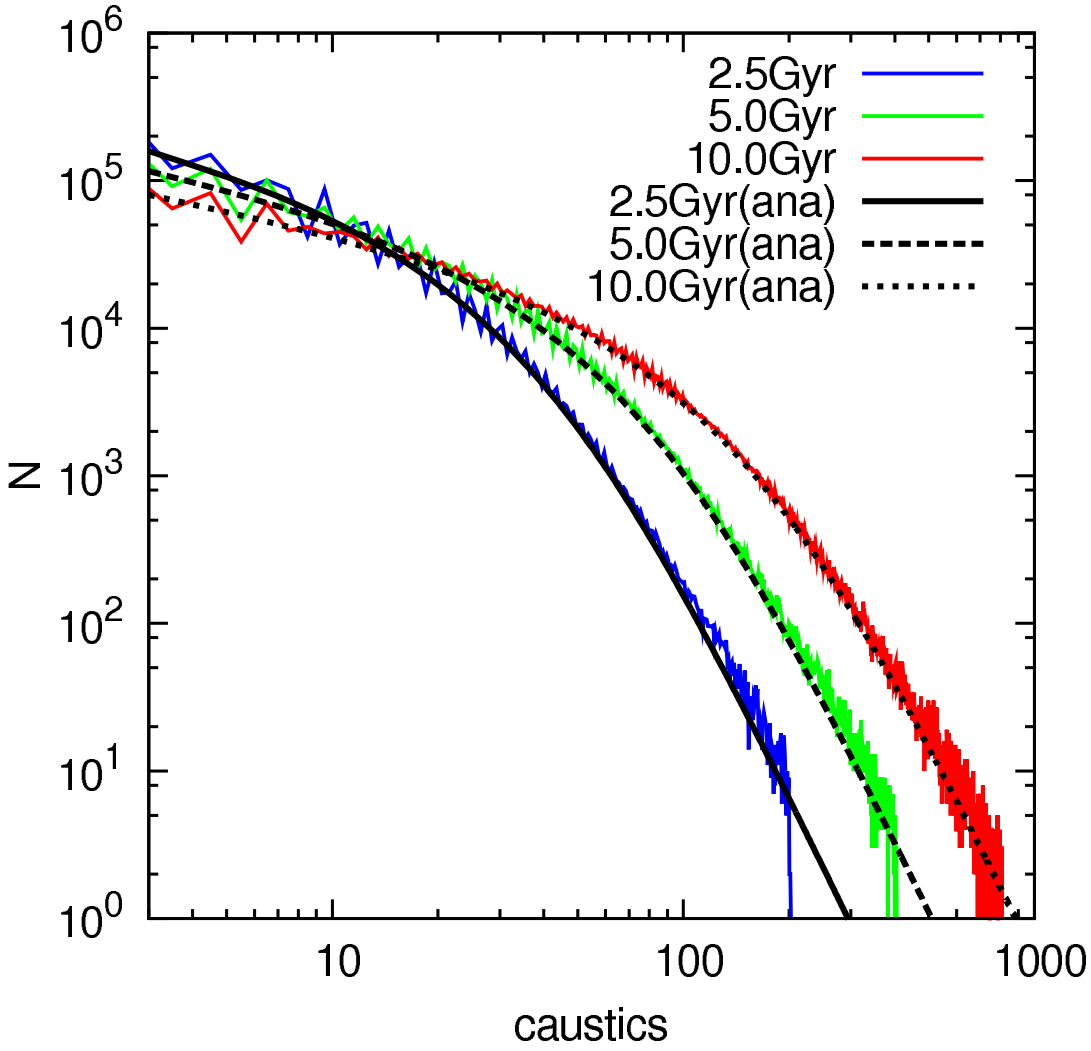

Figure 5.18: The number of particles that have passed through a given number of caustics is plotted against the number of caustics for our $N = 2048000$ simulation after 2.5, 5 and 10 Gyr. The thin black lines are analytic estimates based on Eq. (5.61).

where $r(c, t; \kappa)$ is the inverse function of $c(r, t; \kappa)$. As Fig. 5.18 shows, this formula represents the simulation results very well, suggesting that the variation in caustic count with radius is more important than the scatter in caustic count at given radius for determining the overall shape of the count distribution.

From these first tests we conclude that our N-body implementation is working well, that caustic properties can be predicted very robustly, at least when the caustics reflect large-scale structure in the system, and that stream densities can also be predicted reliably provided care is taken to ensure that discreteness effects are under control.

5.8 Conclusion and Discussion

Direct DM detection experiments operate on length-scales far below the resolution of current structure-formation simulations. The fine-grained phase-space structure on these scales will determine the signal they see. In addition, small-scale structure can substantially enhance the annihilation signal that is the target of current indirect detection experiments. A better understanding of such structure within the current concordance ΛCDM cosmology is thus critical for analysing and interpreting all current DM searches.

We propose a new route to tackle these issues. Rather than improving simulations simply by increasing the number of particles, we attach additional information to each particle, namely a phase-space distortion tensor which allows us to follow the evolution of the fine-grained phase-space distribution in the immediate neighbourhood of the particle. We introduce the Geodesic Deviation Equation (GDE) as a general tool for calculating the evolution of this distortion along any particle trajectory. The projection from phase-space to configuration-space yields the density of the particular CDM stream that particle is embedded in and can also identify when the particle passes through a caustic.

This technique makes the fine-grained phase-space structure accessible. It enables studies of the phase-space structure of general non-integrable static potentials which reproduce all the results previously obtained using frequency analysis methods, identifying chaotic regions and finding substructure in regular regions in the form of resonances. In addition, it can be used to quantify mixing rates and to locate caustics. We demonstrate these capabilities for the complex phase-space structure of the ellipsoidal logarithmic potential with a core. All relevant phase-space regions could be identified by solving the GDE along the orbit. We have written a code, DaMaFlow, that allows us to carry out such stream density analyses for a wide variety of potentials in a very efficient way.

Stream density evolution is very sensitive to the shape of the underlying potential. We demonstrate this by comparing results for a realistic CDM halo with radially varying shape to those for a spherical halo with similar radial density profile. After 100 orbits the predicted stream densities in the inner regions differ by a factor of 100. In general we expect the stream densities to decrease as $(t/t_{\rm orbital})^{-3}$ for regular orbits and even faster for chaotic orbits, rather than as $(t/t_{\rm orbital})^{-2}$, the result found for orbits in a spherical potential. Scaling to the Milky Way leads us to estimate that there should be at least 10^5 streams passing through the solar system.

The potentially revolutionary advantage of our approach, and our main reason for pursuing it, is that it applies equally well to non-symmetric, non-static situations of the kind that generically arise in CDM cosmologies. Indeed, it can be implemented in a relatively straightforward way in current state-of-the-art cosmological N-body codes. We have carried out such an implementation in the GADGET code and have presented some tests based on equilibrium Hernquist models. The N-body implementation is able to conserve 6-D phase-space density to high accuracy along individual particle orbits. In addition, it qualitatively reproduces the results found in the corresponding smooth potential for the evolution of stream density along individual orbits, and it reproduces the statistical results found for ensembles of orbits to impressive accuracy. The identification of caustic passages is particularly robust, showing very little dependence on N-body parameters such as particle number and softening. Thus discreteness effects appear to be well under

control, at least for the large N systems studied here.

In the next chapters we will use these techniques to address mixing and DM detection issues within fully general simulations of the ΛCDM structure formation model.

6

Dark Matter Caustics

Caustics are a generic feature of the nonlinear growth of structure in the dark matter distribution. If the dark matter were absolutely cold, its mass density would diverge at caustics, and the integrated annihilation probability would also diverge for individual particles participating in them. For realistic dark matter candidates, this behaviour is regularised by small but non-zero initial thermal velocities. In this chapter we present a mathematical treatment of evolution from Hot, Warm or Cold Dark Matter initial conditions which can be directly implemented in cosmological N-body codes. It allows the identification of caustics and the estimation of their annihilation radiation in fully general simulations of structure formation. [1]

[1] published in White & Vogelsberger, MNRAS, 392, 1, 281-286 (2009)

6.1 Introduction

In the previous chapter we have shown how the fine-grained phase-space structure of cold dark matter (CDM) haloes should look like. Characteristic features are streams and caustics. If a cold collisionless gas evolves from near-uniform initial conditions under the influence of gravity, the nonlinear phases of growth generically involve caustics analogous to those formed when light propagates through a non-uniform medium. This connection was explored in some depth by Russian cosmologists interested in neutrino-dominated universes (Arnold et al., 1982; Zeldovich et al., 1983). Caustics are also a very evident feature of the similarity solutions for cold spherical infall published by Fillmore and Goldreich (1984) and Bertschinger (1985). It was another 15 years, however, before Hogan (2001) realised that dark matter annihilation could be very substantially enhanced in such caustics. He showed that for absolutely cold dark matter the annihilation probability diverges logarithmically as a particle passes through a caustic, and that for realistic dark matter candidates this divergence is tamed by the small but finite initial thermal velocities of the particles. He argued that the annihilation radiation from dark haloes might be dominated by emission from caustics.

Twenty years earlier Zeldovich and Shandarin (1982) had noted that thermal velocities limit the densities achievable in dark matter caustics, and the first rigorous calculation of annihilation rates in caustics was carried out by Mohayaee and Shandarin (2006) for Bertschinger's (1985) similarity solution. They found caustics to enhance the total annihilation flux substantially in the outer regions for plausible values of the initial dark matter velocity dispersion, but to be progressively less important at smaller radii. It is unclear whether either of these results will apply in general, since the behaviour of the similarity solution is strongly influenced by its spherical symmetry (which reduces its phase-space dimensionality from 6 to 2) and by its lack of small-scale structure.

In this chapter we present a theoretical treatment of the growth of structure which shows how the geodesic deviation equation (GDE) developed in the previous chapter can be used to follow local phase-space structure in a Lagrangian treatment of nonlinear evolution. This formalism is well suited for implementation in N-body simulation codes, allowing the annihilation signal from caustics to be treated in full generality provided numerical artifacts from discretisation and integration error can be kept under control. We have presented results from a first implementation of this scheme in the previous chapter. A closely related but somewhat more complex scheme is described by Alard and Colombi (2005). Here we complement this work by giving a fuller description of the mathematics behind the approach, in particular of the regularisation of caustic densities by the finite velocity dispersion of the dark matter. This point was missing in our discussion of the annihilation rate calculation with the GDE in the last chapter. In the next section we describe our idealisation of the initial conditions for structure formation in WIMP-dominated cosmologies. Section 3 then presents useful general results for nonlinear evolution from these initial conditions. These are used in section 4 to describe the evolution of the local phase-space structure, in particular of its projection onto configuration-space, following individual particle trajectories. Caustic passages can be identified and the associated annihilation signal can be calculated explicitly. A final section discusses possible future uses of this approach.

6.2 Idealised initial conditions for structure formation

In the current standard paradigm for cosmological structure formation, the dark matter is assumed to be a weakly interacting massive particle which decoupled from all other matter and radiation fields at an early epoch, well before the universe became matter-dominated. Since this time, the dark matter has interacted with other components only through gravity. In most such models there is a period after the transition to matter-domination when density fluctuations in all components are linear on all scales, and the residual thermal velocities of the dark matter particles are small compared to the large-scale velocities induced by density inhomogeneities. In this chapter we will take an idealised representation of this situation as the initial condition for later evolution of the dark matter distribution.

Thus we assume that at the initial time t_0 the phase-space density of dark matter particles can be written as

$$f(\underline{q}, \underline{p}, t_0) = \rho(t_0)/m_p \; (1 + \delta(\underline{q})) \; \mathcal{N}((\underline{p} - \underline{V}(\underline{q}))/\sigma), \tag{6.1}$$

where $\rho(t)$ is the (time-varying) mean mass density of dark matter, m_p is the dark matter particle mass, $\underline{q}$ and $\underline{p}$ are position and velocity at the initial time and will be used as Lagrangian coordinates labelling individual dark matter particles as they follow their trajectories. In the phase-space density shown above, $\delta(\underline{q})$ is the initial linear overdensity at position $\underline{q}$, $\underline{V}(\underline{q})$ is the linear peculiar velocity at $\underline{q}$ and, for growing mode linear perturbations in the matter-dominated regime, is related to $\delta(\underline{q})$ through

$$\underline{V}(\underline{q}) \propto \nabla \phi_q \qquad \delta(\underline{q}) \propto \nabla_q^2 \phi, \tag{6.2}$$

where $\phi(\underline{q})$ is the gravitational potential generated by the linear fluctuation field, σ is the thermal velocity dispersion of the dark matter particles at the initial time, and $\mathcal{N}$ denotes the standard normal distribution in three dimensions. Our assumption that the initial density field is linear implies that $\langle \delta^2 \rangle \ll 1$, while our assumption that the initial dark matter distribution is cold implies that $\sigma^2 \ll \langle |\underline{V}|^2 \rangle$. Note that the latter condition applies even in the hot dark matter cosmology, provided the initial time t_0 is taken sufficiently late. We note further that the initial phase-space density in Eq. (6.1) corresponds to the phase-space density given in Eq. (5.30) of the last chapter.

In phase-space the dark matter is thus confined initially very close to the three-dimensional "sheet" $\underline{p} = \underline{V}(\underline{q})$ and its distribution becomes exactly three-dimensional in the cold limit $\sigma \to 0$. The projection of this sheet onto configuration-space (the three-density) is very nearly uniform. It proves useful to work in initial coordinates where the velocities at each point are taken relative to $\underline{V}(\underline{q})$. We therefore define

$$\underline{A}(\underline{q}, \underline{p}) = \underline{p} - \underline{V}(\underline{q}), \tag{6.3}$$

and we approximate the initial phase-space density of the dark matter as

$$f(\underline{q}, \underline{A}, t_0) = f_0 \; \mathcal{N}(\underline{A}/\sigma), \tag{6.4}$$

where we neglect the spatial modulation by the factor $(1 + \delta)$ so that $f_0 = \rho(t_0)/m_p$ and the phase-space density becomes independent of $\underline{q}$. Because $\underline{V}$ is the gradient of a scalar field the second-rank tensor $\partial \underline{A}/\partial \underline{q}$ is symmetric and the transformation of variables $(\underline{q}, \underline{p}) \leftrightarrow (\underline{q}, \underline{A})$ is canonical (Binney and Tremaine, 2008). This will be important below.

6.3 Evolution of the dark matter distribution

We will assume that dark matter particles interact purely gravitationally at all times of interest. Each then moves independently of the others subject only to the collective gravitational potential. Particle accelerations depend on position and time, but not on velocity, and trajectories can be derived from the time-dependent Hamiltonian of the system (e.g. Peebles, 1980). The evolution of the dark matter distribution is thus a Hamiltonian flow. A thorough development of the properties of such flows can be found in Appendix D of Binney and Tremaine (2008). We characterise the phase-space position of a particle at time t by its position $\underline{x}$ and its peculiar velocity $\underline{v}$. In a Hamiltonian flow, particle trajectories through phase-space never intersect, so we can write the phase-space position at time t as a unique and invertible function of the initial phase-space position, i.e.

$$\underline{x} \equiv \underline{x}(\underline{q}, \underline{p}, t), \quad \underline{v} \equiv \underline{v}(\underline{q}, \underline{p}, t)$$

with the well-defined inverse relation

$$\underline{q} \equiv \underline{q}(\underline{x}, \underline{v}, t), \quad \underline{p} \equiv \underline{p}(\underline{x}, \underline{v}, t).$$

This is a standard Hamiltonian map so the transformation $(\underline{q}, \underline{p}) \leftrightarrow (\underline{x}, \underline{v})$ which it defines is canonical, incompressible and symplectic (see Binney and Tremaine, 2008, for the mathematical significance of these terms). As noted above, the transformation of variables $(\underline{q}, \underline{p}) \leftrightarrow (\underline{q}, \underline{A})$ is canonical, so we can restate the (canonical) relation between initial and final configurations as

$$\underline{x} \equiv \underline{x}(\underline{q}, \underline{A}, t), \quad \underline{v} \equiv \underline{v}(\underline{q}, \underline{A}, t)$$

with

$$\underline{q} \equiv \underline{q}(\underline{x}, \underline{v}, t), \quad \underline{A} \equiv \underline{A}(\underline{x}, \underline{v}, t).$$

This simplifies the description of our problem considerably.

The collisionless Boltzmann equation is an immediate consequence of the incompressibility (in 6-D) of Hamiltonian flows – phase-space density is conserved along every trajectory in the flow. Eq. (6.4) then provides a complete formal solution for the evolution of the phase-space density distribution of the dark matter distribution:

$$f(\underline{x}, \underline{v}, t) = f_0 \, \mathcal{N}(\underline{A}(\underline{x}, \underline{v}, t)/\sigma). \tag{6.5}$$

The maximum phase-space density at time t is f_0, and this density is achieved everywhere on a 3-dimensional subspace defined implicitly by $\underline{A}(\underline{x}, \underline{v}, t) = 0$. Phase-space densities are only significantly different from zero at points which are sufficiently close to this

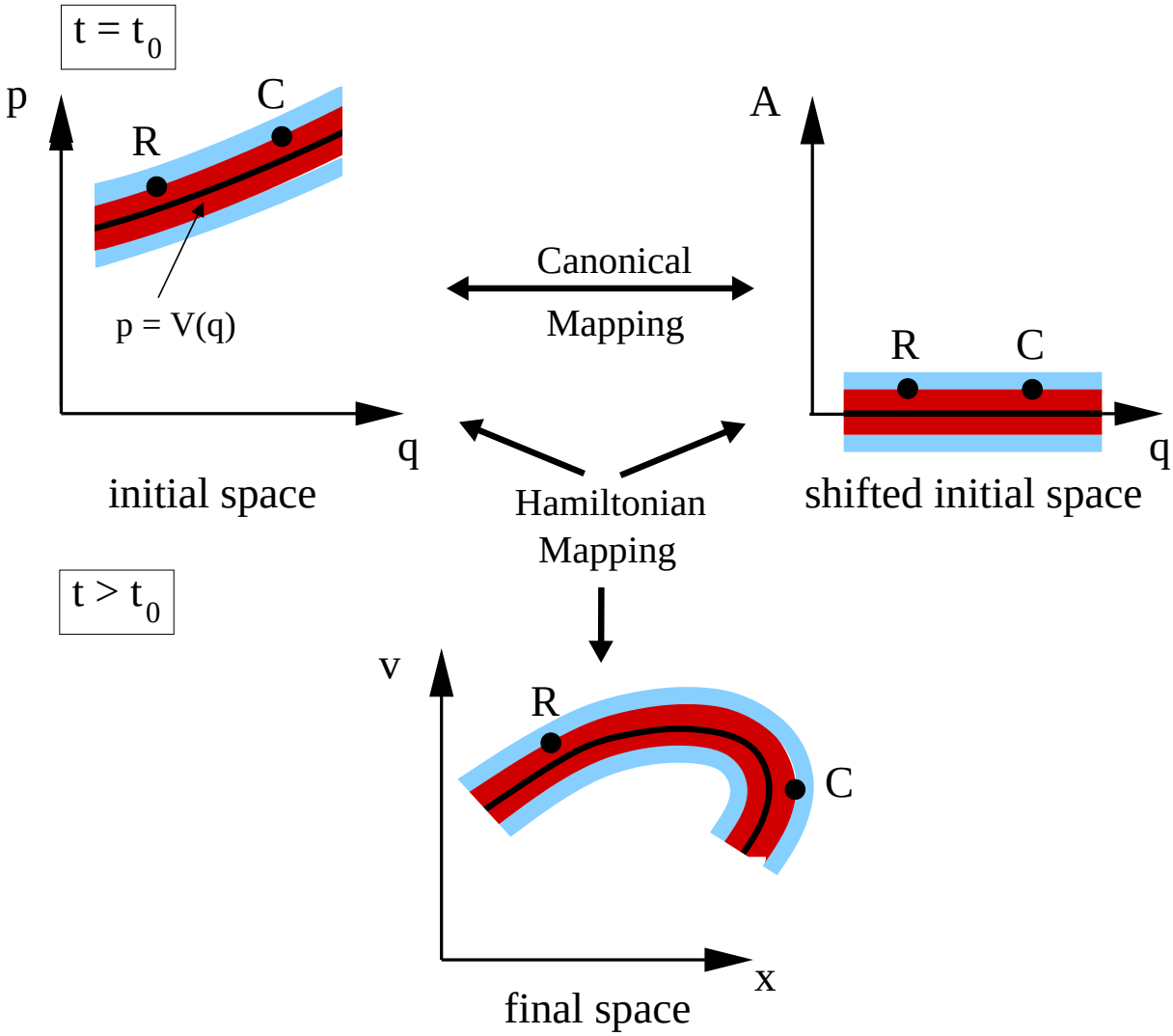

Figure 6.1: Illustration of our calculations for an analogous 1-dimensional system. At the initial time t_0, the dark matter phase-space density is non-zero only in regions of phase-space close to the central sheet $p = V(q)$, indicated by the solid curve in the upper left diagram. The shaded regions surrounding this curve indicate the 1 and 2-σ regions of the (Gaussian) phase-space density distribution. For convenience, we change the initial velocity coordinate in phase-space to $A = p - V(q)$. As shown in the upper right diagram, the equidensity contours of the phase-space density then correspond to $A = \text{const.}$, and the maximum phase space density occurs on the $A = 0$ axis. Dynamical evolution distorts these initial phase-space distributions according to the Hamiltonian flow $(q, p) \leftrightarrow (x, v)$, producing a phase-space distribution at a later time t which is indicated schematically in the lower diagram. The collisionless Boltzmann equation guarantees that the phase-space density is preserved by this map, as indicated by the shaded regions. Our plots indicate how two points R and C, corresponding to two different dark matter particles, are transformed by these maps. The (1-dimensional) space density in the neighbourhood of each is given by projecting the phase-space density down the velocity axis, and is uniform in the initial space. At time t, R is at a regular point of its trajectory ($\partial A/\partial v \neq 0$), whereas C is passing a caustic ($\partial A/\partial v = 0$). Clearly the space density at R depends on the local slope of its $A = \text{const.}$ line, while at C it depends on the curvature of this line and on the offset of C from the central sheet of its stream.

subspace which we refer to below as the "central sheet" of the phase-space distribution. The geometry of this sheet is very simple at early times: its projection onto 3-space is (approximately) uniform and only one point of the sheet projects onto each $\underline{x}$-position. Nonlinear evolution stretches and folds the sheet, but does not tear it. It can then pass through a given $\underline{x}$-position multiple times, producing a series of streams, each with a different velocity $\underline{v}$. Caustics arise on the boundaries between regions with different numbers of streams. Fig. 6.1 illustrates this situation for an analogous 1-dimensional system.

It is important to realise that the solution of Eq. (6.5) depends only on the assumed initial condition and on the fact that the dark matter obeys the collisionless Boltzmann equation. Thus it holds in the absence of any symmetry and during strongly non-equilibrium phases of evolution. In addition, it does not assume the gravitational potential to be generated by the dark matter alone, so it is valid, for example, in the inner regions of galaxies, where the gravitational effects of the baryonic components are dominant. These influence the trajectories of individual dark matter particles, and so the details of $\underline{A}(\underline{x}, \underline{v}, t)$, but they do not affect the Hamiltonian nature of the flow or the validity of Eq. (6.5).

The Hamiltonian nature of the flow has a number of consequences for the map $(\underline{q}, \underline{A}) \leftrightarrow (\underline{x}, \underline{v})$. If we define 6-vectors $\overline{w} \equiv (\underline{q}, \underline{A})$ and $\overline{W} \equiv (\underline{x}, \underline{v})$, then the 6-tensors

$$\overline{\overline{D}} \equiv \frac{\partial \overline{W}}{\partial \overline{w}} \quad \text{and} \quad \overline{\overline{D'}} \equiv \frac{\partial \overline{w}}{\partial \overline{W}}$$

satisfy the relations

$$\overline{\overline{D}}\ \overline{\overline{D'}} = \overline{\overline{D'}}\ \overline{\overline{D}} = \overline{\overline{I}}, \quad \det(\overline{\overline{D}}) = \det(\overline{\overline{D'}}) = 1. \tag{6.6}$$

The first relation merely states that the backward transformation reverses the forward transformation, so the matrix corresponding to the former is the inverse of that corresponding to the latter. The second relation states that both matrices have unit determinant so that the transformations are volume- and orientation-preserving. The conservation of phase-space density expressed by the collisionless Boltzmann equation is a consequence of this second property. Further important properties follow from the fact that these matrices are symplectic. In particular, the velocity and space parts of the forward and backward transformations are related by

$$\frac{\partial \underline{x}}{\partial \underline{q}} = \frac{\partial \underline{A}}{\partial \underline{v}}, \ \frac{\partial \underline{x}}{\partial \underline{A}} = -\frac{\partial \underline{q}}{\partial \underline{v}}, \ \frac{\partial \underline{v}}{\partial \underline{q}} = -\frac{\partial \underline{A}}{\partial \underline{x}}, \ \frac{\partial \underline{v}}{\partial \underline{A}} = \frac{\partial \underline{q}}{\partial \underline{x}}, \tag{6.7}$$

where in each equation the partial derivative on the l.h.s. refers to the forward map so that the independent variables are $\underline{q}$ and $\underline{A}$, while the partial derivative on the r.h.s. refers to the reverse map so that the independent variables are $\underline{x}$ and $\underline{v}$. We will use some of these relations later.

6.4 Variation of the 3-density along particle trajectories

The differential annihilation probability for an individual dark matter particle depends on the (velocity-dependent) annihilation cross-section $\sigma_A(v)$ and the local phase-space distribution as

$$\frac{\mathrm{d}P}{\mathrm{d}t}(\underline{x},\underline{v},t) = \int d^3v' f(\underline{x},\underline{v}',t)\sigma_A\left(|\underline{v}'-\underline{v}|\right)|\underline{v}'-\underline{v}|. \tag{6.8}$$

In the following we will assume that $\sigma_A(v) \propto 1/v$ as is the case for many (but not all) dark matter candidates. This relation then simplifies to

$$\frac{\mathrm{d}P}{\mathrm{d}t}(\underline{x},\underline{v},t) = \langle\sigma_A v\rangle \int d^3v' f(\underline{x},\underline{v}',t) = \frac{\langle\sigma_A v\rangle}{m_p}\,\rho(\underline{x},t), \tag{6.9}$$

where $\rho(\underline{x},t)$ is the local 3-space mass density of dark matter and $\langle\sigma_A v\rangle$ is the thermally averaged velocity-weighted annihilation cross-section. The total annihilation probability over a finite time interval is thus simply obtained by integrating the local dark matter 3-density along the particle trajectory. This density is made up of two distinct components, one due to particles which are part of the same stream as the particle in question, and so were its neighbours in the initial conditions, and one due to particles in other streams, which typically originated in distant parts of phase-space. Caustics arise in the first of these two components and so we will concentrate on it in the following.

For our assumed initial condition, each particle can be specified by its initial phase-space position $(\underline{q}_p, \underline{A}_p)$, where $|\underline{A}_p| \sim \sigma$ is very small. The subscript p here identifies that the coordinates belong to the specific particle under consideration; it has nothing to do with the initial phase-space coordinate $\underline{p}$. The particle's later trajectory is then $\underline{x}_p(t) = \underline{x}(\underline{q}_p, \underline{A}_p, t)$, $\underline{v}_p(t) = \underline{v}(\underline{q}_p, \underline{A}_p, t)$, and the 3-space stream density at its position can be obtained by integrating the phase-space density over all velocities:

$$\rho_s(\underline{x}_p(t)) = \frac{f_0 m_p}{(2\pi\sigma^2)^{3/2}} \int \mathrm{d}^3v\, \exp\left(-\frac{|\underline{A}\left(\underline{x}_p,\underline{v},t\right)|^2}{2\sigma^2}\right). \tag{6.10}$$

The velocity integral is restricted to velocities such that $\underline{q}\left(\underline{x}_p,\underline{v},t\right)$ remains in the neighborhood of $\underline{q}_p$. Since σ is very small, we can simplify by carrying out a Taylor expansion of $\underline{A}\left(\underline{x}_p,\underline{v},t\right)$ around $\underline{v} = \underline{v}_p$,

$$\underline{A}\left(\underline{x}_p,\underline{v},t\right) = \underline{A}_p + \delta\underline{v}\frac{\partial\underline{A}}{\partial\underline{v}} + \frac{1}{2}\delta\underline{v}\frac{\partial^2\underline{A}}{\partial\underline{v}^2}\delta\underline{v}^T, \tag{6.11}$$

where $\delta\underline{v} = \underline{v} - \underline{v}_p$ and the partial derivatives are evaluated at $(\underline{x}_p, \underline{v}_p)$.

Densities at regular points

At almost all points of the particle's trajectory the linear map in the second term on the r.h.s. of Eq. (6.11) is non-singular (i.e. the determinant of the corresponding matrix is non-zero). These will be called "regular points" of the trajectory in the following. At such

points there exists a small value of $\delta\underline{v}$, say $\delta\underline{v}_c$, for which the sum of the first two terms vanishes; $(\underline{x}_p, \underline{v}_p + \delta\underline{v}_c)$ is then the intersection at time t of $\underline{x} = \underline{x}_p$ with the central sheet of the stream to which our particle belongs. The integral for $\rho_s(\underline{x}_p)$ becomes particularly simple if we centre the velocity integration on this point. To lowest order, we have

$$|\underline{A}|^2 = \delta\underline{v}' \frac{\partial \underline{A}}{\partial \underline{v}} \left(\frac{\partial \underline{A}}{\partial \underline{v}} \right)^T \delta\underline{v}'^T, \tag{6.12}$$

where $\delta\underline{v}' = \underline{v} - \underline{v}_p - \delta\underline{v}_c$. The tensor product $(\partial\underline{A}/\partial\underline{v})(\partial\underline{A}/\partial\underline{v})^T$ is clearly symmetric and must have positive eigenvalues. Without loss of generality, let us define the principal axes in velocity space so that these eigenvalues are $s_1^2 \geq s_2^2 \geq s_3^2 > 0$. The condition that our point be regular forces the final strict inequality, since an obvious consequence of Eq. (6.12) is

$$\det\left(\frac{\partial \underline{A}}{\partial \underline{v}} \right) = s_1 s_2 s_3. \tag{6.13}$$

In this velocity frame the integral in Eq. (6.10) takes a simple form which we can easily evaluate,

$$\begin{aligned} \rho_s(\underline{x}_p(t)) &= \frac{f_0 m_p}{(2\pi\sigma^2)^{3/2}} \int \mathrm{d}^3 v \, \exp\left(-\frac{1}{2\sigma^2} \sum_{i=1}^{3} s_i^2 \delta v_i'^2 \right) \\ &= \frac{f_0 m_p}{|s_1 s_2 s_3|} = f_0 m_p \left| \det\left(\frac{\partial \underline{A}}{\partial \underline{v}} \right) \right|^{-1} \\ &= f_0 m_p \left| \det\left(\frac{\partial \underline{x}}{\partial \underline{q}} \right) \right|^{-1}. \end{aligned} \tag{6.14}$$

The last equality follows from one of the relations listed in Eq. (6.7) and demonstrates explicitly that the stream density obtained here is identical to that obtained by forward integration of the geodesic deviation equation in Helmi and White (1999) and the previous chapter. This is a manifestation of the fact that the local velocity distribution in a stream is distorted in a way which exactly mirrors that of the density field. To lowest order, the map rotates each infinitesimal Lagrangian volume and then stretches it by different amounts s_1, s_2 and s_3 along three orthogonal axes. The (initially isotropic) velocity distribution at the central point is compressed by these same factors along the same set of axes.

Densities at caustic crossing

As a particle moves along its trajectory, it will occasionally pass through discrete points where the determinant of $\partial\underline{A}/\partial\underline{v}$ vanishes and the corresponding linear map becomes singular. At such points at least one of the stretch factors must vanish, and Eq. (6.14) predicts an infinite stream density. These points are the caustics of the map. In the following we will neglect higher order singularities, where two or more stretch factors vanish, and assume $s_1^2 \geq s_2^2 > 0, s_3^2 = 0$ at such caustic crossings (see Tremaine, 1999, for discussion of higher order singularities).

To simplify the integral in Eq. (6.10) it is useful to take coordinates in $\underline{v}$-space along

the principal axes of $(\partial \underline{A}/\partial \underline{v})(\partial \underline{A}/\partial \underline{v})^T$. Unit vectors along the axes corresponding to s_1^2 and s_2^2 are rotated into a pair of orthogonal vectors in $\underline{A}$-space by the linear map $\partial \underline{A}/\partial \underline{v}$, and in addition are stretched by factors s_1 and s_2. We use these rotated directions to define our 1 and 2 axes in $\underline{A}$-space. All $\underline{v}$-vectors are then projected onto the 1-2 plane in $\underline{A}$-space. To lowest order, Eq. (6.11) becomes

$$\begin{aligned} \underline{A}(\underline{x}_p, \underline{v}, t) &= s_1\ \delta v_1'\ \underline{e}_1 + s_2\ \delta v_2'\ \underline{e}_2 \\ &+ \left(A_{p,3} + s_3\ \delta v_3 + \frac{1}{2}\ \frac{\partial^2 A_3}{\partial v_3^2}\ {\delta v_3}^2 \right) \underline{e}_3, \end{aligned} \tag{6.15}$$

where the $\underline{e}_i$ are unit vectors along the coordinate directions in $\underline{A}$-space. We have shifted the origin in $\underline{v}$-space in order to simplify the coefficients of $\underline{e}_1$ and $\underline{e}_2$. By allowing the shift to depend on δv_3, all terms independent of δv_1 and δv_2 can be removed; remaining second-order terms are then small compared to the linear term which is retained. A similar manipulation is not possible for the coefficient of $\underline{e}_3$ because its linear term vanishes at caustic crossing (i.e. $s_3 = 0$ when $t = t_c$) and we must retain both constant and quadratic terms. Note that the only quadratic term we need to retain is that involving δv_3 alone, since all others are subdominant to the linear terms involving $\delta v_1'$ and $\delta v_2'$ or are removed by the origin shift made for each value of δv_3. Inserting this expression into Eq. (6.10) and setting $s_3 = 0$ (i.e. $t = t_c$), the integrals over v_1 and v_2 can be carried out as before and we are left with

$$\begin{aligned} \rho_s(\underline{x}_p(t_c)) &= \frac{f_0 m_p}{|s_1 s_2|}\ \frac{1}{(2\pi\sigma^2)^{1/2}} \\ &\times \int_{-\infty}^{+\infty} \mathrm{d}v_3\ \exp\left(-\frac{1}{2\sigma^2} \left(A_{p,3} + \frac{1}{2}\ \frac{\partial^2 A_3}{\partial v_3^2}\ {\delta v_3}^2 \right)^2 \right) \\ &= \frac{f_0 m_p}{|s_1 s_2|}\ \frac{\Gamma'\left(\pm |A_{p,3}|/\sigma\right)}{|\sigma \partial^2 A_3/\partial v_3^2|^{1/2}}\ \exp(-A_{p,3}^2/2\sigma^2) \end{aligned} \tag{6.16}$$

where the dimensionless function Γ' is of order unity and is defined by

$$\Gamma'(X) = \frac{1}{(2\pi)^{1/2}} \int_{-\infty}^{+\infty} \mathrm{d}y\ \exp\left(X^2/2 - (X + y^2/2)^2/2 \right). \tag{6.17}$$

The sign of the argument of Γ' in Eq. (6.16) is positive when $A_{p,3}$ and $\partial^2 A_3/\partial v_3^2$ have the same sign and negative otherwise. Note that Γ' can be expressed in terms of a modified Bessel function, but we forgo the details here.

As before, the mass density at the particle's position is related to the initial density $f_0 m_p$ by the product of three dilution/compression factors. The factors associated with the two axes in the plane of the caustic correspond to those we obtained above for regular points of the trajectory; caustic formation does not significantly effect the distortion of the dark matter distribution in directions parallel to the caustic. The compression/dilution in the direction perpendicular to the caustic is of different form, depending explicitly on how cold the initial conditions were (i.e. on the value of σ) and on how close the

particle is to the central sheet of its stream (i.e. on the value of $A_{p,3}/\sigma$), as well as on the overall structure of the Hamiltonian flow, as encapsulated by the second derivative, $\partial^2 A_3/\partial v_3^2(\underline{x}_p, \underline{v}_p, t_c)$. Note that as the initial conditions are made colder, the maximum density achieved during caustic passage increases as $\sigma^{-1/2}$.

For particles which lie away from the central sheet of the stream, $A_{p,3}$ is non-zero. If $A_{p,3}$ and $\partial^2 A_3/\partial v_3^2$ have the same sign, the maximum of $\rho_s(\underline{x}_p(t))$ then occurs either slightly before or slightly after t_c. This is because a small but non-zero value of s_3 allows the linear term in the coefficient of $\underline{e}_3$ in Eq. (6.15) to be significant. For one particular s_3 the resulting quadratic has an extremum at $A_3 = 0$. This value of s_3 obtains at the moment when our particle is spatially coincident with the caustic of the central sheet of its stream, and so sees the corresponding density (see Fig. 6.1). The exact value of the maximum density is not important in practice, since it appears only in the argument of a logarithm when we estimate the total annihilation radiation from caustic passages. For simplicity, we will set $A_{p,3} = 0$ when we use Eq. (6.16) below to estimate the maximum density during a caustic passage. In this case, Γ' can be expressed in terms of the standard complete Γ-function, $\Gamma'(0) = 2^{5/4}\Gamma(5/4)/\sqrt{\pi}$.

Integrating annihilation rates through caustics

The formalism developed above is particularly powerful when embedded in a high-resolution simulation of cosmic structure formation. In the previous chapter we showed how the geodesic deviation equation can be integrated in parallel with the N-body equations of motion to give the full phase-space distortion tensor $\overline{\overline{D}}$ along the trajectory of each simulation particle. This is then sufficient (through Eq. (6.7)) to give all the first order derivatives of the forward and backward Hamiltonian maps we have been discussing. In particular, this allows the local stream density to be calculated at all regular points of each trajectory using Eq. (6.14), and this can be inserted into Eq. (6.9) to obtain the intra-stream annihilation rate at such points.

Caustic crossings can be recognised in an N-body integration by the change in sign of the determinant of $\partial\underline{x}/\partial\underline{q}$. Let us denote by (s_1, s_2, s_3) and (s_1', s_2', s_3') the stretch factors at the beginning and end of a timestep during which a caustic crossing is detected. Then $s_1 \approx s_1'$ and $s_2 \approx s_2'$, while s_3 and s_3' should be much smaller in absolute magnitude and should have opposite sign. A good approximation to the evolution of the distortion tensor during the timestep is then obtained by assigning mean values to s_1 and s_2 and assuming s_3 to vary linearly between its endpoint values. According to the arguments of Section 2, the maximum value of ρ_s during the timestep is then well approximated as

$$\rho_{\max} = \frac{2^{5/4}\Gamma(5/4)\ f_0 m_p}{\sqrt{\pi}\ |\bar{s_1}\bar{s_2}|\ |\sigma\partial^2 A_3/\partial v_3^2|^{1/2}}. \tag{6.18}$$

Away from caustic crossing (but still within the timestep) Eq. (6.14) can be used to obtain ρ_s which then varies inversely with s_3 and so with $|t - t_c|$, the time to caustic crossing. This suggests the following approximation to the variation of stream density within the timestep:

$$\rho_s(\underline{x}_p(t)) = \frac{f_0 m_p\ \Delta t}{|\bar{s_1}\bar{s_2}|\ |s_3 - s_3'|} \quad \left((t - t_c)^2 + T^2\right)^{-1/2}, \tag{6.19}$$

where Δt is the length of the timestep and T is chosen so that $\rho_s(\underline{x}_p(t_c)) = \rho_{\max}$. The shape of this function in the neighborhood of its maximum is chosen purely for convenience, but the wings and the maximum value itself are correct. If we integrate Eq. (6.9) over the timestep using this formula we obtain

$$\Delta P = \frac{\langle \sigma_A v \rangle \ f_0 \ \Delta t}{|\bar{s_1}\bar{s_2}| \ |s_3 - s_3'|} \ \ln\left(\frac{2^{9/2}\Gamma(5/4)^2 |s_3 s_3'|}{\pi\sigma|\partial^2 A_3/\partial v_3^2|}\right), \tag{6.20}$$

where we have used the fact that $T \ll \Delta t$ and, for simplicity, we have assumed that the caustic occurs well away from either end of the timestep. Since a single simulation particle represents many dark matter particles, ΔP must be multiplied by $m_{\rm sim}/m_p$ (where $m_{\rm sim}$ is the simulation particle mass) to obtain the total number of annihilation events.

The properties of the dark matter appear in Eq. (6.20) through the annihilation cross-section, and through the parameter σ which appears in the argument of the logarithm. Thus we recover the result of Hogan (2001) that in the cold limit the annihilation luminosity of a caustic is logarithmically divergent. For given particle physics parameters, an integration of the N-body and geodesic deviation equations provides all the quantities needed to calculate ΔP for each caustic passage, with the important exception of the second derivative $\partial^2 A_3/\partial v_3^2$. Since this quantity appears only in the argument of the logarithm, it is sufficient to estimate it to order of magnitude, provided the estimator chosen has no strong bias when averaged over many caustic passages.

The condition for caustic passage, $\det(\partial \underline{A}/\partial \underline{v}) = 0$ places no constraint on the values of the second derivatives, so we can estimate the size of a typical component of $\partial^2 \underline{A}/\partial \underline{v}^2$ from the available Galilean-invariant quantities. These are the components of the 6-dimensional distortion tensor $\overline{\overline{D}}$ and the particle acceleration $\underline{a}$. For example, we can note that $\underline{a}(\partial^2 \underline{A}/\partial \underline{v}^2)(\partial \underline{x}/\partial \underline{A})$ is dimensionless and is expected to be of order unity, so that the size of our desired component of the second derivative can be estimated as the inverse of the product of the r.m.s. sizes of the components of $\underline{a}$ and of the components of $\partial \underline{x}/\partial \underline{A}$. This assumption can be checked in simple 1-dimensional cases, and we will give an example based on the similarity solution for spherical collisionless collapse in the next chapter. In this case, at least, the estimate we advocate here works remarkably well.

6.5 Conclusion and Discussion

In this chapter we have developed the mathematical background to enable a relatively precise evaluation of the annihilation radiation from dark matter caustics in fully general simulations of the nonlinear growth of structure. Our scheme allows the annihilation rate to be integrated along the trajectory of each simulation particle, including correctly the contributions from all the caustics in which it participates. Typically each particle experiences several such caustic passages in each orbit around the dark matter halo in which it resides as we demonstrated in the previous chapter. In order to include correctly the annihilation rate between particles which are members of different streams, it is necessary to estimate a local coarse-grained density at the position of each particle, and to add in the contribution due to streams other than its own. This can be done, for example, using the SPH technique, since the smoothing this introduces does not bias the luminos-

ity predicted from inter-stream annihilations. When a particle passes through a caustic occurring in a stream other than its own, the time-integrated annihilation probability is still correctly reproduced in the smoothed system.

By implementing these methods in high-resolution simulations of galaxy formation it should be possible to achieve a complete numerical description of the expected annihilation radiation, limited only by the ability to resolve the smallest collapsed clumps of dark matter. This latter limitation can be severe when attempting to predict the total annihilation radiation from a representative cosmological volume. For a standard supersymmetric neutralino, for example, the emission should be dominated by the smallest collapsed objects, with masses well below that of the Sun (e.g. Taylor and Silk, 2003). Recent work has shown, however, that this problem is much less severe when predicting the observability of annihilation radiation from the Solar System, which lies just 8 kpc from the centre of the Milky Way (Springel et al., 2008b). According to these authors, less than 3 percent of the dark matter within 100 kpc of the Galactic Centre should be in small lumps; almost all the rest should be in extended streams of the kind discussed in this paper (see also Helmi and White, 1999). They argue that the highest signal-to-noise for detecting the annihilation signal will be that of the smooth dark matter distribution in the inner few kiloparsecs of the Galaxy; small subhaloes will be significantly more difficult to detect. Application of the techniques we have presented here should allow a rigorous evaluation of an important and previously unresolved issue: whether the emission structure of this smooth component is significantly modified by caustic emission. In addition, they will allow an assessment of the expected morphology and observability of outer caustics around external galaxies, most notably the Andromeda nebula.

7

Caustics in growing Cold Dark Matter Haloes

In the previous two chapters we presented methods to access the fine-grained phase-space structure of cold dark matter haloes. In this chapter we apply these methods and simulate the growth of isolated dark matter haloes from self-similar and spherically symmetric initial conditions. Our N-body code integrates the geodesic deviation equation in order to track the streams and caustics associated with individual simulation particles. The radial orbit instability causes our haloes to develop major-to-minor axis ratios approaching 10 to 1 in their inner regions. They grow similarly in time and have similar density profiles to the spherical similarity solution, but their detailed structure is very different. The higher dimensionality of the orbits causes their stream and caustic densities to drop much more rapidly than in the similarity solution. This results in a corresponding increase in the number of streams at each point. At 1% of the turnaround radius (corresponding roughly to the Sun's position in the Milky Way) we find of order 10^6 streams in our simulations, as compared to 10^2 in the similarity solution. The number of caustics in the inner halo increases by a factor of several, because a typical orbit has six turning points rather than one, but caustic densities drop by a much larger factor. This reduces the caustic contribution to the annihilation radiation. For the region between 1% and 50% of the turnaround radius, this is 4% of the total in our simulated haloes, as compared to 6.5% in the similarity solution. Caustics contribute much less at smaller radii. These numbers assume a 100 GeV c^{-2} neutralino with present-day velocity dispersion 0.03 cm s^{-1}, but reducing the dispersion by ten orders of magnitude only doubles the caustic luminosity. We conclude that caustics will be unobservable in the inner parts of haloes. Only the outermost caustic might potentially be detectable. [1]

[1] published in Vogelsberger et al, MNRAS (in print)

7.1 Introduction

Dark matter is thought to consist of weakly interacting particles that are cold, meaning that their thermal velocities in unclustered regions of the present Universe are very small. For example, for standard values of the relevant cross-sections, a neutralino with a mass of 100 GeV c^{-2} is predicted to have a velocity dispersion of just 0.03 cm/s in such regions, corresponding to a very high phase-space density. Since the particles are collisionless, this phase-space density is conserved along particle trajectories, and the nonlinear collapse of dark haloes gives rise to caustics. For infinitely cold dark matter, the density is formally infinite at caustics, because the particles occupy a three-dimensional "sheet" in six-dimensional phase-space and projection of this sheet onto configuration space leads to singularities. These singularities are regularised in realistic cases by the small but finite velocity dispersion of the dark matter particles. These caustics were first discussed by Arnold et al. (1982) and Zel'dovich et al. (1983) for the case of a neutrino-dominated Universe. Their properties were worked out in simple, one-dimensional similarity solutions for the growth of spherical haloes by Fillmore and Goldreich (1984) (FG hereafter) and Bertschinger (1985).

It has been suggested that caustics might have an impact on various observables, in particular gravitational lensing (e.g. Gavazzi et al., 2006) or annihilation radiation (e.g. Hogan, 2001; Mohayaee et al., 2007; Mohayaee and Salati, 2008). Over the last 10 years most studies of the properties of caustics have been based on spherical models for self-similar infall such as those of FG and Bertschinger (1985), or extensions where angular momentum is introduced ad hoc to avoid purely radial orbits (White and Zaritsky, 1992; Sikivie et al., 1995; Nusser, 2001; Natarajan and Sikivie, 2006; Natarajan, 2007; Sikivie, 1998). As we will see below, the original similarity solutions are violently unstable to the radial orbit instability (ROI) (Antonov, 1973). Exact density profiles for dark matter caustics were first calculated for the FG model by Mohayaee and Shandarin (2006) (MS hereafter) following an approach originally developed by Zeldovich and Shandarin (1982) and Kotok and Shandarin (1987). In contrast, Hogan (2001) discussed the effect of caustics on annihilation radiation using general arguments which avoid simplified halo models, estimating that caustics might boost the annihilation luminosity by a factor ~ 5 in the outer halo, a significantly larger factor than found by MS for the spherical similarity solution.

Although very large simulations of the formation of dark haloes are now feasible (e.g. Diemand et al., 2008; Springel et al., 2008a; Zemp et al., 2009), it is still not possible to resolve caustics using standard N-body techniques. Here we use the geodesic deviation equation (GDE) formalism together with a rigorous treatment of caustic passages derived in the last two chapter to follow the evolution of caustics in fully three-dimensional simulations of halo formation. For simplicity, we start from self-similar, spherical initial conditions, but the ROI causes our simulated haloes to develop into highly elongated bars with a detailed structure quite different from that of the spherical similarity solution. This has substantial implications for the number of dark matter streams predicted near the Sun and for the importance of annihilation radiation from caustics.

The plan of this chapter is as follows. In section 2 we describe our initial conditions and the numerical techniques used for our simulations. In section 3 we demonstrate that our

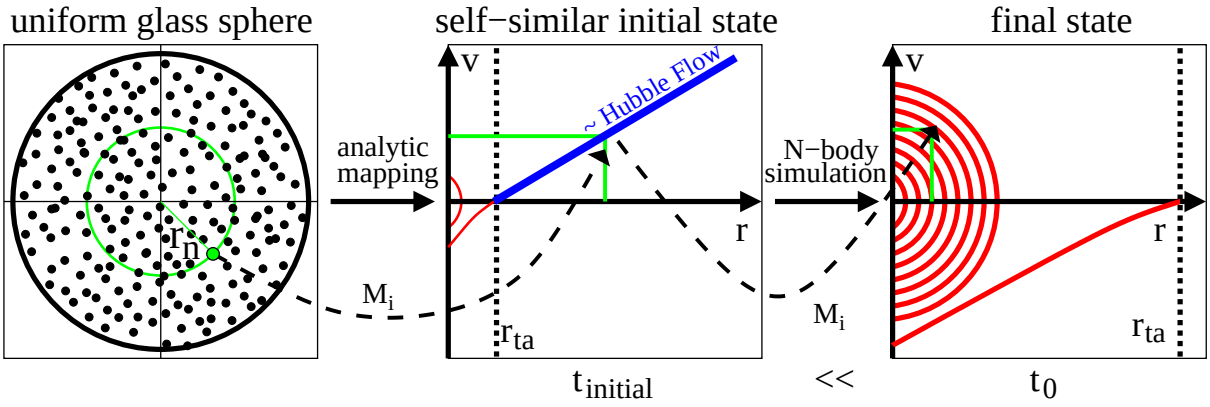

Figure 7.1: Schematic construction of the self-similar initial conditions used throughout the chapter. We map a gravitational glass to a self-similar initial state at time $t_{\rm initial}$. At that time nearly all particles are in the linear regime (Hubble Flow). We put these initial state into our N-body simulation and let it evolve to time t_0. The mapping is provided by the similarity solution and parametrised by the enclosed mass M_i of the particles. This is demonstrated for one particle.

N-body implementation is working correctly by solving a simple spherical test problem. In section 4 we discuss results from our three-dimensional simulations, contrasting them with the predictions of the similarity solution. We begin with the shape and the density and velocity dispersion profiles, and we move on to fine-grained phase-space structure and the caustic annihilation rate. We give our conclusions in section 5.

7.2 Numerical techniques

Initial conditions

We start our simulations from self-similar initial conditions, where most of the particles are in the linear regime, i.e. well beyond the initial turnaround radius. The similarity solutions assume an EdS Universe in which the linear mass perturbation δM_i within a sphere containing unperturbed mass M_i, when extrapolated to the initial time $t_{\rm initial}$, satisfies $\delta M_i/M_i = 1.0624(M_i/M_0)^{-\epsilon}$, where ϵ is a scaling index and M_0 is a reference mass taken to be the mass within the turnaround radius at the initial time. The equations of motion for a particle with radial distance r and radial velocity v can then be cast into similarity form by introducing the variables $\lambda = r/r_{\rm ta}$ and $\tau = t/t_{\rm ta}$, where $r_{\rm ta} \propto M_i^{1/3+\epsilon}$ and $t_{\rm ta} \propto M_i^{3\epsilon/2}$ are the turnaround radius and turnaround time of the particle under consideration. The solution $\lambda(\tau)$ of the resulting equation then fully describes the phase-space structure of the halo at all times (see the Appendix B and FG for more details on these similarity solutions). Note that the turnaround radius $r_{\rm ta}$ can be viewed either as a function of enclosed mass, as here, or as a function of time, as will often be the case in the following.

We set up our initial conditions in the following way. As a first step we create a uniform gravitational glass within a cubic box with periodic boundary conditions (White

1996). We then cut out the largest sphere contained within the box and use it to represent an unperturbed EdS Universe[2]. We construct similarity initial conditions at time $t_{\rm initial}$ by mapping this uniform distribution $\underline{r}_{\rm glass}$ to the desired initial state by scaling the radial coordinate and setting velocities according to the similarity solution $\lambda(\tau)$

$$\begin{aligned}\underline{x}(t_{\rm initial}) &= r_{\rm ta}(M_0)\ \frac{\lambda(\tau)}{\tau^{2/3+2/(9\epsilon)}}\ \frac{\underline{r}_{\rm glass}}{r_{\rm glass}},\\ \underline{v}(t_{\rm initial}) &= \frac{r_{\rm ta}(M_0)}{t_{\rm initial}}\ \frac{{\rm d}\lambda/{\rm d}\tau}{\tau^{-1/3+2/(9\epsilon)}}\ \frac{\underline{r}_{\rm glass}}{r_{\rm glass}},\end{aligned} \tag{7.1}$$

where the similarity time variable τ is determined from the enclosed mass according to $\tau = (M_i/M_0)^{-3\epsilon/2}$.

We run our simulations from $t_{\rm initial}$ to $t_0 = 2/(3\ H_0) \cong 9.1$ Gyr, where we adopt $H_0 = 72$ km s^{-1} Mpc^{-1} as the Hubble constant today. If we require that the turnaround of the bounding sphere occurs at t_0, choosing the scaling index ϵ and the mass fraction $M_0/M_{\rm tot}$ within the initial turnaround radius determines the initial time as $t_{\rm initial} = t_0(M_0/M_{\rm tot})^{3\epsilon/2}$ and defines a unique mapping from the uniform spherical glass to the similarity solution at $t_{\rm initial}$. In the following we will always use this kind of initial conditions.

Simulation code

For our simulations we adapt the GADGET-3 code that was developed originally for the Aquarius project (Springel et al., 2008a). We apply vacuum boundary conditions, use (unless otherwise noted) a spline softening kernel with constant smoothing length in comoving coordinates ($\propto t^{2/3}$ in an EdS Universe), and run our simulations in physical coordinates. We modified the code to integrate the GDE as described in the fifth chapter and to track radiation from each particle due to annihilations within its own fine-grained phase-space stream, as described in the sixth chapter. This automatically accounts for the enhanced radiation as particles pass through caustics. We set the GADGET force accuracy parameter to 10^{-4} and chose a time integration accuracy of 10^{-3} (see Springel, 2005, for the significance of these terms). We checked that these settings are sufficient to produce reliable results.

To gain performance and accuracy we integrate the GDE directly for each particle only after it has passed through turnaround. At turnaround all variables related to the fine-grained phase-space density are set to the values predicted by the analytic FG solution. We implement this by checking in each drift operation whether a given particle is currently turning around and initialising the integration of the phase-space distortion tensor when this is the case. We demonstrate below that using the analytic solution until turnaround is well-justified. As a particle turns around at $t_{\rm ta}$, its phase-space distortion tensor is set to unity and its stream density, i.e. the local 3-density of the particular stream in which it lives, is set to the dark matter density of the similarity solution at the turnaround point $\rho_0 = 9\pi^2/(16(3\epsilon+1))\ \rho_{\rm b}(t_{\rm ta})$, where $\rho_{\rm b}(t_{\rm ta}) = 1/(6\pi G t_{\rm ta}^2)$ is the mean density of the EdS background at time $t_{\rm ta}$. The (fine-grained) dark matter velocity dispersion σ_0 at that time and position can be calculated using conservation of

[2]Note that this cut means that a cubic glass with N^3 particles will produce a sphere with $N^3/(6/\pi) \cong N^3/2$ particles. In the following we will always specify the resolution of our simulations by giving the number of particles in the original cube.

phase-space density $\rho_0/\sigma_0^3 = \rho_{\rm b}(t_0)/\sigma_{\rm b}(t_0)^3$, where $\sigma_{\rm b}(t_0)$ is the dark matter velocity dispersion predicted for unclustered matter today. For a neutralino of mass m_p we have $\sigma_{\rm b}(t_0) \sim 10^{-11}{\rm c}\ ({\rm GeV\ c^{-2}}/m_p)^{1/2}$. Unless otherwise noted, we will assume a 100 GeV c^{-2} neutralino, resulting in $\sigma_{\rm b}(t_0) = 0.03$ cm/s. Finally, the sheet orientation at turnaround is set to

$$V_{q,ij} = \frac{{\rm d}V_i(q)}{{\rm d}q_j} = \frac{x_i x_j}{r^2}\left(\frac{3\pi}{4}\right)^2 \frac{1}{3+1/\epsilon}\frac{1}{t_{\rm ta}}, \tag{7.2}$$

where $V_i(q)$ are the three components of the initial cold dark matter sheet (see chapters 5 and 6). All GDE simulations presented in this chapter have the fine-grained phase-space quantities initialised for each particle at turnaround in this way.

7.3 Results

Embedded 1D tests

To test the GDE implementation in GADGET-3 it is desirable to have a system where we can analytically evaluate the fine-grained phase-space structure. This is straightforward for the FG similarity solution (see the Appendix B for details). Starting with the initial conditions described above we might expect to be able to reproduce the similarity solution with our code. This is not possible, however, because the FG solution is violently unstable to both radial and non-radial perturbations, as we show below. Although this result does not appear to have been demonstrated before for the specific case of the FG solution, it is expected given earlier work on other spherical collapse models. This has found instabilities not only in the fully 3-dimensional case where the radial orbit instability (ROI) turns the system into a highly elongated bar (e.g. Antonov, 1973; Polyachenko, 1981; Barnes, 1985; Carpintero and Muzzio, 1995; Merritt, 1999; MacMillan et al., 2006; Bellovary et al., 2008), but also in 1D (i.e. enforcing spherical symmetry and radial orbits) where the regular phase-space pattern of the similarity solution still gets destroyed (Henriksen and Widrow, 1997, 1999). These instabilities have a dramatic impact on the fine-grained phase-space structure as we will show below, so we cannot follow this route to check our standard code against the known similarity solution.

A test can nevertheless be carried out by keeping the calculation artificially stable. It turns out that the following approach works. We replaced the GADGET-3 tree-code by a shellcode, where radial forces are calculated based purely on the enclosed mass. Particles in the initial conditions then represent mass shells. This removes the degree of freedom exploited by the ROI, but does not stabilise the system against purely 1-D instabilities. To avoid the destruction of the similarity phase-space pattern, we must in addition soften quite strongly the gravitational potential. One can show that a Plummer-softening that scales with the turnaround radius still allows a similarity solution. The similarity equation is then a slight extension to the FG equation

$$\frac{{\rm d}^2\lambda}{{\rm d}\tau^2} = -\frac{2}{9}\left(\frac{3\pi}{4}\right)^2 \tau^{2/(3\epsilon)} \frac{\lambda}{(\lambda^2+(\eta\Lambda)^2)^{3/2}} \mathcal{M}\left(\frac{\lambda}{\Lambda}\right), \tag{7.3}$$

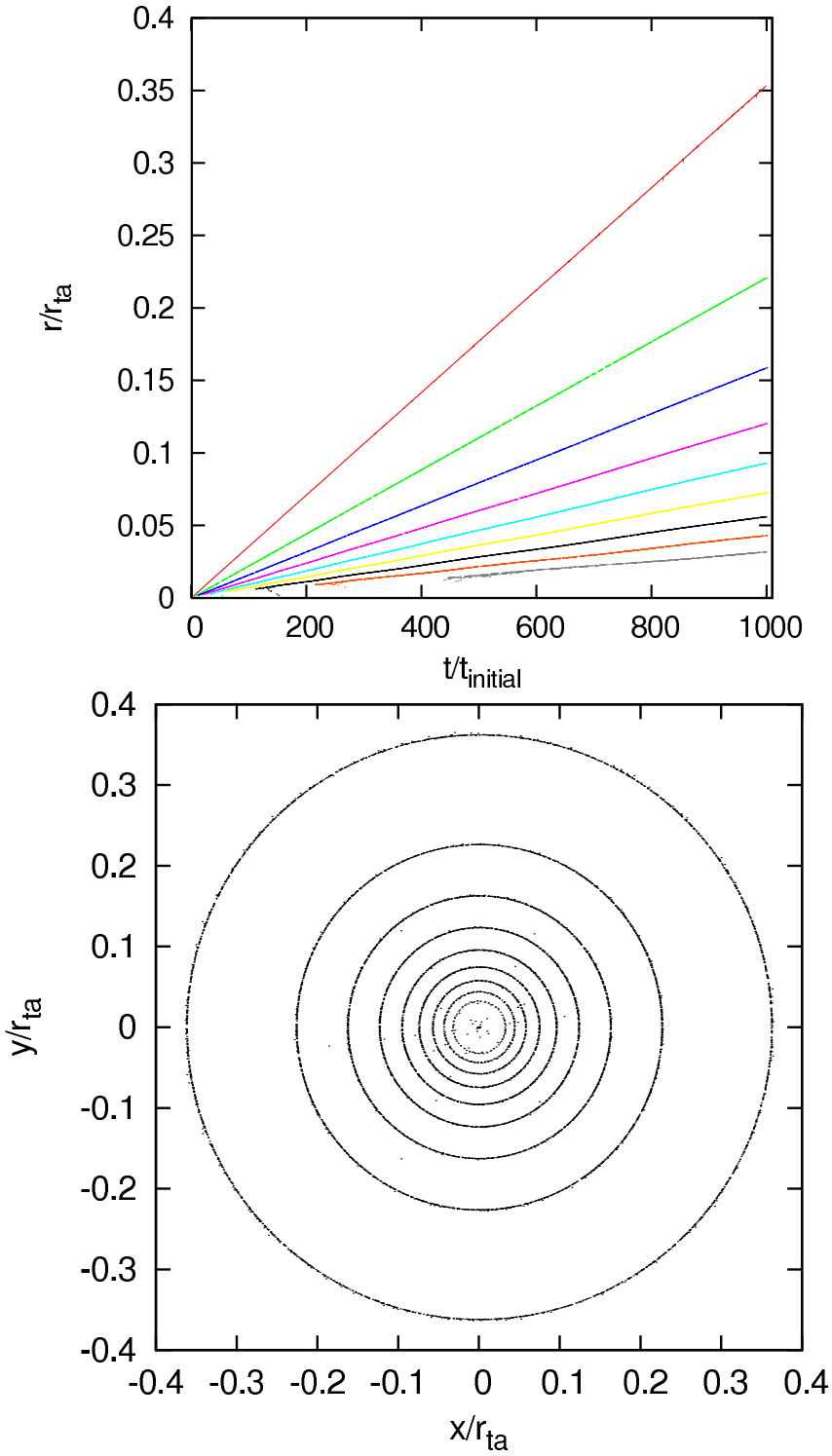

Figure 7.2: Top panel: Time evolution of the caustic radii in the softened similarity solution ($\epsilon = 2/3$, $\eta = 0.15$) simulated with a (one-dimensional) shellcode. Different colours represent different caustics from red (outermost) to grey (innermost). We note that the softened similarity equation only produces a finite number of caustics while the original FG equations produce an infinite number when approaching the halo centre. The sphere radii grow linearly in time because the turnaround radius increases linearly in time for $\epsilon = 2/3$. Bottom panel: Slice through the caustic spheres. The thickness of the slice is 0.0025 $r_{\rm ta}(t)$. We overlaid all caustics for all times using the similarity scaling. This produces exact spheres (rings in this slice). These plots demonstrate that caustics are tracked correctly over the full simulation period by our GDE method.

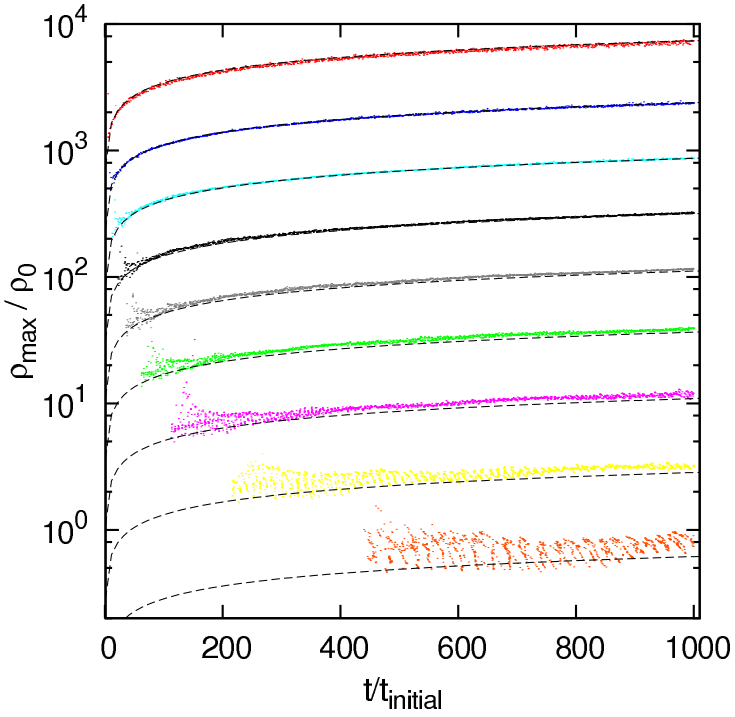

Figure 7.3: Maximum caustic densities in units of the stream density at turnaround ρ_0. Black dashed lines show maximum densities for the analytic solution. The densities increase with time, because the velocity dispersion σ_b decreases with time.

where $\mathcal{M}$ is the dimensionless enclosed mass

$$\mathcal{M}\left(\frac{\lambda}{\Lambda}\right) = \frac{2}{3\epsilon}\int_1^\infty \frac{\mathrm{d}\xi}{\xi^{1+2/(3\epsilon)}}\mathcal{H}\left[\frac{\lambda}{\Lambda} - \frac{\lambda(\xi)}{\Lambda(\xi)}\right], \tag{7.4}$$

$\mathcal{H}$ the Heaviside function, $\Lambda(\tau) = \tau^{2/3+2/(9\epsilon)}$ and η is the Plummer-softening length in units of the turnaround radius. We can solve this softened similarity equation in the same way as the original FG equation, including the parallel GDE integration as described in the Appendix B. With this setup we can check our N-body implementation by comparing the results to the analytic solution of the softened similarity equation.

The following results are based on a $N = 128^3$ simulation with this method. We have chosen $\epsilon = 2/3$, $r_{ta}(t_0) = 1400$ kpc, $t_{initial} = t_0/10^3$ and $\eta = 0.15$, where r_{ta} denotes the global turnaround radius of the halo.

Fig. 7.2 shows how well our code reproduces the caustic structure of this test problem. The top panel shows the time evolution of the caustic radii. They grow linearly in time, because the turnaround radius is proportional to t for $\epsilon = 2/3$. The different colours represent the different caustic spheres (red is the outermost sphere, green the second, and so on). We note that the softened FG equation has only a finite number of caustics for large η (nine for $\eta = 0.15$) while the original FG solution (the $\eta \to 0$ limit) produces an infinite number of caustics. The bottom panel shows a slice through the caustic spheres from a wide range of times after scaling each to its own turnaround radius. In this plot

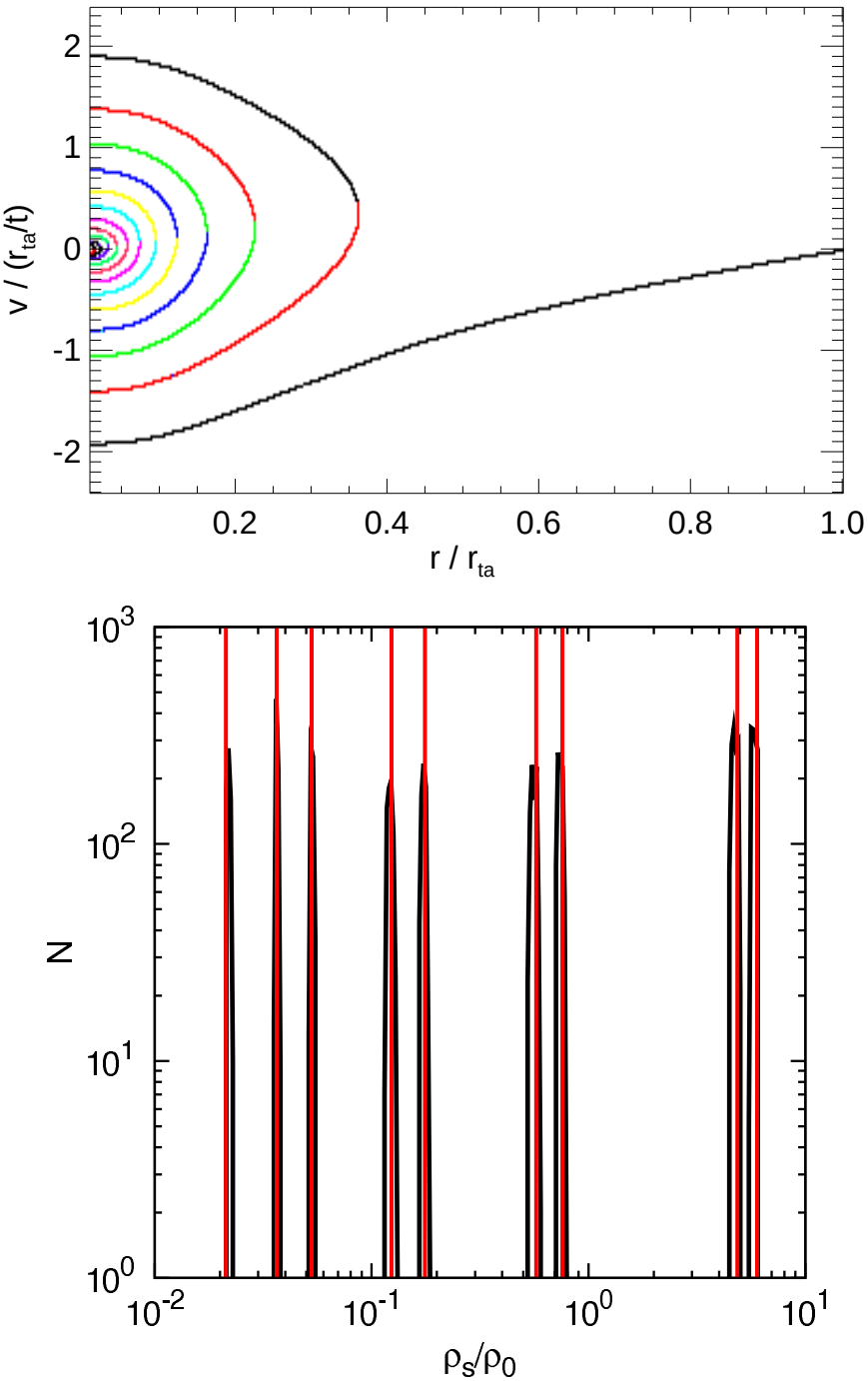

Figure 7.4: Top panel: Phase-space portrait at t_0 for the softened similarity system. The various colours indicate how many caustics each particle has passed. Infalling particles have seen no caustic (black line). They go through the centre, and move out to the first apocentre, where they pass the outermost caustic. The colour changes to red at this point and stays red until the second caustic is reached, and so on. We note that the softened similarity solution has only a finite number of caustics. This is why the phase-space is not densely occupied at low $r/r_{\rm ta}$ as in the case for the original unsoftened FG solution. Bottom panel: Densities of individual dark matter streams in the interval $r/r_{\rm ta} \in (0.1, 0.105)$. At this distance the portrait shows nine streams (the innermost stream is coloured in yellow and particles belonging to it have passed four caustics). In black we show a histogram of their densities in the GDE simulation and in red the analytically predicted stream densities. The agreement is good, demonstrating that our method can correctly recover the density of individual streams.

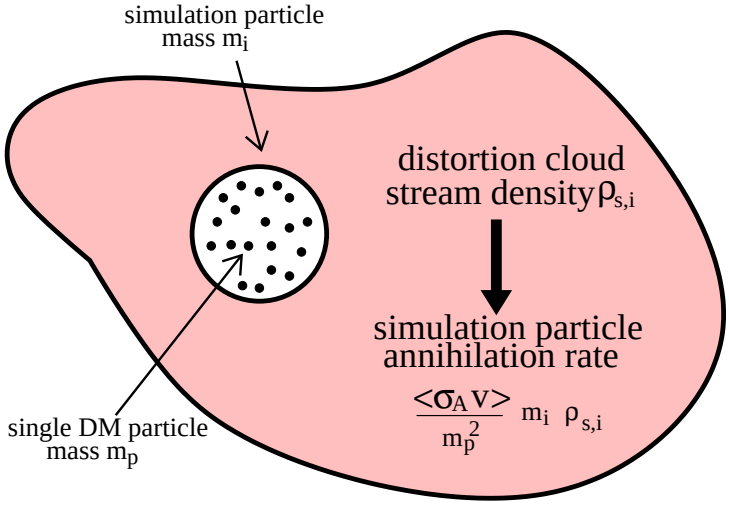

Figure 7.5: Intra-stream annihilation rate calculation with the GDE. Every DM simulation particle (mass m_i) represents m_i/m_p DM particles (mass m_p). All these particles are embedded in the same stream (distortion cloud). The density $\rho_{s,i}$ of this stream is revealed by the GDE. The intra-stream annihilation rate of the simulation particle is then given by the annihilation rate of an individual DM particle multiplied by the number of DM particles represented by the DM simulation particle.

we thus overlay the complete time evolution of the system. One can clearly see that the caustics build perfect spheres that scale exactly as expected.

The maximum densities in these caustics are shown in Fig. 7.3. The agreement of the GADGET-3 shellcode results with the analytic solution (black dashed lines) is good. The maximum density $\rho_{\rm max}/\rho_0$ is proportional to $1/\sqrt{\sigma_b(t)}$ for $\epsilon = 2/3$, and therefore increases with time due to the decrease of the velocity dispersion.

In Fig. 7.4 we focus on the density of individual fine-grained dark matter streams. We determine the density of individual streams by binning $\rho_{s,i}/\rho_{0,i}$ for all particles i in $r/r_{\rm ta} \in (0.1, 0.105)$, where $\rho_{s,i}$ is the density of the stream particle i is embedded in and $\rho_{0,i}$ is its stream density at turnaround. From the phase-space portrait Fig. 7.4 (top panel) one can see that there are 9 distinct streams in this radial interval. In the bottom panel we show the resulting stream density histogram in black. In red we overplot the analytic result for the densities of the nine streams. The agreement is good, showing that we correctly recover the density of individual streams in this system.

We will now briefly described how we calculate the intra-stream annihilation rate for each individual simulation particle, that is the annihilation rate due to encounters with other particles in its own DM stream. Each simulation particle (mass m_i) represents many dark matter particles (mass m_p). The intra-stream annihilation rate of one dark matter particle is given by $(\langle\sigma_A v\rangle/m_p)\rho_{s,i}$. Therefore, the annihilation rate of a simulation particle is given by $(\langle\sigma_A v\rangle/m_p^2)(\rho_{s,i}m_i)$. This is schematically demonstrated in Fig. 7.5. To get an estimate of the intra-stream annihilation rate, we integrate the stream density along the trajectories of all particles as the simulation is run. This yields for every particle

and at each snapshot time t_k the time-integrated rate

$$A_i(t_k) = \int_{t_{\rm initial}}^{t_k} {\rm d}t \;\; \rho_{s,i}(t), \tag{7.5}$$

where we set the particle physics prefactor $\langle \sigma_A v \rangle / m_p^2$ to unity. When passing through a caustic it is necessary to calculate the time integral analytically as described in chapter 6, since the simulation time-stepping is usually not fine enough. Based on $A_i(t_k)$ and $A_i(t_l)$ $(t_k < t_l)$ we can calculate the intra-stream annihilation rate of particle i

$$\langle P_i \rangle_{\rm intra} = m_i \; \frac{A_i(t_l) - A_i(t_k)}{\Delta t}. \tag{7.6}$$

In the following we apply this scheme to calculate the intra-stream annihilation rate of individual particles.

3D results

In this section we study halo formation from the same initial conditions as above, but with fully 3D gravity. Thus we replace the 1D shellcode of the last section with our modified version of the tree-code GADGET-3. In addition, we choose a much smaller softening. The ROI then acts with full force and the system develops a highly elongated bar in its inner regions. Our goal here is to study how this more complicated dynamical structure affects the fine-grained phase-space of the system, and what implications this has for the intra-stream annihilation rate. In the following we use a $N = 128^3$ simulation with a comoving softening length of 0.01 $r_{\rm ta}(t_0)$. We checked that our results do not depend on resolution (either particle number or softening) in any significant way.

In Fig. 7.6 we show the projected density of a slice through the centre of the halo at t_0 with a thickness of 0.25 $r_{\rm ta}(t_0)$. At this time the last simulation particles are just reaching turnaround. The blue region marks the halo beyond the outermost caustic, hence the one-stream regime. The change to red marks the region of multiple streams. The occupied region has a sharp spherical edge at $r_{\rm ta}$, showing that the influence of our vacuum boundary condition has not propagated into the inner regions of interest. We checked this explicitly with other simulations, and also by verifying that the results given below are very similar to those at $0.5t_0$ once these are scaled up according to the similarity scaling. Clearly visible in Fig. 7.6 is a strong bar produced by the ROI. To show it optimally, we have oriented our slice perpendicular to its minor axis. At the time, shown we estimate axis ratios $b/a = 0.41$ and $c/a = 0.22$ from the moment of inertia of all particles within $r_{\rm ta}$, axis ratios $b/a = 0.34$ and $c/a = 0.17$ from all particles within 0.5 $r_{\rm ta}$, and $b/a = 0.28$ and $c/a = 0.12$ from those within 0.1 $r_{\rm ta}$. These numbers are quite similar at $t = 0.5t_0$ suggesting that the system is evolving in a nearly self-similar, though non-spherical fashion.

Although the inner structure of the halo is very different from the FG model, the turnaround radius grows in time just as this model predicts. This is demonstrated in Fig. 7.7, where the dashed black line is the FG prediction for $\epsilon = 2/3$. This behaviour is expected since the growth of the turnaround radius depends on the monopole term in the halo mass distribution and this is not affected by non-spherical contributions from the

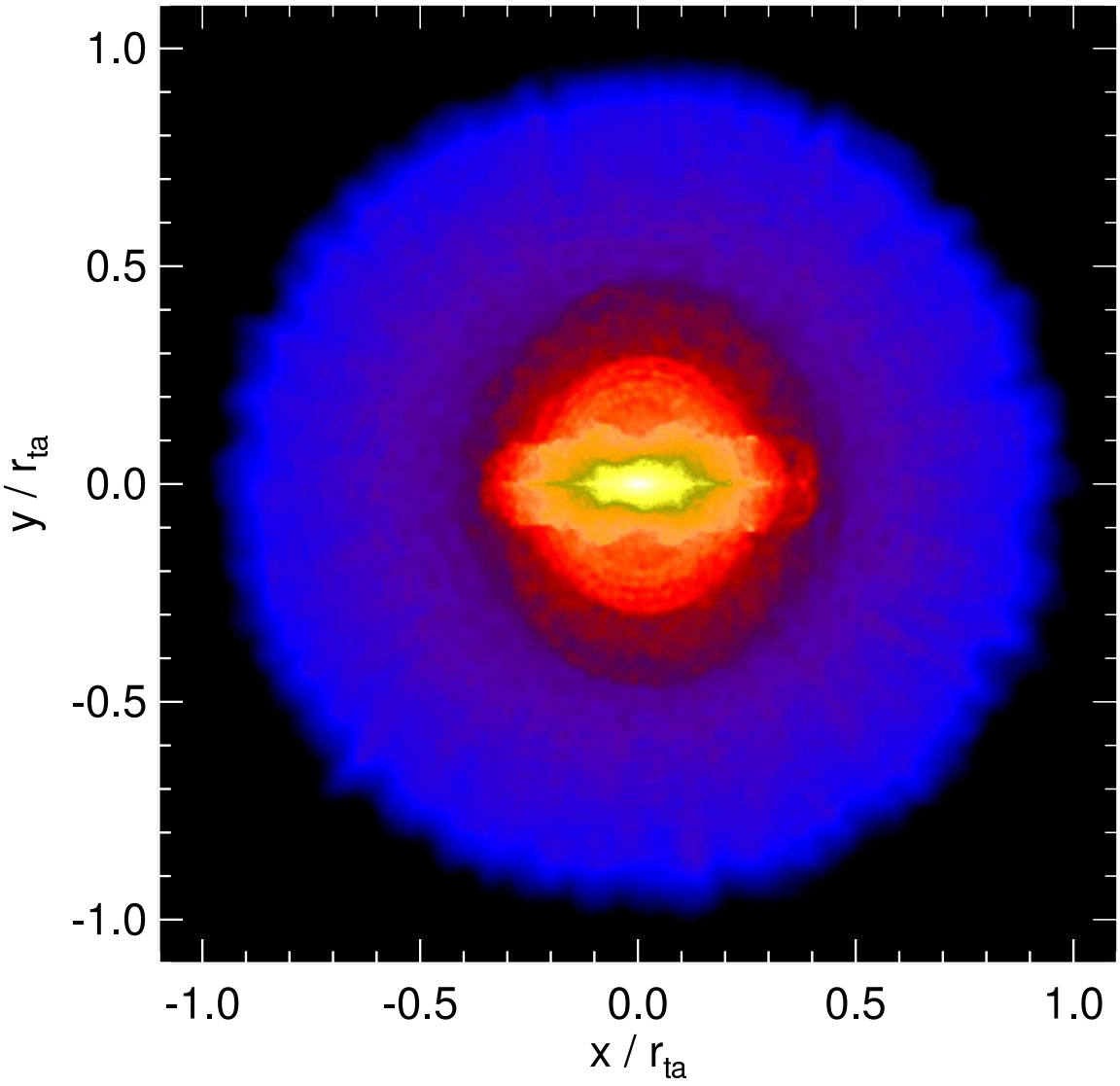

Figure 7.6: Projected density of a slice of thickness $0.25r_{\rm ta}$ through the 3D simulation at the final time when $r_{\rm ta}$ equals the radius of of the entire simulated region. The strong bar is clearly visible and is oriented to lie in the plane of the slice. It formed through the action of the ROI. The red region is bounded by the outermost caustic.

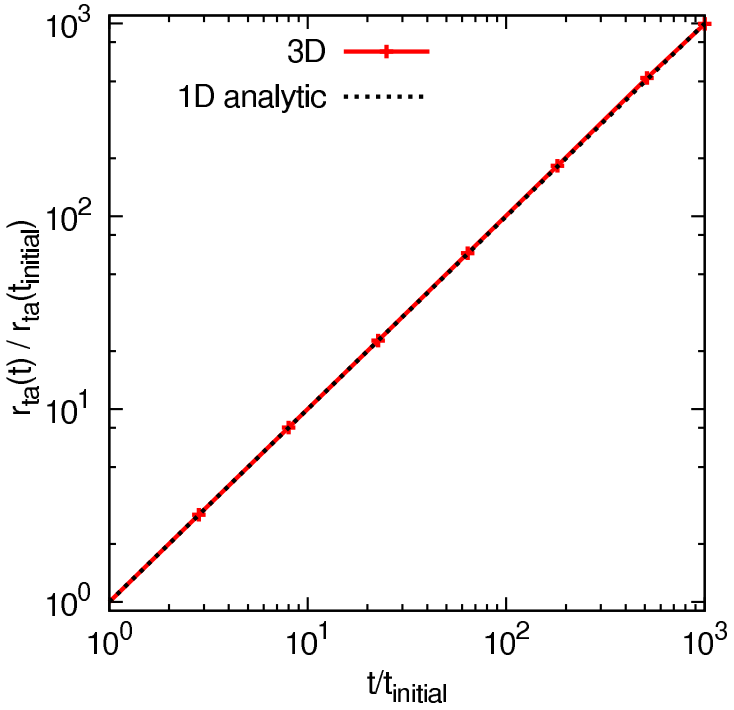

Figure 7.7: The turnaround radius evolution of the 3D simulation is compared to the expectation from the 1D analytic similarity solution. Although the structure of the 3D halo is very different from that of the similarity solution, the turnaround radius grows in exactly the same way, linearly in time for $\epsilon = 2/3$.

inner part. We note that this is important for our GDE integrations because we use the analytic FG solution to initialise the GDE variables at the turnaround radius.

It is obvious that the strong departures from spherical symmetry must nevertheless substantially change the structure of the system. The changes are less dramatic than might be expected, however. In Fig. 7.8 we plot the spherically averaged density profile as a function of radius at t_0 both for the 3D simulation and for the similarity solution. Except for the caustic spikes, the mean halo density profile agrees very well over most of the plotted radial range with the similarity prediction. The deviations visible on the smallest scales in Fig. 7.8 are an effect of force softening. We have performed simulations with 20 times smaller softening, finding that the spherically averaged profile does not deviate significantly from isothermal form ($\rho \propto r^{-2}$) down to 10^{-3} $r_{\rm ta}$. We have also checked that if we change the value of the similarity exponent ϵ in our initial conditions, the inner profiles of the resulting bar-like haloes are always well described by a power law with exponent $9\epsilon/(1+3\epsilon)$, the value predicted by spherical similarity solutions with nonradial orbits (White and Zaritsky, 1992; Sikivie et al., 1995; Nusser, 2001). The pseudo phase-space density ρ/σ^3 (see Taylor and Navarro, 2001) is shown in Fig. 7.9 together with a best-fit powerlaw $r^{-1.96}$.

The ROI disturbs the overall radial structure of the system very little. We see no sign of a tendency to drive the system towards a "universal" NFW-like profile of the kind which MacMillan et al. (2006) and Bellovary et al. (2008) found in their own experiments from non-similarity initial conditions. This demonstrates that the ROI does not of itself produce

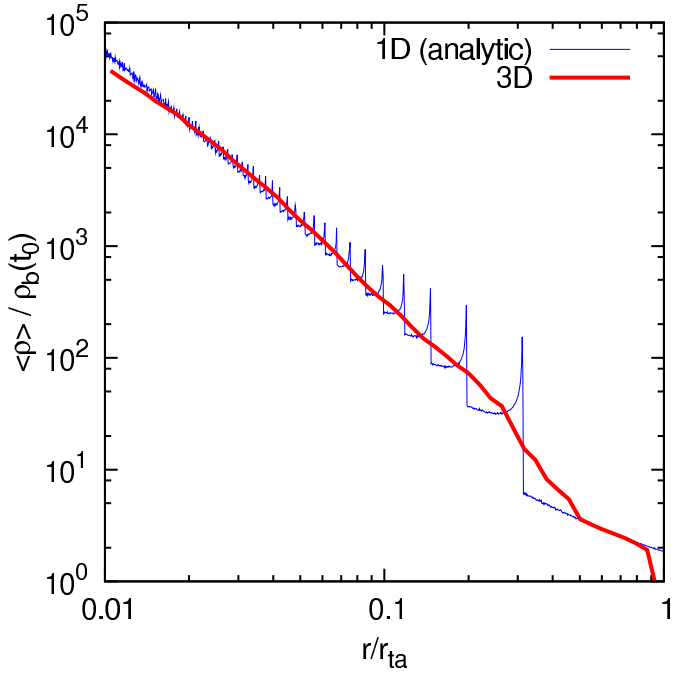

Figure 7.8: Spherically averaged density profile of the 3D simulation compared to the FG similarity solution. Apart from the clear caustic spikes in the 1D case, the two density profiles agree very well despite the very large shape difference between the corresponding objects. The small deviation at $r < 0.015 r_{\rm ta}$ is due to the softening of the simulation.

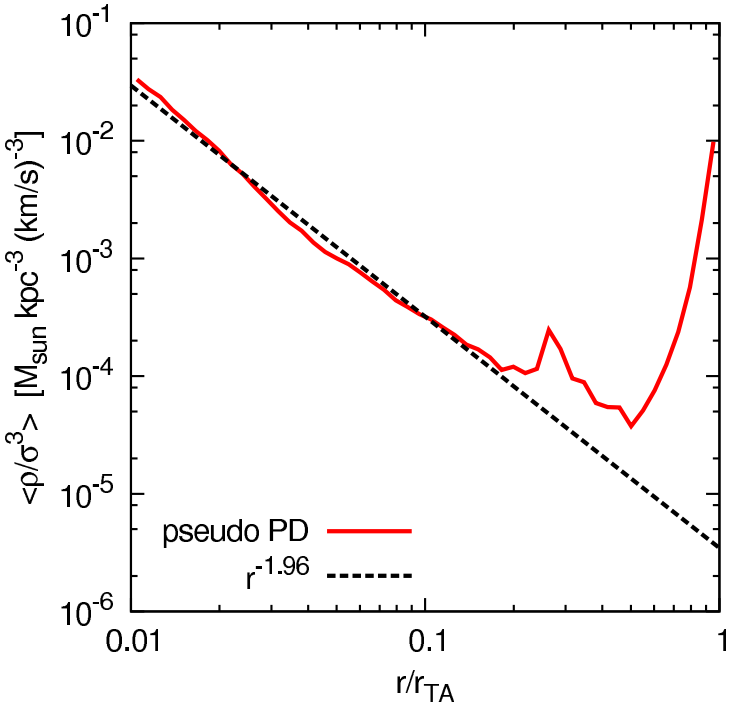

Figure 7.9: Pseudo phase-space density profile ρ/σ^3 of the halo forming in 3D gravity. A powerlaw $r^{-1.96}$ fits the data well.

NFW structure, though it may, of course, be acting in concert with other processes in these earlier experiments.

The aspherical structure of the inner regions induces non-radial motions in the infalling material, producing a phase-space distribution which is six-dimensional rather than two-dimensional as in the similarity solution. We illustrate how this affects the velocity dispersion structure in Fig. 7.10. The upper panel shows total and radial velocity dispersions (relative to mean radial streaming) as functions of radius in units of $r_{\rm ta}$, while the lower panel is a similar plot for the velocity anisotropy parameter $\beta(r)$. In both panels the 3D simulation result (which is at t_0) is compared with the spherical similarity solution. The total velocity dispersion of our 3D halo tracks that in the similarity solution quite accurately down to $0.04r_{\rm ta}$, once the features due to the spherical caustics in the latter are smoothed over. At smaller radii it turns over and drops significantly. This reinforces the conclusion from Fig. 7.8 that the coarse-grained structure of our simulated halo is similar to that of the similarity solution despite their difference in shape. While at $r > 0.05r_{\rm ta}$ orbits in our bar-like halo are predominantly radial and so resemble those in the FG similarity solution, at smaller radii the velocity distribution becomes much closer to isotropic and the radial velocity dispersion begins to decline towards the centre.

The ROI leads to a considerably more complex fine-grained phase-space pattern in our 3D simulation than in the FG similarity solution. Phase-space is two-dimensional in the latter, with the particles occupying a one-dimensional subspace which is fixed in similarity variables. In contrast, phase-space is six-dimensional in our simulation, with the particles occupying a heavily wrapped three-dimensional subspace. When this subspace is projected onto the two-dimensional phase-space of the similarity solution, the fact that the particles occupy a low-dimensional subspace is no longer evident. We show this explicitly in Fig. 7.11, where the pattern of the 1D similarity solution (the grey lines) is compared to the projected particle distribution at t_0 in our simulation. The colours in the 3D case mark the number of caustics each particle has passed. As in the 1D case, this number increases towards the centre, because of the shorter orbital periods at smaller radii. Near and beyond the turnaround radius particles follow the similarity solution, but deviations are already visible at $r \sim 0.5\ r_{\rm ta}$, where the infalling particles no longer lie exactly on the analytic sheet.

The increase in dimensionality of the phase-space distribution has a dramatic effect on the density of individual dark matter streams. Away from caustics the stream density surrounding a particular particle is expected to decrease from its value at turnaround in proportion to $(t/t_{\rm ta})^{-1}$ for an effectively one-dimensional system like the similarity solution, but in proportion to $(t/t_{\rm ta})^{-3}$ for a three-dimensional system like our simulation as we demonstrated in the fifth chapter. In Fig. 7.12 we show the median of the normed stream density (i.e. the stream density relative to its value at turnaround) for particles in radial bins at $t = t_0$, again comparing results for the simulation and for the 1D similarity solution. Beyond the outermost caustic, stream densities are very similar in the two cases. At smaller radii the stream density dilution increases much faster towards the centre in the simulation than in the similarity solution. In the former case the inner behaviour is very close to a power-law. (Recall that for both models the typical orbital period at each radius is roughly proportional to radius, so a power law close to r^1 is expected in the 1D case.) In the simulation the variation of dilution with radius is less smooth, but is still

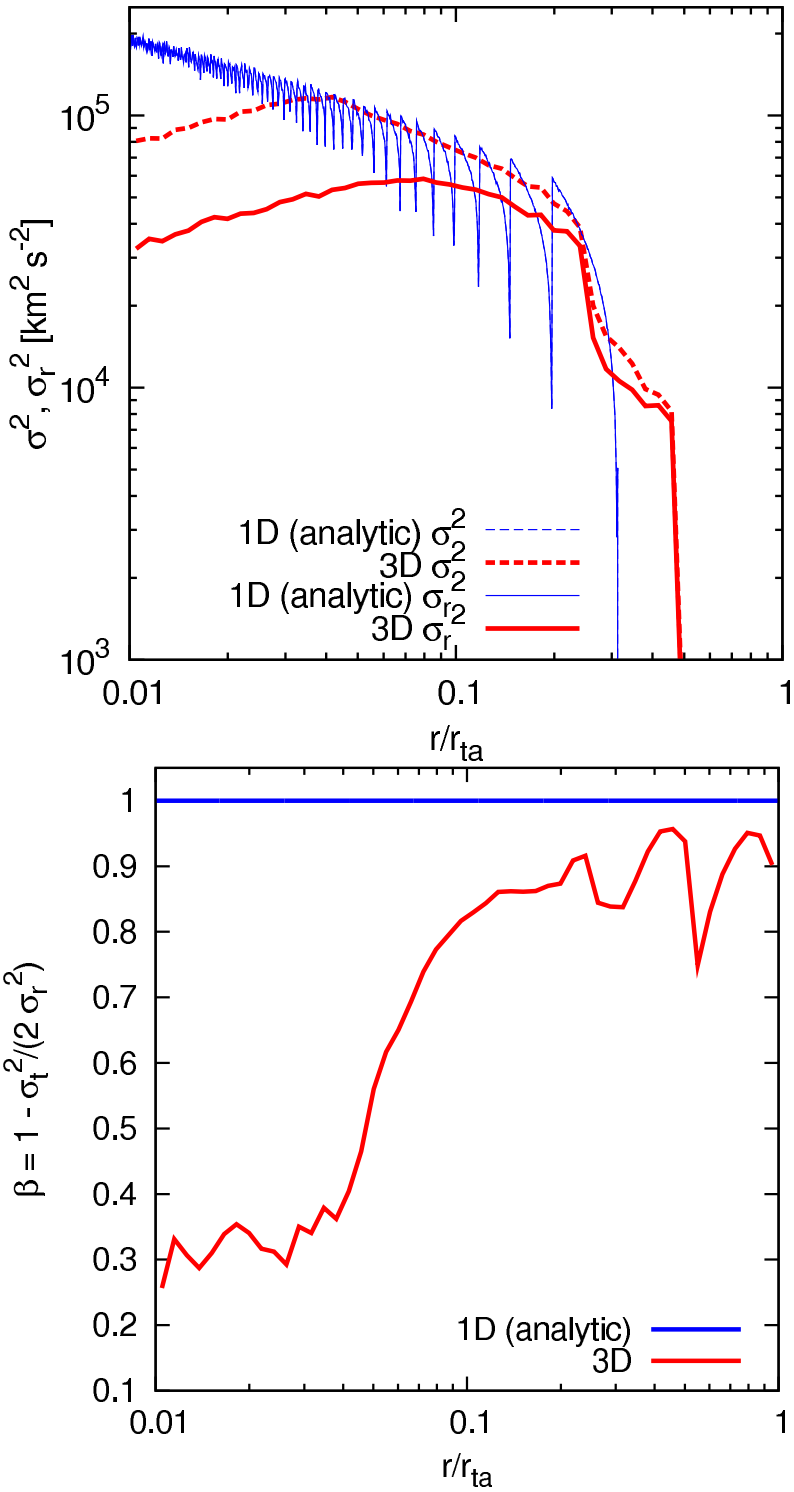

Figure 7.10: Top panel: Total ($\sigma^2 = \sigma_r^2 + \sigma_t^2$, where σ_r and σ_t are the velocity dispersions in the radial and tangential directions, respectively) and radial (σ_r^2) velocity dispersion profiles for the 3D halo are compared to the radial velocity dispersion profile of the FG similarity solution. Bottom panel: Velocity anisotropy profile $\beta = 1 - \sigma_t^2/(2\sigma_r^2)$. Apart from caustic features the total velocity dispersion behaviour is very similar in the two models for $r > 0.04 r_{\rm ta}$. In the outer part of the halo, orbits are primarily radial ($\beta \sim 1$), but the velocity distribution becomes more nearly isotropic for $r < 0.05 r_{\rm ta}$ and this causes both dispersions to drop in the inner regions as in spherical similarity solutions with nonradial orbits.

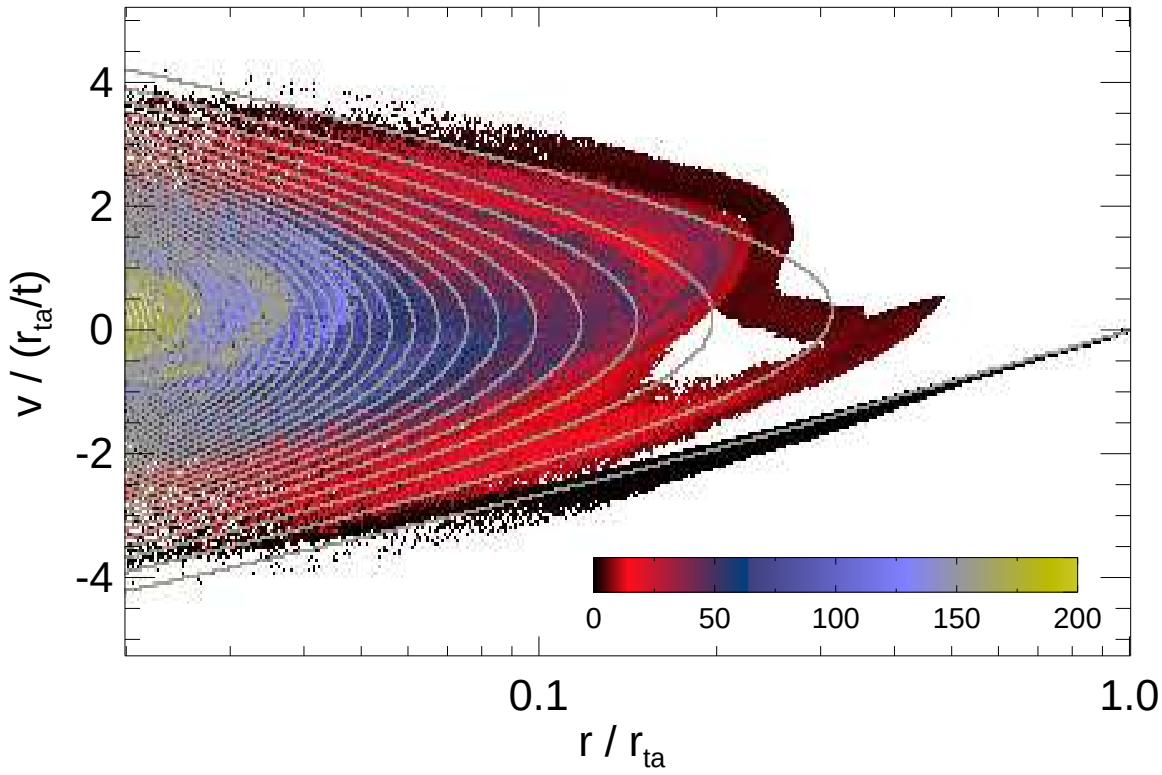

Figure 7.11: Phase-space portrait at t_0 for the 3D simulation and (overplotted in grey) for the 1D similarity solution for $\epsilon = 2/3$. The ROI destroys the clear phase-space pattern seen in the similarity solution. The coarse shape in the two cases is similar, but the 3D solution does not have a simple fine-grained structure in this particular projection of its 6-dimensional phase-space. For the 3D solution the colours encode the number of caustics a given particle has passed (see colourbar). One can clearly see that this grows towards the centre, exceeding 200 in the innermost regions.

moderately well represented by a power-law which, as expected, is the cube of the one which best fits the similarity solution.

Fig. 7.13 (top panel) presents the radial variation of stream density in a slightly different way. The stream density associated with each particle is here divided by the current mean density of the Universe, rather than by its value at turnaround. The plot is then constructed by taking medians in 50 equal logarithmic bins in radius, just as in Fig. 7.12. In the 1D similarity solution, stream densities increase quite strongly (approximately as r^{-1}) towards the centre, because the dilution effect seen in Fig. 7.12 is more than compensated by the fact that particles near the centre typically turned around earlier, and so had higher stream densities at turnaround (this is demonstrated in the bottom panel of Fig. 7.13, where we plot the initial stream density at turnaround). For the 3D simulation, on the other hand, the much stronger dilution towards the centre results in typical stream densities which are approximately constant with radius at any given time. Note that both

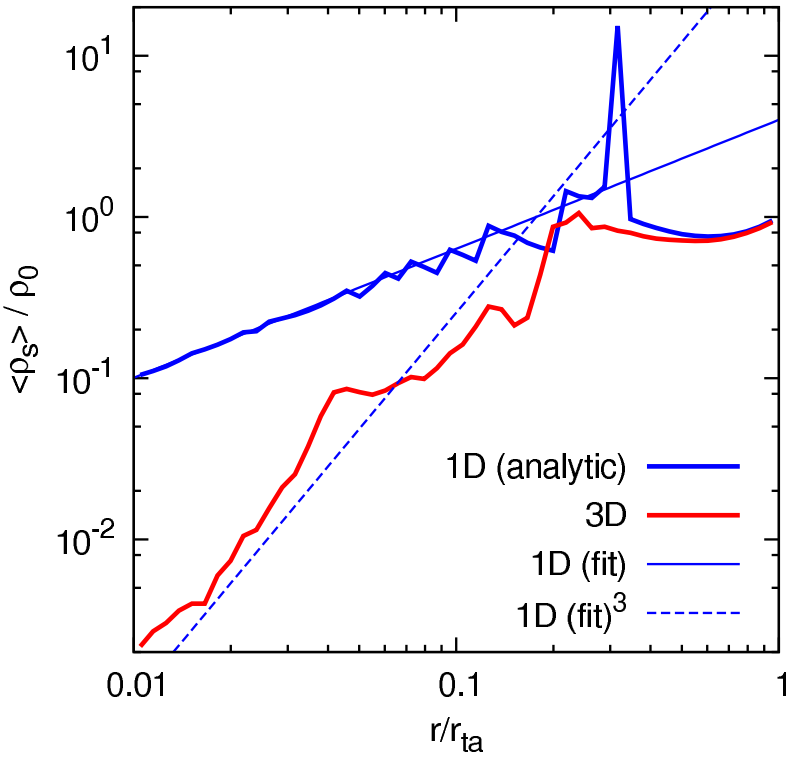

Figure 7.12: Median normed stream density (i.e. the stream density surrounding each particle in units of its value at turnaround) for the 1D similarity solution (the thick blue line) and for the fully 3D simulation (the thick red line). The 1D relation was calculated from the exact (non-softened) similarity solution for $\epsilon = 2/3$. Due to the fully three-dimensional structure of the orbits, stream densities are diluted much faster towards the centre in the simulation than in the similarity solution. In both cases the median was calculated for 50 equal logarithmic bins in radius. This smooths out the caustics of the 1D solution except for the outermost few. The thin blue line is a power-law fit $\rho_s \propto r^{0.8}$ to the normed stream density in the inner part of the similarity solution. The blue dashed line is proportional to the 1D density dilution to the power of three and, as expected, agrees fairly well with the stream dilution in the inner regions of the 3D simulation.

in this figure and in the last, medians are taken over the stream density distribution of the particles in each radial bin. Thus they give the stream density value that splits the mass at each radius in half. As we will see below, this is much larger than the density of a typical stream at that radius.

Typical stream densities are quite similar near the outermost caustics in the 1D similarity solution and in the 3D simulation, but they become very different in the inner regions. In contrast, the typical number of caustics varies with radius in the same way in the two cases. This can be seen in Fig. 7.14, where we plot the median number of caustic passages experienced by particles in a set of logarithmic radial bins. The number is typically three to six times larger for the simulation than for the similarity solution. This is easily understood as reflecting the increased number of turning points along typical orbits. The overshoot in the regions just inside the outermost caustic is related to the feature in phase-space seen in Fig. 7.11.

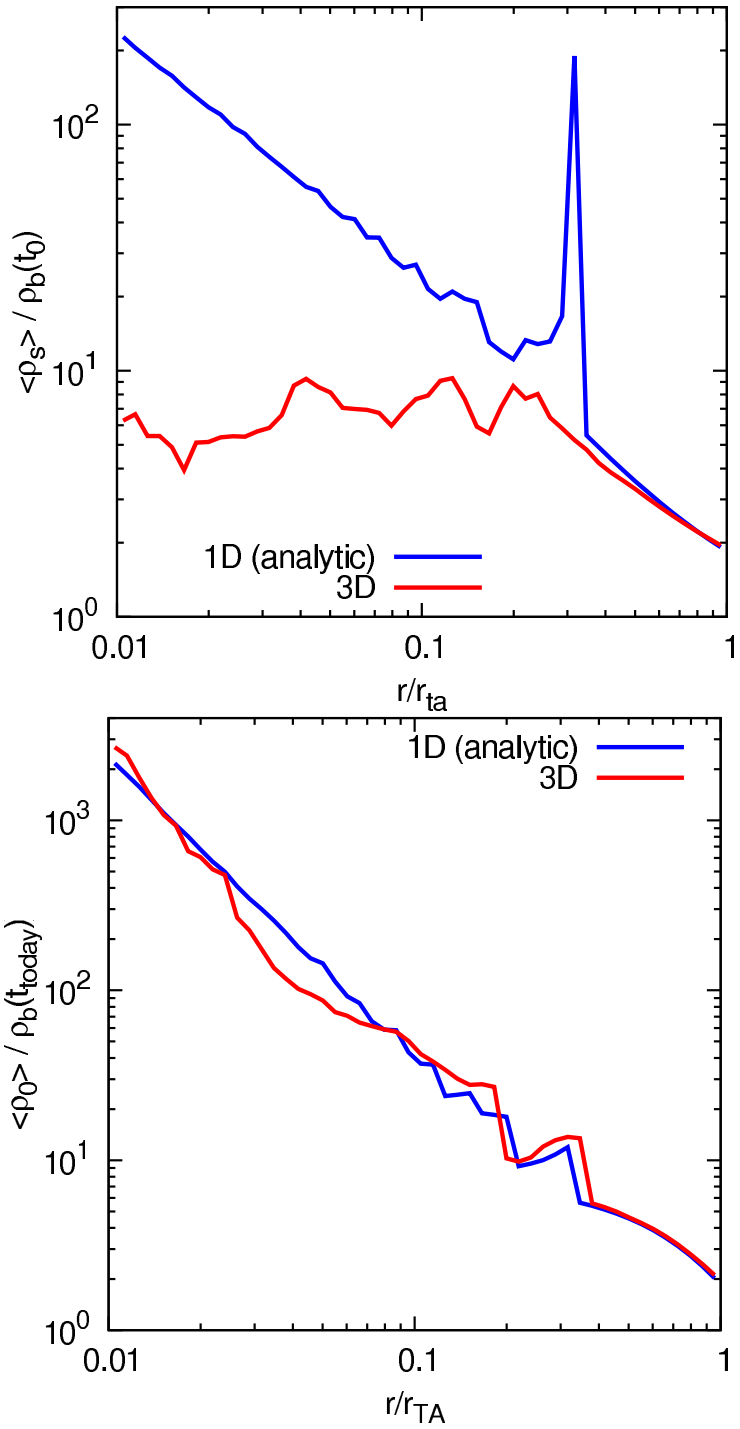

Figure 7.13: Top panel: The median stream density in units of the current cosmic mean density of the particles in each of 50 logarithmic bins in radius at time t_0. Results are shown for the 1D similarity solution (blue) and for the 3D simulation (red). While the stream density increases towards the centre for the similarity solution, it is almost constant with radius in the simulation. Bottom panel: Median initial stream density in terms of the current background density. The median stream density in the top panel is the product of the normed stream density in Fig. 7.12 and the initial density. Since the initial density increases very rapidly towards the centre, the median stream density increases for the 1D case. In 3D the decrease in the normed stream density compensates the increase in the initial stream density. This is why in 3D the stream density slightly decreases towards the centre.

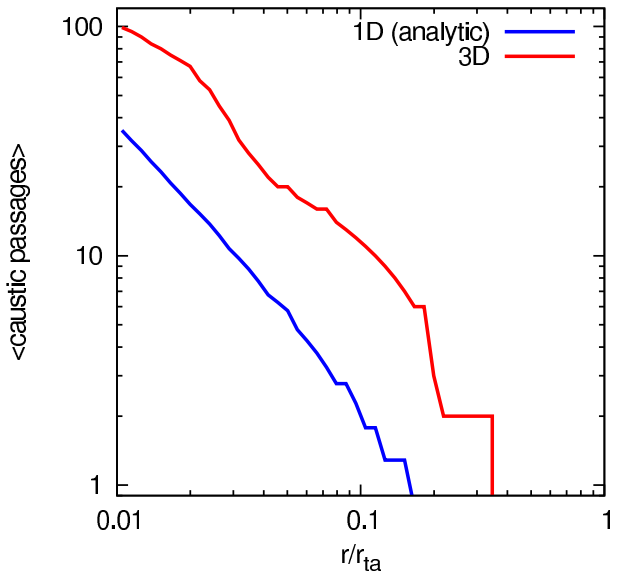

Figure 7.14: Median number of caustic passages experienced by particles in a set of logarithmic bins in radius. The result for the 1D similarity solution is shown as a solid blue line, that for the 3D simulation in red. As expected due to the more complex orbit structure, the number of caustics at a given radius increases by about a factor of three from 1D to 3D. The bump near $r/r_{\rm ta} = 0.1$ is related to the complex feature in phase-space seen in Fig. 7.11.

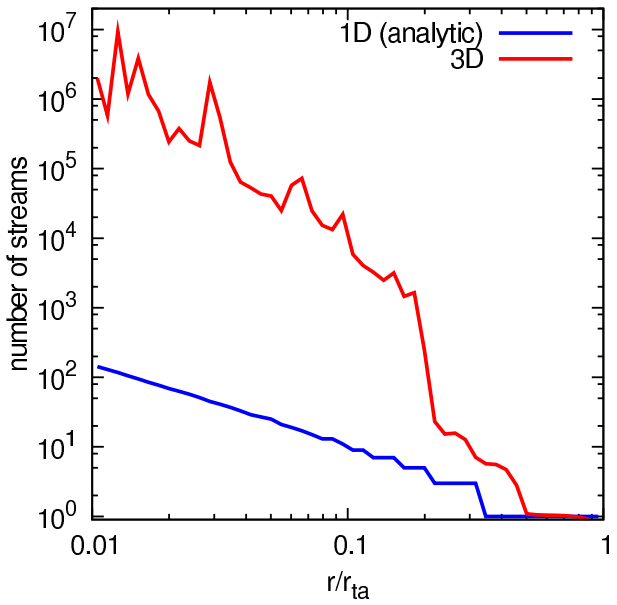

Figure 7.15: Number of streams as a function of radius for the 1D similarity solution (blue) and the 3D simulation (red). In 3D stream stretching reduces individual stream density more efficiently than in 1D, leading to a larger number of streams at each radius. For the 1D similarity case the number of streams in the FG solution is shown. In the 3D case we use the mean harmonic stream density of the particles in a set of logarithmic bins to estimate the number of streams (see text).

Since the mean density profiles are similar in the 3D and 1D cases, the lower stream densities in 3D lead to a larger number of streams at each radius. Counting the number of streams in 1D is straightforward, given the similarity solution. In 3D we can estimate the number of streams crossing a given radial bin as a suitable average over the stream densities of the particles it contains $N_{\rm streams} \sim \rho(r)\ \langle 1/\rho_s \rangle_r$, where $\rho(r)$ is the mean mass density in the bin and $\langle 1/\rho_s \rangle_r$ is the average of the reciprocal of the stream densities of the particles. The comparison is shown in Fig. 7.15. The greatly enhanced mixing in 3D is clearly seen in this figure. At 1% of the turnaround radius there are of order 10^6 streams in the 3D simulation but only of order 100 in the FG solution. Estimates of the number of streams near the Sun based on 1D models (e.g. Natarajan and Sikivie, 2005) give severe underestimates of the expectation in more realistic models.

In Fig. 7.16 we show as a function of radius the median and quartiles of the density at caustic crossing for all particles in the 3D simulation that crossed a caustic in the 0.014 Gyr immediately preceding t_0. For comparison, we also show the mean density profile of the halo in the 1D and 3D case. In the outer regions the density at caustic crossing is typically a thousand times the local mean halo density. Thus one might expect caustics to be visible in the halo annihilation signal at these radii. In the inner halo, however, the densities at caustic crossing do not rise as in the 1D similarity solution (also shown for comparison) but rather stay constant or even drop somewhat. Below $r/r_{\rm ta} = 0.03$ the median density at caustic crossing is smaller than the local mean halo density and one may expect caustics to play no significant role in the annihilation signal.

In the inner regions, stream and caustic densities are much lower in the 3D simulation than in the 1D similarity solution, but the number of caustics is only a few times greater. As a result less caustic-related annihilation radiation is expected in the 3D case. In Fig.7.17 we show the ratio of intra-stream annihilation rate (i.e. the contribution from particles which are both part of the same stream) to the annihilation rate estimated from the smoothed total density. The latter is calculated by SPH techniques using 64 neighbours. Fig.7.17 shows that intra-stream annihilation (which is dominated by caustic annihilation) does not contribute strongly to the overall annihilation rate. This is especially true in the inner region of the halo, where the stream and caustic densities are strongly suppressed. We find that for the radial interval $r/r_{\rm ta} \in (0.01, 0.5)$ the intra-stream contribution is only 4%. If we focus on the outer regions we find a contribution of 24% for $r/r_{\rm ta} \in (0.1, 0.5)$ and 64% for $r/r_{\rm ta} \in (0.2, 0.5)$, the range where the particles turn around for the second time and produce the outermost caustics.

All the above results are based on a present-day neutralino velocity dispersion of $\sigma_{\rm b}(t_0) = 0.03$ cm/s in unclustered regions. The dominant contribution to the intra-stream annihilation rate comes from caustics if the velocity dispersion is small. The densities of caustics are proportional to $1/\sqrt{\sigma_{\rm b}}$, and so are easily scaled to an arbitrary velocity dispersion. This is shown in the top panel of Fig. 7.18. In the bottom panel we show the radial dependence of the intra-stream annihilation rate for a range of velocity dispersions $\sigma_{\rm b}(t_0)$. These results are based on 64^3 particle simulations with a softening length of 0.01 $r_{\rm ta}$. We plot the intra-stream contribution for three different radial ranges as a function of velocity dispersion. A good analytic fit to the numerical results (dashed

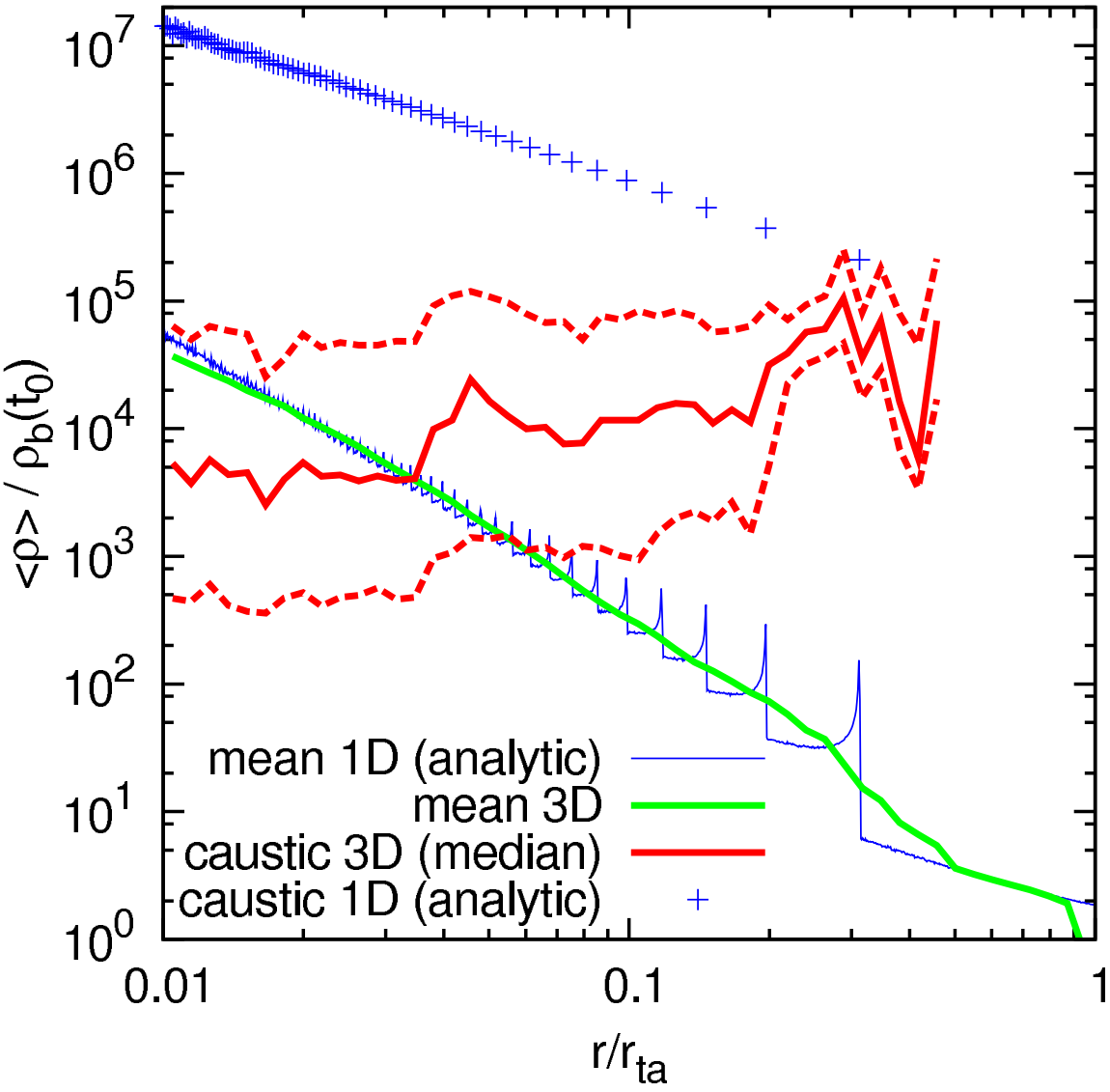

Figure 7.16: Densities at caustic passage as a function of radius and in units of the current mean cosmic density for the 1D similarity solution (blue crosses) and for the 3D simulation (red curves showing the median and quartiles at each radius). These caustic densities are compared to the mean density profiles of the two systems (blue curve for the 1D similarity solution, green curve for the 3D simulation). In 3D the outermost caustics are as dense as those found in 1D, reflecting the more rapid mixing in the three-dimensional system.

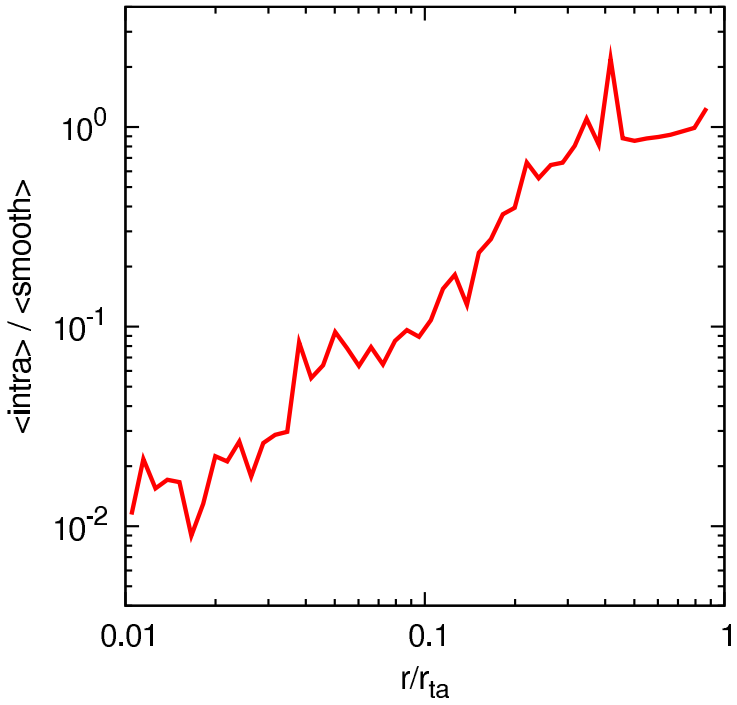

Figure 7.17: Local ratio of the intra-stream annihilation rate to the smoothed annihilation rate as a function of radius. The smoothed annihilation rate is calculated from an SPH-based density estimate using 64 neighbours. As expected, the strongest caustic contributions are found in the outer regions. Near 1% of the turnaround radius the contribution from caustics is at the percent level. This reflects the rapid dilution of stream densities in a 3D system.

lines) for each radial interval is given by

$$\frac{\langle \text{intra} \rangle}{\langle \text{smooth} \rangle} = a + b \ \log \frac{1 \text{ cm/s}}{\sigma_b(t_0)}. \tag{7.7}$$

We note that this logarithmic behaviour is expected given the analysis of the previous chapter and the fact that the dominant contribution comes from caustics.

From Fig. 7.18 we conclude that decreasing the velocity dispersion by 10 orders of magnitude from our standard value only increases the intra-stream annihilation contribution by a factor of about two. In the outer part of the halo, this would boost the total annihilation rate by almost a factor of two for the lowest dispersion shown in the plot, but in the inner regions the caustic contributions would still be small. For a typical neutralino with a mass around 100 GeV c^{-2} we do not confirm the substantial boost factors claimed by Hogan (2001).

7.4 Conclusion and Discussion

We have used the geodesic deviation equation formalism developed in chapter 5 together with the fully general treatment of annihilation in caustics in the previous chapter to understand how fine-grained phase-space structure affects the annihilation radiation from the

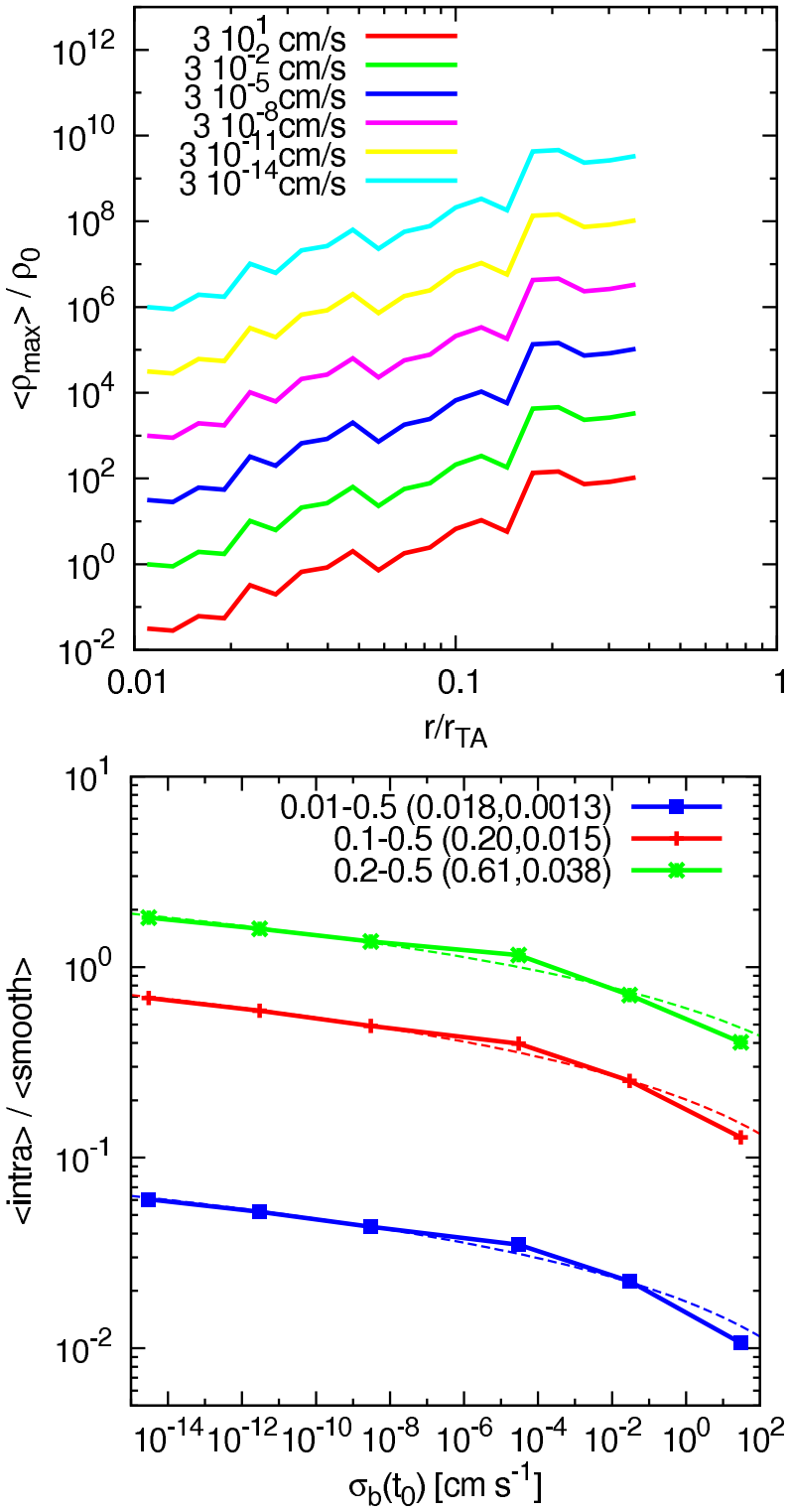

Figure 7.18: Top panel: Median maximum caustic densities for different background velocity dispersions $\sigma_{\rm b}(t_{\rm today})$. The caustic density scales like $1/\sqrt{\sigma_{\rm b}}$, therefore all lines are shifted by a factor of $\sqrt{1000}$. Bottom panel: Intra-stream contribution to the annihilation rate as a function of the present-day neutralino velocity dispersion in unclustered regions and for different radial ranges (distinguished by colour; see legend which gives the range in units of the turnaround radius). The caustic contribution dominates and increases only logarithmically with decreasing dispersion. The dashed lines are analytic fits to the numerical results using Eq. (7.7). The fitting parameters a, b are shown in the brackets in the legend.

dark matter haloes that form from self-similar, spherical initial conditions. Such objects do not evolve according to the well-known one-dimensional similarity solutions. Rather, they turn into highly elongated bars as a result of the radial orbit instability. These bars have mean mass density and total velocity dispersion profiles which are very similar to those of the relevant similarity solutions, but the loss of spherical symmetry results in orbits that fill a 3D volume and along which the stream density typically decreases as $1/t^3$ rather than as $1/t$ as in the similarity solution. At any given time, typical stream densities decrease slightly towards the centre of our simulation, whereas they increase strongly in the similarity solution. As a consequence, there are many more streams in the inner regions of the simulation than in the similarity solution. At 1% of the turnaround radius we find $\sim 10^6$ streams in the simulation but only about 100 in the similarity solution. This contradicts recent claims that the number of streams near the Sun should be relatively small (e.g. Natarajan and Sikivie, 2005) but agrees with the estimates of Helmi et al. (2003). The number of caustics changes much less dramatically between the two cases, with a few times more caustics in the inner regions of the simulation as in the comparable region of the similarity solution. This is as expected given the higher dimensionality of the simulation orbits.

The impact of caustics on the annihilation signal depends on their density and number. Caustic densities in our simulation are much smaller than in the similarity solution, but their abundance is only modestly increased. As a result, annihilation radiation from caustics is less important in 3D than in 1D. For example, within the radial range $r/r_{\rm ta} \in (0.01, 0.5)$ caustics contribute only 4% of the smooth annihilation signal. If we focus on the region containing the outermost caustics, $r/r_{\rm ta} \in (0.2, 0.5)$, this ratio is 64%, similar to that predicted by the similarity solution. Decreasing the velocity dispersion by 10 orders of magnitude from our standard value only increases the caustic contribution to the annihilation luminosity by a factor of about two. This is because the annihilation signal from caustic crossing depends only logarithmically on the dark matter velocity dispersion.

Our results are based on a simplified and unrealistic halo formation model. However, haloes growing from ΛCDM initial conditions are expected to mix even more efficiently, because the fully three-dimensional character of orbits is retained and small-scale structure is expected to enhance the stretching of the phase-space sheets and hence to result in even greater dilution of their 3-densities. Thus, caustics will likely be less important in the ΛCDM case than in the simple isolated halo model discussed in the present chapter. This strengthens our conclusion that 1D similarity solutions are inadequate and misleading models for the evolution of the fine-grained structure of real dark matter haloes. This applies not only to the original FG solutions but also to spherically symmetric generalisations of them (e.g. Sikivie et al., 1995, 1997; Duffy and Sikivie, 2008). These still give qualitatively incorrect predictions for the dynamical dilution of stream densities. The inclusion of baryons would affect the dynamics of the dark matter in the inner halo, but would neither change the dimensionality of the orbits nor substantially modify their characteristic timescales. Thus no qualitative changes in behaviour are expected. The somewhat shorter orbital timescales produced by compression of the inner halo are likely, if anything, to accelerate mixing. Our general conclusions should thus be unaffected.

Our analysis assumes that the annihilation cross-section does not depend on the dark

matter phase-space structure. In general this assumption is correct, but it does not hold for a recently proposed mechanism which adopts an additional attractive force between dark matter particles in order to increase the annihilation cross-section through the well-known Sommerfeld enhancement process (e.g. Sommerfeld, 1931; Hisano et al., 2004, 2005; Cirelli et al., 2007; Arkani-Hamed et al., 2009; Lattanzi and Silk, 2009). Away from resonances and before saturation takes place, the increase in the annihilation cross-section scales like $1/v$, where v is the particle encounter velocity. As a result, annihilation radiation from low-velocity-dispersion regions like subhaloes is enhanced as the inverse of the velocity dispersion (again as long as this dispersion exceeds the saturation level)(e.g. Bovy, 2009). Conversely, annihilation radiation from caustics is suppressed, because the velocity dispersion there is very high. In such a scenario the radiation from individual fine-grained streams is Sommerfeld enhanced *away* from caustics because of their low internal velocity dispersion there. Thus the intra-stream annihilation is no longer dominated by caustics as it is in the standard case we have treated in the bulk of this chapter.

8

Simulating the fine-grained phase-space of ΛCDM Haloes

We present results on the fine-grained phase-space structure of cold dark matter haloes growing in the concordance ΛCDM cosmology. We use the geodesic deviation technique to follow the local phase-space evolution of individual simulation particles, and we apply this method to three different resolutions of the Aq-A halo of the Aquarius project. We use a fixed softening length and change only the particle number. Good convergence is achieved for all fine-grained properties of the halo: caustic passages, stream densities, number of streams and intra-stream annihilation radiation. At the virial radius we expect about 10^7 streams. We find caustic densities to be subdominant within the virial radius: at the virial radius the maximum caustic density is comparable to the mean halo density, whereas at 10% of the virial radius the caustic density is already a factor 10^4 smaller than the mean density. We contribute this to the very efficient phase-space mixing. The contribution of caustics to the annihilation radiation at the turnaround radius is about 10%, but well below 0.1% at 10% of the virial radius.

8.1 Introduction

In the previous chapter we analysed the fine-grained phase-space structure of a single halo forming from self-similar initial conditions. Although this simplified model gives useful insights into the expected phase-space structure, it does not address the general problem of a halo forming in a ΛCDM cosmology. To this end we need to study the growth of a halo from appropriate ΛCDM initial conditions. The goal of this chapter is to combine high resolution simulations with the new GDE technique. We use the initial conditions of the Aquarius project that we already used in chapter 4 and run the simulation with the GDE extension presented in the previous chapters. This allows us to understand the expected fine-grained phase-space structure of ΛCDM haloes and therefore going beyond the simplified treatment of the previous chapter.

8.2 Initial conditions

We use the initial conditions of chapter 4 to follow the fine-grained phase-space evolution of a ΛCDM halo in detail. Therefore, the cosmological parameters for the following simulations are $\Omega_{m0} = 0.25, \Omega_{\Lambda 0} = 0.75, \sigma_8 = 0.9, n_s = 1$ and $H_0 = 100\ h$ km s^{-1} Mpc^{-1} with $h = 0.73$, where all quantities have their standard definitions. Further details can be found in chapter 4. In the following we focus on the Aq-A halo, but this study can also be extended to the other haloes of the Aquarius project to understand the effect of object-to-object scatter.

8.3 Numerical techniques

For the simulations we use the GADGET code with the GDE modifications described in chapters 5 and 6. It is convenient to run general cosmological simulations in comoving coordinates rather than in physical coordinates as we did it in the previous chapter. The comoving integration requires a transformation of the GDE relations from the physical to the comoving frame. We briefly describe how the GDE and the associated tensors can be transformed from physical to comoving space and show how this is implemented in our simulation code. The time-dependent transformation is given by

$$\underline{x}(\underline{x}', \underline{v}') = a\underline{x}', \quad \underline{v}(\underline{x}', \underline{v}') = Ha\underline{x}' + \frac{1}{a}\underline{v}', \tag{8.1}$$

where $H = \dot{a}/a$ denotes the Hubble parameter, a the scale factor, and comoving coordinates are primed. We note that the definition of $\underline{v}'$ differs from that chosen in chapter 2, because we work here in the coordinates used by our simulation code. In physical space the distortion tensor is defined via

$$\overline{\overline{D}} = \frac{\partial \overline{x}}{\partial \overline{q}} = \begin{pmatrix} \partial \underline{x}/\partial \underline{q} & \partial \underline{x}/\partial \underline{p} \\ \partial \underline{v}/\partial \underline{q} & \partial \underline{v}/\partial \underline{p} \end{pmatrix} = \begin{pmatrix} \underline{\underline{D}}_{xq} & \underline{\underline{D}}_{xp} \\ \underline{\underline{D}}_{vq} & \underline{\underline{D}}_{vp} \end{pmatrix}, \tag{8.2}$$

where $\underline{q}$ and $\underline{p}$ denote the initial position and velocity, respectively. In comoving coordinates the distortion tensor is accordingly defined via

$$\overline{\overline{D}}' = \frac{\partial \overline{x}'}{\partial \overline{q}'} = \begin{pmatrix} \partial \underline{x}'/\partial \underline{q}' & \partial \underline{x}'/\partial \underline{p}' \\ \partial \underline{v}'/\partial \underline{q}' & \partial \underline{v}'/\partial \underline{p}' \end{pmatrix} = \begin{pmatrix} \underline{\underline{D}}'_{x'q'} & \underline{\underline{D}}'_{x'p'} \\ \underline{\underline{D}}'_{v'q'} & \underline{\underline{D}}'_{v'p'} \end{pmatrix}, \tag{8.3}$$

where all phase-space coordinates are now expressed in comoving coordinates. The relation between physical and comoving distortion tensor can be derived from the differential relations and this yields

$$\overline{\overline{D}}(t) = \overline{\overline{C}}_{\overline{x}' \to \overline{x}}(t) \overline{\overline{D}}'(t) \overline{\overline{C}}_{\overline{x} \to \overline{x}'}(t_{\text{initial}}), \tag{8.4}$$

where we have defined the two transformation tensors

$$\overline{\overline{C}}_{\overline{x}' \to \overline{x}} = \frac{\partial \overline{x}}{\partial \overline{x}'} = \begin{pmatrix} a\underline{\underline{1}} & \underline{\underline{0}} \\ Ha\underline{\underline{1}} & 1/a\underline{\underline{1}} \end{pmatrix}, \tag{8.5}$$

and

$$\overline{\overline{C}}_{\overline{x} \to \overline{x}'} = \frac{\partial \overline{x}'}{\partial \overline{x}} = \begin{pmatrix} 1/a\underline{\underline{1}} & \underline{\underline{0}} \\ -Ha\underline{\underline{1}} & a\underline{\underline{1}} \end{pmatrix}. \tag{8.6}$$

We note that one of these transformation tensors is evaluated at t whereas the other one is evaluated at initial time t_{initial}. The reason for these different evaluation times is the time dependence of the comoving coordinate transformation as shown above. Therefore, the transformation is different for $\overline{x}$ and for $\overline{q}$, because the scale factor and Hubble parameter change with time. Liouville's theorem guarantees that $\det(\overline{\overline{D}}(t)) = \det(\overline{\overline{D}}'(t)) = 1$ is fulfilled, so the comoving distortion tensor has the same conserved determinant as the physical one. This means that local phase-space elements in the comoving frame conserve volume and orientation during the time evolution of the system. As in the physical frame this can be used to check the accuracy of the time integration and check the results of the simulation code.

To integrate the comoving distortion tensor, we need to derive its equations of motion. To do so, we start with the physical GDE equation

$$\dot{\overline{\overline{D}}} = \overline{\overline{T}}\, \overline{\overline{D}}, \tag{8.7}$$

and introduce the peculiar potential field

$$\phi = a\Phi + \frac{a^2 \ddot{a}}{2} \underline{x}'^2 \tag{8.8}$$

related to the density field via Poisson's equation

$$\underline{\nabla}^2_{x'} \phi = 4\pi G \left(\rho'(\underline{x}') - \rho'_b \right), \tag{8.9}$$

where ρ'_b denotes the comoving mean background density and the Laplacian is taken in comoving space. We note that the force field driving the motion of the particles in the simulation is derived from this peculiar potential field. Since the GDE is directly related

to the equations of motion for the particle trajectory, it is natural to introduce a peculiar configuration-space tidal tensor $\underline{\underline{T}}'$ with components $T'_{ij} = -\partial^2\phi/\partial x'_i \partial x'_j$

$$\frac{1}{a^3}\underline{\underline{T}}' = \underline{\underline{T}} - \frac{\ddot{a}}{a}\underline{\underline{1}}. \tag{8.10}$$

We can use this tidal tensor to write down the equations of motion for the comoving distortion tensors in the following form

$$\begin{aligned} \dot{\underline{\underline{D}}}'_{x'q'} &= \frac{1}{a^2}\underline{\underline{D}}'_{v'q'}, \quad \dot{\underline{\underline{D}}}'_{x'p'} = \frac{1}{a^2}\underline{\underline{D}}'_{v'p'}, \\ \dot{\underline{\underline{D}}}'_{v'q'} &= \frac{1}{a}\underline{\underline{T}}'\underline{\underline{D}}'_{x'q'}, \quad \dot{\underline{\underline{D}}}'_{v'p'} = \frac{1}{a}\underline{\underline{T}}'\underline{\underline{D}}'_{x'p'}. \end{aligned} \tag{8.11}$$

Therefore, the equations of motion for the comoving distortion tensor have exactly the same form as those for the physical ones. The only difference is the appearance of the scale factor a in the comoving equations. The initial conditions for these equations follow from those of the physical distortion tensor taking into account $\overline{\overline{C}}_{\overline{x}'\to\overline{x}}\,\overline{\overline{C}}_{\overline{x}\to\overline{x}'} = \overline{\overline{1}}$

$$\begin{aligned} \underline{\underline{D}}'_{x'q'}(t_{\text{initial}}) &= \underline{\underline{1}}, \quad \underline{\underline{D}}'_{x'p'}(t_{\text{initial}}) = \underline{\underline{0}}, \\ \underline{\underline{D}}'_{v'q'}(t_{\text{initial}}) &= \underline{\underline{0}}, \quad \underline{\underline{D}}'_{v'p'}(t_{\text{initial}}) = \underline{\underline{1}}, \end{aligned} \tag{8.12}$$

Based on these equations we can construct Kick- and Drift-operators for the Leapfrog time integrator similar to those for the position and velocities. It is therefore straightforward to implement the GDE integration in the comoving frame. The only task left is the calculation of the driving tidal field. As described in chapter 5 this can be done in parallel to the force field calculation.

Let us discuss next how to derive the stream density from the comoving integration result. Our goal is to derive an equation that yields directly the physical stream density based on the comoving distortion tensor discussed above. Therefore, we note that the configuration-space distortion tensor can be derived from the phase-space distortion tensor by applying two projection operators in the following way

$$\underline{\underline{D}} = \begin{pmatrix} \underline{\underline{1}} & \underline{\underline{0}} \end{pmatrix} \overline{\overline{D}} \begin{pmatrix} \underline{\underline{1}} \\ \underline{\underline{V}}_q \end{pmatrix}, \tag{8.13}$$

where $\underline{\underline{V}}_q$ is the initial sheet orientation. The physical stream density can then be calculated from the stretching factor of this linear transformation in physical configuration-space

$$\rho = \frac{\rho_0}{\left|\det\left(\underline{\underline{D}}\right)\right|} \tag{8.14}$$

as we described in chapter 5. We can write out the projection and get the following

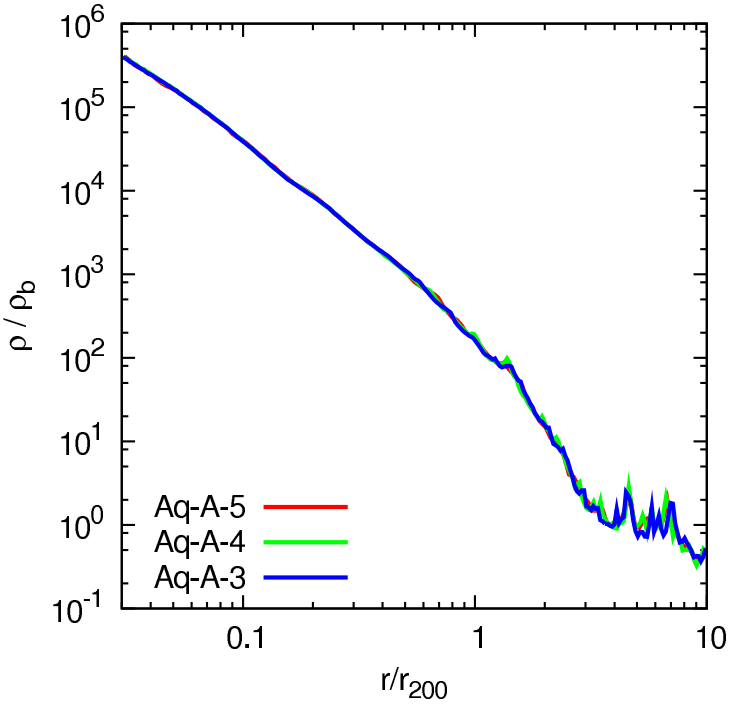

Figure 8.1: Spherically averaged density profile of Aq-A-3,4,5 at $z = 0$. The softening length of all simulations is the same ($\epsilon = 2.5$ kpc$/h$). The convergence between the different resolutions is very good. This was already demonstrated in Springel et al. (2008a).

relation for the physical stream density

$$\rho = \frac{\rho_0}{\left|\det\left[a/a(t_{\rm initial})\underline{\underline{D}}'_{x'q'} + aa(t_{\rm initial})\left(\underline{\underline{V}}_q - H(t_{\rm initial})\underline{\underline{1}}\right)\underline{\underline{D}}'_{x'p'}\right]\right|}. \tag{8.15}$$

The physical initial stream density ρ_0 is related to the comoving initial stream density ρ'_0 in the following obvious way

$$\rho_0 = \frac{\rho'_0}{a(t_{\rm initial})^3}. \tag{8.16}$$

This allows us to rewrite the physical stream density in a form that (nearly) only depends on comoving quantities

$$\rho = \frac{\rho'_0}{a^3\left|\det\left[\underline{\underline{D}}'_{x'q'} + a(t_{\rm initial})^2\left(\underline{\underline{V}}_q - H(t_{\rm initial})\underline{\underline{1}}\right)\underline{\underline{D}}'_{x'p'}\right]\right|}. \tag{8.17}$$

The only quantity left in physical coordinates is the initial sheet orientation $\underline{\underline{V}}_q$. Note that the Hubble flow is subtracted from $\underline{\underline{V}}_q$, so that effectively only the peculiar sheet orientation $\underline{\underline{V}}'_{q'} = \underline{\underline{V}}_q - H(t_{\rm initial})\underline{\underline{1}}$ enters

$$\rho = \frac{\rho'_0}{a^3\left|\det\left[\underline{\underline{D}}'_{x'q'} + a(t_{\rm initial})^2\,\underline{\underline{V}}'_{q'}\,\underline{\underline{D}}'_{x'p'}\right]\right|}. \tag{8.18}$$

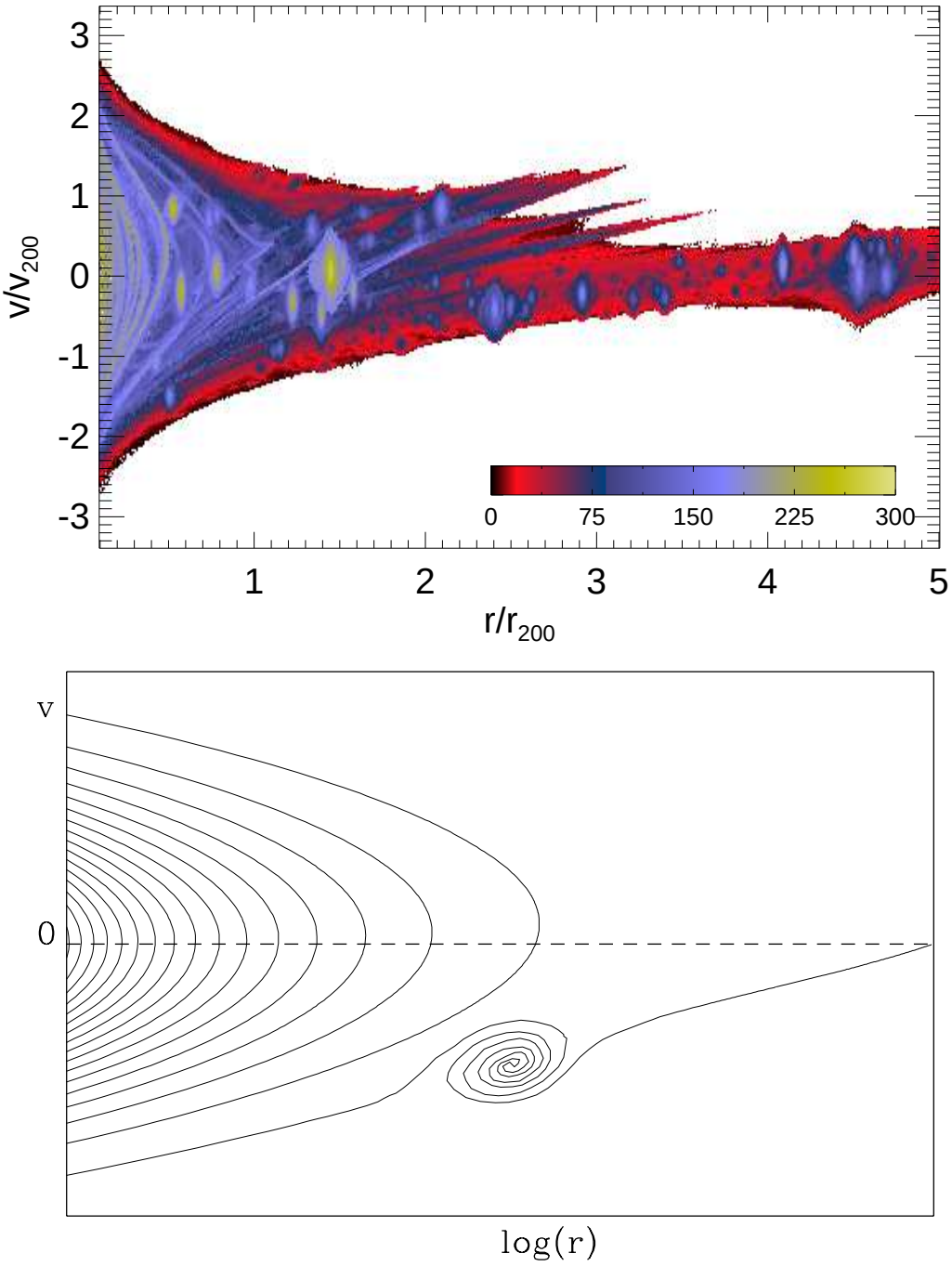

Figure 8.2: Top panel: Phase-space structure of Aq-A-3 halo at redshift $z = 0$. The colour encodes the number of caustics passed by individual simulation particles. The subhaloes clearly stand out in this plot, because the phase-space sheet winding leads to a higher number of caustic passages in the subhaloes and in their tidal streams. This is very different from the phase-space portrait seen for the isolated halo in the previous chapter. Bottom panel: Schematic phase-space sheet that shows the additional wind up in subhaloes.

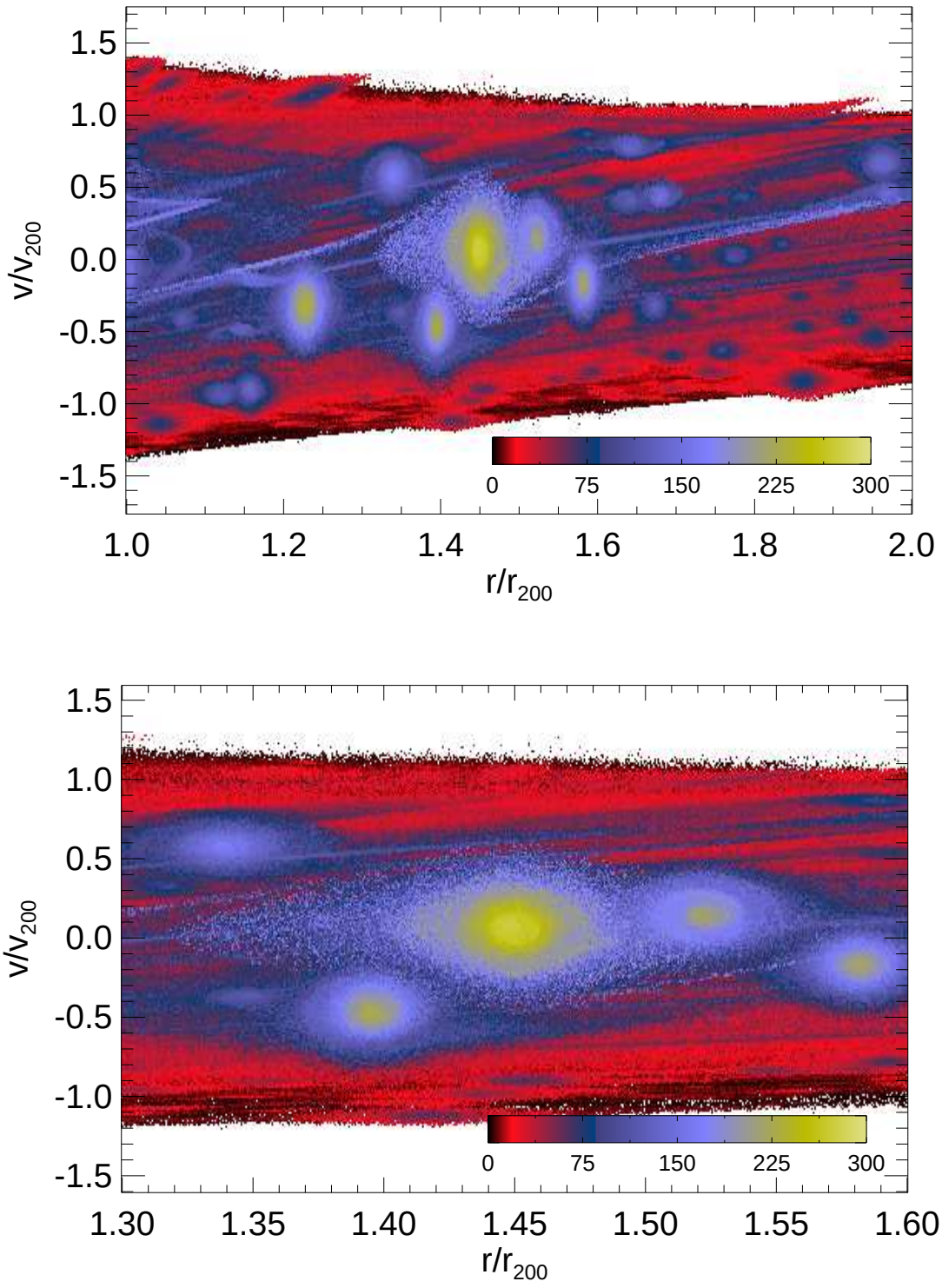

Figure 8.3: Two magnifications of the phase-space structure of Aq-A-3 focusing on one of the prominent subhaloes.

In a perfectly homogeneous and isotropic Universe the initial sheet orientation is simply given by the Hubble flow, because there are no peculiar velocities in zeroth order perturbation theory. In that simplified situation the initial phase-space sheet is given by

$$\left(\underline{q}, \underline{p}\right) : \underline{p} = \underline{V}(\underline{q}) = H(t_{\text{initial}}) \underline{\underline{1}}\, \underline{q}. \tag{8.19}$$

Therefore, the peculiar sheet orientation vanishes in that case and the physical stream

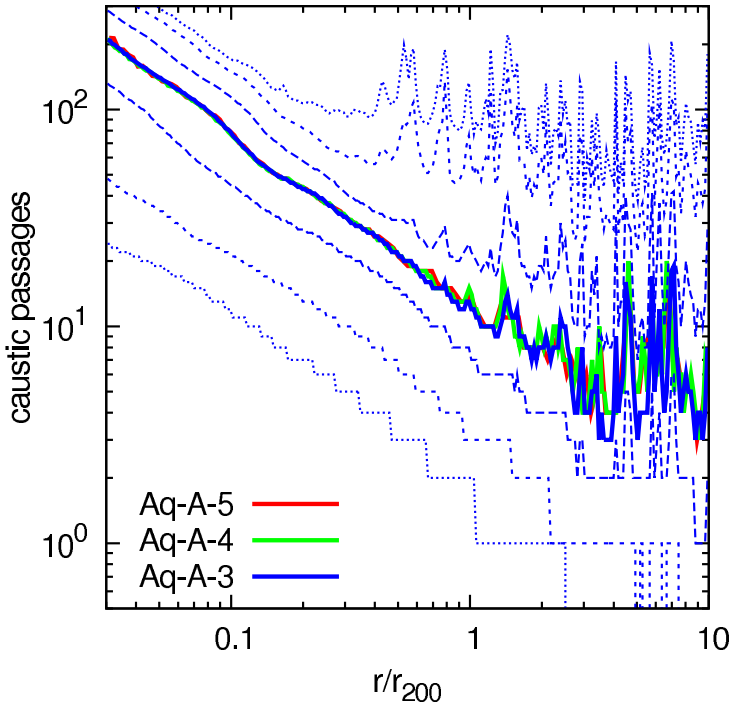

Figure 8.4: Median number of caustic passages (solid thick lines) in Aq-A as a function of radius. In the outer part the subhaloes show up as peaks. As in the isolated halo case the number of caustic passages increases towards the centre of the halo. The convergence between the different resolutions is good and demonstrates that the caustic identification is very stable against numerical parameters. The thin lines show the 25%, 5% and 1% quantiles.

density simplifies to

$$\rho = \frac{\rho_0'}{a^3 \left|\det\left(\underline{\underline{D}}'_{x'q'}\right)\right|}. \tag{8.20}$$

In the following we will assume a vanishing peculiar velocity sheet and stick to the zeroth order approximation. Furthermore we assume that the initial stream density equals the background density

$$\rho_0 = \frac{3H(t_{\text{initial}})^2}{8\pi G}, \tag{8.21}$$

in agreement with zeroth order assumption. For simplicity, we will assume these initial conditions for the fine-grained phase-space setup in the following. We note that these assumptions are reasonable in the $\delta \ll 1$ regime where we start our simulation.

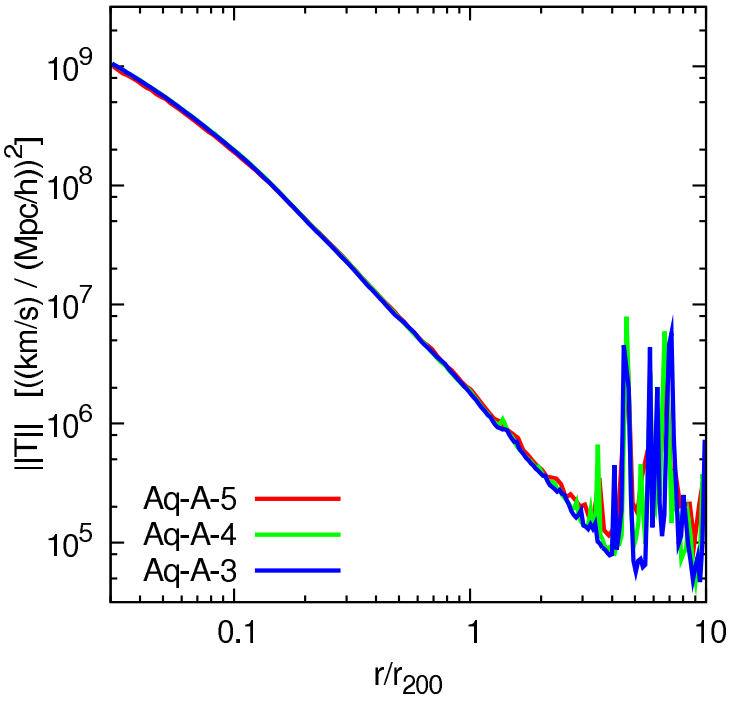

Figure 8.5: Median matrix norm of the tidal tensor for the halo at $z = 0$. The tidal field agrees very well between the different resolutions. As expected it rises in subhaloes and towards the main halo centre.

8.4 Results

The following results are based on simulations of the Aq-A halo in level 3,4 and 5. Details on the setup and numerical parameters for these initial conditions can be found in chapter 4 and Springel et al. (2008a). Furthermore, we assume a neutralino with a velocity dispersion of 0.03 cm/s today, as we did in the previous chapter. This corresponds to a neutralino mass of 100 GeV/c^2. Due to the noise sensitivity of the GDE, we use a significantly larger softening length than usually chosen. For the three runs we used a Plummer-equivalent softening length of 2.5 kpc/h. We will demonstrate in the following that we reach convergence for the level 3 run with this setup. A smaller softening length requires a larger particle number to achieve convergence.

In Fig. 8.1 we show the spherically averaged density profile of the halo at redshift $z = 0$ for all three resolutions. A more detailed study of the coarse-grained structure of the Aquarius haloes can be found in Navarro et al. (2010). The three resolutions shown in Fig. 8.1 convergence very well over the plotted radial range. We note that Navarro et al. (2010) already demonstrated that the coarse-grained features of the Aquarius haloes convergence very well for many properties.

As demonstrated in the previous chapters, the GDE allows to calculate the number of caustics passed by each simulation particle. As in physical coordinates caustics can be identified by observing sign changes in the determinant of the comoving configuration-space distortion tensor. In Fig. 8.2 (top panel) we show the distribution of caustic passages in a phase-space diagram at redshift $z = 0$. The colour encodes the number of caustic

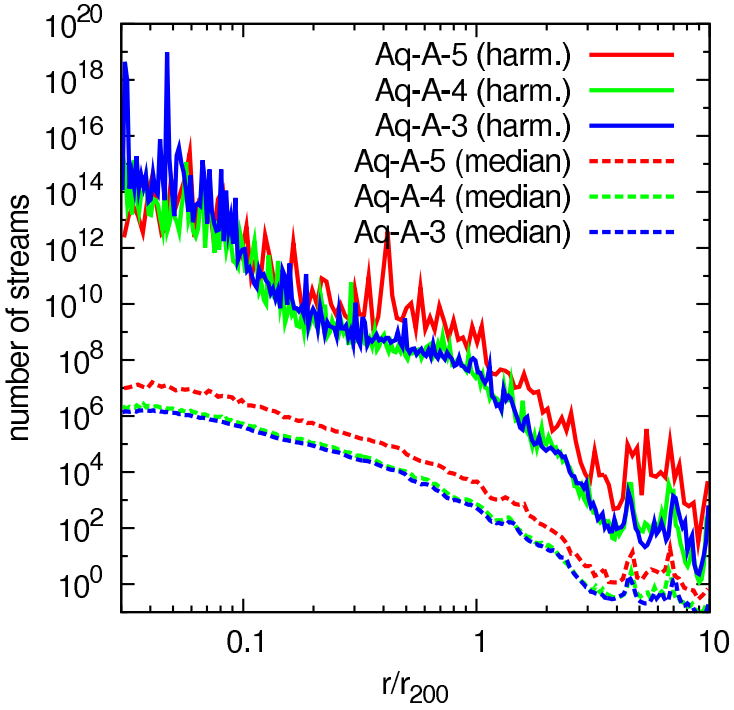

Figure 8.6: Number of streams in Aq-A as a function of radius (solid lines). The stream number estimate is based on the stream density of individual simulation particles and therefore quite sensitive to numerical parameters. This is the reason why the Aq-A-5 simulation has not yet converged, whereas the Aq-A-3 and Aq-A-4 simulations agree reasonably well. The stream number is a lot higher than in the isolated halo simulation of the last chapter (see Fig. 7.15). The dashed lines show the stream number based on the median (half-mass) stream density.

passages of each particle as indicated by the colour bar. The particles were sorted by their internal caustic counter before plotting them onto the phase-space diagram: particles with the highest caustic counter are plotted last. This phase-space diagram can be compared to Fig. 7.11, the corresponding phase-space portrait for an isolated halo in the previous chapter. In both cases the number of caustic passages increases towards the centre of the halo due to the shorter dynamical timescales. The caustic counter measures the dynamical age of the particles since it is directly proportional to the number of orbits. The most important difference between the isolated and the ΛCDM halo lies in the occurrence of substructure in the form of subhaloes and associated subhalo tidal streams that are not visible in the isolated halo. Subhaloes clearly stand out in Fig. 8.2 since they have undergone many caustic passages. The increase of caustic passages is simply due to the higher mixing in subhaloes. This process is schematically demonstrated in Fig. 8.2 (bottom panel). In Fig. 8.3 we show a zoom into the phase-space structure of a prominent subhalo. We note that the visible tidal streams are not the same as the fine-grained streams. These are not visible in the phase-space plots, because there is a huge number of (fine-grained) streams as we are going to show below.

A radial profile of the number of caustic passages is presented in Fig. 8.4. There, the outermost subhaloes also show up as peaks in the caustic counter. We show the profiles for Aq-A-3,4 and 5. As we demonstrated already in the previous chapters, the number

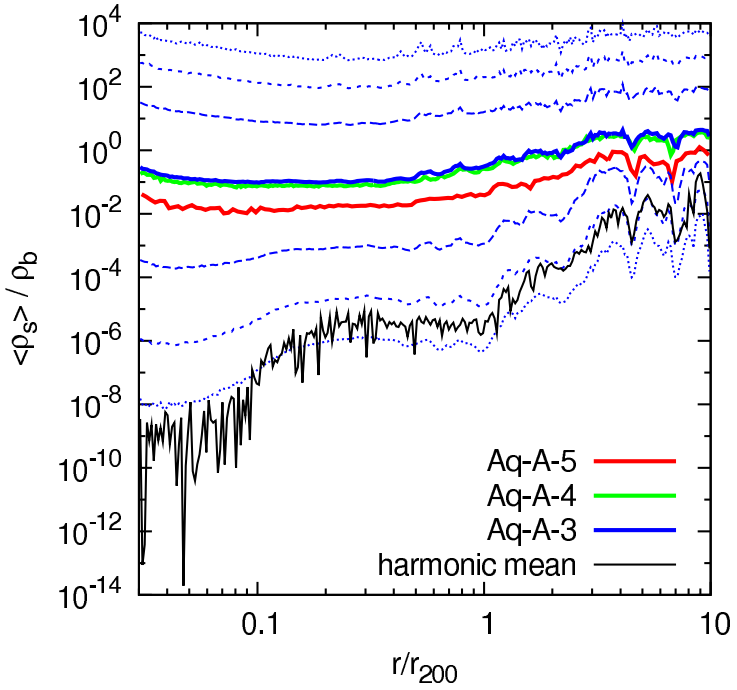

Figure 8.7: Median stream density (solid thick lines) as a function of radius. The slight rise of the stream density at the smallest radii is a softening effect. The Aq-A-5 run has not yet converged. The Aq-A-3 and -4 results agree quite well. The thin blue lines show the 25%, 5% and 1% quantiles. The black line shows the harmonic mean that is also used to calculate the typical number of streams at a given radius in Fig. 8.6.

of caustic passages is very stable w.r.t. numerical parameters. This is the reason why the three resolutions in Fig. 8.4 agree quite well, especially in the inner part of the halo. The number of caustic passages in Aq-A is about two times higher than in the isolated halo of the previous chapter (see Fig. 7.14). This is because of the additional phase-space sheet winding on small-scales that is absent for the halo growing from self-similar initial conditions of chapter 7.

The distortion of the local phase-space and configuration-space elements of each simulation particle is driven by the tidal tensor. In Fig. 8.5 we show the radial profile of the euclidean matrix norm of the peculiar tidal tensors for all simulation particles. This rises towards the centre of the halo and also peaks in the outermost subhaloes. It is the tidal field that stretched the phase-space sheet. As for the caustic counter, the tidal field agrees pretty well between the different runs. This shows that the driving term of the GDE converges well between the different resolutions.

Besides the caustics it is important to know how many streams are expected at a given radius in the halo. We can calculate the number of streams at a given radial distance from the centre as described in the previous chapter by dividing the mean halo density by the harmonic mean of stream densities in each radial bin. In Fig. 8.6 we show the radial profile of the expected number of streams in the halo. As we demonstrated already in the previous chapters, the stream density is quite sensitive to numerical parameters, because its calculation involves all elements of the six-dimensional phase-space distortion

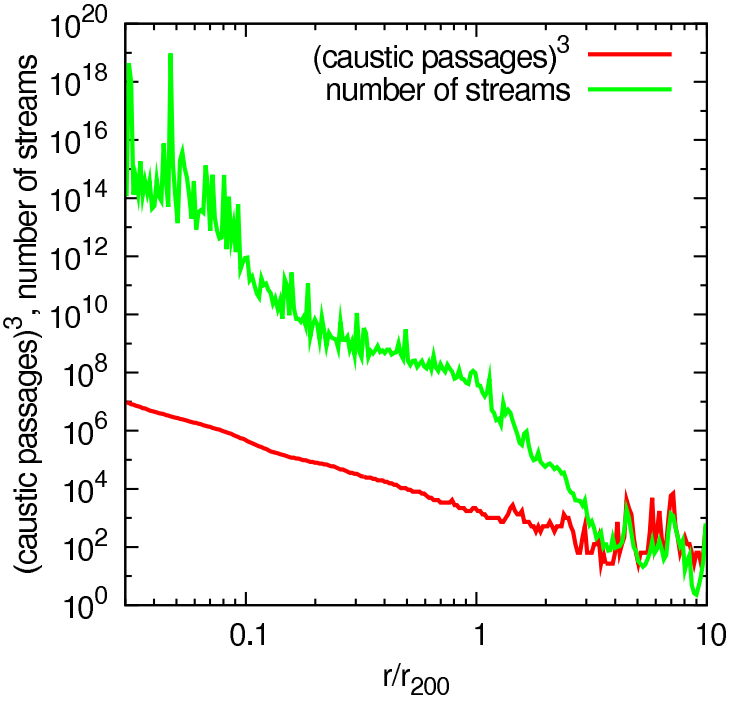

Figure 8.8: Number of streams and caustic passages. Both a high stream density and a high number of caustic passages are due to a strong phase-space sheet winding. It is therefore expected, that places of high stream number also show a high number of caustic passages. To make this clearer, we cubed the caustic counter. In the outer part, where the subhaloes are clearly visible, the relation can nicely be seen.

tensor. The different runs in Fig. 8.6 do not agree. Only the level 3 and 4 runs agree quite well. Aq-A-5 is clearly not converged yet. For this particular setup the combination of softening length and particle number produces too much noise in the tidal field. And this leads to a faster decaying stream density. This is demonstrated in Fig. 8.7, where we show the median stream density for the three different runs as a function of radius. The Aq-A-5 clearly produces lower stream densities, whereas Aq-A-3 and -4 agree quite well. For Aq-A-3 we also show different quantiles (thin blue lines) to quantify the distribution. Due to the tail to very low stream densities the harmonic mean of the stream densities in a radial bin is very small at the centre. For that kind of stream density distribution the median is significantly larger than the harmonic mean. The dashed lines in Fig. 8.6 show the number of streams calculated based on the median stream density: we divided the mean halo density by the median stream density. This leads to a lower number of streams. The general reason for the higher stream number in Aq-A compared to the isolated halo of chapter 7 is related to the ΛCDM initial conditions. Small-scale structure enhances the stretching of the phase-space sheet, and the three-dimensional character of the motion in the halo is retained. This leads to a decrease in stream density and therefore to an increase in the number of streams at a given radius.

Clearly, the median number of caustic passages must be correlated to the typical number of streams at a given position in the halo. The reason for this is that both numbers depend on the winding of the phase-space sheet. We demonstrate this relation

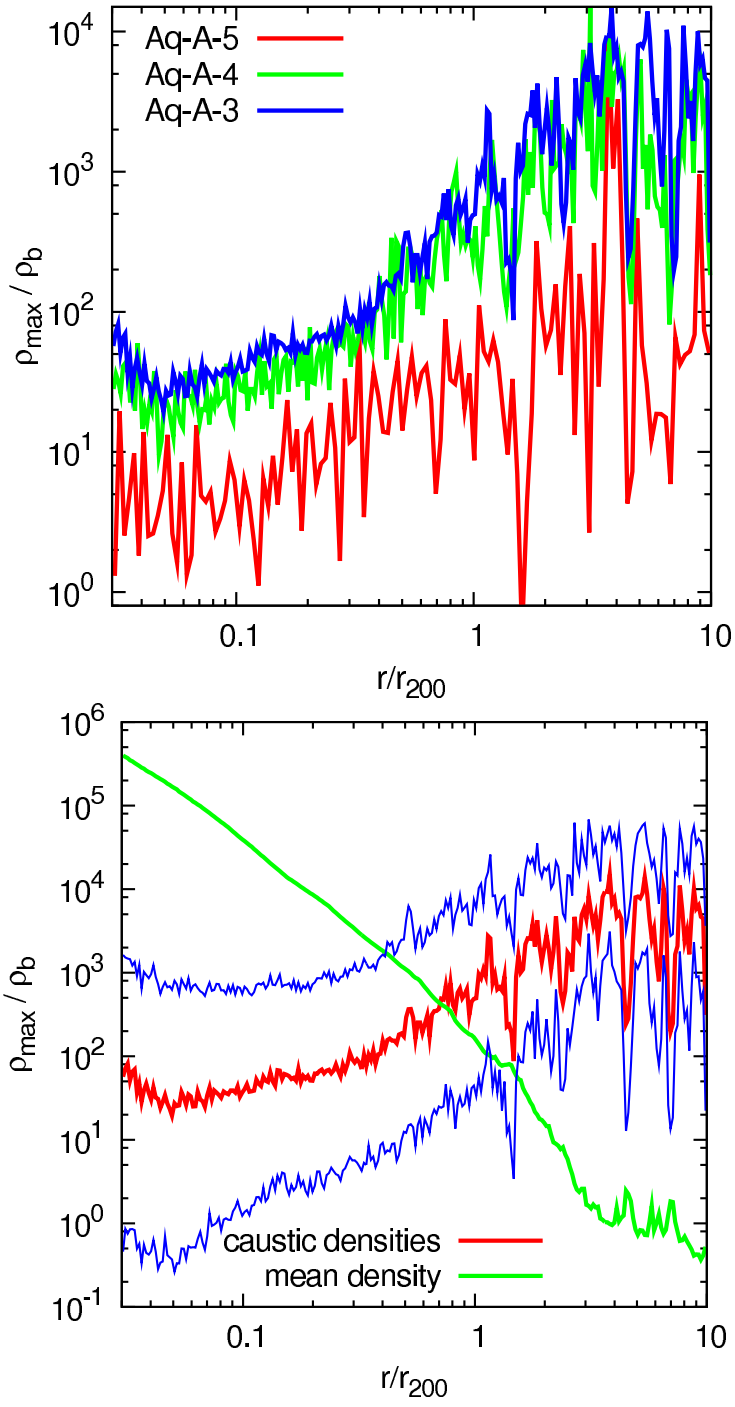

Figure 8.9: Top panel: Radial profile of the maximum caustic density for the three different resolutions. As for the stream density and number of streams, the Aq-A-5 run has not yet converged. Bottom panel: Mean density and caustic density profile for Aq-A-3 including the quartiles of the caustic density (thin blue lines). Beyond the virial radius, the densities of caustics are higher than the mean density. In the inner halo, caustic densities are very small compared to the mean density.

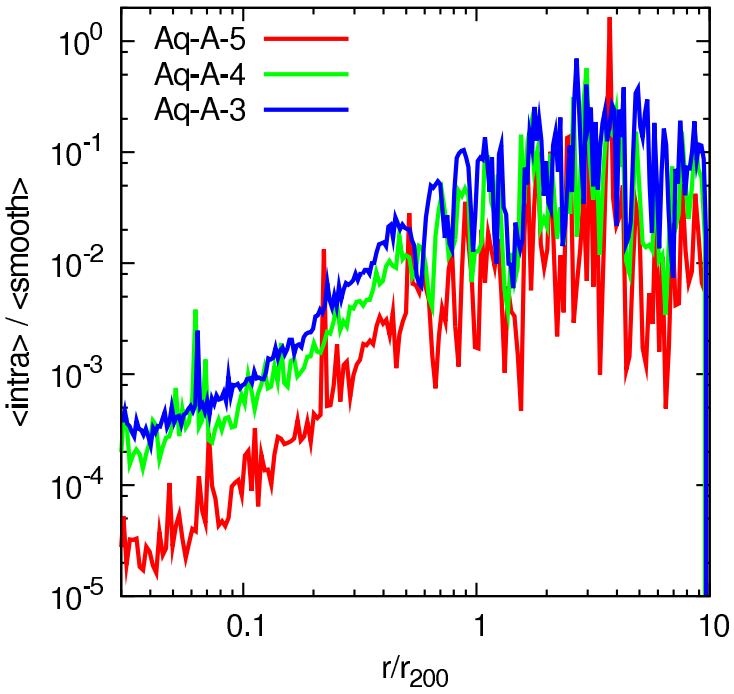

Figure 8.10: Local ratio of the intra-stream annihilation rate to the smoothed annihilation rate as a function of radius. The smoothed annihilation rate is calculated from an SPH-based density estimate using 64 neighbours. This boost factor profile shows that caustics play essentially no role for the dark matter annihilation in the inner halo.

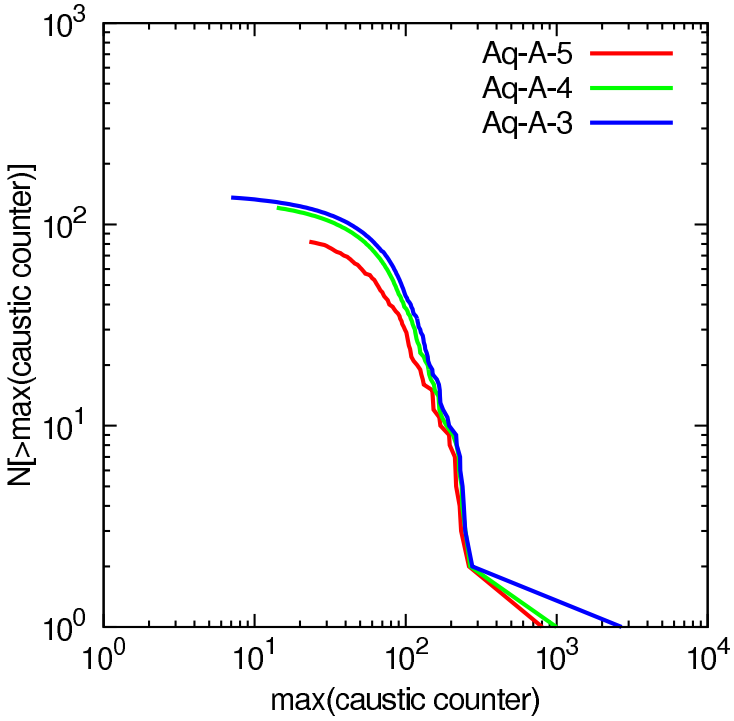

Figure 8.11: Maximum caustic counter function for all subhaloes of Aq-A-3,4,5. The convergence between the different resolution is quite good. We show all subhaloes of the halo FoF group.

in Fig. 8.8, where we plot both the median caustic counter and the number of streams as a function of radius. To make the relation more obvious we cubed the caustic counter. The plot clearly shows that places of strong phase-space sheet winding, subhaloes in the case here, are associated with a large number of streams and a high number of caustic passages.

The importance of caustics for the annihilation radiation of the halo depends on their number and their density . In Fig. 8.9 we focus on the median maximum caustic densities. The top panel plot shows the result for the three different resolutions Aq-3,4,5. Again, it is obvious that Aq-A-5 does not converge, whereas the level 3 and 4 runs agree reasonably well. In the bottom panel we compare the mean density profile of Aq-A-3 with the maximum caustic density profile. The thin blue lines show the quartiles of the maximum caustic densities. Caustics in the inner part of the halo have a density that is significantly lower than the mean density profile of the halo.

Due to the low caustic density in the inner halo, we do not expect a large annihilation radiation boost. This was already the case for the isolated halo studied in the previous chapter. The corresponding boost factor profile for Aq-A is shown in Fig. 8.10 for the different resolutions. The convergence between the level 3 and 4 is good, whereas level 5 is clearly off. Furthermore, the figure shows, that indeed the boost of annihilation radiation in the inner halo is very small. Only beyond the virial radius we can expect a boost of the order 0.1 due to caustics. We note that this is already significantly smaller than the boost expected from the isolated halo calculation of the last chapter. The reason for this is the substructure that was not included in the self-similar calculation of the previous chapter.

In Fig. 8.11 we show the maximum caustic counter function of all subhaloes of the Aq-A FoF group for the different resolutions. This plot therefore shows how many subhaloes with a given maximum caustic counter exist within the main halo. The plot includes all subhaloes of the main FoF group. Due to the good convergence of the caustic counter characteristic, the results in this figure converge quite well, especially for the highest resolutions.

As we already pointed out, the caustic counter is proportional to the dynamical timescale, as demonstrated more clearly in Fig. 8.12 (top panel), where we plot the highest subhalo particle SPH density against the maximum caustic counter of the subhalo particles. Since the dynamical time scales like $1/\sqrt{\rho}$, we expect more caustic passages in the denser subhaloes. And this trend is visible in Fig. 8.12 (top panel). The bottom panel of Fig. 8.12 shows a similar relation. Here we plot the maximum caustic counter of each subhalo against the subhalo mass. More massive subhaloes tend to undergo more caustic passages. The plots of Fig. 8.12 include all subhaloes of the main FoF group.

8.5 Conclusion and Discussion

We have used the GDE to study the fine-grained phase-space structure of a cold dark matter halo forming in the ΛCDM cosmology. Our simulations used the Aquarius Aq-A initial conditions in three different resolution levels: Aq-A-3,4,5. We showed that discreteness effects are under control for all relevant fine-grained properties. The level 3 and 4 runs

show good agreement in all fine-grained characteristics. We used the stream density of the individual simulation particles to estimate the number of streams as a function of radius. At the virial radius we find about 10^7 streams. The velocity distribution is expected to be very smooth with no sign of individual streams. We do not find any dense caustics in the centre of the halo. At the virial radius the maximum caustic density is comparable to the mean halo density, whereas at 10% of the virial radius the caustic density is already a factor 10^4 smaller than the mean density. The contribution of caustics to the annihilation radiation at the turnaround radius is about 10%, but well below 0.1% at 10% of the virial radius. Outside the virial radius the caustic annihilation contribution can nearly reach 100%, and double the expected mean annihilation radiation.

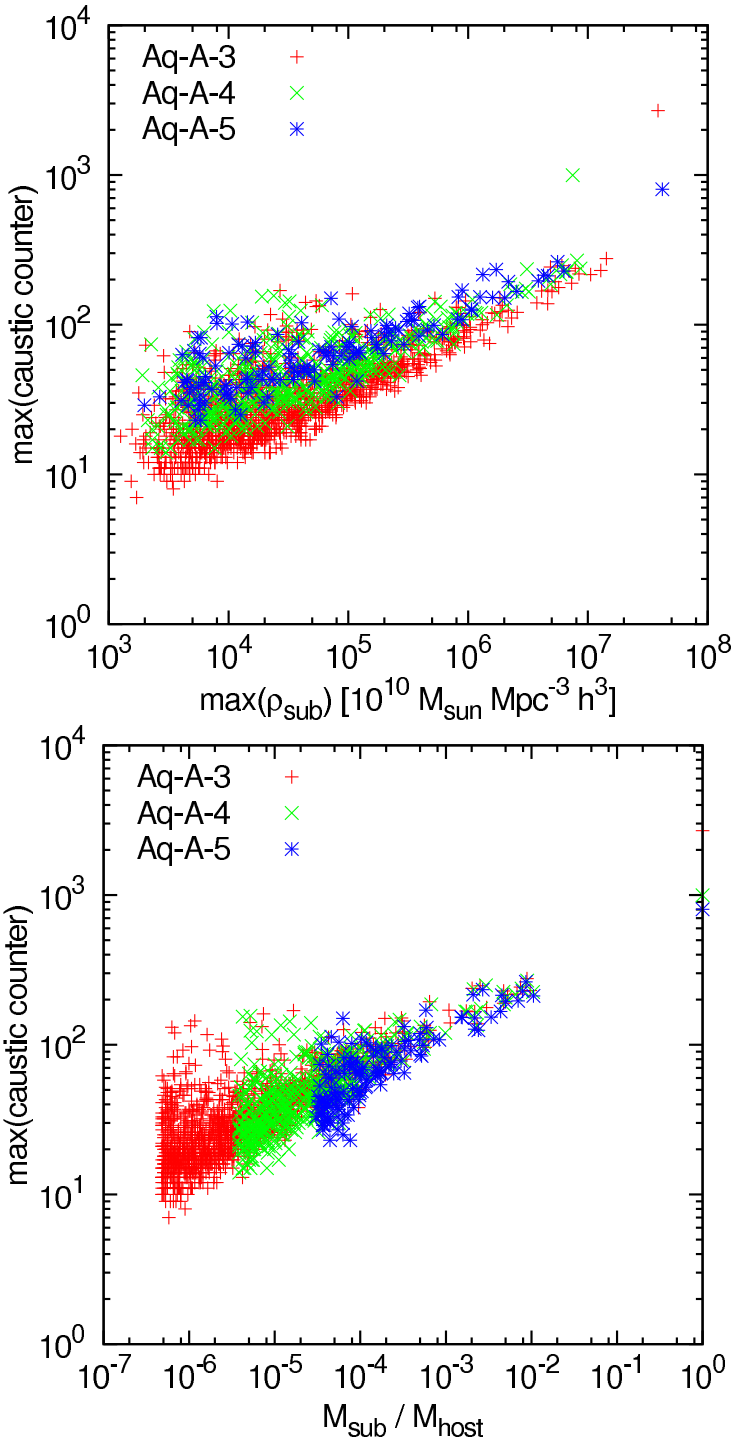

Figure 8.12: Top panel: Maximum caustic counter of a subhalo against the highest SPH particle density in the subhalo. There is a clear correlation between higher subhalo density and higher caustic counter. Bottom panel: Similar plot showing the maximum caustic counter of a subhalo against the subhalo mass. In both cases we show all subhaloes of the halo FoF group.

Part IV

Conclusions

9 Conclusions

In this thesis we studied the phase-space structure of cold dark matter haloes. We used computer simulations to predict the expected phase-space structure of these haloes near the Sun. This information is of great importance for the current search for dark matter particles.

We started with a detailed analysis of the coarse-grained phase-space structure of six simulated cold dark matter haloes that are supposed to be similar to the dark matter halo of our own Galaxy, the Milky Way. Our focus was on the phase-space structure near the position of the Sun. We have measured the probability distribution function of the dark matter mass density between 6 and 12 kpc from the centre of the halo, finding it to be made up of two components: a truly smooth distribution, which scatters around the mean on ellipsoidal shells by less than 5% in all the haloes of our sample, and a high-density tail associated with subhaloes. The smooth dark matter component dominates the local dark matter distribution. With 99.9% confidence we can say that the Sun lies in a region where the density departs from the mean on ellipsoidal shells by less than 15%. Experimentalists can safely adopt smooth models to estimate the dark matter density near the Sun.

Furthermore, we found that the local velocity distribution is also expected to be very smooth, with no sign of massive streams or subhalo contributions. The standard assumption of a Maxwellian velocity distribution is not correct for our haloes, because the velocity distribution is clearly anisotropic. The velocity ellipsoid at each point aligns very well with the shape of the halo. A better fit to the simulations is given by a multivariate Gaussian. Even this description does not reproduce the exact shape of the distributions perfectly. In particular, the modulus of the velocity vector shows marked deviations from such model predictions. Velocity distributions in our six different haloes share common features with respect to the multivariate Gaussian model: the low-velocity region is more populated in the simulation; the peak of the simulation distribution is depressed compared to the Gaussian; at high velocities there is typically an excess in the simulation distribution compared to the best-fit multivariate Gaussian. Furthermore, the velocity

distribution shows features that are stable in time, are reproduced from place to place within a given halo, but differ between different haloes. These are related to the formation history of each individual halo.

The imprints in the modulus of the velocity vector reflect features in the energy distribution. We explicitly show that the phase-space distribution function as a function of energy contains characteristic wiggles. The amplitude of these wiggles with respect to the average distribution function of our sample of six haloes rises from high to low-binding energies. The weakly bound part of the distribution, on the other hand, can deviate in any given halo by an order of magnitude from the mean.

We have used our simulations to predict detector signals for WIMP and axion searches. We find that WIMP recoil spectra can deviate about 10% from the recoil rate expected from the best-fit multivariate Gaussian model. The energy dependence of these deviations looks similar in all six haloes; especially at higher binding energies. We find that the annual modulation signal peaks around the same day as expected from a multivariate Gaussian model with no clear trend over our halo sample for varying recoil velocity thresholds. The maximum recoil modulation amplitude, on the other hand, shows a clear threshold-dependent difference between the signal expected for a multivariate Gaussian model and that estimated from the simulation. We have also explored the expected signal for direct detection of axions. We find the axion spectra to be smooth without any sign of massive streams. The spectra show characteristic deviations from those predicted by a multivariate Gaussian model; the power at low and high frequencies is higher than expected. The most pronounced effect is that the spectra peak at lower frequencies than predicted. Since the frequencies in the axion detector are directly proportional to the kinetic energy of the axion particles, the bumps in the dark matter velocity and energy distributions are also clearly visible in the axion spectra. All the effects on the various detector signals are driven by differences in the velocity distribution. Individual subhaloes or streams do not influence the detector signals, however, since they are sub-dominant by a large factor in all six haloes.

Our study of the coarse-grained phase-space structure shows that once direct dark matter detection has become routine, the characterisation of the dark matter energy distribution will provide unique insights into the assembly history of the Milky Way halo. In the next decade, a new field may emerge, that of "dark matter astronomy".

In the next part of this thesis we refined our analysis and presented a method to go beyond the coarse-grained phase-space analysis. This is important because direct dark matter detection experiments operate on length-scales far below the resolution of current structure-formation simulations. The fine-grained phase-space structure on these scales will determine the signal they see. In addition, small-scale structure can substantially enhance the annihilation signal that is the target of current indirect detection experiments. A better understanding of such structure within the current concordance ΛCDM cosmology is thus critical for analysing and interpreting all current dark matter searches.

We proposed a new route to tackle these issues. Rather than improving simulations simply by increasing the number of particles, we attached additional information to each particle, namely a phase-space distortion tensor which allows us to follow the evolution of the fine-grained phase-space distribution in the immediate neighbourhood of the particle. We introduced the geodesic deviation equation (GDE) as a general tool for calculating the

evolution of this distortion along any particle trajectory. The projection from phase-space to configuration-space yields the density of the particular cold dark matter stream that particle is embedded in and can also identify when the particle passes through a caustic.

This technique makes the fine-grained phase-space structure accessible. It enables studies of the phase-space structure of general non-integrable static potentials which reproduce all the results previously obtained using frequency analysis methods, identifying chaotic regions and finding substructure in regular regions in the form of resonances. In addition, it can be used to quantify mixing rates and to locate caustics. We demonstrated these capabilities for the complex phase-space structure of the ellipsoidal logarithmic potential with a core. All relevant phase-space regions could be identified by solving the GDE along the orbit. We have written a code, DaMaFlow, that allows us to carry out such stream density analyses for a wide variety of potentials in a very efficient way.

Stream density evolution is very sensitive to the shape of the underlying potential. We demonstrated this by comparing results for a realistic cold dark matter halo with radially varying shape to those for a spherical halo with similar radial density profile. After 100 orbits the predicted stream densities in the inner regions differ by a factor of 100. In general we expected the stream densities to decrease as $(t/t_{\rm orbital})^{-3}$ for regular orbits and even faster for chaotic orbits, rather than as $(t/t_{\rm orbital})^{-2}$, the result found for orbits in a spherical potential. Scaling to the Milky Way leads us to estimate that there should be at least 10^5 streams passing through the solar system.

The potentially revolutionary advantage of our approach, and our main reason for pursuing it, is that it applies equally well to non-symmetric, non-static situations of the kind that generically arise in cold dark matter cosmologies. Indeed, it can be implemented in a relatively straightforward way in current state-of-the-art cosmological N-body codes. We have carried out such an implementation in the GADGET code and have presented some tests based on equilibrium Hernquist models. The N-body implementation is able to conserve 6-D phase-space density to high accuracy along individual particle orbits. In addition, it qualitatively reproduces the results found in the corresponding smooth potential for the evolution of stream density along individual orbits, and it reproduces the statistical results found for ensembles of orbits to impressive accuracy. The identification of caustic passages is particularly robust, showing very little dependence on N-body parameters such as particle number and softening. Thus discreteness effects appear to be well under control, at least for the large N systems studied here.

We have also developed the mathematical background to enable a relatively precise evaluation of the annihilation radiation from dark matter caustics in fully general simulations of the nonlinear growth of structure. Our scheme allows the annihilation rate to be integrated along the trajectory of each simulation particle, including correctly the contributions from all the caustics in which it participates. Typically each particle experiences several such caustic passages in each orbit around the dark matter halo in which it resides as we demonstrated in chapter 5. In order to include correctly the annihilation rate between particles that are members of different streams, it is necessary to estimate a local coarse-grained density at the position of each particle, and to add in the contribution due to streams other than its own. This can be done, for example, using the SPH technique, since the smoothing this introduces does not bias the luminosity predicted from inter-stream annihilations. When a particle passes through a caustic occurring in a

stream other than its own, the time-integrated annihilation probability is still correctly reproduced in the smoothed system.

In the remaining chapters, we applied these methods to analyse the fine-grained phase-space structure of haloes forming in different cosmological frameworks.

In a first attempt, we analysed the phase-space structure of haloes forming from spherical symmetric self-similar initial conditions in an Einstein-de Sitter cosmology. We could show that such objects do not evolve according to the well-known one-dimensional similarity solutions, that is predicted analytically. Rather, they turn into highly elongated bars as a result of the radial orbit instability. These bars have mean mass density and total velocity dispersion profiles which are very similar to those of the relevant similarity solutions, but the loss of spherical symmetry results in orbits that fill a 3D volume and along which the stream density typically decreases as $1/t^3$ rather than as $1/t$ as in the similarity solution. At any given time, typical stream densities decrease slightly towards the centre of our simulation, whereas they increase strongly in the similarity solution. As a consequence, there are many more streams in the inner regions of the simulation than in the similarity solution. At 1% of the turnaround radius we found $\sim 10^6$ streams in the simulation but only about 100 in the similarity solution. This contradicts recent claims that the number of streams near the Sun should be relatively small (e.g. Natarajan and Sikivie, 2005) but agrees with the estimates of Helmi et al. (2003). The number of caustics changes much less dramatically between the two cases, with a few times more caustics in the inner regions of the simulation as in the comparable region of the similarity solution. This is as expected given the higher dimensionality of the simulation orbits.

The impact of caustics on the annihilation signal depends on their density and number. Caustic densities in our simulation are much smaller than in the similarity solution, but their abundance is only modestly increased. As a result, annihilation radiation from caustics is less important in 3D than in 1D. For example, within the radial range $r/r_{\rm ta} \in (0.01, 0.5)$ caustics contribute only 4% of the smooth annihilation signal. If we focus on the region containing the outermost caustics, $r/r_{\rm ta} \in (0.2, 0.5)$, this ratio is 64%, similar to that predicted by the similarity solution. Decreasing the velocity dispersion by 10 orders of magnitude from our standard value only increases the caustic contribution to the annihilation luminosity by a factor of about two. This is because the annihilation signal from caustic crossing depends only logarithmically on the dark matter velocity dispersion.

These results are based on a simplified and unrealistic halo formation model. However, haloes growing from ΛCDM initial conditions are expected to mix even more efficiently, because the fully three-dimensional character of orbits is retained and small-scale structure is expected to enhance the stretching of the phase-space sheets and hence to result in even greater dilution of their 3-densities. Thus, caustics will likely be less important in the ΛCDM case than in the simple isolated halo model discussed in the present chapter. This strengthens our conclusion that 1D similarity solutions are inadequate and misleading models for the evolution of the fine-grained structure of real dark matter haloes. This applies not only to the original self-similar solutions but also to spherically symmetric generalisations of them (e.g. Sikivie et al., 1995, 1997; Duffy and Sikivie, 2008). These still give qualitatively incorrect predictions for the dynamical dilution of stream densities.

The inclusion of baryons would affect the dynamics of the dark matter in the inner halo, but would neither change the dimensionality of the orbits nor substantially modify their characteristic timescales. Thus no qualitative changes in behaviour are expected. The somewhat shorter orbital timescales produced by compression of the inner halo are likely, if anything, to accelerate mixing. Our general conclusions should thus be unaffected.

In the last chapter of the thesis we used the GDE to study the fine-grained phase-space structure of a cold dark matter halo forming in the ΛCDM cosmology. Our simulations used the Aquarius Aq-A initial conditions in three different resolution levels: Aq-A-3,4,5. We showed that discreteness effects are under control for all relevant fine-grained properties. The level 3 and 4 runs show good agreement in all fine-grained characteristics. We used the stream densities of the individual simulation particles to estimate the number of streams as a function of radius. At the virial radius we find about 10^7 streams. We do not find any dense caustics in the centre of the halo. At the virial radius the maximum caustic density is comparable to the mean halo density, whereas at 10% of the virial radius the caustic density is already a factor 10^4 smaller than the mean density. The contribution of caustics to the annihilation radiation at the turnaround radius is about 10%, but well below 0.1% at 10% of the virial radius. Outside of the virial radius the caustic annihilation contribution can nearly reach 100%, and double the expected mean annihilation radiation.

Part V

Appendices

A

Mean phase-space density calculation

Here we give a brief description of our mean phase-space density estimation. Let $\mathcal{V}$ be an arbitrary volume in configuration-space. In addition, let $f(\underline{x}, \underline{v})$ be the phase-space density of the system under consideration and $\Phi(\underline{x})$ its potential energy. Now we ask what the typical phase-space density at energy E in $\mathcal{V}$ is. We therefore define the mean phase-space density $\bar{f}(E, \mathcal{V})$ in $\mathcal{V}$ at energy E in the following natural way

$$\bar{f}(E, \mathcal{V}) \quad \mathrm{d}\Gamma(E, \mathcal{V}) \quad \equiv \quad \mathrm{d}M(E, \mathcal{V}), \tag{A.1}$$

where $\mathrm{d}\Gamma(E, \mathcal{V})$ is the available phase-space volume in $\mathcal{V}$ for orbital energies in $(E, E+\mathrm{d}E)$, and $\mathrm{d}M(E, \mathcal{V})$ is the mass in $\mathcal{V}$ for these energies.

Let us first calculate the phase-space volume $\mathrm{d}\Gamma(E, \mathcal{V})$. To do this we must integrate over all available infinitesimal phase-space volume elements $\mathrm{d}\underline{x}\ \mathrm{d}\underline{v}$:

$$\begin{aligned}
\mathrm{d}\Gamma(E, \mathcal{V}) &\equiv \int\limits_{\underline{x}\in\mathcal{V}} \mathrm{d}\underline{x} \int\limits_{\frac{1}{2}v^2+\Phi(\underline{x})\in(E,E+\mathrm{d}E)} \mathrm{d}\underline{v} \\
&= \int\limits_{\underline{x}\in\mathcal{V}, E>\Phi(\underline{x})} \mathrm{d}\underline{x} \int\limits_{v\in(\sqrt{2(E-\Phi(\underline{x}))}, \sqrt{2(E+\mathrm{d}E-\Phi(\underline{x}))})} \mathrm{d}\underline{v} \\
&= \int\limits_{\underline{x}\in\mathcal{V}, E>\Phi(\underline{x})} \mathrm{d}\underline{x} \quad 4\pi \int\limits_{v\in(\sqrt{2(E-\Phi(\underline{x}))}, \sqrt{2(E+\mathrm{d}E-\Phi(\underline{x}))})} \mathrm{d}v \quad v^2 \\
&= 4\pi \int\limits_{\underline{x}\in\mathcal{V}, E>\Phi(\underline{x})} \mathrm{d}\underline{x} \quad \sqrt{2(E-\Phi(\underline{x}))} \quad \mathrm{d}E \\
&\equiv \quad g(E, \mathcal{V})\, \mathrm{d}E,
\end{aligned} \tag{A.2}$$

where we defined $g(E, \mathcal{V})$ as

$$g(E, \mathcal{V}) \;=\; 4\pi \int\limits_{\mathcal{V}, E>\Phi(\mathbf{x})} \mathrm{d}^3\mathbf{x} \;\sqrt{2\,(E-\Phi(\mathbf{x}))}. \tag{A.3}$$

The mass element $\mathrm{d}M(E, \mathcal{V})$ is given by the integral of $f(\underline{x}, \underline{v})$ over the volume $\mathcal{V}$ in the energy range $(E, E + \mathrm{d}E)$

$$\mathrm{d}M(E, \mathcal{V}) = \int\limits_{\underline{x}\in\mathcal{V}} \mathrm{d}\underline{x} \int\limits_{\frac{1}{2}v^2+\Phi(\underline{x})\in(E,E+\mathrm{d}E)} \mathrm{d}\underline{v} \quad f(\underline{x}, \underline{v}). \tag{A.4}$$

This quantity can be calculated by summing up the masses of all particles in $\mathcal{V}$ with energies in $(E, E + \mathrm{d}E)$. Putting all this together we get

$$\bar{f}(E, \mathcal{V}) \quad g(E, \mathcal{V})\,\mathrm{d}E \quad = \quad \mathrm{d}M(E, \mathcal{V}), \tag{A.5}$$

and this is equivalent to Eq. 4.1

$$\bar{f}(E, \mathcal{V}) \quad = \quad \frac{\mathrm{d}M}{\mathrm{d}E}(E, \mathcal{V}) \quad \frac{1}{g(E, \mathcal{V})}. \tag{A.6}$$

For the calculation in the haloes, we have chosen $\mathcal{V}$ to be a spherical shell between 6 and 12 kpc. We note that we have checked explicitly that although both $\mathrm{d}M(E, \mathcal{V})$ and $g(E, \mathcal{V})$ depend strongly on the volume $\mathcal{V}$, the mean phase-space density $\bar{f}(E, \mathcal{V})$ depends only very weakly on this volume. In particular, we subdivided $\mathcal{V}$ into 2 kpc boxes $\mathcal{V}_i$ and verified that $\bar{f}(E, \mathcal{V}_i) \cong \bar{f}(E, \mathcal{V}_j)$ for all $i \neq j$. In addition, we calculated the mean phase-space density for thinner radial shells with boundaries between 6 and 12 kpc, finding good agreement independent of the radii chosen. Thus, in the region of interest our mean phase-space density depends weakly on the size and position of the averaging volume, so that $\bar{f}(E)$ has a well defined and intuitive meaning, which is (almost) independent of $\mathcal{V}$, whereas $\mathrm{d}M(E, \mathcal{V})$ and $\mathrm{d}M(E, \mathcal{V})/\mathrm{d}E$ do not. We chose to average over the thick spherical shell from 6 to 12 kpc in order to maximise the statistics for our analysis.

We note that for a system where $f(\underline{x}, \underline{v})$ is only a function of energy $f(E)$, our averaging consistently recovers the correct phase-space density, since Eq. A.4 then becomes

$$\mathrm{d}M(E, \mathcal{V}) = f(E) \quad \mathrm{d}\Gamma(E, \mathcal{V}), \tag{A.7}$$

so that $\bar{f}(E, \mathcal{V}) = f(E)$ for arbitrary volume $\mathcal{V}$. The fact that we find $\bar{f}(E, \mathcal{V})$ to be almost independent of $\mathcal{V}$ for our triaxial systems implies that, when carrying out the averaging procedure outlined above, the weighting over the additional integrals I_2 and I_3 is not very sensitive to the size, shape and position of the averaging volume, at least for the kinds of volumes we have explored.

B

GDE analysis of the 1D self-similar infall

We start from the equations of motion in the similarity variables $\lambda = r/r_{\rm ta}$ and $\tau = t/t_{\rm ta}$ introduced by FG ($t_{\rm ta}$ and $r_{\rm ta}$ are the turnaround time and radius of the particle under consideration)

$$\frac{{\rm d}^2\lambda}{{\rm d}\tau^2} = -\frac{2}{9}\left(\frac{3\pi}{4}\right)^2 \frac{\tau^{2/(3\epsilon)}}{\lambda^2}\mathcal{M}\left(\frac{\lambda}{\Lambda}\right), \tag{B.1}$$

where $\mathcal{M}$ is the dimensionless enclosed mass, $\Lambda(\tau) = \tau^{\Theta}$ and $\Theta = 2/3 + 2/(9\epsilon)$. The initial conditions are $\lambda(1) = 1$ and ${\rm d}\lambda/{\rm d}\tau(1) = 0$, corresponding to the Lagrangian physical coordinates $q = r_{\rm ta}$ (radial distance) and $p = 0$ (radial velocity). The physical distortion tensor can be related to the equivalent tensor expressed in terms of similarity variables through

$$\begin{aligned} D_{rq} &= D_{\lambda\lambda_0}, & D_{rp} &= \frac{t}{\tau}D_{\lambda\lambda_0'}, \\ D_{vq} &= \frac{\tau}{t}D_{\lambda'\lambda_0}, & D_{vp} &= D_{\lambda'\lambda_0'}. \end{aligned} \tag{B.2}$$

$D_{\lambda\lambda_0}$ and $D_{\lambda\lambda_0'}$ are two solutions to the the geodesic deviation equation in two-dimensional phase-space

$$\widetilde{D}'' = \frac{2}{9}\left(\frac{3\pi}{4}\right)^2 \tau^{2/(3\epsilon)}\left(\frac{2\mathcal{M}(\lambda)}{\lambda^3} - \frac{1}{\lambda^2}\frac{{\rm d}\mathcal{M}(\lambda)}{{\rm d}\lambda}\right)\widetilde{D}, \tag{B.3}$$

where $\widetilde{D} = D_{\lambda\lambda_0}$ or $\widetilde{D} = D_{\lambda\lambda_0'}$. The initial conditions are $\widetilde{D}(1) = 1, \widetilde{D}'(1) = 0$ for $D_{\lambda\lambda_0}$ and $\widetilde{D}(1) = 0, \widetilde{D}'(1) = 1$ for $D_{\lambda\lambda_0'}$. The two missing tensor components are given by τ derivatives of $\widetilde{D}$. To determine the stream density as a function of τ we need the linear and second order terms

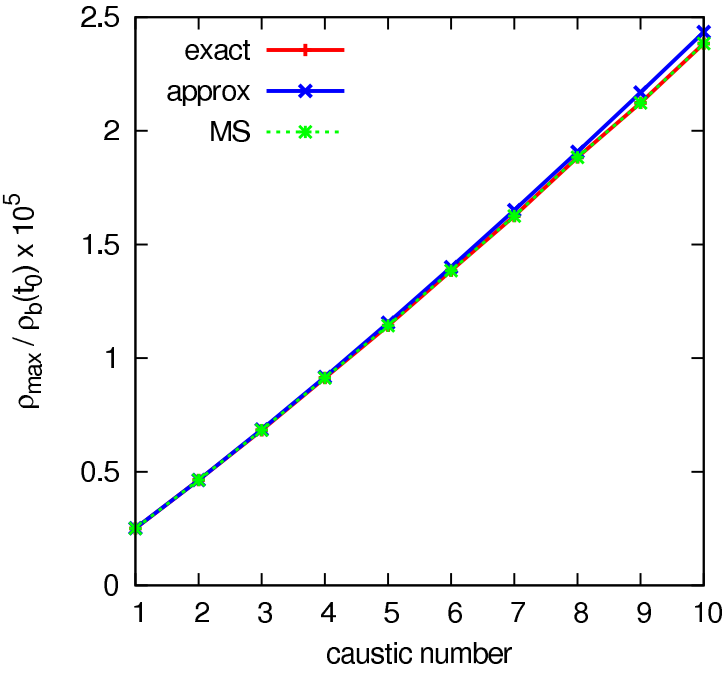

Figure B.1: Caustic density for the 1D similarity solution with $\epsilon = 1$. Red shows the densities using the exact $\partial^2 A/\partial v^2$ values from the solution, while the blue line shows the result using the Galilean-invariant estimate discussed in the text. The green line is the result obtained by Mohayaee and Shandarin (2006). The agreement of our results with those presented in Mohayaee and Shandarin (2006) shows that our different approaches to calculating densities at caustic passage give the same result.

$$\begin{aligned}\frac{\partial A}{\partial v} &= D_{\lambda\lambda_0} + \left(\frac{3\pi}{4}\right)^2 \frac{1}{3+1/\epsilon} D_{\lambda\lambda_0'},\\ \frac{\partial^2 A}{\partial v^2} &= -t_{\rm ta} D_{\lambda\lambda_0'}\ \frac{\tau^{1+\Theta}}{r_{\rm ta}\Theta^2}\left((1-\Theta)\frac{{\rm d}\lambda}{{\rm d}\tau} + \tau\frac{{\rm d}^2\lambda}{{\rm d}\tau^2}\right),\end{aligned} \tag{B.4}$$

where $A(q,p) = p - V(q)$ and $r_{\rm ta}$ is the current turnaround radius. The stream density for a particle is the integral of the phase-space density over velocity space. Using the linear and second order results from above, this yields

$$\rho_s(\tau) = \frac{\rho_0\ e^\beta K_{1/4}(\beta)}{\lambda^2\sqrt{2\pi}\sigma_0}\left|\frac{\partial A}{\partial v}\Big/\frac{\partial^2 A}{\partial v^2}\right|,\ \beta = \left(\frac{\partial A}{\partial v}\right)^4\Big/\left(2\frac{\partial^2 A}{\partial v^2}\sigma_0\right)^2 \tag{B.5}$$

for the central particle of a phase-sheet, where the factor $1/\lambda^2$ is due to the $1/(s_1 s_2)$ prefactor associated with the stretching of the non-caustic directions and $K_{1/4}$ is the modified Bessel function. The intra-stream annihilation rate contribution of a small mass element ${\rm d}M_i$ is given by ${\rm d}P_{\rm intra} = \rho_s(\tau)\ {\rm d}M_i$. Integrating over all mass elements yields the total intra-stream annihilation rate

$$P_{\rm intra} = \frac{2M_{\rm ta}}{3\epsilon}\int_1^\infty \frac{{\rm d}\tau}{\tau^{1+2/(3\epsilon)}}\rho_s(\tau), \tag{B.6}$$

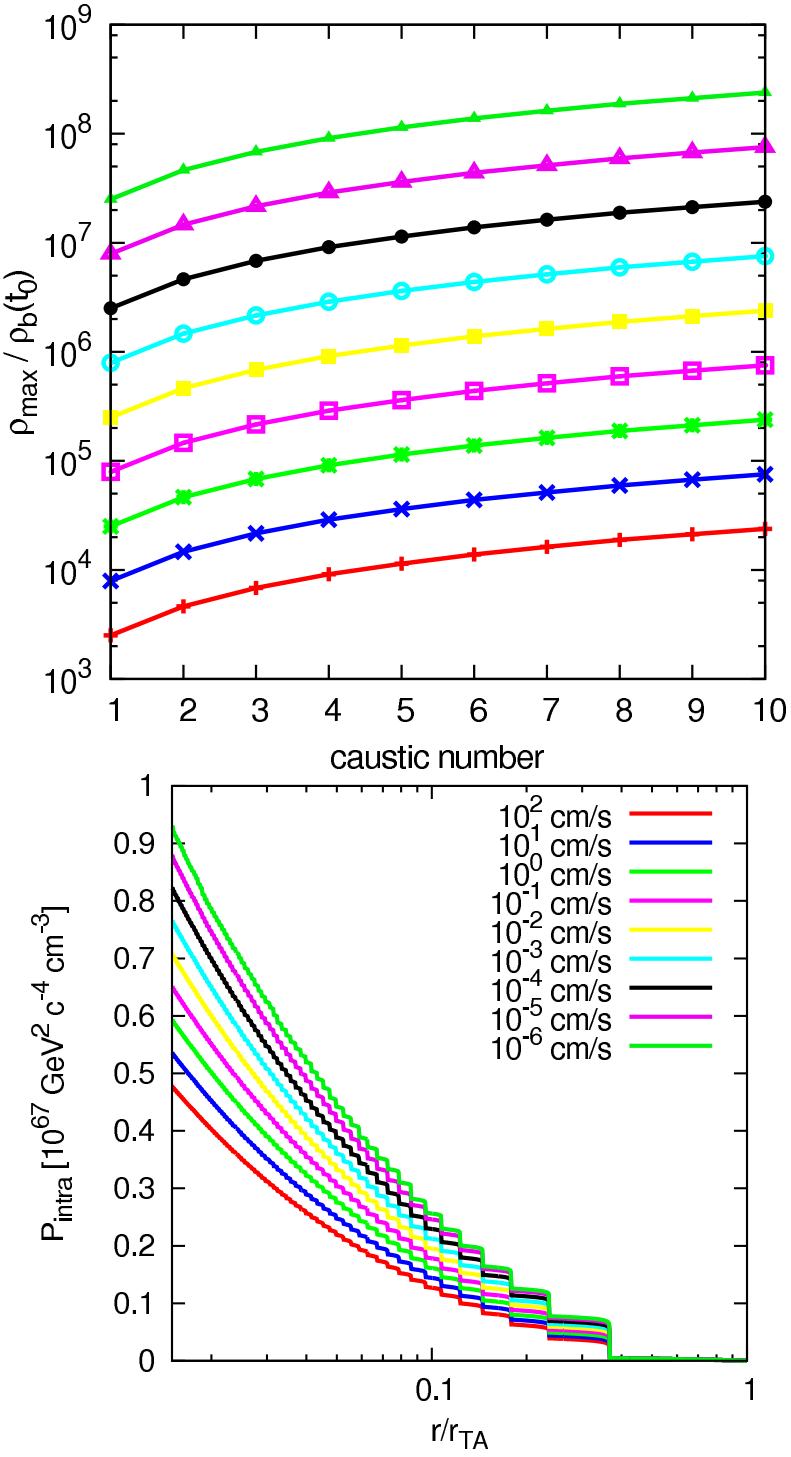

Figure B.2: Top panel: Density at caustic crossing in units of the cosmic mean density and for different velocity dispersions. Density scales like $1/\sqrt{\sigma_b}$ at each caustic. The dispersions differ by factors of 10 so that the caustic densities differ by factors of $\sqrt{10}$. Bottom panel: Cumulative intra-stream annihilation rate counted outside to inside for the same set of dispersions. Although the dispersions change by 8 orders of magnitude, the intra-stream annihilation rate only changes by a factor of 2 over the radial range shown. This is due to the logarithmic σ_b dependence of the annihilation contribution from caustic crossing.

where $M_{\rm ta}$ is the turnaround mass.

In Fig. B.1 we show the densities of the first 10 caustics calculated using this GDE approach. For comparison to previous work we have chosen $\epsilon = 1$ and $r_{\rm ta}(t_0) = 1400$ kpc. We used both the exact second-order term of the similarity solution and an estimate based on Galilean-invariant first-order quantities (see WV)

$$\left|\frac{\partial^2 A}{\partial v^2}\right| \sim \left|\frac{\partial A}{\partial x}\right| \frac{1}{|a|} = \left|\frac{\partial v}{\partial q}\right| \frac{1}{|a|}. \tag{B.7}$$

The green dashed line shows the results of Mohayaee and Shandarin (2006). All results show good agreement. In Fig. B.2 (top panel) we show the caustic density for velocity dispersions ranging from 10^2 cm/s down to 10^{-6} cm/s. The maximum density scales as $1/\sqrt{\sigma_b}$ (see WV) so that all lines in this plot are separated by a factor of $\sqrt{10}$. The bottom panel shows the corresponding cumulative intra-stream annihilation rate (outside to inside). Although the dispersion varies over eight orders of magnitude, the total intra-stream contribution only changes by about a factor of 2. This is a consequence of the logarithmic divergence of the intra-stream annihilation luminosity near caustics (see WV).

C

Sommerfeld enhancement effect

Here we briefly describe the mechanism of the Sommerfeld enhancement effect (SEE hereafter) that allows larger annihilation cross-sections for dark matter particles. The annihilation of dark matter particles can therefore be more efficient today than expected from the standard thermal cross-section that is deduced from relic abundance calculations. To present the basic features of the SEE we assume an attractive Yukawa type force mediated by a boson $\mathcal{B}$ between the dark matter particles. For non-relativistic s-wave annihilation we have to solve the radial Schrödinger equation (in natural units)

$$\frac{1}{m_p}\frac{\mathrm{d}^2\psi(r)}{\mathrm{d}r^2} + \frac{\alpha}{r}e^{-m_{\mathcal{B}}r}\psi(r) = -m_p\beta^2\psi(r), \tag{C.1}$$

where m_p is the dark matter particle mass, $m_{\mathcal{B}}$ the boson mass, α the force coupling constant, and $\beta = v/c$ the encounter velocity. It is convenient to rescale the radial coordinate according to $r \to \alpha m_p r$ so that the Schrödinger equation becomes

$$\frac{\mathrm{d}^2\psi(r)}{\mathrm{d}r^2} + \frac{1}{r}e^{-m_{\mathcal{B}}r/(\alpha m_p)}\psi(r) = -\frac{\beta^2}{\alpha^2}\psi(r) \tag{C.2}$$

with boundary condition

$$\psi \propto e^{i\beta r/\alpha} \qquad \text{as } r \to \infty. \tag{C.3}$$

The Sommerfeld enhancement S is then given by

$$S = \frac{|\psi(\infty)|^2}{|\psi(0)|^2}. \tag{C.4}$$

It is clear from the Schrödinger equation above, that the SEE only depends on two parameters that we denote by

$$a_1 = \frac{m_{\mathcal{B}}}{\alpha m_p}, \qquad a_2 = \frac{\beta}{\alpha}. \tag{C.5}$$

In general the equation needs to be solved numerically, but the characteristic features can be discussed analytically. In the Coulomb regime ($m_p\beta^2 \ll \alpha m_{\mathcal{B}}$) the Yukawa interaction can be approximated by an attractive Coulomb interaction for which an analytic solution in terms of hypergeometric functions exists. The Sommerfeld enhancement is then given by

$$S = \frac{\pi\alpha}{\beta}\left(1 - e^{-\pi\alpha/\beta}\right)^{-1} = \frac{\pi}{a_2}\left(1 - e^{-\pi/a_2}\right). \tag{C.6}$$

The $1/v$ dependence of the SEE in this regime is the reason why the SEE is also known as "$1/v$"' enhancement for small velocities $\beta \ll 1$. In the limit of vanishing interaction ($\alpha/\beta \ll 1$) the SEE disappears as $S \to 1$. The $1/v$ behaviour saturates for small β as a consequence of the finite range of the Yukawa interaction at a velocity $\beta \cong m_{\mathcal{B}}/m_p$.

At some a_1, a_2 combinations the Yukawa potential has bound states, at which there are large boosts to the annihilation cross-section which go approximately as $S \propto \beta^2$. These resonance states are also cutoff at small β.

As we already said the full solution of the Schrödinger equation above needs to be found by numerical integration. We can do this in the a_1, a_2 parameter plane. Such a parameter scan is shown in Fig. C.1. The horizontal lines in this plot are due to resonances, where the enhancement S can approach large values. In general, decreasing a_1 or a_2 increases S.

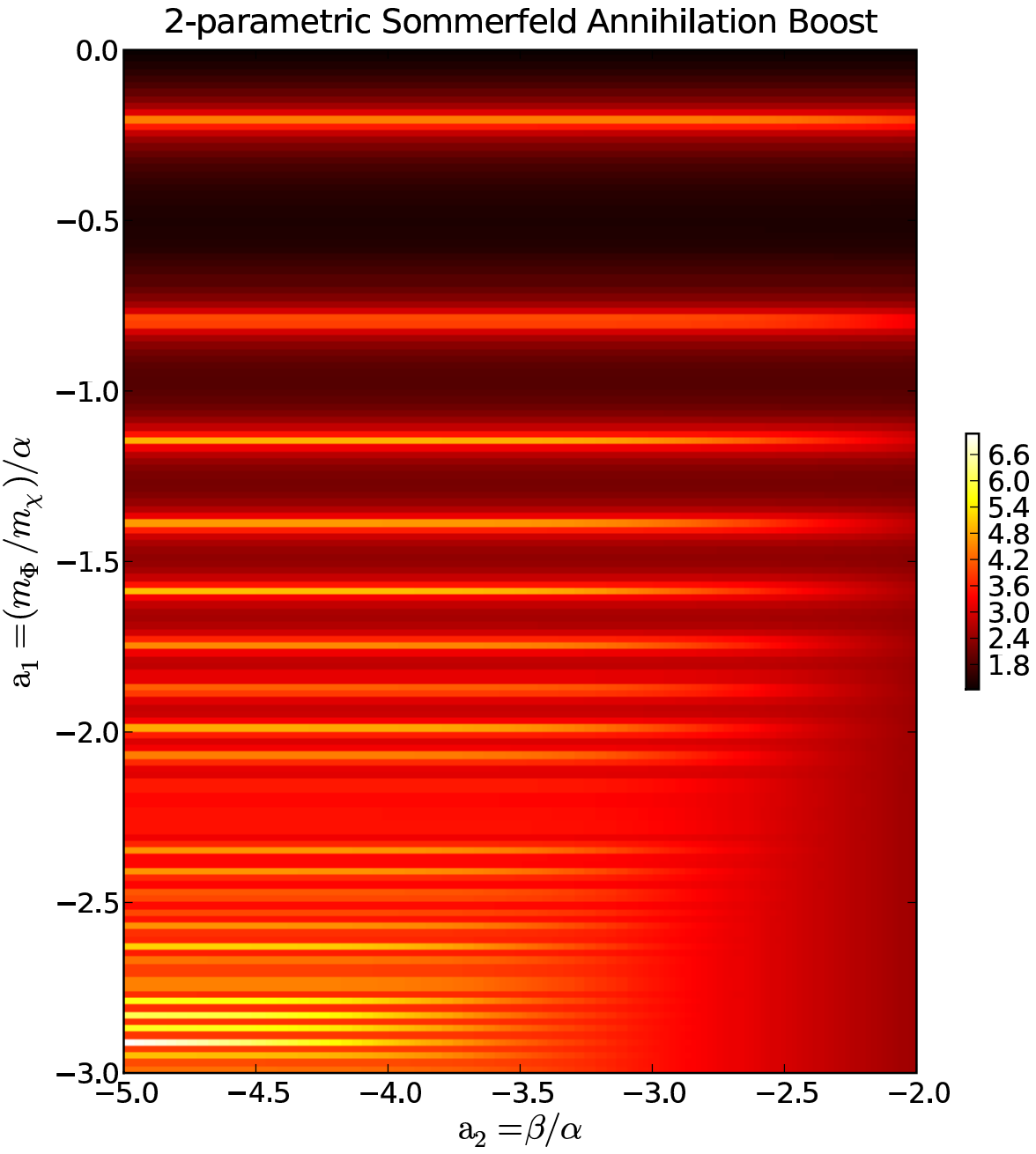

Figure C.1: Sommerfeld enhancement for different values of a_1 and a_2. The colour scale indicates the strength S of the enhancement. The horizontal lines with large S correspond to the resonances.

Acknowledgement

Many people helped me in various ways to finish this thesis. First of all, I want to thank my supervisor Simon D.M. White for accepting me as a PhD student, offering me a very exciting project and being enthusiastic and motivating during my time at MPA. Volker Springel always helped with any algorithmic or scientific problem. Amina Helmi helped me to understand my project a lot better especially in the first months of my thesis.

Besides these people, I want to thank the following individuals for ideas and interesting discussions: Raul Angulo, Mike Boylan-Kolchin, Stephane Colombi, Dima Docenko, Klaus Dolag, Margot Grossi, Eric Hayashi, Craig Hogan, Michal Maciejewski, Roya Mohayaee, Scott Tremaine, Jie Wang, Jesus Zavala.

Finally, I want to thank my parents and grandparents for their support.

Part VI

Bibliography

Bibliography

Aarseth, S. J., Turner, E. L., and Gott, III, J. R. (1979). N-body simulations of galaxy clustering. I - Initial conditions and galaxy collapse times. *ApJ*, 228:664–683.

Adams, F. C., Bloch, A. M., Butler, S. C., Druce, J. M., and Ketchum, J. A. (2007). Orbital Instabilities in a Triaxial Cusp Potential. *arXiv:astro-ph/0708.3101*, 708.

Ahmad, A. and Cohen, L. (1973). A numerical integration scheme for the N-body gravitational problem. *Journal of Computational Physics*, 12:389–402.

Akerib, D. S. and et al (2004). First Results from the Cryogenic Dark Matter Search in the Soudan Underground Laboratory. *Physical Review Letters*, 93(21):211301–+.

Alard, C. and Colombi, S. (2005). A cloudy Vlasov solution. *MNRAS*, 359:123–163.

Antonov, V. A. (1973). On the instability of stationary spherical models with merely radial motions. In *Dynamics of Galaxies and Star Clusters*, pages 139–143.

Aprile, E., Baudis, L., and Cabrera, B. (2007). Search for Weakly Interacting Massive Particles with CDMS and XENON. *Journal of Physics Conference Series*, 60:58–65.

Arkani-Hamed, N., Finkbeiner, D. P., Slatyer, T. R., and Weiner, N. (2009). A theory of dark matter. *Phys. Rev. D*, 79(1):015014–+.

Arnold, V. I., Shandarin, S. F., and Zeldovich, I. B. (1982). The large scale structure of the universe. I - General properties One- and two-dimensional models. *Geophysical and Astrophysical Fluid Dynamics*, 20:111–130.

Ascasibar, Y. and Binney, J. (2005). Numerical estimation of densities. *MNRAS*, 356:872–882.

Athanassoula, E., Fady, E., Lambert, J. C., and Bosma, A. (2000). Optimal softening for force calculations in collisionless N-body simulations. *MNRAS*, 314:475–488.

Bagla, J. S. (2002). TreePM: A Code for Cosmological N-Body Simulations. *Journal of Astrophysics and Astronomy*, 23:185–196.

Barnes, J. (1985). Dynamical instabilities in spherical stellar systems. In Goodman, J. and Hut, P., editors, *Dynamics of Star Clusters*, volume 113 of *IAU Symposium*, pages 297–299.

Bekenstein, J. D. (2004). Relativistic gravitation theory for the modified Newtonian dynamics paradigm. *Phys. Rev. D*, 70(8):083509–+.

Bellovary, J. M., Dalcanton, J. J., Babul, A., Quinn, T. R., Maas, R. W., Austin, C. G., Williams, L. L. R., and Barnes, E. I. (2008). The Role of the Radial Orbit Instability in Dark Matter Halo Formation and Structure. *ApJ*, 685:739–751.

Bergström, L., Edsjö, J., and Gunnarsson, C. (2001). Neutralino gamma-ray signals from accreting halo dark matter. *Phys. Rev. D*, 63(8):083515–+.

Bergström, L. and Hooper, D. (2006). Dark matter and gamma rays from Draco: MAGIC, GLAST and CACTUS. *Phys. Rev. D*, 73(6):063510–+.

Bernabei, R., Belli, P., Montecchia, F., Nozzoli, F., Cappella, F., Incicchitti, A., Prosperi, D., Cerulli, R., and et al (2007). DAMA at GRAN SASSO: Results and Perspectives. In Sissakian, A., Kozlov, G., and Kolganova, E., editors, *High Energy Physics: ICHEP '06*, pages 214–+.

Bertone, G., Hooper, D., and Silk, J. (2005). Particle dark matter: evidence, candidates and constraints. *Phys. Rep.*, 405:279–390.

Bertschinger, E. (1985). Self-similar secondary infall and accretion in an Einstein-de Sitter universe. *ApJS*, 58:39–65.

Bertschinger, E. and Gelb, J. M. (1991). Cosmological N-body simulations. *Computers in Physics*, 5:164–175.

Binney, J. and Merrifield, M. (1998). *Galactic astronomy.* Princeton University Press.

Binney, J. and Spergel, D. (1982). Spectral stellar dynamics. *ApJ*, 252:308–321.

Binney, J. and Tremaine, S. (2008). *Galactic Dynamics: Second Edition.* Princeton University Press.

Bode, P., Ostriker, J. P., and Xu, G. (2000). The Tree Particle-Mesh N-Body Gravity Solver. *ApJS*, 128:561–569.

Bovy, J. (2009). Substructure boosts to dark matter annihilation from Sommerfeld enhancement. *Phys. Rev. D*, 79(8):083539–+.

Capuzzo-Dolcetta, R., Leccese, L., Merritt, D., and Vicari, A. (2007). Self-consistent Models of Cuspy Triaxial Galaxies with Dark Matter Halos. *ApJ*, 666:165–180.

Carpintero, D. D. and Aguilar, L. A. (1998). Orbit classification in arbitrary 2D and 3D potentials. *MNRAS*, 298:1–21.

Carpintero, D. D. and Muzzio, J. C. (1995). Radial orbit instability in a Hubble-expanding universe. *ApJ*, 440:5–21.

Cirelli, M., Strumia, A., and Tamburini, M. (2007). Cosmology and astrophysics of minimal dark matter. *Nuclear Physics B*, 787:152–175.

Coles, P. and Lucchin, F. (1995). *Cosmology. The origin and evolution of cosmic structure.*

Couchman, H. M. P. (1991). Mesh-refined P3M - A fast adaptive N-body algorithm. *ApJL*, 368:L23–L26.

de Boer, W. (2005). Evidence for dark matter annihilation from galactic gamma rays? *New Astronomy Review*, 49:213–231.

de Boer, W., Sander, C., Zhukov, V., Gladyshev, A. V., and Kazakov, D. I. (2005). EGRET Excess of Diffuse Galactic Gamma Rays Interpreted as a Signal of Dark Matter Annihilation. *Physical Review Letters*, 95(20):209001–+.

Dehnen, W. (2001). Towards optimal softening in three-dimensional N-body codes - I. Minimizing the force error. *MNRAS*, 324:273–291.

Diemand, J., Kuhlen, M., and Madau, P. (2007). Dark Matter Substructure and Gamma-Ray Annihilation in the Milky Way Halo. *ApJ*, 657:262–270.

Diemand, J., Kuhlen, M., Madau, P., Zemp, M., Moore, B., Potter, D., and Stadel, J. (2008). Clumps and streams in the local dark matter distribution. *Nature*, 454:735–738.

Drukier, A. K., Freese, K., and Spergel, D. N. (1986). Detecting cold dark-matter candidates. *Phys. Rev. D*, 33:3495–3508.

Duffy, L., Sikivie, P., Tanner, D. B., Asztalos, S., Hagmann, C., Kinion, D., Rosenberg, L. J., van Bibber, K., Yu, D., and Bradley, R. F. (2005). Results of a Search for Cold Flows of Dark Matter Axions. *Physical Review Letters*, 95(9):091304–+.

Duffy, L. D. and Sikivie, P. (2008). Caustic ring model of the MilkyWay halo. *Phys. Rev. D*, 78(6):063508–+.

Efstathiou, G., Davis, M., White, S. D. M., and Frenk, C. S. (1985). Numerical techniques for large cosmological N-body simulations. *ApJS*, 57:241–260.

Einstein, A. (1916). Die Grundlage der allgemeinen Relativitätstheorie. *Annalen der Physik*, 354:769–822.

Einstein, A. (1917). Kosmologische Betrachtungen zur allgemeinen Relativitätstheorie. *Sitzungsberichte der Königlich Preußischen Akademie der Wissenschaften (Berlin), Seite 142-152.*, pages 142–152.

El-Zant, A. A. (2002). Regular and chaotic motion in softened gravitational systems. *MNRAS*, 331:23–39.

Ellis, J., Engvist, K., Nanopoulos, D. V., Olive, K. A., and Srednicki, M. (1984). SU(N,1) inflation. *NASA STI/Recon Technical Report N*, 85:26469–+.

Evans, N. W., Carollo, C. M., and de Zeeuw, P. T. (2000). Triaxial haloes and particle dark matter detection. *MNRAS*, 318:1131–1143.

Fall, S. M. (1978). On the evolution of galaxy clustering and cosmological N-body simulations. *MNRAS*, 185:165–178.

Fellhauer, M., Belokurov, V., Evans, N. W., Wilkinson, M. I., Zucker, D. B., Gilmore, G., Irwin, M. J., Bramich, D. M., Vidrih, S., Wyse, R. F. G., Beers, T. C., and Brinkmann, J. (2006). The Origin of the Bifurcation in the Sagittarius Stream. *ApJ*, 651:167–173.

Fillmore, J. A. and Goldreich, P. (1984). Self-similar gravitational collapse in an expanding universe. *ApJ*, 281:1–8.

Freese, K., Frieman, J., and Gould, A. (1988). Signal modulation in cold-dark-matter detection. *Phys. Rev. D*, 37:3388–3405.

Gavazzi, R., Mohayaee, R., and Fort, B. (2006). Probing dark matter caustics with weak lensing. *A&A*, 445:43–49.

Gehrels, N. and Michelson, P. (1999). GLAST: the next-generation high energy gamma-ray astronomy mission. *Astroparticle Physics*, 11:277–282.

Gelmini, G. B. (2006). DAMA detection claim is still compatible with all other DM searches. *Journal of Physics Conference Series*, 39:166–169.

Gilmore, R. (1982). *Catastrophe Theory For Scientists And Engineers*. Wiley, Dover, Chichester, Brisbane, Toronto.

Giuricin, G., Mardirossian, F., Mezzetti, M., and Santangelo, P. (1984). N-body simulations of small groups of galaxies. *ApJ*, 277:38–42.

Gnedin, O. Y., Kravtsov, A. V., Klypin, A. A., and Nagai, D. (2004). Response of Dark Matter Halos to Condensation of Baryons: Cosmological Simulations and Improved Adiabatic Contraction Model. *ApJ*, 616:16–26.

Gondolo, P. and Gelmini, G. (2005). Compatibility of DAMA dark matter detection with other searches. *Phys. Rev. D*, 71(12):123520–+.

Green, A. M. (2001). Weakly interacting massive particle annual modulation signal and non-standard halo models. *Phys. Rev. D*, 63(4):043005–+.

Gunn, J. E., Lee, B. W., Lerche, I., Schramm, D. N., and Steigman, G. (1978). Some astrophysical consequences of the existence of a heavy stable neutral lepton. *ApJ*, 223:1015–1031.

Hagmann, C., Kinion, D., Stoeffl, W., van Bibber, K., Daw, E., McBride, J., Peng, H., Rosenberg, L. J., and et al (1996). First results from a second generation Galactic axion experiment. *Nuclear Physics B Proceedings Supplements*, 51:209–212.

Hairer, E., Norsett, S. P., and Wanner, G. (1993). *Solving Ordinary Differential Equations I.* Springer Series in Computational Mathematics. Springer Verlag, Berlin.

Hayashi, E., Navarro, J. F., and Springel, V. (2007). The shape of the gravitational potential in cold dark matter haloes. *MNRAS*, 377:50–62.

Helmi, A. (2004a). Is the dark halo of our Galaxy spherical? *MNRAS*, 351:643–648.

Helmi, A. (2004b). Velocity Trends in the Debris of Sagittarius and the Shape of the Dark Matter Halo of Our Galaxy. *ApJL*, 610:L97–L100.

Helmi, A. and Gomez, F. (2007). Miller's instability, microchaos and the short-term evolution of initially nearby orbits. *arXiv:astro-ph/0710.0514*, 710.

Helmi, A., White, S. D., and Springel, V. (2002). The phase-space structure of a dark-matter halo: Implications for dark-matter direct detection experiments. *Phys. Rev. D*, 66(6):063502–+.

Helmi, A. and White, S. D. M. (1999). Building up the stellar halo of the Galaxy. *MNRAS*, 307:495–517.

Helmi, A., White, S. D. M., and Springel, V. (2003). The phase-space structure of cold dark matter haloes: insights into the Galactic halo. *MNRAS*, 339:834–848.

Hemsendorf, M. and Merritt, D. (2002). Instability of the Gravitational N-Body Problem in the Large-N Limit. *ApJ*, 580:606–609.

Hénon, M. H. (1971). The Monte Carlo Method (Papers appear in the Proceedings of IAU Colloquium No. 10 Gravitational N-Body Problem (ed. by Myron Lecar), R. Reidel Publ. Co. , Dordrecht-Holland.). *Ap&SS*, 14:151–167.

Henriksen, R. N. and Widrow, L. M. (1997). Self-Similar Relaxation of Self-Gravitating Collisionless Particles. *Physical Review Letters*, 78:3426–3429.

Henriksen, R. N. and Widrow, L. M. (1999). Relaxing and virializing a dark matter halo. *MNRAS*, 302:321–336.

Hernquist, L. (1990). An analytical model for spherical galaxies and bulges. *ApJ*, 356:359–364.

Hisano, J., Matsumoto, S., and Nojiri, M. M. (2004). Explosive Dark Matter Annihilation. *Physical Review Letters*, 92(3):031303–+.

Hisano, J., Matsumoto, S., Nojiri, M. M., and Saito, O. (2005). Nonperturbative effect on dark matter annihilation and gamma ray signature from the galactic center. *Phys. Rev. D*, 71(6):063528–+.

Hogan, C. J. (2001). Particle annihilation in cold dark matter micropancakes. *Phys. Rev. D*, 64(6):063515–+.

Hooper, D. and Serpico, P. D. (2007). Angular signatures of dark matter in the diffuse gamma ray background. *Journal of Cosmology and Astro-Particle Physics*, 6:13–+.

Ibata, R., Lewis, G. F., Irwin, M., Totten, E., and Quinn, T. (2001). Great Circle Tidal Streams: Evidence for a Nearly Spherical Massive Dark Halo around the Milky Way. *ApJ*, 551:294–311.

Johnston, K. V., Law, D. R., and Majewski, S. R. (2005). A Two Micron All Sky Survey View of the Sagittarius Dwarf Galaxy. III. Constraints on the Flattening of the Galactic Halo. *ApJ*, 619:800–806.

Jungman, G., Kamionkowski, M., and Griest, K. (1996). Supersymmetric dark matter. *Phys. Rep.*, 267:195–373.

Kamionkowski, M. and Koushiappas, S. M. (2008). Galactic substructure and direct detection of dark matter. *Phys. Rev. D*, 77(10):103509–+.

Kandrup, H. E. and Sideris, I. V. (2002). Chaos in cuspy triaxial galaxies with a supermassive black hole: a simple toy model. *Celestial Mechanics and Dynamical Astronomy*, 82:61–81.

Kandrup, H. E. and Sideris, I. V. (2003). Smooth Potential Chaos and N-Body Simulations. *ApJ*, 585:244–249.

Kandrup, H. E. and Siopis, C. (2003). Chaos and chaotic phase mixing in cuspy triaxial potentials. *MNRAS*, 345:727–742.

Kazantzidis, S., Kravtsov, A. V., Zentner, A. R., Allgood, B., Nagai, D., and Moore, B. (2004). The Effect of Gas Cooling on the Shapes of Dark Matter Halos. *ApJL*, 611:L73–L76.

Kerr, F. J. and Lynden-Bell, D. (1986). Review of galactic constants. *MNRAS*, 221:1023–1038.

Kinney, W. H. and Sikivie, P. (2000). Evidence for universal structure in galactic halos. *Phys. Rev. D*, 61(8):087305–+.

Komatsu, E., Dunkley, J., Nolta, M. R., Bennett, C. L., Gold, B., Hinshaw, G., Jarosik, N., Larson, D., and et al (2008). Five-Year Wilkinson Microwave Anisotropy Probe (WMAP) Observations: Cosmological Interpretation. *ArXiv e-prints*.

Komatsu, E., Dunkley, J., Nolta, M. R., Bennett, C. L., Gold, B., Hinshaw, G., Jarosik, N., Larson, D., Limon, M., Page, L., Spergel, D. N., Halpern, M., Hill, R. S., Kogut, A., Meyer, S. S., Tucker, G. S., Weiland, J. L., Wollack, E., and Wright, E. L. (2009). Five-Year Wilkinson Microwave Anisotropy Probe Observations: Cosmological Interpretation. *ApJS*, 180:330–376.

Kotok, E. V. and Shandarin, S. F. (1987). Maximum Density Attainable in the Nonlinear Stage of Gravitational Instability in a Collisionless Medium with a Thermal Velocity Scatter. *Soviet Astronomy*, 31:600–+.

Larson, R. B. (1978). A finite-particle scheme for three-dimensional gas dynamics. *Journal of Computational Physics*, 27:397–409.

Laskar, J. (1988). Secular evolution of the solar system over 10 million years. *A&A*, 198:341–362.

Laskar, J. (1990). The chaotic motion of the solar system - A numerical estimate of the size of the chaotic zones. *Icarus*, 88:266–291.

Laskar, J. (2003). Frequency map analysis and quasiperiodic decompositions. *arXiv:math/0305364*.

Lattanzi, M. and Silk, J. (2009). Can the WIMP annihilation boost factor be boosted by the Sommerfeld enhancement? *Phys. Rev. D*, 79(8):083523–+.

Law, D. R., Johnston, K. V., and Majewski, S. R. (2005). A Two Micron All-Sky Survey View of the Sagittarius Dwarf Galaxy. IV. Modeling the Sagittarius Tidal Tails. *ApJ*, 619:807–823.

Lee, B. W. and Weinberg, S. (1977). Cosmological lower bound on heavy-neutrino masses. *Physical Review Letters*, 39:165–168.

Lewin, J. D. and Smith, P. F. (1996). Review of mathematics, numerical factors, and corrections for dark matter experiments based on elastic nuclear recoil. *Astroparticle Physics*, 6:87–112.

Lichtenberg, A. and Lieberman, M. (1983). *Regular and Stochastic Motion*. Springer, New York, Heidelberg, Berlin.

Lucy, L. B. (1977). A numerical approach to the testing of the fission hypothesis. *AJ*, 82:1013–1024.

Lynden-Bell, D. (1962). Stellar dynamics. Potentials with isolating integrals. *MNRAS*, 124:95–+.

MacMillan, J. D., Widrow, L. M., and Henriksen, R. N. (2006). On Universal Halos and the Radial Orbit Instability. *ApJ*, 653:43–52.

Martin, S. P. (1998). A Supersymmetry Primer. In Kane, G. L., editor, *Perspectives on Supersymmetry*, pages 1–+.

Merritt, D. (1996). Optimal Smoothing for N-Body Codes. *AJ*, 111:2462–+.

Merritt, D. (1999). Elliptical Galaxy Dynamics. *Publ. Astr. Soc. Pac.*, 111:129–168.

Merritt, D. and Fridman, T. (1996). Triaxial Galaxies with Cusps. *ApJ*, 460:136–+.

Merritt, D. and Valluri, M. (1996). Chaos and Mixing in Triaxial Stellar Systems. *ApJ*, 471:82–+.

Merritt, D. and Valluri, M. (1999). Resonant Orbits in Triaxial Galaxies. *AJ*, 118:1177–1189.

Milgrom, M. (1983). A modification of the Newtonian dynamics as a possible alternative to the hidden mass hypothesis. *ApJ*, 270:365–370.

Miller, R. H. (1964). Irreversibility in Small Stellar Dynamical Systems. *ApJ*, 140:250–+.

Misner, C. W., Thorne, K. S., and Wheeler, J. A. (1973). *Gravitation*.

Mohayaee, R. and Salati, P. (2008). The cosmic ray signature of dark matter caustics. *MNRAS*, 390:1297–1310.

Mohayaee, R., Shandarin, S., and Silk, J. (2007). Dark matter caustics and the enhancement of self-annihilation flux. *Journal of Cosmology and Astro-Particle Physics*, 5:15–+.

Mohayaee, R. and Shandarin, S. F. (2006). Gravitational cooling and density profile near caustics in collisionless dark matter haloes. *MNRAS*, 366:1217–1229.

Moore, B., Calcáneo-Roldán, C., Stadel, J., Quinn, T., Lake, G., Ghigna, S., and Governato, F. (2001). Dark matter in Draco and the Local Group: Implications for direct detection experiments. *Phys. Rev. D*, 64(6):063508–+.

Natarajan, A. (2007). Weakly interacting massive particle annihilation in caustics. *Phys. Rev. D*, 75(12):123514–+.

Natarajan, A. and Sikivie, P. (2005). Robustness of discrete flows and caustics in cold dark matter cosmology. *Phys. Rev. D*, 72(8):083513–+.

Natarajan, A. and Sikivie, P. (2006). Inner caustics of cold dark matter halos. *Phys. Rev. D*, 73(2):023510–+.

Navarro, J. F., Ludlow, A., Springel, V., Wang, J., Vogelsberger, M., White, S. D. M., Jenkins, A., Frenk, C. S., and Helmi, A. (2010). The diversity and similarity of simulated cold dark matter haloes. *MNRAS*, 402:21–34.

Nusser, A. (2001). Self-similar spherical collapse with non-radial motions. *MNRAS*, 325:1397–1401.

Onemli, V. and Sikivie, P. (2007). Dark Matter Caustics in Galaxy Clusters. *arXiv:astro-ph/0710.4936*, 710.

Papaphilippou, Y. and Laskar, J. (1996). Frequency map analysis and global dynamics in a galactic potential with two degrees of freedom. *A&A*, 307:427–449.

Papaphilippou, Y. and Laskar, J. (1998). Global dynamics of triaxial galactic models through frequency map analysis. *A&A*, 329:451–481.

Peacock, J. A. (1999). *Cosmological Physics*.

Peccei, R. D. and Quinn, H. R. (1977a). Constraints imposed by CP conservation in the presence of pseudoparticles. *Phys. Rev. D*, 16:1791–1797.

Peccei, R. D. and Quinn, H. R. (1977b). CP conservation in the presence of pseudoparticles. *Physical Review Letters*, 38:1440–1443.

Peebles, P. J. E. (1980). *The large-scale structure of the universe*. Princeton University Press.

Peebles, P. J. E. (1982). Large-scale background temperature and mass fluctuations due to scale-invariant primeval perturbations. *ApJL*, 263:L1–L5.

Pieri, L. and Branchini, E. (2005). γ-ray flux from dark matter annihilation in galactic caustics. *Journal of Cosmology and Astro-Particle Physics*, 5:7–+.

Polyachenko, V. L. (1981). Nonlinear Evolution of Spherical Stellar Systems. *Soviet Astronomy Letters*, 7:79–+.

Press, W. H., Teukolsky, S. A., Vetterling, W. T., and Flannery, B. P. (1992). *Numerical Recipes in C: The Art of Scientific Computing*. Cambridge University Press, New York, NY, USA.

Primack, J. R., Seckel, D., and Sadoulet, B. (1988). Detection of cosmic dark matter. *Annual Review of Nuclear and Particle Science*, 38:751–807.

Rodionov, S. A. and Sotnikova, N. Y. (2005). Optimal Choice of the Softening Length and Time Step in N-body Simulations. *Astronomy Reports*, 49:470–476.

Rubin, V. C. and Ford, W. K. J. (1970). Rotation of the Andromeda Nebula from a Spectroscopic Survey of Emission Regions. *ApJ*, 159:379–+.

Sanglard, V. and et al (2005). Final results of the EDELWEISS-I dark matter search with cryogenic heat-and-ionization Ge detectors. *Phys. Rev. D*, 71(12):122002–+.

Savage, C., Freese, K., and Gondolo, P. (2006). Annual modulation of dark matter in the presence of streams. *Phys. Rev. D*, 74(4):043531–+.

Savage, C., Gondolo, P., and Freese, K. (2004). Can WIMP spin dependent couplings explain DAMA data, in light of null results from other experiments? *Phys. Rev. D*, 70(12):123513–+.

Schnee, R. W. (2006). Status of direct searches for WIMP dark matter. *arXiv:astro-ph/0612565*.

Siegal-Gaskins, J. M. and Valluri, M. (2007). Signatures of LCDM substructure in tidal debris. *arXiv:astro-ph/0710.0385*, 710.

Sikivie, P. (1983). Experimental tests of the 'invisible' axion. *Physical Review Letters*, 51:1415–1417.

Sikivie, P. (1985). Detection rates for "invisible"-axion searches. *Phys. Rev. D*, 32:2988–2991.

Sikivie, P. (1998). Caustic rings of dark matter. *Physics Letters B*, 432:139–144.

Sikivie, P. (1999). Caustic ring singularity. *Phys. Rev. D*, 60(6):063501–+.

Sikivie, P. (2003). Evidence for ring caustics in the Milky Way. *Physics Letters B*, 567:1–2.

Sikivie, P., Tkachev, I. I., and Wang, Y. (1995). Velocity Peaks in the Cold Dark Matter Spectrum on Earth. *Physical Review Letters*, 75:2911–2915.

Sikivie, P., Tkachev, I. I., and Wang, Y. (1997). Secondary infall model of galactic halo formation and the spectrum of cold dark matter particles on Earth. *Phys. Rev. D*, 56:1863–1878.

Sommerfeld, A. (1931). Über die Beugung und Bremsung der Elektronen. *Annalen der Physik*, 403:257–330.

Spergel, D. N., Verde, L., Peiris, H. V., Komatsu, E., Nolta, M. R., Bennett, C. L., Halpern, M., Hinshaw, G., and et al (2003). First-Year Wilkinson Microwave Anisotropy Probe (WMAP) Observations: Determination of Cosmological Parameters. *ApJS*, 148:175–194.

Spooner, N. J. (2007). Direct Dark Matter Searches. *arXiv:astro-ph/0705.3345*, 705.

Springel, V. (2005). The cosmological simulation code GADGET-2. *MNRAS*, 364:1105–1134.

Springel, V., Di Matteo, T., and Hernquist, L. (2005a). Modelling feedback from stars and black holes in galaxy mergers. *MNRAS*, 361:776–794.

Springel, V., Wang, J., Vogelsberger, M., Ludlow, A., Jenkins, A., Helmi, A., Navarro, J. F., Frenk, C. S., and White, S. D. M. (2008a). The Aquarius Project: the subhaloes of galactic haloes. *MNRAS*, 391:1685–1711.

Springel, V., White, S. D. M., Frenk, C. S., Navarro, J. F., Jenkins, A., Vogelsberger, M., Wang, J., Ludlow, A., and Helmi, A. (2008b). Prospects for detecting supersymmetric dark matter in the Galactic halo. *Nature*, 456:73–76.

Springel, V., White, S. D. M., Jenkins, A., Frenk, C. S., Yoshida, N., Gao, L., Navarro, J., Thacker, R., Croton, D., Helly, J., Peacock, J. A., Cole, S., Thomas, P., Couchman, H., Evrard, A., Colberg, J., and Pearce, F. (2005b). Simulations of the formation, evolution and clustering of galaxies and quasars. *Nature*, 435:629–636.

Springel, V., Yoshida, N., and White, S. D. M. (2001). GADGET: a code for collisionless and gasdynamical cosmological simulations. *New Astronomy*, 6:79–117.

Stadel, J., Potter, D., Moore, B., Diemand, J., Madau, P., Zemp, M., Kuhlen, M., and Quilis, V. (2009). Quantifying the heart of darkness with GHALO - a multibillion particle simulation of a galactic halo. *MNRAS*, 398:L21–L25.

Stiff, D. and Widrow, L. M. (2003). Fine Structure of Dark Matter Halos and its Effect on Terrestrial Detection Experiments. *Physical Review Letters*, 90(21):211301–+.

Stiff, D., Widrow, L. M., and Frieman, J. (2001). Signatures of hierarchical clustering in dark matter detection experiments. *Phys. Rev. D*, 64(8):083516–+.

Stoehr, F., White, S. D. M., Springel, V., Tormen, G., and Yoshida, N. (2003). Dark matter annihilation in the halo of the Milky Way. *MNRAS*, 345:1313–1322.

Taylor, J. E. and Navarro, J. F. (2001). The Phase-Space Density Profiles of Cold Dark Matter Halos. *ApJ*, 563:483–488.

Taylor, J. E. and Silk, J. (2003). The clumpiness of cold dark matter: implications for the annihilation signal. *MNRAS*, 339:505–514.

Tremaine, S. (1999). The geometry of phase mixing. *MNRAS*, 307:877–883.

Ullio, P. and Kamionkowski, M. (2001). Velocity distributions and annual-modulation signatures of weakly-interacting massive particles. *Journal of High Energy Physics*, 3:49–+.

Valluri, M. and Merritt, D. (1998). Regular and Chaotic Dynamics of Triaxial Stellar Systems. *ApJ*, 506:686–711.

van Albada, T. S. (1968). Numerical integrations of the N-body problem. *Bulletin of the Astronomical Institutes of the Netherlands*, 19:479–+.

Wachlin, F. C. and Ferraz-Mello, S. (1998). Frequency map analysis of the orbital structure in elliptical galaxies. *MNRAS*, 298:22–32.

Weinberg, S. (1972). *Gravitation and Cosmology: Principles and Applications of the General Theory of Relativity*.

Weinberg, S. (1978). A new light boson? *Physical Review Letters*, 40:223–226.

White, S. D. M. (1976). The dynamics of rich clusters of galaxies. *MNRAS*, 177:717–733.

White, S. D. M. (1978). Simulations of merging galaxies. *MNRAS*, 184:185–203.

White, S. D. M. and Zaritsky, D. (1992). Models for Galaxy halos in an open universe. *ApJ*, 394:1–6.

Wilczek, F. (1978). Problem of strong P and T invariance in the presence of instantons. *Physical Review Letters*, 40:279–282.

Xu, G. (1995). A New Parallel N-Body Gravity Solver: TPM. *ApJS*, 98:355–+.

Zeldovich, I. B., Mamaev, A. V., and Shandarin, S. F. (1983). Laboratory observation of caustics, optical simulation of the motion of particles, and cosmology. *Soviet Physics Uspekhi*, 139:153–163.

Zeldovich, Y. B. and Shandarin, S. F. (1982). The maximum density in heavy-neutrino clouds. *Sov. Astron. Lett.*, 8:139.

Zemp, M., Diemand, J., Kuhlen, M., Madau, P., Moore, B., Potter, D., Stadel, J., and Widrow, L. (2009). The graininess of dark matter haloes. *MNRAS*, 394:641–659.

Zhan, H. (2006). Optimal Softening for N-Body Halo Simulations. *ApJ*, 639:617–620.

Zwicky, F. (1933). Die Rotverschiebung von extragalaktischen Nebeln. *Helvetica Physica Acta*, 6:110–127.